UNIVERSITÉ PARIS XIII – SORBONNE PARIS NORD

École doctorale Sciences, Technologies, Santé Galilée

Tailoring mechanical behavior of metallic thin films through nanoengineering design strategies: Investigation of metallic glass and high entropy alloy films

Control du comportement mécanique des couches minces métalliques à travers des stratégies de nano-ingénierie: étude de couches minces de verre métallique et des alliages à haute entropie

Modifica del comportamento meccanico di film metallici attraverso il controllo della nanostruttura: studio dei vetri metallici e delle leghe ad alta entropia

---

THÈSE DE DOCTORAT

présentée par

Francesco Bignoli

Laboratoire des sciences des procédés et des matériaux

pour l’obtention du grade de
docteur en Science des matériaux

soutenue le 18/06/2024 devant le jury d’examen constitué de :

BARICCO Marcello	Professeur, Università di Torino	Rapporteur
LAZZARI Remi	Professeur, Institute des NanoSciences de Paris	Rapporteur
PUTZ Barbara	Docteur, Swiss Federal Laboratories for Materials Science and Technology, Empa	Examinatrice
IVANISENKO Julia	Professeur, Karlsruhe institute of technology	Examinatrice
DJEMIA Philippe	Professeur, Université Sorbonne Paris Nord	Examinateur
FAURIE Damien	Professeur, Université Sorbonne Paris Nord	Directeur de thèse au USPN
LI BASSI Andrea	Professeur, Politecnico di Milano	Directeur de thèse au Polimi
GHIDELLI Matteo	Professeur, Université Sorbonne Paris Nord	Directeur de thèse au USPN

POLITECNICO DI MILANO

Department of Energy

Doctoral program in Energy and Nuclear Science and Technology

---

Tailoring mechanical behavior of metallic thin films through nanoengineering design strategies: Investigation of metallic glass and high entropy alloy films

Control du comportement mécanique des couches minces métalliques à travers des stratégies de nano-ingénierie: étude de couches minces de verre métallique et des alliages à haute entropie

Modifica del comportamento meccanico di film metallici attraverso il controllo della nanostruttura: studio dei vetri metallici e delle leghe ad alta entropia

---

Doctoral dissertation of:
Francesco BIGNOLI

Thesis supervisor at Université Sorbonne Paris Nord: Prof. Damien Faurie
Thesis supervisor at Politecnico di Milano: Prof. Andrea Li Bassi
Thesis supervisor at Université Sorbonne Paris Nord: Prof. Matteo Ghidelli
Tutor: Prof. Carlo Spartaco Casari
The chair of the doctoral program at Université Sorbonne Paris Nord: Prof. Olivier Bodini
The chair of the doctoral program at Politecnico di Milano: Prof. Vincenzo Dossena

---

Year 2024 – Cycle XXXVI

Abstract

Metallic thin films have become object of intense research in recent years due to the activation of mechanical size effects, improving strength, plasticity and affecting the deformation behavior. However, the study of the connection between the local structure and the mechanical properties is not fully understood yet, while the research for new nanostructures capable to further improve and tailor their mechanical properties is still an open subject.

In this PhD project, we exploit the potential of Pulsed Laser Deposition (PLD) to synthetize novel thin film metallic glasses (TFMGs) and high entropy alloys (TFHEAs) with unique and tailored composition-microstructures among which cluster-assembled films and nanolaminates, while tuning local chemistry (especially with O incorporation) to improve strength-plasticity balance as probed with *in situ* SEM techniques. Among the main results the control of the local- and microstructure in TFMGs allows the delay and suppression of shear band instabilities together with an improvement of yield strength (> 3 GPa) plasticity (15% deformation). For the case of TFHEAs, the fine control of grain size leads to large hardness (up to 11 GPa, Hall-Petch strengthening) and improved crack resistance on tensile tests on polymeric substrates (3.44%) way above the sputtered deposited counterparts (8.3 GPa and 2%).

Overall, within this thesis we open the way to the use of PLD as a new technique to synthetize metallic films with unique nanostructure and composition leading to large and tailored mechanical properties with potential for various applications as high-performance structural coatings.

Keywords: Metallic glasses, high entropy alloys, nanoengineered thin films, Pulsed Laser Deposition, mechanical properties, *in situ* SEM characterization.

Resumé

Les films minces métalliques sont devenus l'objet de recherches ces dernières années en raison de l'activation d'effets mécaniques de taille, améliorant la résistance, la plasticité et le comportement à la déformation. Cependant, l'étude de la connexion entre la structure locale et le comportement mécanique d'un film mince n'est pas pleinement comprise et la recherche de nouvelles nanostructures capables d'améliorer leurs propriétés mécaniques est encore un sujet ouvert.

Dans ce projet de doctorat, nous exploitons le potentiel du dépôt laser pulsé (PLD) pour synthétiser de nouveaux verres métalliques (TFMG) et des alliages à haute entropie en films minces (TFHEA) avec une microstructure unique, y compris assemblée en grappes, en nanolaminés, ajustant la chimie locale (avec l'oxygène) pour améliorer l'équilibre résistance-plasticité, comme le prouvent les techniques *in situ* MEB. Parmi les principaux résultats, le contrôle de la structure locale des TFMG permet de supprimer les bandes de cisaillement ainsi qu'une amélioration de la plasticité de la limite d'élasticité (> 3 GPa) (15%). Pour le cas des TFHEA, le contrôle de la taille des grains conduit à une dureté élevée (jusqu'à 11 GPa, renforcement Hall-Petch) et à une résistance aux fissures lors des essais de traction sur substrats polymères (3.44 %) bien au-dessus des homologues déposés par pulvérisation (8.3 GPa et 2%).

Dans l'ensemble, dans cette thèse, nous ouvrons la voie à l'utilisation du PLD comme nouvelle technique de synthèse de films métalliques avec une nanostructure et une composition uniques et de grandes propriétés mécaniques pour des applications en revêtements structuraux haute performance.

Mots-clés: Verres métalliques, alliages à haute entropie, couches minces nano-ingénierie, dépôt laser pulsé, comportement mécanique, *in situ* MEB caractérisation.

Riassunto

I film sottili metallici sono diventati oggetto di intensa ricerca negli ultimi anni a causa dell'attivazione di effetti di confinamento geometrico, che migliorano la resistenza, la plasticità e influenzano il comportamento di deformazione. Tuttavia, lo studio della connessione tra la struttura locale e le proprietà meccaniche non è ancora del tutto compresa, mentre la ricerca di nuove nanostrutture in grado di migliorare ulteriormente le loro proprietà meccaniche è ancora un argomento di ricerca aperto.

In questo progetto di dottorato, sfruttiamo il potenziale della deposizione laser pulsata (PLD) per sintetizzare nuovi film sottili di vetri metallici (TFMG) e leghe ad alta entropia (TFHEA) con microstrutture e composizioni controllate su misura, tra cui film nanolaminati e assemblati in cluster, mentre si controlla la chimica locale (con l'incorporazione di O) per migliorare l'equilibrio resistenza-plasticità sondato con tecniche *in situ* SEM. Tra i principali risultati il controllo della microstruttura locale e della microstruttura nei TFMG consente il ritardo e la soppressione delle instabilità della banda di taglio insieme ad un miglioramento della plasticità del carico di snervamento (> 3 GPa) (deformazione del 15%). Nel caso dei TFHEA, il controllo accurato della dimensione del grano porta a un'elevata durezza (fino a 11 GPa, rinforzo Hall-Petch) e a una migliore resistenza alle fessurazioni nei test di trazione su substrati polimerici (3.44%) molto al di sopra delle controparti depositate mediante magnetron sputtering (8.3 GPa e 2%).

Nel complesso, all'interno di questa tesi apriamo la strada all'uso del PLD come una nuova tecnica per sintetizzare film metallici con nanostruttura e composizione uniche che portano a proprietà meccaniche ampie e su misura con potenziale per varie applicazioni come rivestimenti strutturali ad alte prestazioni.

Parole chiave: vetri metallici, leghe ad alta entropia, film sottili nano-ingegnerizzati, comportamento meccanico, caratterizzazione *in situ* SEM.

Acknowledgements

I recognize that this project has been very difficult for me, and I wouldn't have been able to obtain all the results that have been presented here in this thesis without the help of other people.

At the first place, I would like to thank my thesis supervisor Prof. **Matteo Ghidelli** for having offered to me his maximum support and guidance during my PhD helping me in improving my scientific capabilities and allowing me to experience this path between France and Italy giving me great opportunities inside and outside the field of material sciences.

I would also like to thank my other two supervisors Profs. **Andrea Li Bassi** and **Damien Faurie** for their help during this project in the field of physical vapor deposition and mechanical characterization of the samples.

In second place I would like to thank the other professors in Italy and France that helped in the training of the instruments used during this project namely **David Dellasega** of Polimi and **Philippe Djemia** of USPN.

I would also like to thank the profs. **Hahn Horst** and **Julia Ivanisenko** for their collaboration with us which allowed me to go for a month at Karlsruhe institute of technology to further improve my scientific skills and perform advanced characterization of my samples.

Lastly, I would like to thank my fellow PhD students at LSPM in France, namely **Cristiano Poltronieri**, **Davide Vacirca**, **Arjun Bharath Curam, Marco Alejandro Ezequiel Alvarado** and **Hatem Ben Mahmoud** for the ideas shared during these three years and all the joyous and sad moments that we had in this PhD.

Of course I thank also my Italian colleagues at Nanolab, **Cristina Mancarella**, **Luigi Bana**, **Davide Orecchia** and **Gabriele Alberti** for the company shared during my period at Milan for this PhD project.

I extend my thanks to all the people that I did not mention above for all the help that they gave me during these three years.

I sincerely thank all of you.

Papers in peer review journals

Within this PhD thesis we have published three papers in peer review journals, while other three are in preparation. A detailed list is reported below:

1. **F. Bignoli**, S. Rashid, E. Rossi, S. Jaddi, P. Djemia, G. Terraneo, A. Li Bassi, H. Idrissi, T. Pardoen, M. Sebastiani, M. Ghidelli. *Effect of annealing on mechanical properties and thermal stability of ZrCu/O nanocomposite amorphous films synthetized by pulsed laser deposition,* Materials & Design, 221, 110972, 2022.
2. C. Poltronieri, A. Brognara, **F. Bignoli**, S. Evertz, P. Djemia, D. Faurie, F. Challali, C. H. Li, L. Belliard, G. Dehm, J. P. Best, M. Ghidelli. *Mechanical properties and thermal stability of ZrCuAlx thin film metallic glasses: Experiments and first-principle calculations*, Acta Materialia, 258, 119226, 2023.
3. **F. Bignoli**, P. Djemia, G. Terraneo, G. Abadias, C. Gammer, A. Lassnig, C. A. Teixeira, S. Lee, A. Ahmadian, A. Li Bassi, D. Faurie, M. Ghidelli. *Novel class of crystal/glass ultrafine nanolaminates with large and tunable mechanical properties*, accepted the 17/04/2024 by ACS Applied Materials & interfaces with minor revisions. The results of this paper can be found in Chapter V of the PhD thesis.
4. **F. Bignoli**, S. Kalacska, P. Djemia, G. Abadias, D. Faurie, A. Li Bassi, M. Ghidelli, *Viscoelastic behavior of nanostructured film metallic glasses deposited by pulsed laser deposition,* Scripta Materialia, work in progress. The results of this paper can be found in Chapter IV of the PhD thesis.
5. D. Vacirca, **F. Bignoli**, A. Li Bassi, Y. Dai, A. Ahmadian, G. Abadias, P. Djemia, G. Dehm, J. P. Best, M. Ghidelli. *Size dependent mechanical properties of nanocrystalline high entropy alloys thin films with tunable microstructure*, Acta Materialia, work in process.
6. E. Boltynjuk, **F. Bignoli**, S. H. Nandam, J. Ivanisenko, R. Kruk, P. Djemia, D. Faurie, H. Hahn, M. Ghidelli. *Nanocolumnar thin film metallic glasses with enhanced and tunable mechanical and electrical properties for flexible electronic applications*, Scripta Materialia, work in progress.

List of contributions to national and international conferences

Within this PhD thesis our work has been presented to three international conferences with three oral presentations and one poster as shown in the list below:

1. **F. Bignoli**, D. Faurie, P. Djemia, F. Tetard, F. Challali, G. Terraneo, G. Abadias, L. Belliard, A. Li Bassi, M. Ghidelli: *Synthesis of nanoengineered ZrCuAl thin film metallic glasses by pulsed laser deposition with enhanced mechanical properties*, European materials research society spring meeting 2022, virtual conference, 30/05-03/06/2022, oral presentation.
2. **F. Bignoli**, D. Vacirca, D. Faurie, P. Djemia, F. Challali, G. Abadias, A. Li Bassi, M. Ghidelli: *Synthesis and mechanical behaviour of nanostructured high entropy alloy thin films by pulsed laser deposition*, journeés annuelles du GDR-HEA, Toulouse 13/09-14/09/2022, oral presentation.
3. **F. Bignoli**, D. Faurie, C. Gammer, A. Lassnig, S. Lee, C. A. Teixeira, A. Li Bassi, M. Ghidelli: *Engineering nanostructured metallic thin films by pulsed laser deposition with an outstanding combination of mechanical properties*, ICMCTF conference, San Diego California, 21/05-26/05/2023, oral presentation.
4. **F. Bignoli**, S. Rashid, E. Rossi, P. Djemia, M. Sebastiani, A. Li Bassi, M. Ghidelli, *Effect of annealing treatment on mechanical properties of nanostructured metallic films deposited by pulsed laser deposition*, ICMCTF conference, San Diego California, 21/05-26/05/2023, poster.

List of seminars

We presented our results to different research laboratories in three seminars as shown in the list below:

1. **F. Bignoli**, D. Faurie, A. Li Bassi, M. Ghidelli. *Toward new multielemental thin film metallic glasses with enhanced mechanical properties and thermal stability*, 09/07/2021, LSPM.
2. **F. Bignoli**, D. Faurie, A. Li Bassi, M. Ghidelli. *Novel nanostructured metallic thin films with enhanced mechanical properties deposited by pulsed laser deposition*, 22/09/2022, KIT.
3. **F. Bignoli**, D. Faurie, A. Li Bassi, M. Ghidelli. *Engineering new nanostructured metallic film by pulsed laser deposition*, 11/05/2023, KIT.

Table of contents

Preamble

This thesis is the result of a PhD project, originated from a collaboration between the Université Sorbonne Paris Nord (USPN, France) and the Politecnico di Milano (Polimi, Italy) within the framework of a Vinci program (Chapter III) of the Université Franco Italienne (UFI).

The UFI is an international organization which aims to favor the cooperation between French and Italian institutions, the Vinci program (Chapter III) financed joint PhD (cotutelle) between IT and FR universities. Specifically, the original project was entitled "*Vers des nouveaux alliages multi-éléments amorphes en couche minces aux propriétés mécaniques et stabilité thermique élevées - Verso nuove leghe amorfe multielementali in film sottile con elevate proprietà meccaniche e stabilità termica*" (Grant: #C3-2286).

In the frame of this collaboration, I worked between the Micro and Nanostructured Materials Lab (Nanolab) of Polimi (Italy) under the supervision of Prof. Andrea Li Bassi and the Laboratoire des Sciences des Procédés et des Matériaux (LSPM) of USPN (France) under the supervision of Profs. Matteo Ghidelli and Damien Faurie.

At the end of this project, two PhD diplomas will be delivered, respectively, from USPN and Polimi according to the cotutelle agreement. Following the mobility rules of UFI Chapter III grant I spent two years of the PhD in France at LSPM and one in year in Italy at Nanolab with the possibility to travel between the institutions to perform the different scientific experiments involved in the project.

Moreover, during this PhD project additional collaborations were established especially with the group of Prof. Christoph Gammer of the Erich Schmidt Institute of Materials Science of the Austrian Academy of Sciences (OAW, Austria) and the collaboration with the group of Prof. Hahn Horst of the Institute of Nanotechnology of the Karlsruhe Institute of Technology (KIT, Germany) which resulted in two research stay for one month and two weeks, respectively (2022-2023).

UNIVERSITÉ
FRANCO
ITALIENNE
UNIVERSITÀ
ITALO
FRANCESE

Introduction

In recent times, the study of metallic thin films has become increasingly important for many applications especially after the experimental observation of mechanical size effects, increasing the mechanical properties (i.e. yield strength) and affecting in the deformation mechanisms for micrometric sized samples. This has opened new approaches in the research of high-performance materials and structures with larger mechanical performances.

An example of a class of materials which benefit from the activation of mechanical size effects are metallic glasses especially if their characteristic size is below the micrometer scale. Specifically, metallic glasses (MGs), or amorphous metals, are known in their bulk form from sixty years and are characterized by an absence of long-range order and defects typical of crystalline metals, which confers them unique mechanical properties such as high yield strength (> 2 GPa) and elastic deformation (2%). However, they show limited plasticity due to their inherent brittleness caused by nucleation and the catastrophic propagation of shear bands. The transition from bulk to the thin film (thickness < 1 mm) allows to improve the plasticity of the metallic glasses by preventing the nucleation of shear bands, due to geometrical confinement.

A second class of materials that has become more and more important in the last years are the compositionally complex alloys also known as high entropy alloys (HEAs). Discovered in the late 1990s independently by the groups of Cantor and Yeh these alloys are obtained by mixing four or more metallic elements in equiatomic concentration, obtaining a single-phase crystalline structure with a heavily distorted lattice due to the differences between the interatomic radii of the single components. The structure of these alloys with a highly distorted lattice allows them to have good mechanical properties which remain stable in harsh work conditions (ie. high temperature environments), unlike conventional alloys like steels. While most of the studies on HEAs are based on bulk samples, the investigation of HEA thin films (HEAs-TF) has gained interest, due to the activation of size effect and a better control of the microstructure and grain size and the avoidance of the intergranular segregation of elements and chemical gradients observed in the microstructures of bulk samples.

However, for both cases, namely TFMGs and TFHEAs, the correlation between the local structure (chemical composition, crystalline structure, etc.…) and the mechanical behavior is still far from being completely understood, and the investigation of this correlation is still an open field of research.

In parallel, the development of new nanostructuring strategies (i.e multilayers, etc…) has gained interest as a way to further improve the strength and plasticity of these materials by introducing heterogeneities in the atomic structure to control the movement of plasticity carriers like shear bands and dislocations. For example, in multilayers two or more materials with different chemical compositions and crystallographic structures are alternated to increase the overall strength and plasticity of the film thanks to the presence of interfaces which confine the movement of dislocations for crystalline materials and shear bands for the amorphous ones, thus reducing the risks of brittle failures. Another possible nanostructuring strategy employed mainly in MGs is the controlled introduction of local density and chemistry modulations through the mechanical sintering of nanometric powders forming the so called “nanoglasses”, which can mitigate localized deformation phenomena.

In all the cases, the most popular physical vapor deposition method, i.e. magnetron sputtering, has a limited range of working conditions which limit the possible parameters that can be changed to nanostructure thin films MGs (TFMGs) and HEAs (TFHEAs). A second factor to be considered is the difference in sputtering yields of different elements, which increases the difficulty in controlling the chemical composition of sputtered films with complex stoichiometry like HEAs. Considering the current challenges in the field of metallic thin films, Pulsed Laser Deposition (PLD) has a great potential to easily deposit different films’ morphologies by changing the films’ growth mechanisms from atom-by-atom to cluster-assembled growth (via modulation of the deposition pressure), thus opening new doors for the deposition of nanostructured metallic thin films. PLD also offers other advantages among which the possibility to form out-of-equilibrium phases during the film's growth thanks to the high kinetic energy of the PLD plasma plume, the possibility to deposit very fine nanolayered structures by modifying the surface of the target and exploiting its roto-translation during deposition.

Nevertheless, despite its great potential, the literature regarding MGs and HEAs deposited by PLD is quite scarce up to present day due to the limited compositional flexibility with respect to sputtering and the difficulty to scale up PLD to industrial scale applications.

In this context, the objective of this PhD thesis is the synthesis of nanoengineered TFMGs and TFHEAs by exploiting the versatility of PLD, while investigating the interplay with the mechanical properties and deformation behavior exploiting a panel of mechanical characterization techniques. Specifically, a wide range of controlled nanostructures have been deposited the first being compact and cluster-assembled (nanogranular) monolithic TFMGs with higher free volume to improve plasticity and TFHEAs with controlled grain size to control the mechanical behavior. Crystalline/amorphous ultra-fine nanolaminates were deposited whose high number of interfaces can block shear bands propagation greatly improving their strength and plasticity. Dual-phase amorphous oxide-metal glasses were deposited which are able to deform homogeneously due to the free volume associated with covalent O bonds to fully suppress localized plastic behavior and fully amorphous multilayers alternating compact and nanogranular morphologies combining the points of strengths of the morphologies of the single sublayers.

The atomic structure and the mechanical properties of these new nanostructures has been examined through several techniques. Scanning electron microscopy (SEM), X-ray diffraction and reflectivity (XRD and XRR) and transmission electron microscopy (TEM) were used to study the morphology and the nanostructure of the films, while optoacoustic techniques like Brillouin spectroscopy (BS) and picosecond ultrasonics (PU), nanoindentation, tensile tests on polymer substrate and micropillar compression were used to investigate at various scales the mechanical response of the various nanostructures and compositions explored in this PhD project.

The PLD TFMGs and TFHEAs were also compared with magnetron sputtered counterparts to study the differences related to the deposition method highlighting the differences in mechanical strength related to it. I personally performed the deposition by PLD of all the films and performed all structural and mechanical characterizations presented in this project except for TEM characterization and micropillar compression tests which were the result of the external collaborations of OAW and KIT.

Nevertheless, I personally analyzed all the data obtained by the different characterizations, studying the different correlations between atomic structure and mechanical properties and organized them in this manuscript.

The PhD thesis is divided in 9 chapters:

- **Chapter I – State–of-the-art on metallic glasses.** In this Chapter, the structure and the mechanical properties of metallic glasses focusing also on deformation phenomena with the nucleation and propagation of shear bands (SBs) are presented. The main nanostructuring strategies described in literature to improve the plasticity of MGs to understand the physical mechanisms exploited to prevent the propagation of SBs and how they affect the mechanical performances of the MGs are also shown. The objectives of this PhD thesis regarding the structure and mechanical properties of PLD TFMGs are also exposed. The literature data presented in this Chapter will be used to underline the novelty of our results as well as to explain the mechanical behavior of MG samples deposited by PLD presented in the Chapters from IV to VII.
- **Chapter II – State–of-the-art on high entropy alloys.** The definition of high entropy alloys, their range of local structures and relationship with their mechanical properties are presented to highlight the interest of this class of materials and what are the current limits in the literature. I also present the objectives of this PhD thesis regarding the structure and mechanical properties of PLD TFHEAs. This Chapter will give

the elements to understand the mechanical behavior of the TFHEAs deposited by PLD shown in Chapter VIII and highlight their improved mechanical properties with respect to sputtered films.

- **Chapter III – Synthesis processes and characterization methods.** In this chapter the PLD process for the deposition of thin films is described together with the different deposition parameters to obtain the different nanostructures studied in this work. Moreover, the characterization techniques used for the investigation and of the structure and of the mechanical properties are presented in this Chapter.
- **Chapter IV – Effect of nanostructure and local chemistry on the mechanical behavior of monolithic thin film metallic glasses.** In this Chapter the structure and the mechanical properties of nanostructured $Zr_{50}Cu_{50}$ and $Zr_{46}Cu_{46}Al_8$ monolithic thin film metallic glasses (TFMGs) deposited by PLD at different pressures (i.e. compact and nanogranular) are presented. I show that the PLD TFMGs have higher density and improved mechanical properties when compared to sputtered counterparts and that the change in morphology can nearly double the plastic deformation necessary to cause plastic failure (6-7% strain failure for nanogranular films vs 3-4% for compact films).
- **Chapter V – Synthesis of $Zr_{50}Cu_{50}$/Al amorphous/crystalline ultrafine-nanolaminates with large and tunable mechanical properties.** In this Chapter the local structure of $Zr_{50}Cu_{50}$/Al nanolaminates deposited in vacuum and 5 Pa He by combining the $Zr_{50}Cu_{50}$ target with Al strips of different width is studied. These nanolaminates possess high strength, higher than the TFMGs studied in Chapter IV, thanks to the high number of interfaces and can reach large values of plastic deformation without percolative SBs (up to 15%) when the nanolayered and nanogranular structures are combined.
- **Chapter VI – Controlling the mechanical behavior of thin film metallic glasses through the controlled addition of oxygen.** In this chapter compact and nanogranular $Zr_{50}Cu_{50}$ and $Zr_{46}Cu_{46}Al_8$ films in which O has been incorporated by changing the vacuum conditions are studied. The presence of O causes the formation of a Zr-O rich phase and a Cu-rich phase in the films hinting at a multilayered structure and these films show large yield strength > 4 GPa and the nanogranular films can deform homogeneously > 15% without failure.
- **Chapter VII – Towards the development of new amorphous multilayered nanoarchitectures by alternating compact and nanogranular layers.** In this chapter the preliminary results on the local structure and mechanical properties of new multilayers based of $Zr_{50}Cu_{50}$ and alternating compact and nanogranular sublayers are presented. The aim of these multilayers is to combine the advantages of the two morphologies studied in the previous chapters to obtain films that have the large strength of compact films and high deformability of nanogranular films at the same time.
- **Chapter VIII – Synthesis and mechanical properties of nanostructured high entropy alloy thin films.** In this chapter the effect of the deposition pressure on the crystalline structure and mechanical properties of CoCrCuFeNi films is examined. The grain size and degree of texturing of the films decreases with the increase of deposition pressure and results in values of hardness > 10 GPa much larger than sputtered films (8.3 GPa). PLD films also show an incredibly high onset of crack formation (>2.7%) in tensile tests on polymer substrate reporting large toughness and film-substrate adhesion when compared to sputtered films.
- **Chapter IX – Conclusions & future perspectives.** This chapter summarizes all the main discoveries presented in this PhD thesis. The possible future continuations of the study begun in this project are presented in this chapter.

I. State–of-the-art on metallic glasses

In this Chapter the current state-of-the-art regarding metallic glasses in their bulk and thin film form together with their relative challenges and the objectives of this PhD project regarding these materials are presented.

1.1 Atomic structure of metallic glasses (MGs)

In this first section of the state-of-the-art the metallic glasses (MGs) are introduced together with their main strengths and limitations, especially focusing on their mechanical behavior. Bulk metallic glasses (BMGs) are a class of materials formed by metallic and or metalloid atoms obtained by liquid quenching at very high cooling rates (10^5-10^6 K/s) to obtain an amorphous (liquid-like) structure lacking the long-range order typical of crystals [1-3]. The amorphous structure of the BMGs usually appears as a random group of spheres when studied with high resolution transmission electron microscopy (HRTEM) and is characterized by broad diffraction peaks in the selected area electron diffraction (SAED) pattern [4-6], as shown in Figure 1.1a.

The absence of long-range order (LRO) indicated by the SAED pattern doesn't mean the material doesn't possess some degree of short (SRO) and medium range order (MRO) can be observed with synchrotron XRD (sXRD) to study the radial distribution function (RDF) associated with the glassy structure [7-9].

Molecular dynamics (MD) simulations like *ab initio* or reverse Monte Carlo simulations can be used to generate polyhedral structures that can fit the short and medium range order observed by RDF like the Voronoi tessellation presented in Figure 1b [9-11]. These polyhedral can be connected through vertexes, faces and edges but due to their shape. However, they cannot be arranged in a regular manner over a long range like normal crystalline structures (FCC, HCP, etc.) and thus leave an excess of free volume [7, 12].

In addition to the high cooling rate necessary to produce an amorphous structure, the chemical composition can be tuned to increase the glass forming ability (GFA), which is the ability to form an amorphous glass instead of a crystalline structure. Specifically, the Inoue's empirical rules to obtain a composition which can turn in a BMG consist in:

1. Mixing at the least three different atomic species.
2. The difference between the atomic radii of the different components must be > 12%.
3. The enthalpy of mixing between the components must be negative.

Following these rules increase the disorder of the structure and stabilize a supercooled temperature range in which the polyhedral can safely form [13-15].

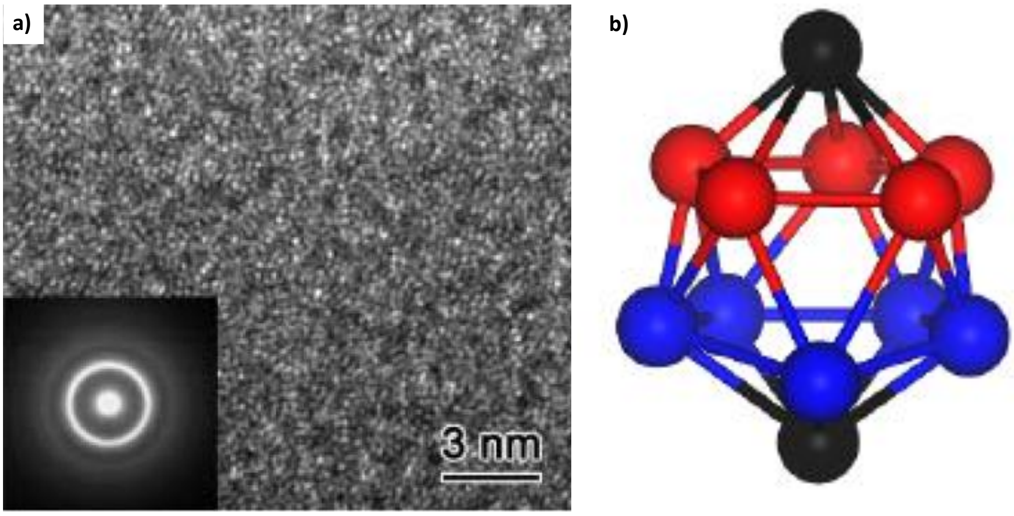

Figure 1.1: *HRTEM image of a ZrCuAlNi BMG with associated SAED from Ref. [4] (a) and an example of a <0 0 12 0> Voronoi cell from MD simulations used to describe the short-range order of a BMG adapted from Ref. [10].*

1.2 Mechanical properties of MGs

The mechanical properties of metallic glasses are intimately connected with their liquid-like isotropic atomic structure with the absence of defects typical of crystalline materials such as grain boundaries and dislocations which make them potential candidates for structural applications [1, 16-18]. The high amount of free volume related to the amorphous structure lowers the density ρ of the BMGs with respect to their crystalline counterparts and, consequently, reduces the elastic modulus *E* of the MGs [1]. BMGs have very high yield strength (σ_y) up to 2 GPa and elastic deformation ε (up to 2%), near the theoretical limit of σ_y equal to *E/20*, as shown in Figure 1.2, due to the absence of dislocations which activate plastic deformation at low stresses [16, 18, 19]. The high strength associated to the structure of BMGs confers them high wear and abrasion resistance [16, 20, 21]. When compared with traditional crystalline materials BMGs have high performance indexes like σ_y/ρ, the ration between yield strength and density, and resilience σ_y^2/E, a measure of the amount of the elastic energy that can be stored inside the material [16]. Moreover, most of the Zr-based and Pd-based BMGs present in literature possess high fracture toughness K_C (20-100 MPa*m$^{1/2}$) comparable with most metals because plastic deformation is activated at very large stresses [16, 22]. The toughness of BMGs can also be correlated with the Poisson's ratio ν and in literature the transition from brittle to tough and ductile glasses is observed when ν is higher than 0.32 [23, 24].

Nevertheless, the high σ_y of the BMGs reduces the process zone size $d = K_C^2/\pi\sigma_y$ (around 1 mm), which is the minimum dimension of a crack tip which is required for brittle fracture, making the BMGs macroscopically brittle [16, 25].

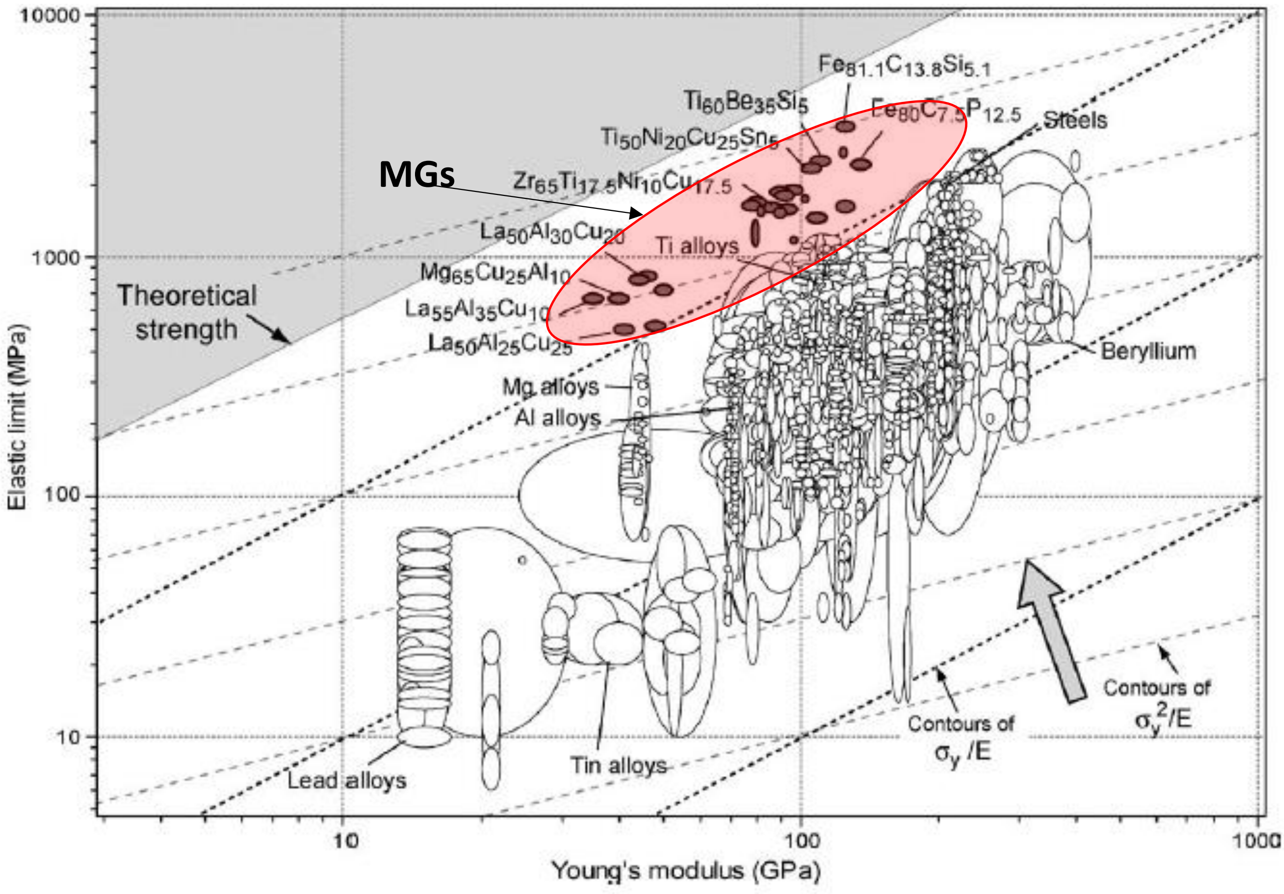

Figure 1.2: *Ashby chart of elastic limit vs Young's modulus of different classes of materials highlighting MGs adapted from Ref. [16].*

1.3 Fundamental deformation mechanism of MGs

The absence of defects such dislocations and grain boundaries in BMGs is responsible for their brittle deformation behavior mediated by shear bands (SBs) which can be considered the main weak point in their practical applications [26]. In the model proposed by Argon to explain the plastic behavior of BMGs shear transformation zones (STZs), small groups of atoms which are susceptible to inelastic deformation when subjected to shear stresses (Figure 1.3a), whose density of population and size is highly dependent on the amount of free volume and composition of the glass [26-28].

During mechanical testing the stress applied starts activating the different STZs and once surpassed the yielding stress, as shown in the stress-strain curve of Figure 1.3b, the STZs percolate together at speeds as high as the sound velocity inside the material and form a shear band of dimensions around 20-100 nm along the plane maximum shear stress like in the inset of Figure 1.3b [18, 29, 30]. The propagation of a SB is associated with a sudden increase of temperature (up to thousands of degrees) on the newly formed fracture surfaces during the crack propagation (around 100 ns) causing the formation of a thin fluid layer which leaves vein-like structures like the one presented in Figure 1.3c on the fracture surface which can be considered the fingerprint of SBs propagation [31, 32].

The high speed of the nucleation and propagation of SBs make the MGs macroscopically brittle and limit their practical applications [26] and for this reason different nanostructuring strategies are employed to try to suppress the propagation of SBs or at least reduce their speed.

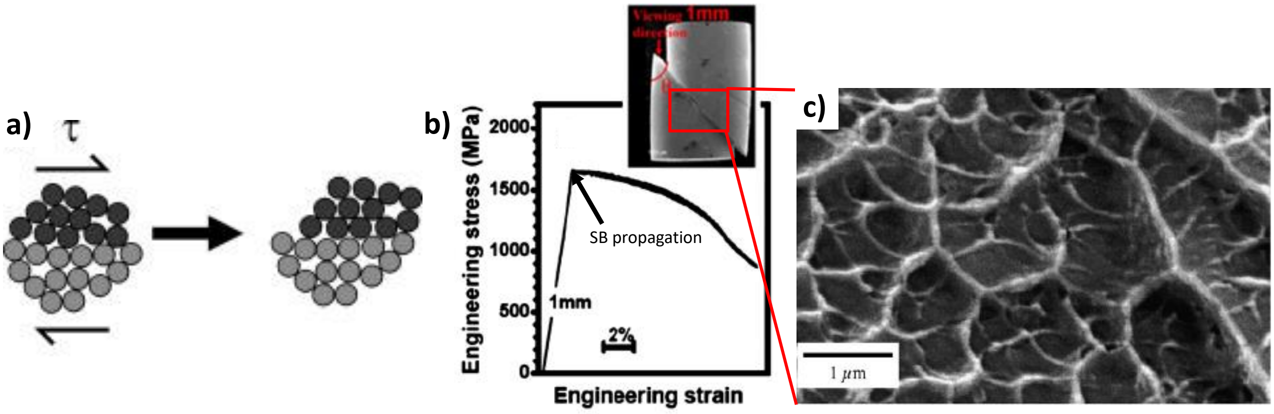

Figure 1.3: *(a) Schematic of a STZ under shear stress adapted from Ref. [18], (b) typical engineering stress-strain curve of a BMGs indicating the moment in which the SB propagates through the sample adapted from Ref.[33] and (c) SEM image of the fracture surface highlighting the corrugations generated by the sudden increase of temperature during the SB propagation adapted from Ref. [32].*

1.4 Strategies to mitigate the propagation of SBs:

1.4.1 Synthesis of thin film metallic glasses

One first possibility to limit the brittle behavior of MGs is to reduce the size of the sample below a critical size, like the process zone size *d* (~1 mm for BMGs), to activate mechanical size effects able to increase the strength and ductility with the possibility to mitigate or suppress the formation of shear bands (SBs) [34, 35]. Such strategy is often employed for the case of thin film metallic glasses (TFMGs) or when dealing with very small volumes such as nanopillars with dimensions below the micrometer.

A practical observation of the activation of size effects can be done with *in situ* SEM or TEM compression of micropillars with different diameters produced by focused ion beam (FIB) milling. As shown in Figure 1.4a by reducing the diameter of the examined pillar from 300 to 95 nm the propagation of SBs inside the sample is suppressed even at high strains and at the same time, as shown in Figure 1.4b, the stress necessary for yielding is increased.

This behavior can be connected to the progressive disappearance of heterogeneous defects acting as stress concentrators causing a transition towards a homogeneous activation of the STZs inside the material which require higher applied stresses [25, 36].
The transition from deformation through shear bands to homogeneous deformation can be explained by using Griffith theory for crack propagation and doing a balance between the elastic energy stored during deformation presented in Figure 1.4c. The elastic energy stored during deformation is equal to $\pi E\varepsilon_y^2 d^2 L/8$, where d and L are the diameter and height of the pillar having an aspect ratio $a = L/d$ and σ_y is the yield strain. The shear band energy equal to $\pi d^2\Gamma/2cos\theta$, where θ is the angle of propagation of the shear band and Γ is the shear band energy per unit area, from which a critical stress σ_c for the propagation of shear bands can be obtained as a function the diameter which is equal to $\sqrt{4\Gamma E/adcos\theta}$ and, as shown in in Figure 1.4c, plastic deformation can be achieved when σ_c is higher than σ_y [37-39]. Another factor to take into account for the homogeneous deformation of MGs is the deformation rate of the pillar as it is observed in the article of Tönnies *et al*. [40] in which pillars with 1 μm could be deformed homogeneously at a loading rate of 0.032 MPa/s. This result can be related to an increasing overlap of neighboring embryonic shear bands which hinder their maturation and catastrophic propagation [41, 42].

However, there are some cases of Pd-based [43], Zr-based [44, 45] and Mg-based [46] MGs in which the size effects observed above in Figure 4 are not observed and shear bands appear even in pillars with diameter as low as 50 nm. This result that can be related to a low Γ, which can go from values as low as 0.2 J/m^2 [47] to 10 J/m^2 [37], and consequently lower the critical diameter for the transition to values in the order of ~4 nm making the material response practically size independent [38].

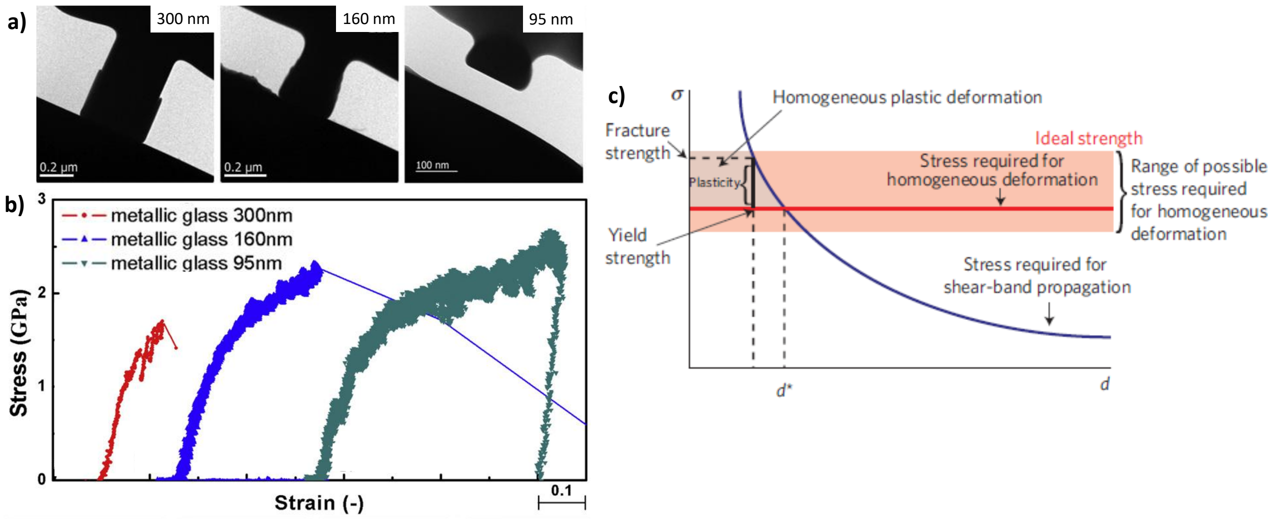

Figure 1.4: *(a) Postmortem TEM images of the $Sc_{75}Fe_{25}$ pillars with different diameters compressed pillars and (b) their relative stress-strain curves adapted from Ref. [48]. (c) Schematic of the necessary stress required to achieve shear bands vs homogeneous deformation as a function of the diameter of the sample adapted from Ref. [39].*

1.4.2 Multilayered architectures

The synthesis of multilayered architectures to combine the points of strength of different compositions and local structures is already practiced for crystalline materials with the aim to use the interfaces between the sublayers to block the movement of dislocation, increasing the hardness of the multilayer and promote the ductility of brittle metals by confining them between more ductile sublayers [49-51]

The main idea behind the deposition of multilayered nanostructure with MGs is to combine the activation of the mechanical size effects with the introduction of interface density and/or crystalline sublayers to delay and/or block the propagation of SBs to further improve the strength and the ductility of the MGs [52, 53].

The multilayers can be composed either alternating crystalline (FCC/BCC) and amorphous layers [54-56] or different amorphous layers with different composition [57-59]. In the case of crystalline/amorphous multilayers, the aim is to use a ductile crystalline metal like Cu to confine the shear bands in the amorphous layer, which also has a larger σ_y with respect to a crystalline layer, and promote a uniform co-deformation of the sample [54, 55, 60]. For example, ZrCu/Cu multilayers with bilayer period ranging from 200 to 20 nm can deform in compression plastically up to 10% without formation of SBs, while still having a σ_y of ~2.4 GPa and reaching very ultimate strengths depending on the bilayer period, as shown in Figure 1.5a [54].

The multilayer structures have also shown improved tensile strength and ductility with Kim *et al.* [61] producing freestanding 68/16 nm ZrCu/Cu multilayers with tensile strength of 2.5 GPa able to homogeneously deform up to 4% while pure ZrCu films fail at 2 GPa by shear banding.

The ratio between the thickness of the amorphous sublayer t_a and the crystalline sublayer t_c also influences the mechanical response of the film as presented in Figure 1.5b.

- When $t_c >>> t_a$ (right part of Figure 1.5b) only the crystalline layer is subjected to plastic deformation while the amorphous layer remains in the elastic regime [62, 63].
- When $t_c \sim t_a$ (central part of Figure 1.5b) it is possible to achieve a co-deformation of both layers obtaining a good combination of strength and plasticity by confining the shear bands in the amorphous layer and hindering the movement of dislocations in the crystalline layer [54, 55, 62, 64].
- When $t_c <<< t_a$ (left part of Figure 1.5b) the multilayer the crystalline layers can't stop the propagation of shear bands through the material and, while maintaining a high strength, most of the plasticity is lost [55, 62, 64].

The number of crystalline/amorphous interfaces has an important strengthening role since a high number of interfaces increases the energy necessary to propagate for a shear band thus increasing the strength of the film [54, 65, 66].

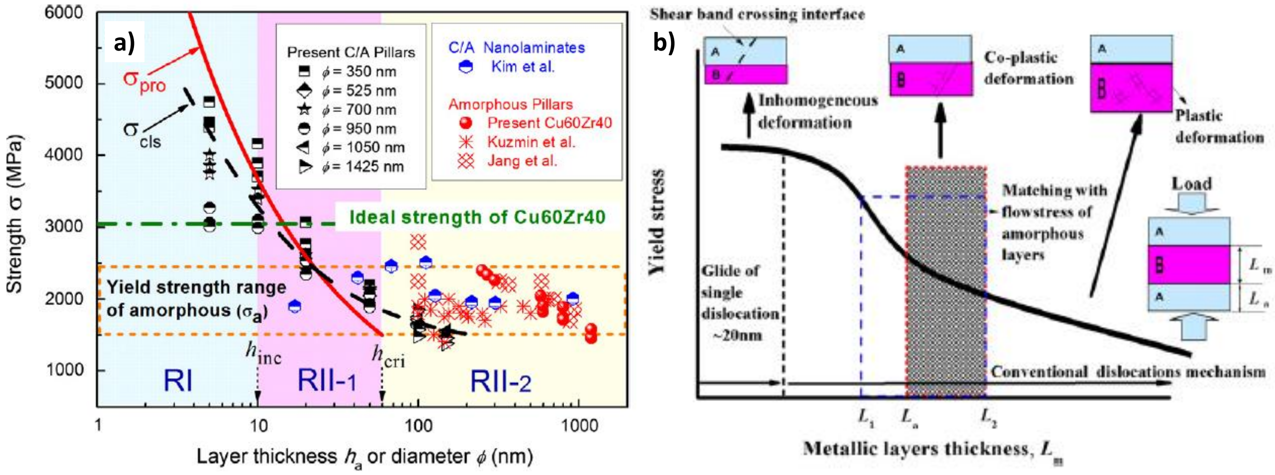

Figure 1.5. *(a) Ultimate strength vs layer thickness* h_a *of* h_a/h_a $Zr_{40}Cu_{60}$ *multilayers with* σ_{pro} and σ_{cls} *being the stress necessary to propagate shear bands and glide of dislocations in Cu adapted from Ref. [54]. (b) Schematic of the possible deformation mechanisms crystalline/amorphous multilayers depending on thickness of the crystalline layer adapted from Ref. [62].*

Alternatively, fully amorphous multilayers have been considered to improve the mechanical properties of TFMGs for applications in which the low corrosion resistance and radiation tolerance of crystalline metals could degrade the mechanical properties of the multilayer. Kuan *et al.* [57, 67] fabricated 50/50 nm $Zr_{55}Cu_{31}Ti_{14}/Pd_{77}Cu_6Si_{17}$ multilayers with improved hardness (6.5 GPa) with respect to their single components (5.3 and 5.8 GPa), able to delay of the formation of shear bands.

Micropillar compression experiments of 50/50 nm $Zr_{55}Cu_{31}Ti_{14}/Pd_{77}Cu_6Si_{17}$ show the presence of multiple shear bands propagating irregularly inside the pillar, being deviated at the interfaces between layers, and indicating a more homogeneous deformation with respect to monolithic MGs.

Zhou *et al.* [68] also report an improvement of the hardness for $Zr_{60}Cu_{40}/Zr_{61}Cu_{17.5}Ni_{10}Al_{7.5}Si_4$ multilayers with hardness increasing with the reduction of bilayer period reaching a maximum of 7.9 GPa for 5/5 nm nanolaminates which are attributed to the high density of interfaces hindering and deviating the SB during deformation. Molecular dynamics simulations of tensile tests of amorphous multilayers with different bilayer periods demonstrate that the strength and deformation mechanisms of multilayers are connected with the thickness of the single sublayers as shown in Figure 1.6 [69]. During deformation, the first SBs form in the sublayer with lower hardness and if the soft layer is larger than a critical thickness t_{cr0}, dependent on the elastic properties of the soft layer and thickness of the shear band, the sample will break (Right section of the graph in Figure 1.6). Otherwise (thickness < t_{cr0}) the SBs are blocked at the interface with the adjacent hard layers requiring more energy to continue the propagation in the structure.

The energy necessary for the propagation of the SB is directly proportional to the number of interfaces to pass through and at the same time the interaction between adjacent shear bands allows the transition to an increasingly homogeneous deformation of the sample (left part of the graph of Figure 1.6) [69].

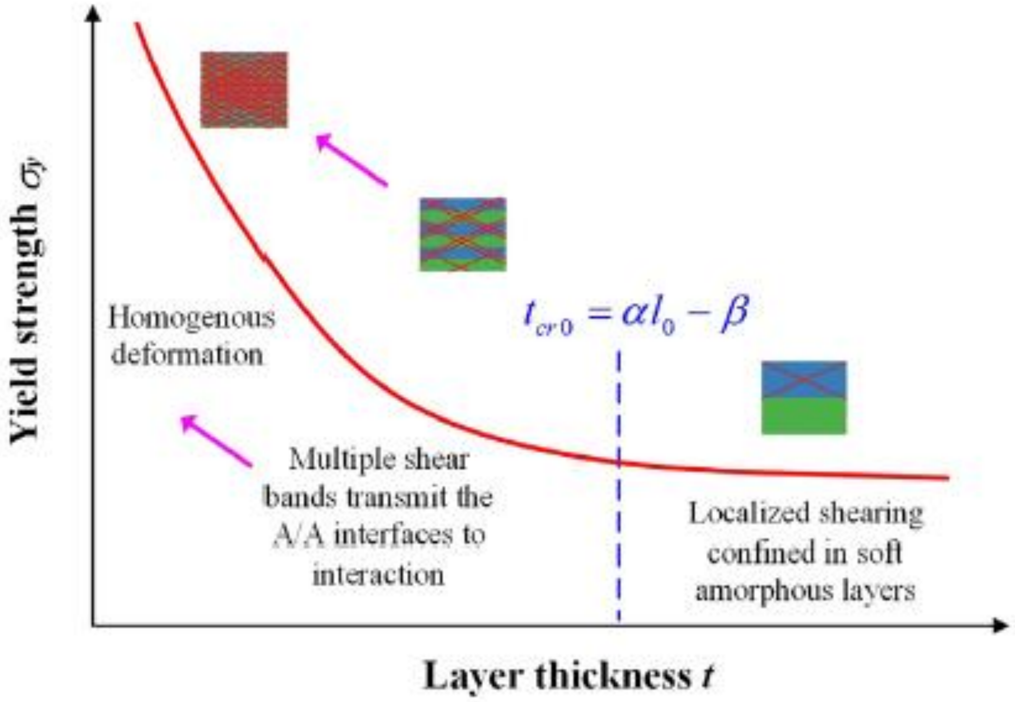

Figure 1.6. *Schematic of the mechanical behavior of amorphous/amorphous multilayers as a function of the layer thickness adapted from Ref. [69].*

In practical experiments this trend is not always confirmed. For example, Chen *et al.* [58] reports that for NiNb/ZrCuNiAl multilayers with bilayer period between 2/2 nm and 100/100 nm the hardness suddenly drops when the bilayer period goes below 25/25 nm after having followed the trend expected from Figure 1.6 for periods between 100/100 and 25/25 nm. The authors suggest that at low bilayer periods the deformation is carried by the activation of multiple STZ at the interfaces, which require less stress to activate with respect to mature shear bands [70], and the effective hardness is lower than what it is expected from theory [58].

1.4.3 Nanoglasses

Another nanostructuring strategy able to improve the mechanical properties of MGs is represented by the synthesis of "nanoglasses" [71, 72]. The production of nanoglasses can be a one or two-step process as schematized in Figure 1.7.

In the two-step process first step nanometric sized (5 - 12 nm) fully amorphous powders are deposited on a cold finger by inert gas condensation, then the powders are compacted at high pressures (up to 5 GPa) to form the final sample [71, 73, 74]. It is also possible to use magnetron sputtering at relatively high deposition pressures to deposit nanometric clusters, but it is only possible for very specific compositions [75, 76].
The structure of a nanoglass is thus like a nanocrystalline material with "cores" connected by interfaces with different local order similar to grain boundaries except that the whole structure is amorphous.

The differences in the local structure can be seen immediately when comparing the XRD of a MG and its nanoglass counterpart and the XRD of the nanoglass has a larger full width half maximum vs a normal MG indicating, on a qualitative level, a more disordered structure [73]. More detailed structural characterizations such as high energy X-ray diffraction, Mössbauer measurements and positron annihilation spectroscopy show that the nanoglass usually has two phases. Specifically, a core comparable to a traditional MG and a less dense structure confined to the boundary of the nanoparticle (NP), this density fluctuation between the core and outer shell of the nanograin is caused by the cooling of the NP on the substrate during the NP production step [72, 77-79].

Atom probe tomography and energy loss spectroscopy reveal that there is a fluctuation of the chemical composition of the NP associated with the density fluctuation described before [73, 80]. This segregation results in a more relaxed structure that can be obtained only with vapor deposition techniques and not the rapid quenching typical of BMGs [75].

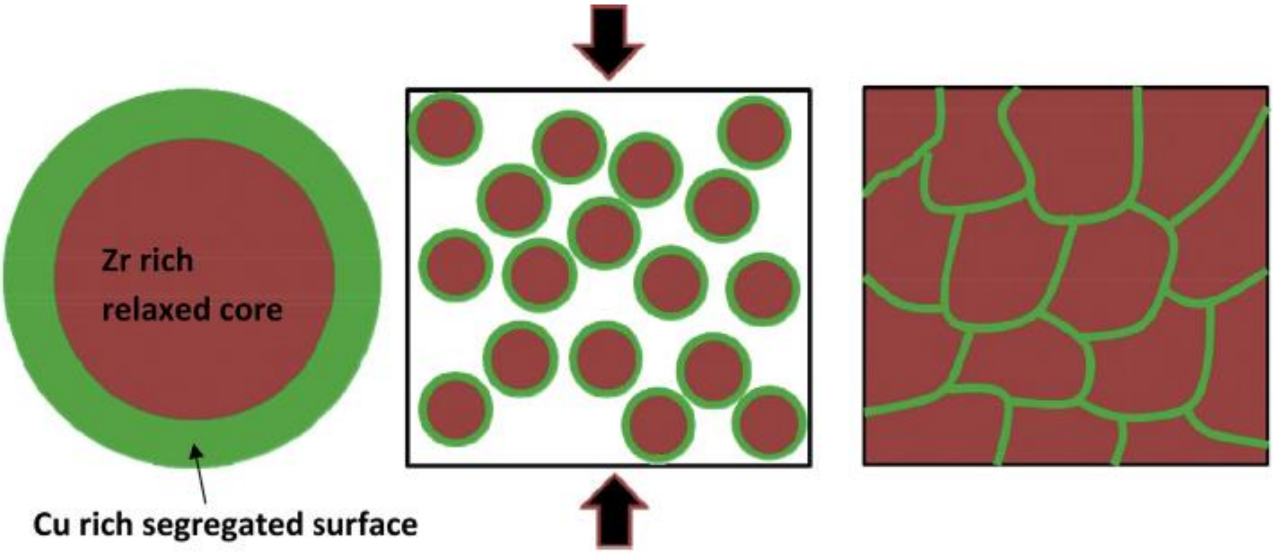

Figure 1.7. *Schematic of the production of a nanoglass from sputtered amorphous nanopowders adapted from Ref. [73].*

The nanostructure of the nanoglasses with its high amount of free volume, density and compositional fluctuations confer them interesting mechanical properties. Nanoglasses have higher elastic modulus *E* and hardness *H* with respect to their BMGs counterparts, for example $Zr_{36}Cu_{64}$ nanoglasses have *E* and *H* equal to 104.8 and 7.4 GPa respectively while melt-spun ribbons BMGs with the same composition have *E* and *H* equal to 93.9 and 6.7 GPa [73]. Similar improvements of *E* and *H* are observed in $Fe_{25}Sc_{75}$ [81] and Au-based [76] nanoglasses and they can be related to a combination of chemical effects (different mechanical properties of cores and shells) [74] and densification of the interfaces during deformation which increases the energy required for plastic deformation [82]. Much more important is the change of deformation mechanism observed in nanoglasses. As shown from the nanoindentation curves of Figure 1.8a,b SBs propagate during the indentation of a MG (pop ins in Figure 1.8a, pillar in Figure 1.8c) while the curves of the nanoglass in Figure 1.8b do not show sign of the pop-ins related to SB propagation meaning that nanoglasses are deformed homogeneously without formation of shear bands (Figure 1.8d) [73, 74, 81, 83] and can deform up to 18% in tension as shown in Ref. [84]. This drastic improvement of the plasticity of nanoglasses is connected to the large amount of free volume and composition fluctuations in the interfaces between amorphous grains which activates multiple STZs at the same time during deformation [71, 73, 83].

MD simulations of deformation of nanoglasses confirm this hypothesis by showing that during deformation the first embryonic shear bands start to form inside the interfaces of the glassy grains and then start to hinder each other propagation resulting in a more homogeneous deformation of the sample [85, 86]. This phenomenon prevents the accumulation of energy for a shear band to fully mature and causing the localized catastrophic shear band propagation typical of normal MGs [85, 86].

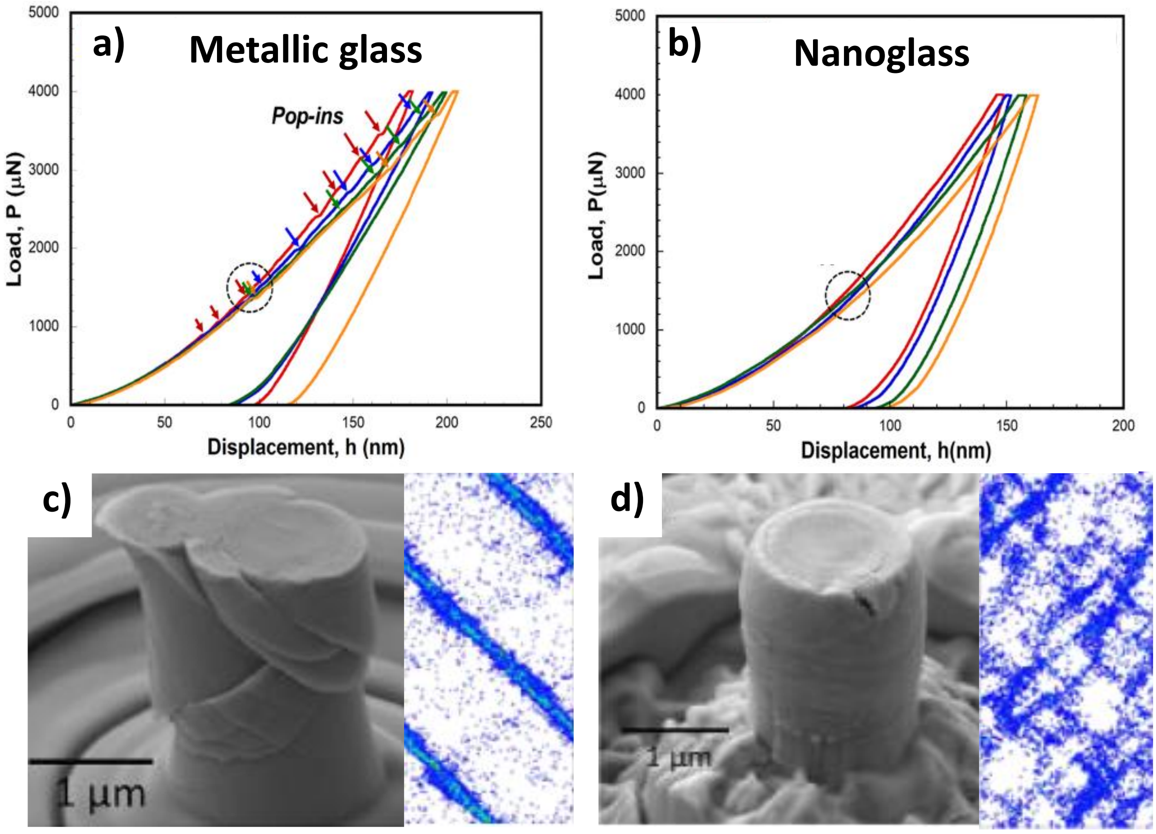

Figure 1.8. *(a) Nanoindentation load-displacement curves of ZrCu MG with the arrows highlighting the pop-ins related to the propagation of shear bands (a) and nanoglasses which do not have pop ins indicating homogeneous deformation (b) adapted from Ref. [83]. Compressed micropillars of ZrCu of MGs (c) and nanoglasses (d) highlighting the different distribution of shear bands adapted from Refs. [74, 85].*

1.5 Challenges for TFMGs

Having covered most of the properties of MGs in bulk and thin film form in the previous sections some of the possible challenges that can be tackled in the field of TFMGs are presented here.

The first and most important is the research of a synthesis method which can easily control the quantity of local structural and chemical heterogeneities during the deposition step which is very important in MGs to prevent the formation of SBs. Current magnetron sputtering systems have low flexibility in the control of their deposition parameters and, while multitarget systems can be give large flexibility in the control of the composition, the main morphology produced is either homogeneous or nanocolumnar morphology [87].

Furthermore, magnetron sputtering systems have many difficulties in the production of ultrafine nanolaminate structures due to the fast opening/closing cycles of the shutters and rapid power changes at the targets necessary to deposit multilayers with sublayer thickness < 10 nm. It is also currently impossible to couple different nanostructuring strategies (i.e multilayers and cluster assembled growth of “nanoglasses”) in the same deposition step in magnetron sputtering which prevents the development of finely tuned nanostructures which could combine high strength and ductility. A second challenge in the development of TFMGs is understanding well the correlation between the changes in the composition and the morphology and the mechanical behavior of the films.

Being able to decouple the effects of different nanostructures and compositions on the overall mechanical response of a sample would give a great advantage in the design of new thin film nanostructures for a wide variety of applications from structural coatings for reinforcement and protection of macrostructures to microelectronics and energy storage.

1.6 Objectives of the PhD project for MGs

This project aims to develop new nanostructured thin films metallic glasses by using pulsed laser deposition (PLD) and investigate the correlation between the different nanostructures and their mechanical behavior.

PLD is a deposition technique which uses short laser pulses (the duration of the pulses ranges from ns to ps) to ablate a target in a chamber with controlled atmosphere generating a plasma plume that deposit the elements of the target on a substrate. This technique is mainly utilized for the deposition of complex oxides and nitrides since it is able replicate precisely complex stoichiometries and is able to deposit a wide range of materials unlike magnetron sputtering [88, 89]. A secondary feature of PLD is the possibility to introduce a wide range of pressures (up 1000 Pa) of inert and/or reactive gasses during deposition to change the energy of the plasma allowing the deposition of different microstructures depending on the pressure and the type of gas used [90]. Despite its great flexibility and potential literature regarding the possible nanostructures and mechanical behavior of MGs produced by PLD is almost absent and only very recently Ghidelli *et al*. [91] has produced $Zr_{50}Cu_{50}$ thin film metallic glasses in vacuum and in He pressures between 10 and 100 Pa which had different morphologies (compact like a BMG for the films deposited in vacuum and cluster assembled similar to a nanoglass for the films deposited in He). These films have shown strong and controllable mechanical behavior with the films deposited in vacuum reaching a σ_y of 3 GPa and the films deposited in He being able to deform homogeneously in tension up to 10% without formation of SBs [91].

This project will expand from this starting point to study the possible nanostructures that can be obtained by changing the deposition parameters and then connect them to the changes in the mechanical behavior and compare them with more traditional magnetron sputtered TFMGs.

The different changes in the deposition parameters and relative nanostructures can be summarized as:

1. Observe the effects of the changes in chemical composition on the structure and mechanical properties are explored by depositing $Zr_{50}Cu_{50}$ and $Zr_{46}Cu_{46}Al_8$ respectively.
2. Change in the deposition pressure ranging from vacuum ($1x10^{-3}$ Pa) to 5 Pa He to change the growth regime of the film atom-by-atom to cluster-assembled growth to obtain compact films similar to traditional MGs [92] and nanogranular films similar to nanoglasses [71], respectively and compare them magnetron sputtered films.
3. Deposit amorphous/crystalline $Zr_{50}Cu_{50}$/Al ultrafine nanolaminates in vacuum and 5 Pa He by modifying the $Zr_{50}Cu_{50}$ target to introduce a controlled amount of heterogeneities through interfaces and exploit the increase in strength and ductility related to them [54] in synergy with compact and nanogranular morphology.
4. Change the baseline vacuum of the deposition chamber to incorporate O during the deposition of compact and nanogranular $Zr_{50}Cu_{50}$ and $Zr_{46}Cu_{46}Al_8$ films to study how the O interacts with the different amorphous structures with the aim to achieve substantial improvements of plasticity as observed for some MGs [93].

5. Explore the possibility to deposit compact/nanogranular multilayers alternating compact and nanogranular sublayers to combine the points of strength of the different nanostructures in a single sample.
6. Comparison with magnetron sputtered TFMGs to better understand the differences in local structure and mechanical properties related to the different deposition methods.

1.7 Conclusions

In this Chapter the state-of-the-art of MGs is explored together with the possible strategies to mitigate the brittle behavior related to the plastic deformation mediated by SBs which afflict MGs. It is shown that MGs do not possess long range order like crystalline materials but only some short and medium range order related to the composition and cooling history of the material. The absence of a crystalline structure removes all the features typical of crystalline metals like dislocations and grain boundaries and this confers interesting mechanical properties to MGs among which a high yield strength, elastic deformation and toughness.

However, MGs are limited by being macroscopically brittle since their main deformation mechanism is the formation of localized SBs propagating almost instantaneously through the sample after nucleation. Different strategies are presented to mitigate or suppress the propagation of SBs in MGs ranging from geometrical confinement by reducing the dimensions of the sample at the micrometric scale to multilayered architectures and nanoglasses. By reducing the size of the MG to the microscale it is possible to increase its strength and plasticity by reducing the number of defects which can favor the propagation of SBs.

In multilayered structures layers of different chemical composition and structures are combined and by controlling the bilayer period and the thickness of the different sublayers it is possible to confine the shear bands in single layers and promote a more homogeneous deformation of the structure.

In the nanoglasses a controlled amount of chemical and density fluctuations is present in the amorphous structure activating multiple small SBs propagation processes which are evenly distributed in the nanoglass and preventing the localization of the deformation in single brittle SBs.

The challenges regarding the research of new nanostructures to improve the mechanical properties of MGs are presented in this Chapter together with how this project is going to use PLD to produce TFMGs with improved strength and plasticity.

II. State–of-the-art on high entropy alloys

In this Chapter, the state-of-the-art of the high entropy alloys (HEAs) is presented in their bulk and thin film form together with their relative challenges and the objectives of this PhD project regarding these materials are presented.

2.1 High entropy alloys (HEAs): definition and structures

The high entropy alloys (HEAs) are defined as a class of metallic materials with four or more principal elements with the concentration of each element being between 5 and 35 %at. characterized by a single solid phase structure without formation of intermetallic compounds [94-96].

The first examples of this class of materials were a FeCrMnNiCo equiatomic alloy studied by Cantor *et al.* [97] which had a single FCC phase and the CoCrCuFeNi equiatomic FCC alloy studied by Yeh *et al.* [98] that could transform into a BCC phase with the addition of elements like Al, Fe, Ti, V and these alloys could achieve better mechanical and functional properties better than traditional alloys like steels and superalloys [99, 100]. This makes the HEAs interesting for a wide range of applications ranging from mechanical components in harsh environments to energy storage and radiation protection [96, 101]. The first criterion to use to see if an alloy can be identified as a HEA is its entropy of configuration S_{conf} defined as $-R\sum_{i=1}^{N}\chi_i ln\chi_i$, where R is the universal gas constant, N is the number of elements and χ_i is the atomic fraction of each element, and for conventional alloys, called also low entropy alloys, have $S_{conf} < 0.69R$, alloys with 3 or 4 elements are called medium entropy alloys (MEA) and have $0.69R < S_{conf} < 1.6R$, and lastly proper HEAs have $S_{conf} > 1.6R$ [102-104]. However, S_{conf} is a too generic criterion to produce HEAs and additional parameters are needed to know which phases and crystalline structures can be obtained when choosing the atoms for a new HEA. The first two parameters to be taken into account are the total enthalpy of mixing of the solution ΔH_{mix}, defined as $\sum_{i=1,j\neq i}^{N} 4\Delta H_{ij}^{mix}\chi_i\chi_j$ where ΔH_{ij}^{mix} is the mixing enthalpy of two of the elements chosen for the alloy [105], and the atomic size mismatch δ calculated as $\sqrt{\sum_{i=1}^{N}\chi_i(1-\frac{r_i}{r_{av}})^2}$, where r_i is the atomic radius of a single component and r_{av} is the average radius of all the atoms chosen for the alloy [106], which consider the lattice distortion of the system exemplified in Figure 2.1a. From these two parameters it is possible to build a map, presented in Figure 2.1b, in which it is shown that to obtain a solid solution with a single crystalline structure a ΔH_{mix} between -10 and 10 kJ/mol and a δ between 0 and 5 [96, 107] while for $\delta > 5$ and for lower ΔH_{mix} multiphase intermetallic inclusions or amorphous structures are obtained.

To further refine the selection of the atoms two other parameters can be considered which are the average valence electron concentration (VEC) of the alloy and ϕ, a dimensionless parameter groups together the entropy contribution of configuration S_{conf}, mixing S_{mix} ($\Delta H_{mix}/T_m$ with T_m being the average melting point of all the elements) and atomic mismatch S_E, directly proportional to δ and equal to $(S_{conf} - S_{mix})/S_E$ [108].

When these parameters are used together as in Figure 2.1c it is shown that a $\phi > 20$, synonym with high total entropy, is necessary to have a single phase crystalline structure and that depending on the VEC it is possible to obtain HCP (VEC ≈ 2.8), BCC (VEC ≈ 5) or FCC (VEC ≈ 8.5) phases [96, 109]. The reason why the formation of a single crystalline phase in HEAs is favored instead of the segregation of intermetallic is thermodynamically explained with minimization of the Gibbs free energy $\Delta G = \Delta H - T\Delta S$ which HEAs achieve thanks to their high ΔS contribution while intermetallic usually have very low ΔS [94, 104, 110].

A consequence of mixing together many different elements to obtain a HEA is that the resulting crystalline structure will be subjected to several lattice distortion which is observed in practice with a reduction of intensity and broadening of the XRD diffraction patterns [98, 111] and source of interesting mechanical and functional properties [101, 112].

Furthermore, the distorted lattice structure reduces the kinetics of diffusion, grain growth and phase transformation since the presence of many different elements results in a highly fluctuating lattice potential which can creates many low potential traps that block diffusing atoms. Since each element also has a different diffusion rate, all the phenomena which require a collective redistribution of all the atoms, like grain growth or phase transformation, are severely slowed down by the least diffusing element in the system and consequently the thermal stability of the grain structure of the HEAs is far superior to traditional ones [96, 104, 113].

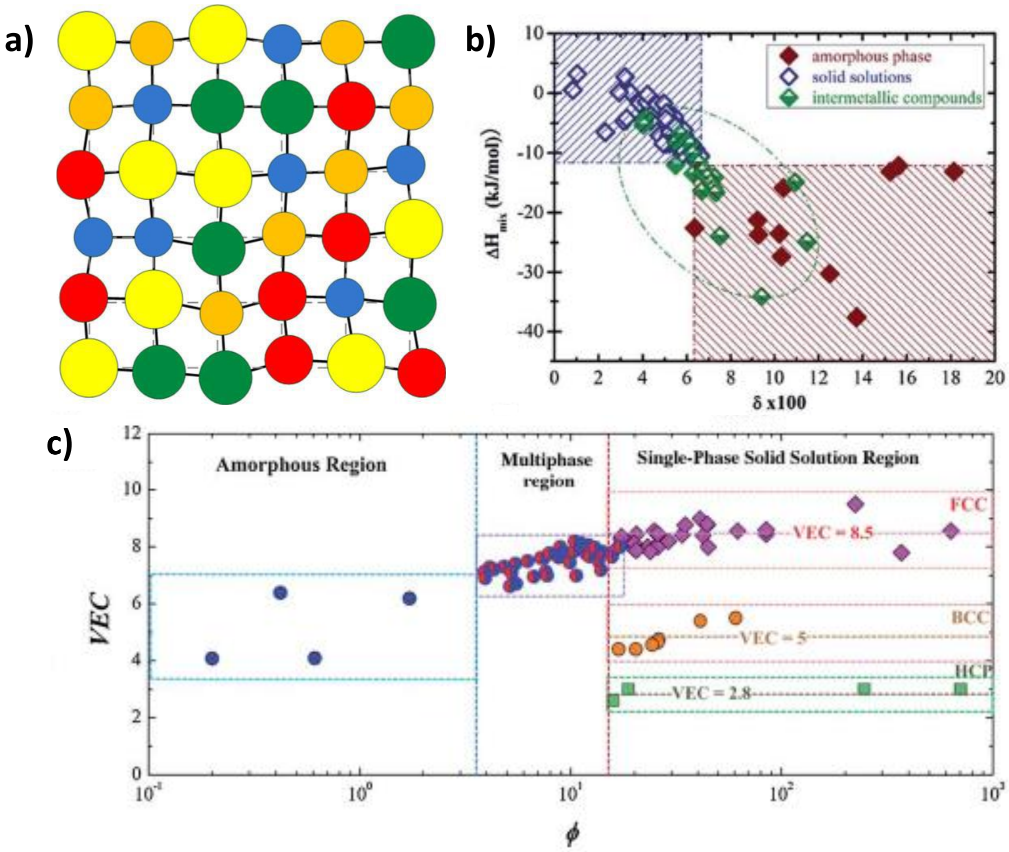

Figure 2.1 : *(a) Model of the crystalline structure of a HEA highlighting the lattice distortion caused by the mismatch of the different atomic radii adapted from Ref. [103],* ΔH_{mix}*-* δ *classifying the different atomic structures that can be obtained when choosing the elements for a HEA adapted from Ref. [107] and (c) the VEC -* ϕ *graph predicting the possible crystalline structures of HEAs adapted from Ref. [109].*

2.2 Mechanical properties of HEAs

HEAs became a quite important field of research because the high tunability of the composition allows to obtain materials with outstanding mechanical properties that are difficult, if not impossible, to obtain with conventional alloys.

For example, HEAs have a wide range of mechanical properties depending on the composition and can generally reach higher combinations of strength and failure deformation than common alloys in both compression (σ_y >3 GPa with 40% deformation) (Figure 2.2a) and in tension (σ_y > 0.6 GPa with 60% deformation) (Figure 2.2b) [109, 114, 115] overcoming in some cases the classic trade-off between strength and ductility of conventional alloys through grain refinement and activation of nanotwinning deformation [109]. Some HEAs can also achieve very high specific strengths by combining together light elements to reduce the average mass density while keeping a high strength thanks to the lattice distortion of the structure like in the case of a FCC $Al_{20}Li_{20}Mg_{10}Sc_{20}Ti_{30}$ which reached a hardness of 6 GPa while keeping a density 2.67 g/cm^3 [116]. The improved hardness related to the distorted lattice structure of HEAs is also responsible to an improved wear resistance as in the case of AlCoCrCuFeNiV [117, 118]. More importantly, HEAs can keep their high mechanical performances at high temperatures where even specific superalloys designed for applications at extreme temperature collapse [104, 109]. For example, HEAs like $NbCrMo_{0.5}Ta_{0.5}TiZr$ [119] can keep a σ_y above 700 MPa at 1000 °C, as shown in Figure 2.2a, thanks to the sluggish diffusion of their components in the distorted crystalline structure which delay the atomic reconfiguration phenomena responsible for the mechanical loss at high temperatures [96, 104, 113].

HEAs can also achieve large fracture toughness, as shown in Figure 2.2b, and for example CrMnFeCoNi can keep a constant toughness of 220 MPa*m$^{1/2}$ combined with a strain at failure > 60% from ambient temperature to 77 K which is attributed to the formation of nanotwins during deformation.

The slow diffusion rates inside the crystalline structure of HEAs and the possibility to form strong and stable passivation layers makes the HEAs highly resistant to corrosion [120, 121] making them interesting for structural applications in harsh environments.

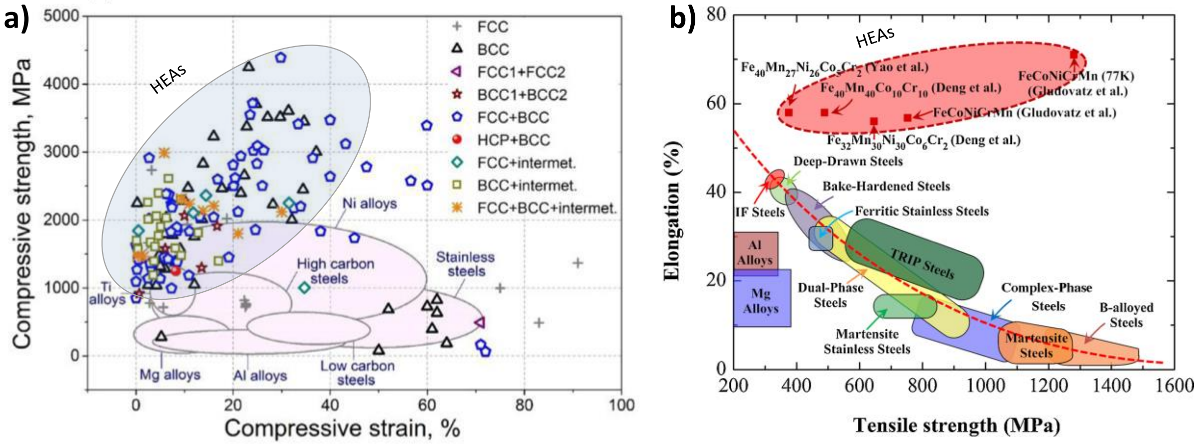

Figure 2.2: *(a) Compressive strength and failure strain of HEAs and traditional alloys adapted from Ref. [114] and (b) tensile strength vs maximum elongation for HEAs and traditional alloys adapted from Ref. [109].*

2.3 Transition bulk - thin film HEAs

The majority of works on HEAs revolves around the production and characterization of macroscopic ingots from casting and arc melting and only recently the study of thin films through physical vapor deposition has gained interest [122, 123].

The production of thin films using techniques like magnetron sputtering has some advantages with respect to traditional casting of bulk samples. Firstly, the higher cooling rate during vapor phase deposition process avoids the segregation of elements or the formation of dendritic structures which can happen during the crystallization of bulk samples and instead promotes the formation of a more homogeneous structure like in the case of as-cast bulk CoCrCuFeNi having a dendritic structure with Cu segregation at the interfaces as shown in the EDX map of Figure 2.3a [124]. This is absent for magnetron sputtered CoCrCuFeNi of Figure 2.3b due to the atom-by-atom growth mechanism and high cooling rates associated with vapor deposition [125, 126].

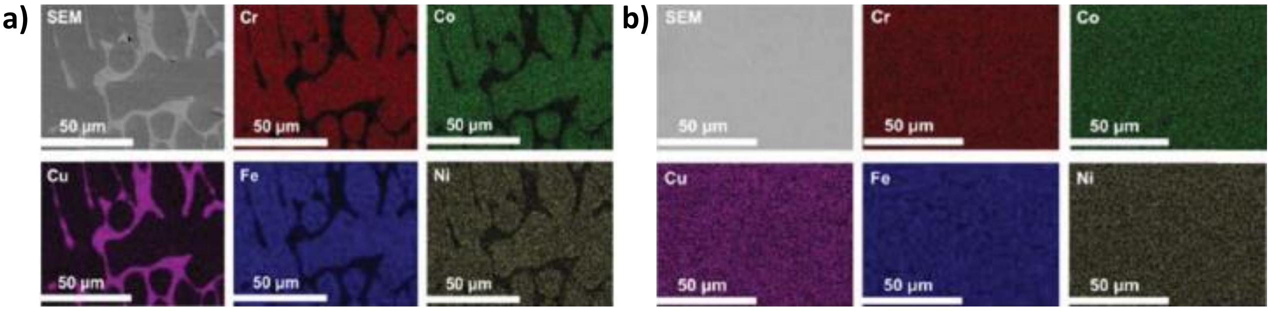

Figure 2.3. *EDX maps of the surfaces of (a) bulk and (b) sputtered CoCrCuFeNi highlighting the different distribution of elements adapted from Ref. [126].*

Co-sputtering with multiple single element targets make it also easy to produce HEAs films controlled and highly tunable composition that can arise in the production of a multielement target with a complex composition [122]. The rapid cooling rate related to sputtering also reduces the crystalline grain size which consequently increases the density of grain boundaries and dislocations which in turn increases the strength of the alloy [127, 128]. The distorted lattice structure and relative sluggish diffusion typical of HEAs offset the low thermal stability of nanocrystalline films which are subjected to recrystallization and rapid grain growth due to the high density of unstable grain boundaries [101, 129].

The reduction of size of the samples can also activate mechanical size effects which can increase the strength and the ductility of a film like in the case of nanocrystalline NbMoTaW, a strong but brittle alloy in bulk form, that can achieve high plasticity in compression up to 30% and σ_y around 8 GPa for pillars of 70 nm diameter as shown in Figure 2.4 [130].

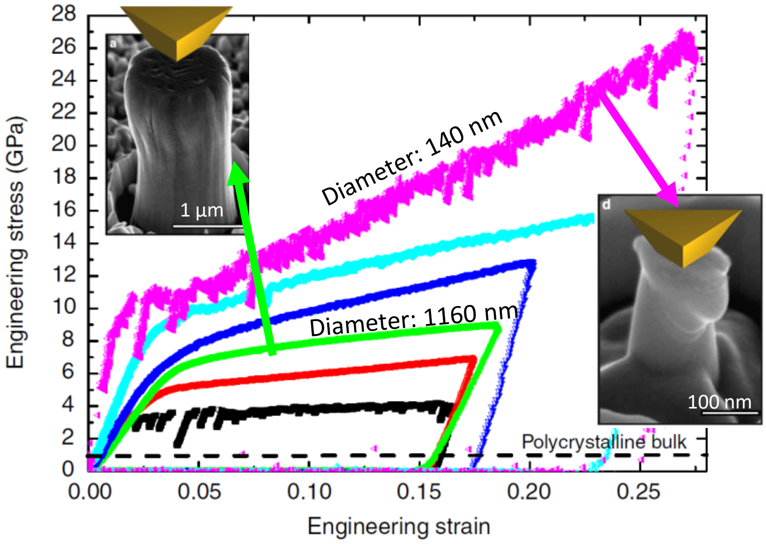

Figure 2.4. *Evolution of the stress-strain behavior of NbMoTaW HEA in compression due to increasing geometrical confinement adapted from Ref. [130].*

The control of the thickness of a deposited HEA sample can be used to change the local structure of the alloy like in the case of CoCrFeMnNi films deposited by magnetron sputtering with thicknesses between 300 and 1400 nm in which a transition from an amorphous phase to an FCC phase is observed with the increase of thickness [131]. This results in a decrement of hardness from 9 to 8 GPa that is connected with the transition from incomplete island growth of the film at 300 nm to the formation of a columnar crystalline layer rich in nanotwins for larger thicknesses [131]. A similar behavior is documented by Li *et al.* [132] for FeAlCuCrCoMn thin films deposited by direct current magnetron sputtering which has an amorphous structure for thicknesses below 1 µm with Young's modulus and hardness equal to 122 and 8.2 GPa which then increase drastically to 186 and 17.5 GPa for higher thicknesses when the structure turns into FCC crystal structure.

By changing the temperature of the substrate it is possible to have a small control of the morphology of the film during deposition as shown in the article of M. Hu *et al.* regarding sputtered FeCoNiCrMn [133]. As presented in Figure 2.5a the morphology of the film changes with the temperature of the substrate going from nanocolumnar with voids at room temperature to compact nanocolumnar at 573 K and non-textured crystalline structure at 773 K due to the increased mobility of sputtered adatoms during deposition at high temperatures [133]. The change in morphology affects the mechanical behavior of the films with the FeCoNiCrMn deposited at room temperature being brittle and breaking after yielding at 0.3 GPa and at 1% strain due to the voids between the nanocolumns as shown in Figure 2.5b.

Nanocolumnar compact FeCoNiCrMn yields at 18% strain and then deform plastically up to 2.3% strain before cracking while reaching high fracture strengths (1.4 GPa) thanks to their more compact structure. The polycrystalline FeCoNiCrMn films deposited at 773 K has bigger grains than the nanocolumnar films deposited at 573 K and for this reason can deform more (2.7%) before cracking at the cost of having a lower fracture strength (1.1 GPa) [133].

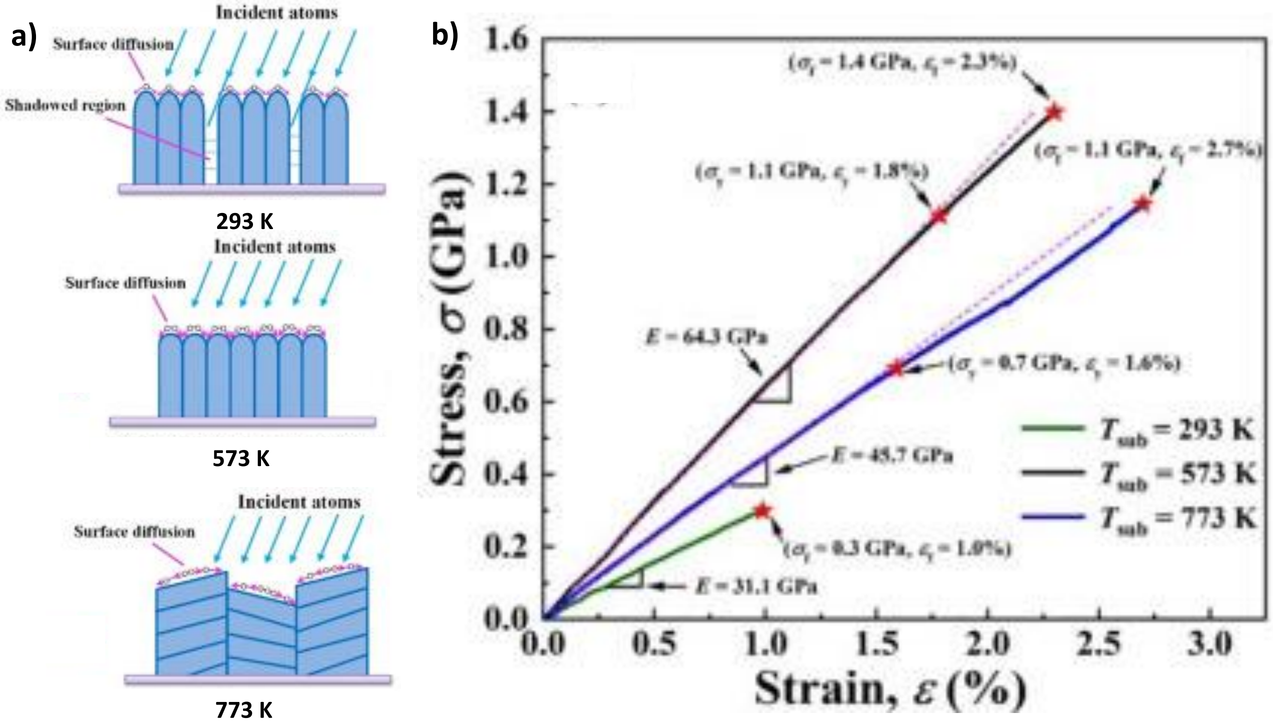

Figure 2.5.*(a) Evolution of the morphology of FeCoNiCrMn depending on the substrate temperature and (b) tensile stress-strain curves of the different morphologies of FeCoNiCrMn adapted from Ref [133].*

2.4 Multilayered thin films

The passage from bulk to thin film production opens the possibility to use the multilayer strategy to further improve the mechanical properties of HEAs.

Multilayered structures are interesting because they allow the combination of sublayers with different crystalline structure and mechanical properties which can results in new architectures with improved mechanical behavior by introducing interfaces which can block the propagation of dislocation and/or promote phase transition during deformation [49, 51, 134]. For example, Wu *et al.* [135] deposited 18/12 nm CoCrNi/TiZrNbHf nanolaminates which alternated a HCP structure for CoCrNi, different from the normal FCC structure observed in bulk CoCrNi, and an amorphous structure for TiZrNbHf, instead of the usual BCC structure, as shown in Figure 2.6a-c, which is explained with a combination of the high cooling rate of sputtering (10^{10} K/s) and interdiffusion of small quantities of Co, Cr and Ni in TiZrNbHf, which favor its amorphization [13], due to its small thickness with respect to the CoCrNi layer. The nanolaminate structure possesses a σ_y of 3.6 GPa and ductility of 15% well above its single components, as presented in Figure 2.6d, which could be surprising since HCP and amorphous phases are known to be brittle.

However, advanced TEM characterization show that the crystalline HCP phase goes through a phase transition to FCC during deformation and this new more plastic FCC phase becomes the main carrier of the deformation, preventing the premature failure related to a full HCP structure, while the amorphous phase deforms homogeneously since its low thickness prevents the formation of mature shear bands and acts as a dislocation sink for the dislocations generated in the crystalline layer further increasing the plasticity [135].

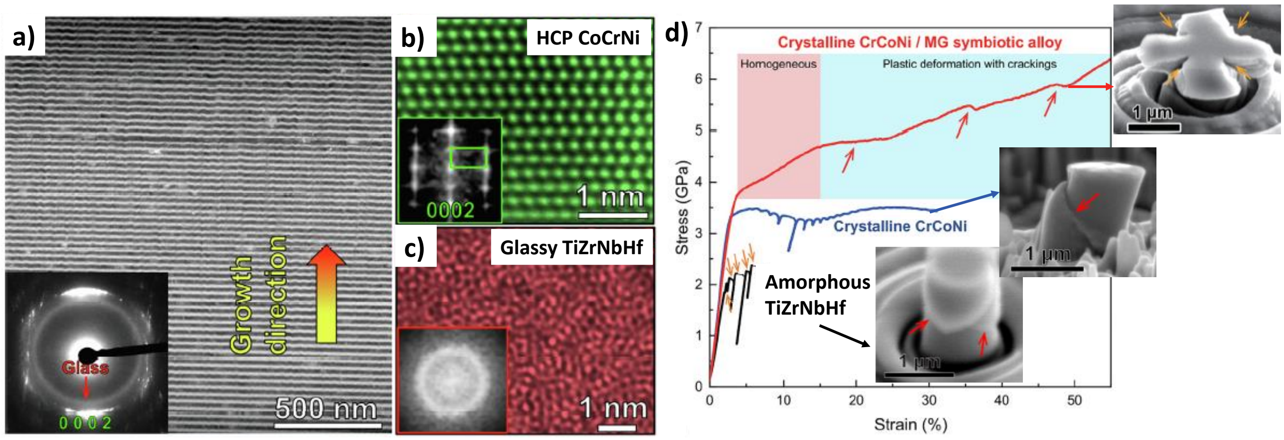

Figure 2.6: *(a) High annular dark field transmission microscopy (HAADF-TEM) image of a 18/12 nm CoCrNi/TiZrNbHf HEA multilayer, (b) high resolution TEM (HRTEM) of the single crystalline CoCrNi layer and (c) amorphous TiZrNbHf layer and (d) stress-strain curves of the pillar compression of the single components and multilayer with arrows indicating the formation of fractures highlighting the different deformation mechanisms adapted from Ref. [135].*

Other multilayer films like the crystalline/amorphous CrCoFeNi/TiNbZrTa with bilayer period between 5 and 50 nm studied by Rao *et al.* [136] have a mechanical behavior in line with crystalline/amorphous architectures of Section 1.4.2. In these multilayers the hardness increases from 10.6 GPa for 50 nm bilayers to a maximum of 12.6 GPa for the 20 nm, 21% above its parent alloys, due to the increased density of interfaces [54]. Meanwhile, for bilayer periods below 20 nm there is a decrement of hardness to values around 8.6-8.8 GPa connected to the amorphization of CoCrFeNi thus passing from crystalline/amorphous to fully amorphous multilayers.

These multilayers can have a relatively low hardness for small bilayer periods due to shear transformation zones mediated deformation which require lower stresses to activate with respect to mature shear bands [58].

2.5 Challenges for HEAs

Having covered most of the properties of HEAs in bulk and thin film form in the previous Sections some of the possible challenges that can be tackled in the field of thin films and with complex compositions and local structures like HEAs are presented here.

Like in the case of MGs of Chapter I it is important to research of a synthesis method which can easily control the quantity of local structural and chemical heterogeneities during the deposition step which in the case of HEAs would allow a better control of the grain size and the formation of chemical segregations in the crystalline structure. Current magnetron sputtering systems have low flexibility in the control of their deposition parameters and, while multitarget systems can be give large flexibility in the control of the composition, they do not have a fine control of the grain size and texturing of the films which are usually nanocolumnar. Furthermore, magnetron sputtering systems have many difficulties in the production of ultrafine nanolaminate structures due to the fast opening/closing cycles of the shutters and rapid power changes at the targets necessary to deposit multilayers with sublayer thickness < 10 nm.

The second challenge regarding the study HEAs is fully comprehending how the changes in growth mechanisms, chemical composition, crystallographic structure and grain size can influence the mechanical response of the material in order to select the best deposition conditions for a desired application.

2.6 Objectives of the PhD project for HEAs

This project aims to deposit nanostructured high entropy alloys thin films by PLD and connect the changes in local structure with the mechanical properties of the films.

PLD allows to control the morphology of the deposited films by changing the deposition pressure during deposition to change the energy of the plasma allowing the deposition of different microstructures depending on the pressure and the type of gas used [90]. This would allow to easily control the grain size and texturing of the deposited film and tune the mechanical properties of the films to a desired target [137]. The high energies connected to the plasma plume of PLD can also cause the formation of out-of-equilibrium phases that can have an improved mechanical behavior with respect to the structures usually obtained by magnetron sputtering. Despite its great flexibility of deposition parameters and versatility regarding the possible nanostructures that can be obtained the literature on HEA thin films by PLD is scarce and doesn't explore the full potential of the technique [138, 139].

In this project CoCrCuFeNi alloy (also known as Cantor alloy), one of the first HEAs studied in literature in bulk and thin film form [97, 140], will be deposited by PLD to explore the possible nanostructures that can be obtained by PLD with the possible changes in deposition conditions summed as:

1. Explore different deposition pressures going from vacuum ($1x10^{-3}$ Pa) to 0.1, 1, 5 Pa He to observe the changes in crystalline structure, grain size and consequently, the mechanical properties of the films related to the deposition pressure.
2. The preliminary study of Al/CoCrCuFeNi nanolaminates by modifying the CoCrCuFeNi target to introduce interfaces to further control the grain size and hinder the movement of dislocations thus increasing the mechanical properties of the films [49, 141].
3. In parallel CoCrCuFeNi and $Al_x(CoCrCuFeNi)_{100-x}$ films are deposited by magnetron sputtering to compare their structure and mechanical properties with PLD films.

2.7 Conclusions

In this Chapter the state-of-the-art regarding high entropy alloys in bulk and thin film form is presented highlighting the properties of their structure.

High entropy alloys are formed by four or more different elements in equimolar or quasi-equimolar concentrations and the differences in enthalpy of mixing and mismatch of atomic radii define the total entropy of the system which determines the crystalline structure and number of phases of the material. The differences between the atomic radii of distort the lattice structure slowing grain growth, diffusion and recrystallization phenomena greatly increasing the stability of the high entropy alloys. These materials can possess a combination of high mechanical strength and plastic deformation before failure thanks to their refined grain structure and the possibility to activate multiple deformation mechanisms from dislocation glide to nanotwinning to avoid cracking.

The passage from bulk to thin film samples helps to further improve the mechanical performance of high entropy alloys by preventing the segregation of elements thanks to the high cooling rates related to physical vapor deposition and activate mechanical size effects by reducing the thickness of the sample below the micrometric scale. The passage from bulk to thin film form opens the possibility to produce multilayered structures with a controlled number of interfaces which can control the movement of dislocations through the sample during deformation and activate phase changes in the sublayers due to the geometrical confinement of the single layers.

The challenges regarding the research of new nanostructures to improve the mechanical properties of high entropy alloys are presented in this Chapter together with how this project will use PLD to deposit high entropy alloys films with controlled microstructure and mechanical properties.

III. Synthesis processes and characterization methods

In this Chapter, the synthesis processes and characterization methods employed during this PhD project to deposit the TFMGs and the TFHEAs and study their structural and mechanical properties.

3.1 General overview of Pulsed laser deposition (PLD)

Pulsed Laser deposition (PLD) is a physical vapor deposition (PVD) technique which employs intermittent laser pulses which can last from few nanoseconds down to tens of femtoseconds to ablate a target inside a deposition chamber with controlled pressure [88, 142].

The main advantages related to PLD are the high energy of the ablated species allowing to deposit denser films vs other deposition methods like thermal evaporation and magnetron sputtering [143, 144]. Secondly, the possibility to replicate complex target stoichiometries without difficulty thanks to the nearly instantaneous evaporation of the ablated volume independent from its chemical composition [90, 145]. The PLD system used for deposition of films in the PhD project is located at the Nanolab of Politecnico of Milan and uses a Nd-YAG laser with a pulse duration of 5-7 ns and it is shown in Figure 3.1. The fundamental wavelength in the IR (1064 nm) was used for the deposition of metallic glasses while the 2nd harmonic (532 nm) was instead used for the deposition of the high entropy alloys. Si (100) and Kapton® polymer substrates were used for the deposition of the films. A $Zr_{50}Cu_{50}$ (99.99% pure by Mateck®), a $Zr_{46}Cu_{46}Al_8$ (99.95% pure by Kurt J. Lesker®) and a CoCrCuFeNi (99.9% pure by IMR Shenyang®) target were used for the deposition of the MGs and HEAs thin films (TFHEAs). For all the depositions the target-substrate distance was kept equal to 7 cm.

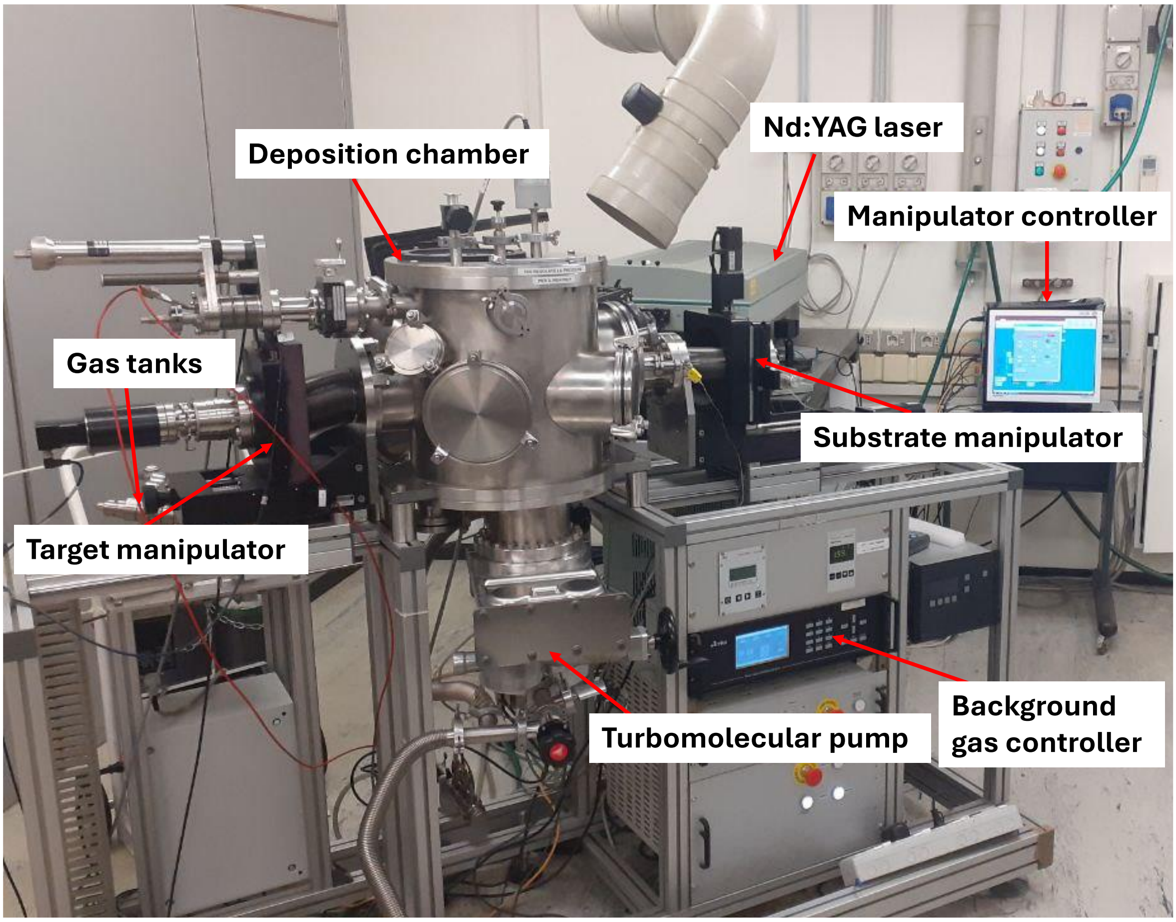

Figure 3.1: *Photo of the PLD system at Nanolab.*

The schematic of a typical PLD chamber is presented in Figure 3.2a showing how the laser enters inside the deposition chamber from a window and impacts on a roto-translating target with a 45° angle with respect to the target. The plasma plume generated by the laser-target interaction develops perpendicular to the target's surface and reach the rotating substrate put at a fixed distance from the target. The schematic of the temporal evolution of the interaction between the laser pulse and the target in a nanosecond PLD like the one used in this project is presented in Figure 3.2b [146]. In the first phase, the photon is absorbed by the surface of the target and the photon energy is converted into electronic excitation. This raises the temperature of the affected area up to several thousand of kelvins in few nanoseconds in a thickness proportional to the optical penetration depth and the thermal diffusion length, usually in the order of hundreds of nm [90]. After heating, the affected volume is vaporized and ejected as a plasma plume containing a combination of electrons, positive and negative ions and neutral species with a degree of ionization between 10% and 100% depending on fluence and laser wavelength.

Lastly, the plasma plume expands from the target at high speed and the particles inside the plume usually have a kinetic energy between 10 and 100 eV to condense onto a substrate [88, 146].

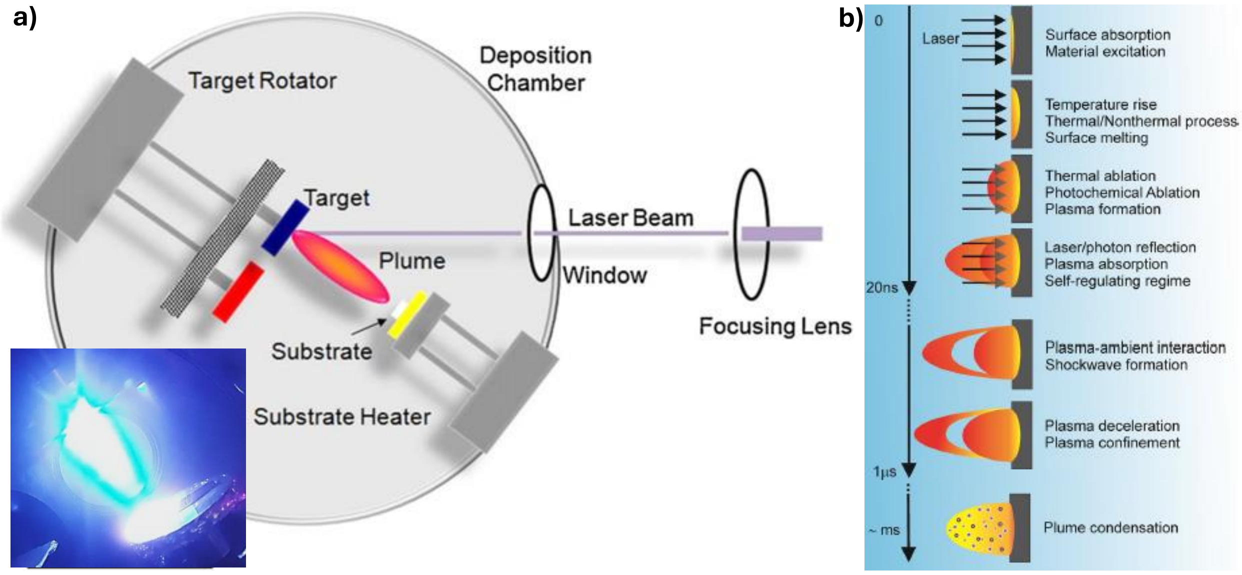

Figure 3.2: *(a) Schematic of a PLD deposition chamber from Ref. [88] and (b) of the evolution of the interaction between laser and target during a nanosecond pulse [146].*

3.1.1 Control of the morphology of the films

In PLD it is possible to control the morphology of the deposited films by tuning the kinetic energy of the ablated particles. The simplest way to do this is to add a background gas that confines the plasma plume [90, 142] as schematized in Figure 3.3. When the plasma plume expands in vacuum the ablated species travel without collisions towards the substrate and the new film follows an atom-by-atom growth creating a compact film as shown in Figure 3.3a. On the other hand, when a gas, either inert or reactive, is inserted into the deposition chamber the plasma plume is confined and the particles start to collide against each other losing energy through radiative de-excitation and some clusters begin to form [90, 147]. Furthermore, as shown in Figure 3.3b, the clusters and the plume species travel in the gas after the plume "front" and so their kinetic energy is strongly decreased if the target-substrate distance is larger than the plume length.

The films deposited in gas thus follow a type of growth defined as "cluster-assembled" and with the increase of the deposition pressure the clusters become progressively bigger while their kinetic energy is lowered resulting in more and more porous structure transforming into foam pressures > 100 Pa gas [148].

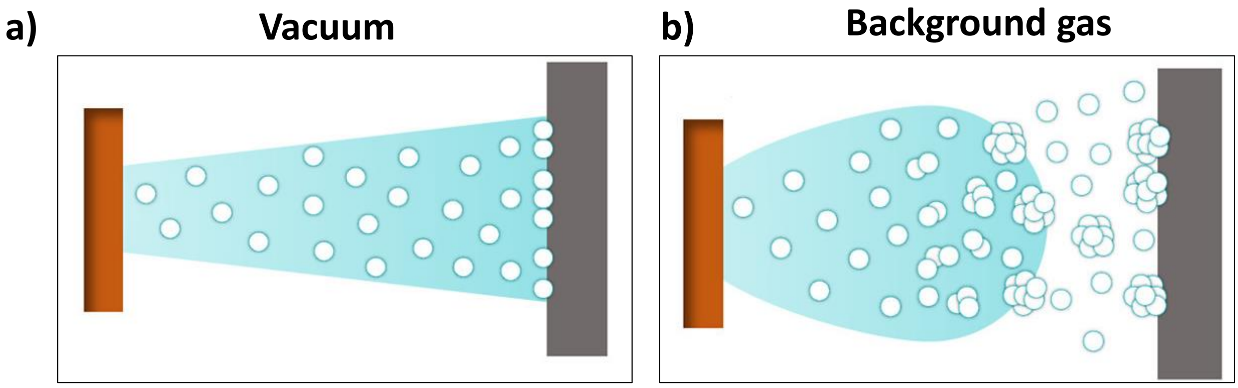

Figure 3.3: *Schematic of the plasma plume in vacuum (a) and in a background gas with the formation of clusters (b) adapted from Ref. [149].*

The $Zr_{50}Cu_{50}$ and $Zr_{46}Cu_{46}Al_8$ TFMGs were deposited in vacuum ($1x10^{-3}$ Pa) to deposit compact films and in 5 Pa He to form nanogranular films which have local fluctuations of density and chemistry between the cores and the surfaces of clusters while avoiding microporosities.

CoCrCuFeNi TFHEAs were deposited at different pressures ranging from vacuum to 5 Pa He to identify the pressure at which the growth of the film changes from atom-by-atom to cluster-assembled.

All the characteristics of the PLD TFMGs and TFHEAs studied in Chapter IV and VIII of the PhD manuscript are summed up in the Table 3.1.

Composition	Deposition pressure	Morphology	Thickness [nm]	Substrates
$Zr_{50}Cu_{50}$	$1x10^{-3}$ Pa	Compact	800	Si/Kapton®
$Zr_{50}Cu_{50}$	5 Pa He	Nanogranular	800	Si/Kapton®
$Zr_{50}Cu_{50}$	$1x10^{-3}$ Pa	Compact	3000	Si
$Zr_{50}Cu_{50}$	5 Pa He	Nanogranular	3000	Si
$Zr_{46}Cu_{46}Al_8$	$1x10^{-3}$ Pa	Compact	800	Si/Kapton®
$Zr_{46}Cu_{46}Al_8$	5 Pa He	Nanogranular	800	Si/Kapton®
$Zr_{46}Cu_{46}Al_8$	$1x10^{-3}$ Pa	Compact	3000	Si
$Zr_{46}Cu_{46}Al_8$	5 Pa He	Nanogranular	3000	Si
CoCrCuFeNi	$2x10^{-3}$ Pa	Compact	800	Si/Kapton®
CoCrCuFeNi	0.1 Pa	Compact	800	Si/Kapton®
CoCrCuFeNi	1 Pa	Nanogranular	800	Si/Kapton®
CoCrCuFeNi	5 Pa	Nanogranular	800	Si/Kapton®

Table 3.1: *List of the characteristics of the PLD samples used for the study of the effects of deposition pressure.*

An exploratory series of compact/nanogranular multilayers was produced by alternating sublayers deposited in vacuum and sublayers deposited in 5 Pa He to try to combine the properties related to the different morphologies whose preliminary results are presented in Chapter VII.

All the characteristics of the PLD of the compact/nanogranular multilayers present in the PhD thesis are summed up in the Table 3.2.

Composition	Bilayer period [nm]	Single sublayer thickness [nm]	Total thickness [nm]	Deposition pressure compact layer [Pa]	Deposition pressure nanogranular layer [Pa He]	Substrates
$Zr_{50}Cu_{50}$	200	100	2200	$1x10^{-3}$	5	Si/Kapton®
$Zr_{50}Cu_{50}$	300	150	2250	$1x10^{-3}$	5	Si/Kapton®
$Zr_{50}Cu_{50}$	400	200	2400	$1x10^{-3}$	5	Si/Kapton®

Table 3.2: *List of the characteristics of the compact/nanogranular PLD multilayers.*

3.1.2 *Deposition of metallic nanolaminates*

The change in morphology caused by the addition of a background gas is not the only strategy used to produce nanostructured films explored within this PhD project.

Amorphous/crystalline and fully crystalline nanolayered films were deposited by modifying the original $Zr_{50}Cu_{50}$ and CoCrCuFeNi targets with the addition of Al strips as shown in Figure 3.4a.

In this configuration the rapid roto-translation of the target during deposition enable to ablate alternatively the Al strip and the base $Zr_{50}Cu_{50}$ or CoCrCuFeNi target generating an ultrafine nanolaminate (U-NL) structure with a bilayer period lower than 20 nm thanks to the different deposition rates of Al and of the base target. The width of the different Al strips is changed together with the number of laser shots that would hit the base target and the strips determining the thickness of the base alloy layer and of the Al layer. Specifically for the Al/ $Zr_{50}Cu_{50}$ U-NLs of Chapter V, 55-80 laser shots ablate the $Zr_{50}Cu_{50}$ target (corresponding to 6 and 9 nm sublayers, respectively), while a fixed number (~20) of laser shots ablate the Al strip (corresponding to ~4 nm sublayers). For the Al/CoCrCuFeNi preliminary U-NLs of Chapter VIII, ~50 laser shots ablate the CoCrCuFeNi target (corresponding to 5 nm sublayers), while ~20 laser shots ablate the Al strip (corresponding to ~2 nm sublayers).

An example of a PLD nanolaminate is presented in Figure 3.4b which shows the TEM image of a $Zr_{50}Cu_{50}$/Al amorphous/crystalline nanolaminates described in Chapter V of the manuscript highlighting the different sublayers.

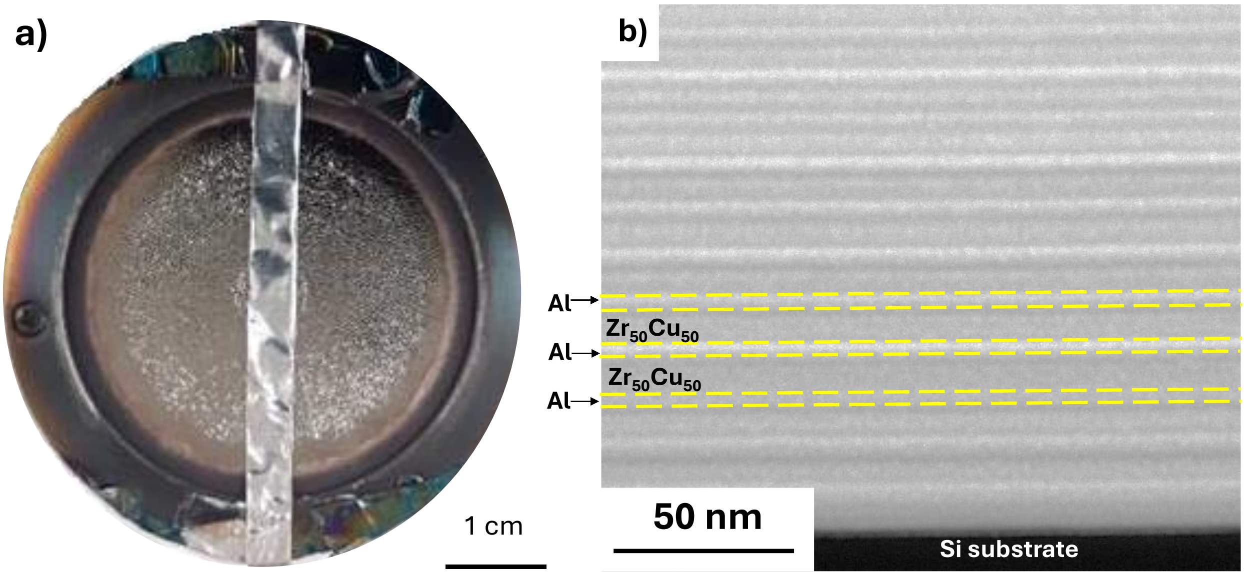

Figure 3.4: *(a) Photo of the modified $Zr_{50}Cu_{50}$ target with the Al strip used for the deposition of $Zr_{50}Cu_{50}$/Al nanolaminates and (b) TEM image of compact $Zr_{50}Cu_{50}$/Al nanolaminates showing the different sublayers.*

All the characteristics of the nanolaminates studied in Chapter V and the future perspectives of Chapter VIII of the PhD thesis are summed up in the Table 3.3.

Composition	Deposition pressure	Bilayer period [nm]	Morphology	Thickness [nm]	Substrates
$Zr_{50}Cu_{50}$/Al	1x10^{-3} Pa	9/4	Compact	800	Si/Kapton®
$Zr_{50}Cu_{50}$/Al	5 Pa He	9/4	Nanogranular	800	Si/Kapton®
$Zr_{50}Cu_{50}$/Al	1x10^{-3} Pa	9/4	Compact	3000	Si
$Zr_{50}Cu_{50}$/Al	5 Pa He	9/4	Nanogranular	3000	Si
$Zr_{50}Cu_{50}$/Al	1x10^{-3} Pa	6/4	Compact	800	Si/Kapton®
$Zr_{50}Cu_{50}$/Al	5 Pa He	6/4	Nanogranular	800	Si/Kapton®
CoCrCuFeNi/Al	2x10^{-3} Pa	5/2	Compact	800	Si
CoCrCuFeNi/Al	5 Pa He	5/2	Nanogranular	800	Si

Table 3.3: *List of the characteristics of the PLD samples used for the study of the nanolaminates.*

3.1.3. Incorporation of non-metallic elements in thin films by PLD

In the case of the $Zr_{50}Cu_{50}$ and $Zr_{46}Cu_{46}Al_8$ targets it is possible to incorporate O inside the atomic structure of the TFMGs by increasing the baseline vacuum as shown in Figure 3.5. To control the baseline vacuum the target is ablated before the deposition for a time between 10 and 20 minutes, to use the plasma of Zr as an O getter which reduces the quantity of O in the deposition chamber and macroscopically lowers the base pressure below 1x10^{-3} Pa.

When the cleaning time of the target is reduced, and the baseline vacuum is increased to 2x10^{-3} Pa the amount of O observed with EDX goes above 10 %at. at which O starts to affect the local structure and mechanical properties of the films.

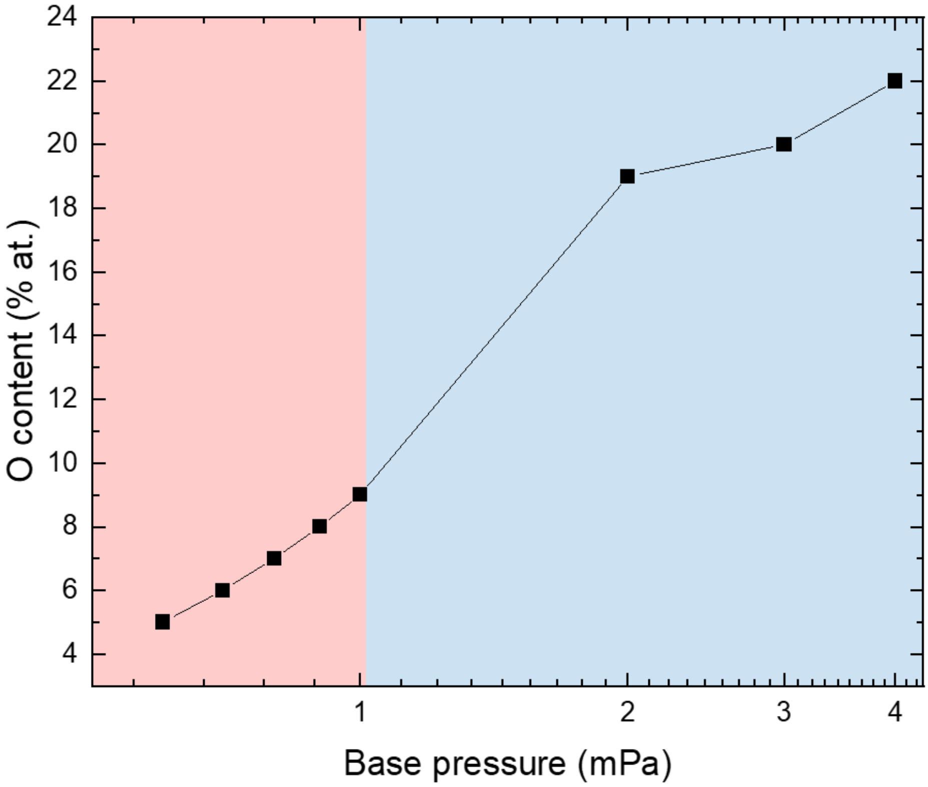

Figure 3.5: *Evolution of the O content in the amorphous ZrCu-based films as a function of the base deposition pressure with the red zone indicating the pressure range in which O has no effect on the structure and properties of the films while the blue zone indicates the deposition pressures for which O is incorporated in the structure of the film and affects the mechanical behavior.*

The amount of O incorporated in the PLD films is also dependent on the deposition pressure with the nanogranular films having a nominal O content equal to 40 %at. by EDX while the compact films contain roughly 20 %at. when examined by EDX. It should be noted that EDX can have problems estimating the quantity of elements with low atomic number like O and so the O content reported for the films described in this Section can be considered an approximation and future more precise characterizations will investigate more in detail the true O content. All the characteristics of the amorphous films with O studied in Chapter VI of the PhD thesis are presented in the Table 3.4.

Sample Name	**Deposition pressure**	**Composition [% at.]**	**Morphology**	**Thickness [nm]**	**Substrates**
ZrCu/O	$3x10^{-3}$ Pa	$(Zr_{50}Cu_{50})_{80}O_{20}$	Compact	800	Si/Kapton®
ZrCu/O	5 Pa He	$(Zr_{50}Cu_{50})_{60}O_{40}$	Nanogranular	800	Si/Kapton®
ZrCu/O	$3x10^{-3}$ Pa	$(Zr_{50}Cu_{50})_{80}O_{20}$	Compact	3000	Si
ZrCu/O	5 Pa He	$(Zr_{50}Cu_{50})_{60}O_{40}$	Nanogranular	3000	Si
ZrCuAl/O	$3x10^{-3}$ Pa	$(Zr_{46}Cu_{46}Al_8)_{80}O_{20}$	Compact	800	Si/Kapton®
ZrCuAl/O	5 Pa He	$(Zr_{46}Cu_{46}Al_8)_{60}O_{40}$	Nanogranular	800	Si/Kapton®
ZrCuAl/O	$3x10^{-3}$ Pa	$(Zr_{46}Cu_{46}Al_8)_{80}O_{20}$	Compact	3000	Si
ZrCuAl/O	5 Pa He	$(Zr_{46}Cu_{46}Al_8)_{60}O_{40}$	Nanogranular	3000	Si

Table 3.4: *List of the characteristics of the PLD samples used for the study of the effects of O on the structure and mechanical properties of the amorphous films.*

3.2 Magnetron sputtering (MS)

Magnetron sputtering (MS) is a PVD technique widely used in many laboratories and industries to deposit metallic thin films. In a sputtering process a plasma of an inert gas (usually Ar^+) is ignited in a vacuum chamber at pressure around 0.1-1.5 Pa and then directed towards the targets of the materials that are to be deposited with a negative bias [150].

When the Ar^+ ions collide with the target surface secondary electrons are emitted and accelerated at high speed due to the negative bias of the target ionizing other Ar atoms in the chamber creating a self-sustaining electrical discharge [150]. The ion bombardment causes the erosion of the target, and its atomic species are then deposited on the substrates (Si (100) and Kapton®). In the case of magnetron sputtering configuration a magnetic field is applied to the target surface to confine the plasma and reduce the pressure necessary for a self-sufficient discharge. In this project $Zr_{50-x/2}Cu_{50-x/2}Al_x$ TFMGs and CoCrCuFeNi TFHEAs were deposited at LSPM by sputtering on Si (100) and Kapton® substrate as a reference film which are then compared with PLD counterparts of Chapter IV. Zr, Cu and Al targets (99.99% pure by Kurt J. Lesker®) were used for the deposition of $Zr_{50-x/2}Cu_{50-x/2}Al_x$ TFMGs with the applied powers on the Zr (100 W) and Cu (200 W) targets calibrated to deposit $Zr_{50}Cu_{50}$ and different applied powers between 10 and 25 W were imposed on the Al target to tune the Al content between 0 and 12 % at. For all the films the target-substrate distance was kept equal to 7 cm and the working pressure equal to 0.5 Pa.

A CoCrCuFeNi target was used for the deposition of the CoCrCuFeNi (99.9% pure by IMR Shenyang) films with 200 W applied power. For all the films the target-substrate distance was kept equal to 7 cm and the working pressure equal to 0.5 Pa. The power on the Al target was changed between 21 W and 95 W to produce the different $Al_x(CoCrCuFeNi)_{100-x}$ presented in the future perspectives of Chapter VIII.

All the compositions, thicknesses, and substrates on which the MS films have been deposited are presented in the Table 3.5.

Composition	Al applied power [W]	Zr-Cu applied powers [W]	CoCrCuFeNi applied power [W]	Thickness [nm]	Substrates
$Zr_{50}Cu_{50}$	0	100-200	0	800	Si/Kapton®
$Zr_{47}Cu_{47}Al_6$	10	100-200	0	800	Si/Kapton®
$Zr_{46}Cu_{46}Al_8$	15	100-200	0	800	Si/Kapton®
$Zr_{45.5}Cu_{45.5}Al_8$	20	100-200	0	800	Si/Kapton®
$Zr_{44}Cu_{44}Al_{12}$	25	100-200	0	800	Si/Kapton®
CoCrCuFeNi	0	0	200	800	Si/Kapton®
$Al_{10}(CoCrCuFeNi)_{90}$	21	0	200	800	Si/Kapton®
$Al_{17}(CoCrCuFeNi)_{83}$	42	0	200	800	Si/Kapton®
$Al_{22}(CoCrCuFeNi)_{78}$	58	0	200	800	Si/Kapton®
$Al_{25}(CoCrCuFeNi)_{75}$	66	0	200	800	Si/Kapton®
$Al_{28}(CoCrCuFeNi)_{72}$	80	0	200	800	Si/Kapton®
$Al_{32}(CoCrCuFeNi)_{68}$	95	0	200	800	Si/Kapton®

Table 3.5: *List of the characteristics of the MS TFMGs and TFHEAs used for comparison purposes in this PhD thesis.*

3.3 Structural characterizations:

3.3.1 Scanning electron microscopy (SEM)-energy dispersive X-ray spectroscopy (EDX)

A field emission scanning electron microscope (FE-SEM) Zeiss Supra 40 was used to investigate the surface and cross-section morphology of the films deposited on Si (100) substrates.

The images were done by using an in-lens detector collecting the secondary electron generated by the direct impact between the primary electron beam accelerated at 7 kV and the sample while keeping the detector-sample distance equal to 3 mm to have detailed images well representing the morphology of the sample with a resolution between 100000x and 300000x. The FE-SEM is equipped with a Bruker energy dispersive X-ray spectroscopy (EDX) to study the chemical composition of the films by using an acceleration voltage of 15 kV to avoid substrate interference and keeping a detector-sample distance equal to 8.5 mm to optimize the signal for EDX spectra calculation.

The composition of each film was measured in 10 areas of 1000x resolution and then averaged to obtain the official composition.

3.3.2 Transmission electron microscopy (TEM)

Selected TEM analyses were performed to get high resolution information of the layered structures and elemental distribution of the as deposited $Zr_{50}Cu_{50}$/Al nanolayered structures using a JEOL 2200 FS operating at 200 kV at the Austrian Academy of Science.

A combination of high-angle annular dark-field scanning TEM (HAADF-STEM), selected area electron diffraction (SAED) and STEM-EDX were acquired to characterize morphology structure and chemistry at the nanoscale. The lamellae used for TEM characterization were prepared with a Ga Focused Ion Beam (FIB) with and extremely low current equal to 50 pA, while protecting the sample with a 100 nm Pt layer to minimize damaging. For the post-mortem characterization of tested $Zr_{50}Cu_{50}$/Al pillars and of the as deposited HEA films, TEM and STEM-EDX was carried out in an aberration probe-corrected Thermo Fisher Titan Themis 60-300 equipped with the ChemiSTEM Super X EDX detector operated at 300 kV at the Karlsruhe institute of technology.

3.3.3 X-ray based characterizations: X-ray diffraction (XRD) and reflectivity (XRR)

The crystallographic structure of the U-NLs was investigated by XRD using a θ-2θ Bruker D8 Advanced system with Cu Kα radiation (λ = 1.5406 Å). The measurements were carried out in grazing incidence geometry with an incidence angle of 0.95° to avoid substrate signal with a scan range 20-90°. Data were acquired overnight by Lynx Eye detector in continuous scanning mode with a step size of 0.14°.

An X-ray Diffraction Inel EQUINOX 1000 diffractometer with Cu Kα radiation equipped with a curved detector with data acquired overnight and angle of incidence equal to 2° to avoid Si was used at Université Sorbonne Paris Nord for the $Zr_{46}Cu_{46}Al_8$ TFMGs by PLD.

The TFHEAs were characterized with a D8 discovery diffractometer powder diffractometer in grazing incidence mode using Cu-Kα radiation (λ=0.154 nm). Measurements were performed in 20°-70° range with grazing angle of 0.5° using continuous scan mode with step size of 0.03° and in Bragg-Brentano configuration. The average interatomic distance *d* in amorphous films was calculated by using the Ehrenfest equation [151]:

$$1.23\boldsymbol{\lambda} = 2d sin\theta \text{ (1)}$$

where λ is Cu Kα (1.5406 Å) and θ is the position of the amorphous halo from the XRD peak. For crystalline films the Bragg equation [152] was used to estimate the interplanar distance d_{hkl} related to the peaks:

$$n\boldsymbol{\lambda} = 2d_{hkl} sin\theta \text{ (2)}$$

where n is an integer number and θ is the peak position from the XRD spectrum. From the full width half maximum (FWHM) of the peak it is possible to obtain the average crystallite size *c* with the Scherrer's equation [153]:

$$c = \frac{K\lambda}{FWHMcos\theta} \text{ (3)}$$

with K being a dimensionless parameter equal to 0.9.

X-ray reflectivity (XRR) scans were obtained with a Seifert XRD 3000 diffractometer operating at 40 kV and 40 mA using a Cu Kα source at the Pprime institute of Poitiers to evaluate the mass density of the films and their bilayer period in the case of nanolaminates.

The scans were carried out between 0.2° and 2.2° with a step of 0.05° to determine the density of the films and observe eventual multilayer structures. From the XRR scans, using Parratt formalism [154], it can be obtained the critical angle θ_C, shown in Figure 3.6, at which X-rays start to penetrate the film and from it we can obtain the density of the material by the following equation:

$$\rho = \frac{\theta_C^2}{2(\frac{r_e\lambda^2}{2\pi})N_A\frac{\sum_i x_i(Z_i)}{\sum_i x_i M_i}} \text{ (4)}$$

in which ρ is the density, r_e is the classical radius of the electron, λ is the Cu Kα wavelength, N_A is the Avogadro's number, x_i is the atomic ratio of the elements obtained from EDX, Z_i is the atomic number of the elements and M_i is the atomic weight of the elements.

A first approximation of the nanolayering period *a* of the U-NLs films by knowing the position of the satellite peak θ_i and comparing it with the critical angle θ_C as shown in Figure 3.6:

$$m\boldsymbol{\lambda} = 2a(sin^2\theta_i - sin^2\theta_C)^{1/2} \text{ (5)}$$

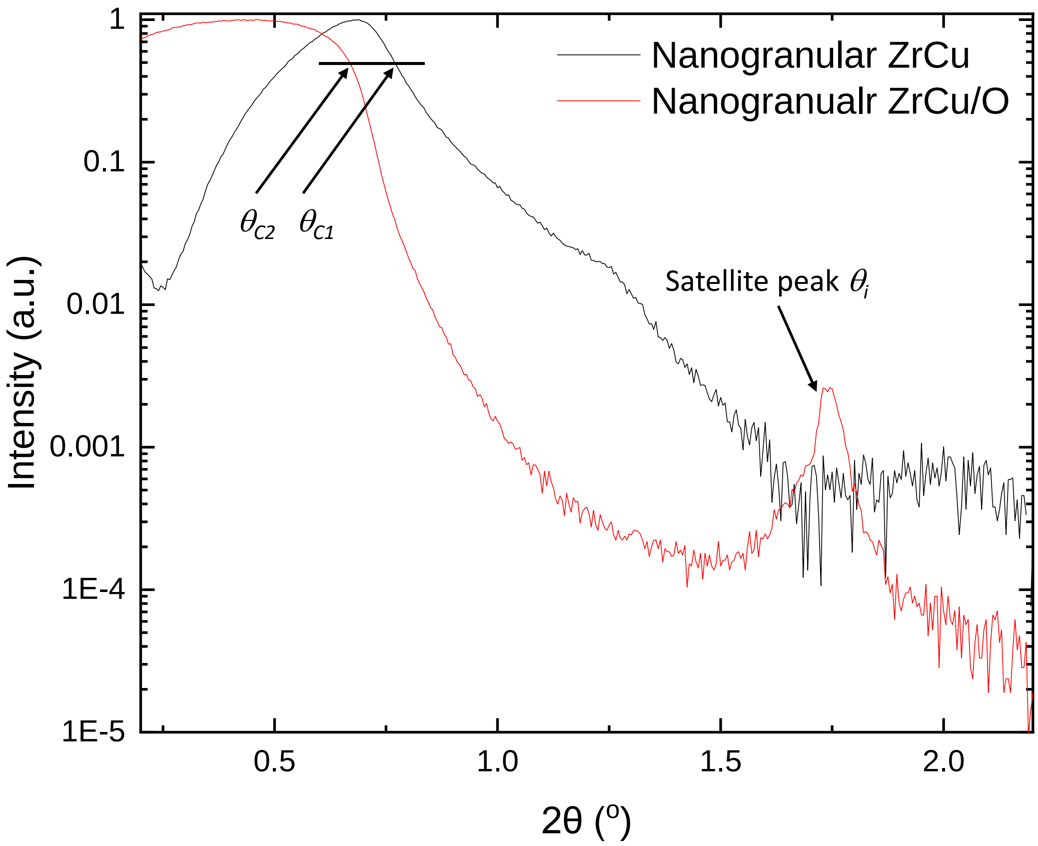

Figure 3.6: *XRR spectra of nanogranular ZrCu and ZrCu/O self-assembled nanolayered structure deposited by PLD highlighting the critical angle θ_C of both films and the satellite peak θ_i.*

3.4 Mechanical characterizations:

3.4.1 Optoacoustic techniques: Brillouin light scattering (BLS) and picosecond ultrasounds (PU)

In Brillouin light scattering (BLS) a monochromatic laser incident on a surface is inelastically scattered by thermally excited acoustic waves with a frequency shifted by $\pm A$, which is the frequency of the acoustic phonons, that can be observed with a Sandercock tandem Fabry-Pérot interferometer.

The BLS spectra were obtained in air at room temperature with an incidence angle of 65°, acquisition time between 30 and 60 minutes and 200 mW of a p-polarized incident light (wavelength λ = 532 nm). For opaque films, the scattering mechanism is restricted to the scattering of light by the dynamical corrugation of the free surface by surface acoustic waves (SAWs) travelling parallel to the film plane which are also called Rayleigh waves and the sound velocity of these waves is defined as $V_R = A\lambda/(2\sin\theta)$ [155], which is the peak called R observed in Figure 3.7a. V_R is closely related to the transversal sound velocity V_T and it can approximated as $V_R \sim 0.92 V_T$ [156]. From V_T, the shear modulus G ($=C_{44}$) can be obtained through the relationship $G = \rho V_T$ with ρ being the density of the film. In films with thickness below 500 nm it is possible to observe well defined secondary peaks called Sezawa peaks, which can be used to generate a mathematical fit to obtain the other elastic constants to calculate the Young's modulus *E*.

Alternatively, for thicker films a shoulder formed by the merging of the Sezawa peaks, called longitudinal threshold, can form, and help to calculate the mathematical fit to obtain the elastic properties of the films. However, for the 800 nm films studied in this project neither the Sezawa peaks nor the longitudinal threshold are observed for most BLS spectra, and picosecond ultrasounds was used to know the other elastic constants.

With picosecond ultrasounds experiments, an ultrashort light pulse is focused on an opaque thin film generating an elastic strain pulse consisting mainly of longitudinal acoustic phonons that propagate as coherent waves [157]. The waves are then reflected at the interface between film and substrate and the time of flight (*TOF*) of the wave is thus measured, as presented in PU graph of Figure 3.7b.

By knowing the thickness *t* of the film, it is possible to obtain the longitudinal velocity V_L with the relationship $V_L = 2t/TOF$. From V_L I can obtain the parameter $C_{11} = \rho V_L^2$ which can be used together with C_{44} to obtain the Young's modulus E and the Poisson's ratio ν with the following equations (assuming isotropic elasticity assumption):

$$E = \frac{C_{44}(3C_{11}-4C_{44})}{(C_{11}-C_{44})} \quad (5)$$

and

$$\nu = \frac{(C_{11}-2C_{44})}{(C_{11}-C_{44})} \quad (6)$$

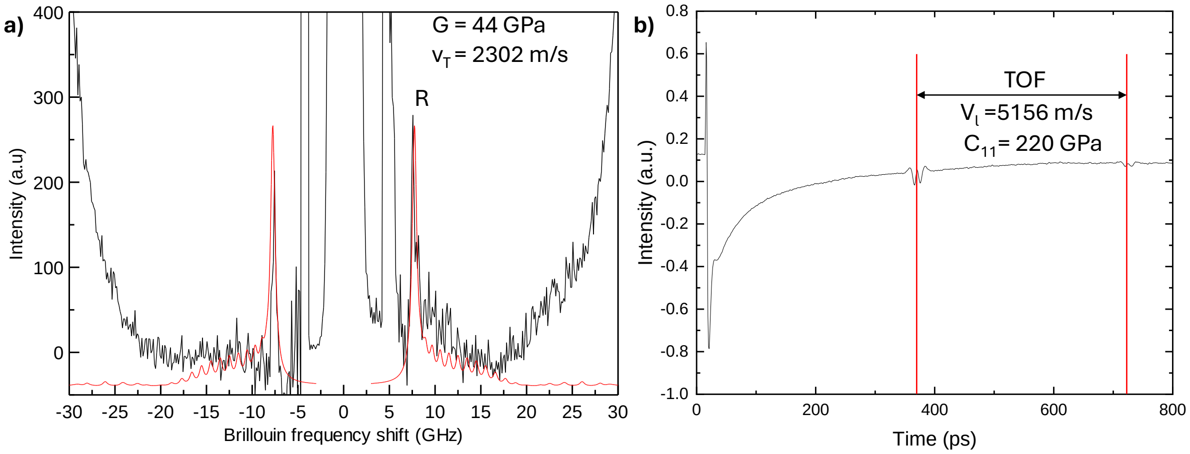

Figure 3.7: *BLS spectrum (black dash-dot line) with the fit (red continuous line) from which* C_{44} *is extracted thanks to Rayleigh peak (R) (a) and picosecond ultrasound (b) of 800 nm* $Zr_{50}Cu_{50}$ *film deposited in vacuum by PLD.*

3.4.2 Nanoindentation

In a nanoindentation test the surface of a sample is indented with a three-sided pyramidal tip (known as Berkovich tip) and the force P as a function of the displacement into the film's surface h is measured.

The Oliver and Pharr model is applied to extract the elastic modulus E and the hardness H as a function of the displacement from load-displacement curve [158, 159].

The hardness H of the film can be calculated as:

$$H = P/A \quad (7)$$

with A being the projected area of the indenter into the surface as a function of h, which is can be written, for a Berkovich tip, as:

$$A = 24.56h^2 + C_1h + C_2h^{1/2} + \ldots.C_8h^{1/128} \quad (8)$$

where C_1, C_2… C_8 are parameters that consider geometrical deviations of the shape of the tip from the ideal shape of the Berkovich tip caused by the blunting of the tip.

The Young's modulus E of a film can be inferred by the contact stiffness S of the P-h curve which can be written as:

$$S = \frac{dP}{dH} = 2\alpha\sqrt{\frac{A}{\pi}}E_r \quad (9)$$

with α being a geometrical parameter related to the tip (1.034 for Berkovich tip) and E_r being the reduced modulus of the tested film which can be written as:

$$\frac{1}{E_r} = \frac{1-\nu^2}{E} - \frac{1-\nu_i^2}{E_i} \quad (10)$$

With E and ν being the Young's modulus and Poisson's ratio of the film and E_i and ν_i being the Young's modulus and Poisson's ratio of the tip of the indenter, usually diamond (E_i = 1141 GPa, ν_i = 0.07).

Nanoindentation experiments have been performed with a KLA G200 equipped with a Berkovich diamond tip operated in continuous stiffness measurement (CSM) mode to measure the E and the H as a function of the indentation depth. A standard fused silica sample was tested before and after the measurements for tip area function and frame stiffness calibrations.

The drift rate of the measurement was limited to 0.05 nm/s, the maximum indentation depth was set to 500 nm and the loading rate $\dot{P}/P$ was kept equal to 0.05 s^{-1} for all the measurements. A minimum of 25 indentations were performed for each sample. In the nanoindentation of thin films deposited on a substrate the different mechanical properties of the substrate itself will influence the value of *E* and *H* reported in the curves as a function of the displacement into surface.

For this reason the final *E* and *H* of the films are calculated from the first 10% of the curve in a region indicated as II in Figure 3.8 where there aren't distorting effects related to the surface rugosity (region I) and the *E* and *H* of the substrate do not influence yet the measure of the nanoindentation (region III).

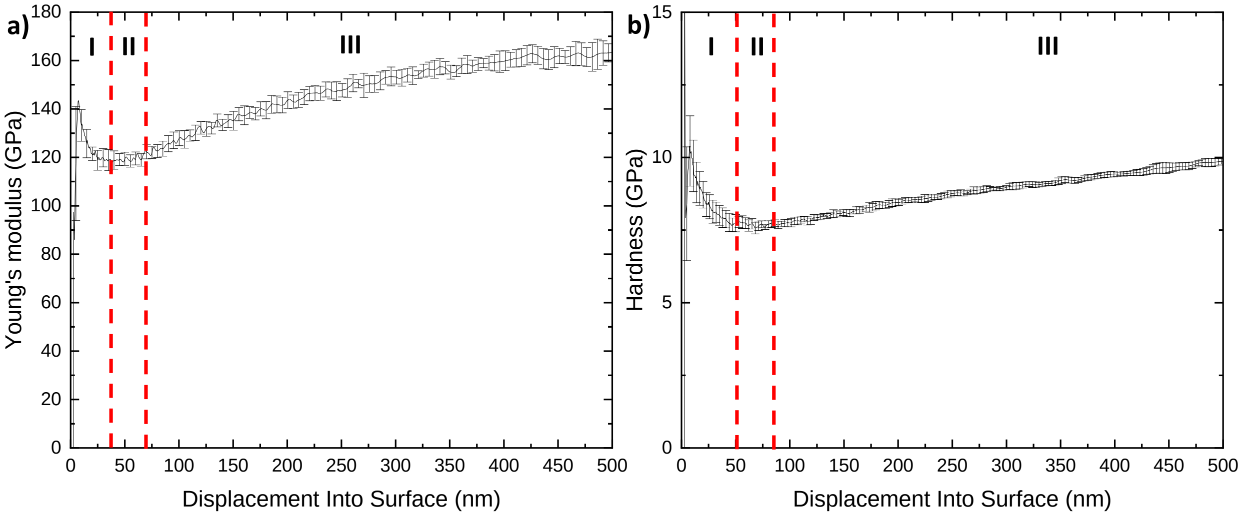

Figure 3.8*: Evolution of the (a) Young's modulus and (b) hardness as a function of the indentation depth highlighting the three regions corresponding to surface effects (I), plateau where the properties of the film are calculated (II) and region in which the effect of the substrate appears (III).*

3.4.3 Tensile tests on polymer substrate

Tensile test of films deposited on a polymer substrate were performed to qualitatively study the fracture behavior of the films deposited by PLD and magnetron sputtering by following the nucleation and propagation of cracks on the film's surface as a function of the applied strain.

From these test it is possible to obtain the crack onset strain (*COS*), when the first crack appears, the saturation crack density (*CSD*), which is the maximum amount of fragments in which a film can break after high strains (>10%) and the buckle initiation strain (*BIS*), which is the strain at which the film start to delaminate from the substrate due to stresses perpendicular to loading direction [160].

From the curvature of the film deposited on the polymer substrate it is possible to estimate the residual stresses σ_{res} [161] following the equation:

$$\sigma_{res} = E_f \left(\frac{t_f + t_s}{2R}\right) \frac{1 + 2\frac{t_f}{t_s} + \frac{E_f}{E_s}\frac{t_f^2}{t_s^2}}{\left(1+\frac{t_f}{t_s}\right)\left(1+\frac{E_f}{E_s}\frac{t_f}{t_s}\right)} \quad (11)$$

Where t_f and t_f are the thicknesses of the film and the substrate, respectively, and E_f and E_s are the Young's moduli of the film and the substrate, respectively.

R is the curvature of the film which can be defined as:

$$R = \frac{c^2+4d^2}{8d} \quad (12)$$

where *c* is the base of the arc of curvature and *d* is its height.

By knowing all these parameters it is possible to estimate the fracture toughness of a film by using the Beuth model [162] combining *COS*, *CSD*, the reduced modulus of the film E_r, and the stress at fracture of the film ($COS*E+ s_{res}$) to obtain the fracture energy G_{Beuth}:

$$G_{Beuth} = \frac{(COSE\sigma_{res})^2}{1.34CSDE_r} \quad (13)$$

which can be used to calculate the fracture toughness K_{IC} expressed as:

$$K_{IC} = \sqrt{E_r G_{Beuth}} \quad (14)$$

The adhesion energy J_0 of the films to the substrate can be estimated from the buckling initiation strain (*BIS*), *CSD*, film's thickness *h*, the reduced modulus of the film E_r, and σ_{res} by using strain energy delamination model [163]:

$$J_0 = \frac{E_r h \beta^2}{2}\left(BIS + \frac{\sigma_{res}}{E_r\beta}\right)^2 \quad (15)$$

with β being a dimensionless factor depending on *CSD* roughly equal to -0.47 for all PLD films.

Tensile tests were performed on films deposited on polyimide Kapton® substrates, using a 300 N Deben tensile machine combined with a Keyence confocal microscope shown in Figure 3.9a. The Kapton® substrates were 4 cm long and 4 mm wide and the films were deposited in the center of the substrate in an area 1 cm long and 4 mm wide to avoid artifacts of the measurement related to inhomogeneous thickness of the films. The tensile speed was set equal to 0.5 mm/min and the sample length was 40 mm corresponding to a strain rate of ~2.1×10^{-4} s^{-1}. A 10x objective was used for visualizing the evolution of the crack density as a function of the strain. The linear crack density was calculated by measuring the number of cracks (orthogonal to the loading direction) over the area of the sample (1412 µm x 1059 µm) captured by the microscope objective and reported in a graph like the one presented in Figure 3.9b in which the crack onset strain and the crack saturation density are shown.

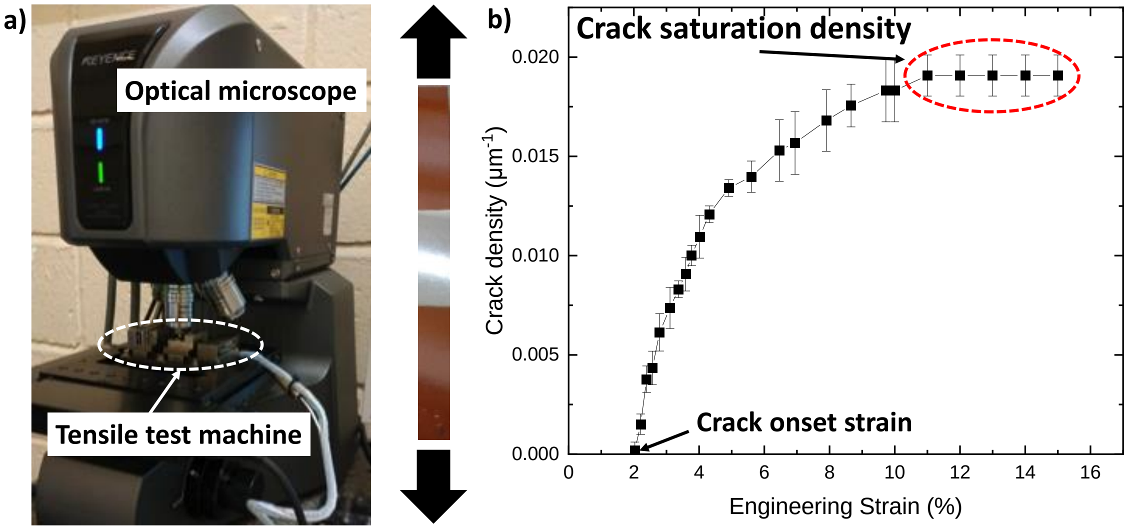

Figure 3.9: *(a) image of the experimental setup for the tensile tests and loading direction of a sample. (b) Example of a crack density – engineering strain highlighting the possible information that can be obtained.*

3.4.4 Micropillar compression

Micropillar compression tests were performed to determine the strength and observe the deformation behavior of the different nanostructures in collaboration with the Karlsruhe institute of technologies and the université Mines des Saint-Etienne.

Some pillars were tested with a Bruker PIE 89 at indenter in displacement control mode. Micropillars were machined with a Ga focus ion beam (FIB, Crossbeam 550L Zeiss) operated at an acceleration voltage of 30 kV using a 3-step process; coarse milling with a current of 7 nA, 1.5 nA for intermediate and 300 pA for fine milling. Four pillars with diameter equal to ~720 nm and height ~2 µm were milled for each sample. Each pillar was compressed up to 15% strain with three incremental steps of 5% strain with a strain rate $\dot{\varepsilon}$ equal to 10^{-2} s^{-1}. Other micropillars were tested with an Alemnis nanoindenter. The pillars, with diameter of 1.3 µm and height ~3 µm were compressed at five different $\dot{\varepsilon}$ (10^{-3}, 10^{-2}, 10^{-1}, 1, 10 s^{-1}) and compressed up to 30 % strain in a single step and five pillar were compressed for each strain rate. The diameters of the pillars were chosen to best adapt to the different indenters and to avoid the activation of mechanical size effects which increase extrinsically the yield strength σ_y and plasticity when the diameter of the tested samples goes below 300 nm [164, 165]. The yield strength σ_y of each sample is obtained by horizontally shifting the fit of the elastic modulus *E* of 0.2% to the right and checking its intersection with the stress-strain curve as shown in Figure 3.10a.

The strain at which the first shear band develops in the pillar has been determined manually by correlating the time frame at which the shear bands appear on the record of the pillar compression with the strain as a function of experiment time. The many stress-drops of the engineering stress - strain curve, highlighted by the black arrows, correspond to the formation of shear bands inside the pillar can be also identified in the post-mortem SEM image of Figure 3.10b.

The strain rate sensitivity *m* of the films was calculated as $\partial\sigma_y / \partial\dot{\varepsilon}$ [166] for the compact $Zr_{46}Cu_{46}Al_8$, the nanogranular $Zr_{46}Cu_{46}Al_8$ TFMGs.

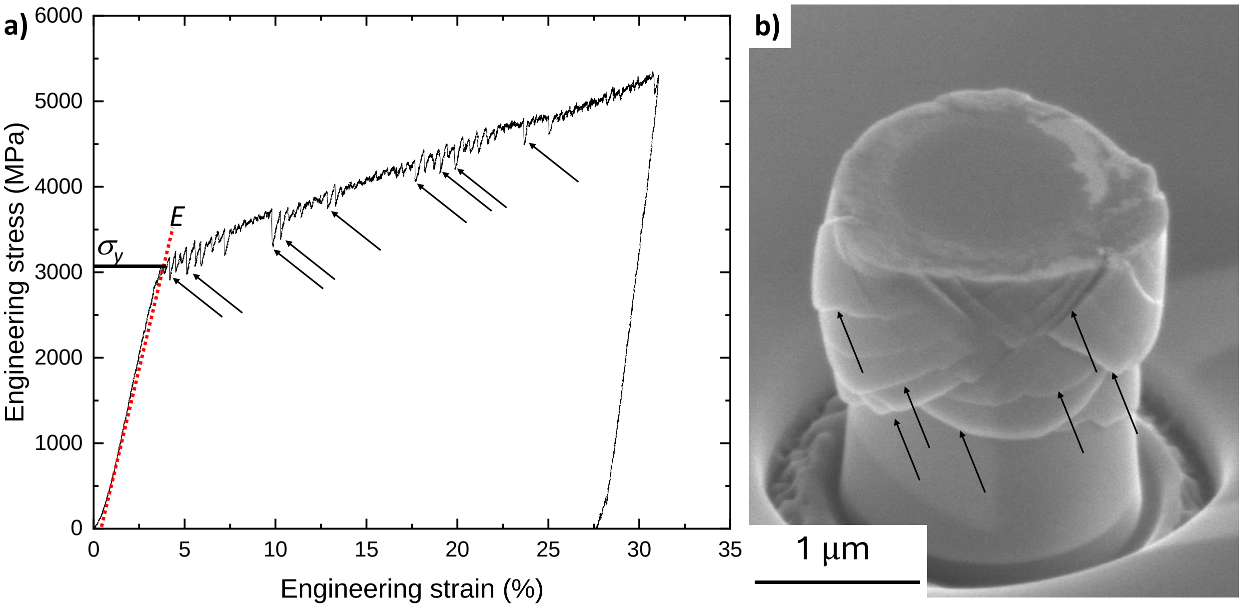

Figure 3.10: *(a) Engineering stress – strain curve of a compact* $Zr_{46}Cu_{46}Al_8$ *pillar compressed at* 10^{-3} s^{-1} *with the E fit (red dotted line) shifted of 0.2% to obtain the* σ_y *of the pillar and the black arrows showing the shear banding events during the pillar's compression and (b) postmortem SEM images of the compact and nanogranular compressed micropillars after 30% strain.*

A list of all the nanostructured films by PLD for which micropillar compression has been performed is presented in the Table 3.6.

Composition	Deposition pressure	Morphology	Thickness [nm]	Substrates
$Zr_{50}Cu_{50}$	$1x10^{-3}$ Pa	Compact	3000	Si
$Zr_{50}Cu_{50}$	5 Pa He	Nanogranular	3000	Si
$Zr_{50}Cu_{50}$	$1x10^{-3}$ Pa	Compact	3000	Si
$Zr_{50}Cu_{50}$	5 Pa He	Nanogranular	3000	Si
$Zr_{46}Cu_{46}Al_8$	$1x10^{-3}$ Pa	Compact	3000	Si
$Zr_{46}Cu_{46}Al_8$	5 Pa He	Nanogranular	3000	Si
$Zr_{46}Cu_{46}Al_8$	$1x10^{-3}$ Pa	Compact	3000	Si
$Zr_{46}Cu_{46}Al_8$	5 Pa He	Nanogranular	3000	Si
$(Zr_{50}Cu_{50})_{80}O_{20}$	$3x10^{-3}$ Pa	Compact	3000	Si
$(Zr_{50}Cu_{50})_{60}O_{40}$	5 Pa He	Nanogranular	3000	Si
$(Zr_{46}Cu_{46}Al_8)_{80}O_{20}$	$3x10^{-3}$ Pa	Compact	3000	Si
$(Zr_{46}Cu_{46}Al_8)_{60}O_{40}$	5 Pa He	Nanogranular	3000	Si
$Zr_{50}Cu_{50}$/Al 9/4 nm	$1x10^{-3}$ Pa	Compact	3000	Si
$Zr_{50}Cu_{50}$/Al 9/4 nm	5 Pa He	Nanogranular	3000	Si

Table 3.6: *List of the characteristics of all the PLD films that have been used for micropillar compression in this PhD project.*

IV. Effect of nanostructure and local chemistry on the mechanical behavior of monolithic thin film metallic glasses

4.1 Overview on the investigated samples

In this Chapter, the structure and mechanical properties of the $Zr_{50}Cu_{50}$ and $Zr_{46}Cu_{46}Al_8$ TFMGs deposited by PLD in vacuum ($1x10^{-3}$ Pa) and in 5 Pa He are presented. These films have been deposited from monolithic $Zr_{50}Cu_{50}$ and $Zr_{46}Cu_{46}Al_8$ targets with an IR (1064 nm) laser with an average energy around 1650 ± 10 mJ with the optics set up to have a fluence of 14 J/cm^2. The characteristics of the films examined here can be found in Table 3.1 of Chapter III. The objective of this study is to investigate the effect of local chemistry with the addition of Al to $Zr_{50}Cu_{50}$ and of the nanostructure (atom-by-atom to a cluster assembled growth) to study the effects of the introduction of local heterogeneities to the mechanical properties of the films.

Magnetron sputtered (MS) $Zr_{50}Cu_{50}$ and $Zr_{46}Cu_{46}Al_8$ films (Table 3.5 Chapter III) have been deposited for comparison purposes whose results have been used in Ref. [167].

4.2 Structural properties:

4.2.1 Morphology

The SEM cross-sections after mechanical cleavage of the $Zr_{50}Cu_{50}$ and $Zr_{46}Cu_{46}Al_8$ films deposited in vacuum and in 5 Pa He are presented in Figure 4.1a-d. All samples present the corrugations typical of MGs related to the propagation of shear bands during fracture[168].

However, some minor differences can be found between the samples that can be connected to the different compositions and morphologies. For example, the width of the corrugations on the surface of the cross-section decreases with the addition of Al going from 70 ± 4 nm for compact $Zr_{50}Cu_{50}$ (Figure 4.1a) to 59 ± 3 nm for compact $Zr_{46}Cu_{46}Al_8$ (Figure 4.1b). The widths of the corrugations of the compact films are in line with the values reported in other articles regarding Zr-based TFMGs [167, 169, 170] indicating a surface level similarity with magnetron sputtered TFMGs. This change, in literature, is related to a change in the free volume of the local structure due to the presence of Al favoring a less localized nucleation of shear bands [171]. The transition from atom-by-atom (compact) to cluster-assembled (nanogranular) growth further reduces the size of the corrugations which go from 61 ± 2 nm for nanogranular $Zr_{50}Cu_{50}$ (Figure 4.1c) down to 40 ± 3 nm for nanogranular $Zr_{46}Cu_{46}Al_8$ (Figure 4.1d). The reduction of the size of the corrugations can be connected to the local clustering favoring the delocalization of SBs and promoting the nucleation of multiple small SBs like in the case of nanoglasses [71, 74].

The XRD patterns for the compact and nanogranular $Zr_{50}Cu_{50}$ and $Zr_{46}Cu_{46}Al_8$ by PLD are presented in Figures 4.1e,f. Both compact and nanogranular films have a single hump, typical of amorphous materials, centered around $2\theta=37°-38°$ which is independent on the composition in agreement with the values observed for magnetron sputtered films and already reported in literature corresponding to an average interatomic distance of 2.5-2.6 Å [172, 173]. The absence of a shift in the peak position towards smaller interatomic distances due to the addition of Al is too small to see with Cu Kα XRD due to its low resolution and it is instead observed in literature with synchrotron XRD [167].

However, the full width at half maximum (FWHM) of the nanogranular film in Figure 4.1f is larger (8.8°) than the one of the compact counterparts in Figure 4.1e (7.5°), a confirmation of the increased disorder and heterogeneity of the local structure related to the cluster-assembled growth of the film forming a structure similar to the aforementioned nanoglasses [73].

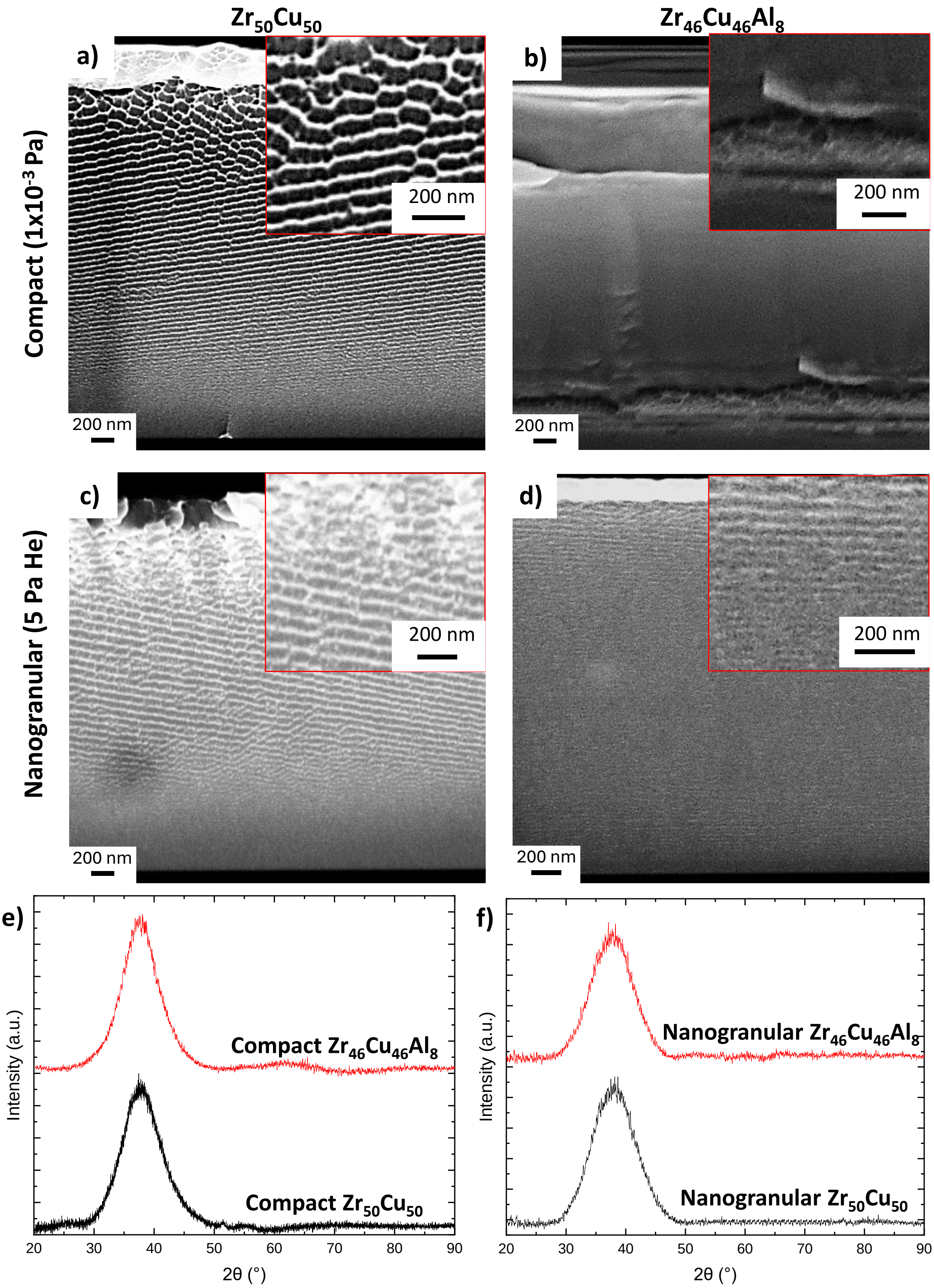

Figure 4.1: *SEM cross-section of compact (a,b) and nanogranular (c,d)* $Zr_{50}Cu_{50}$ *and* $Zr_{46}Cu_{46}Al_8$ *TFMGs deposited by PLD with insets to better show the differences in the dimensions of corrugations. XRD patterns of (e) compact and (f) nanogranular* $Zr_{50}Cu_{50}$ *and* $Zr_{46}Cu_{46}Al_8$ *TFMGs deposited by PLD.*

4.2.2 Evolution of density

The evolution of the mass density of the TFMGs deposited by PLD as a function of the Al content and morphology is shown in Figure 4.2.

The compact $Zr_{50}Cu_{50}$ films have a density equal to 8.35 g/cm^3 and it decreases down to 7.92 g/cm^3 for compact $Zr_{46}Cu_{46}Al_8$ due to the addition of a lighter element like Al (mass density = 2.7 g/cm^3) in substitution of the heavier Zr (mass density = 6.505 g/cm^3) and Cu (mass density = 8.94 g/cm^3) while keeping a constant interatomic distance (and thus volume) as observed from the XRDs of Figure 4.1e,f. Furthermore, the density of the compact films, 8.35 and 7.92 g/cm^3 for $Zr_{50}Cu_{50}$ and $Zr_{46}Cu_{46}Al_8$ respectively, is 10% higher than the density of their MS counterparts, equal to 7.4 and 7.17 g/cm^3 for $Zr_{50}Cu_{50}$ and $Zr_{46}Cu_{46}Al_8$ respectively. This is related to the high fluence used in PLD which increase the kinetic energy of the particles of the plasma plume resulting in a more closely packed atomic structure [144], a phenomenon already observed in literature for carbon [174] and oxide [143] films.

The transition from compact to nanogranular morphology also reduces the mass density of the films down to 7.98 and 7.1 g/cm^3 for nanogranular $Zr_{50}Cu_{50}$ and $Zr_{46}Cu_{46}Al_8$, respectively. This reduction of density is connected to the higher amounts of free volume as a result of the cluster-assembled growth similarly to what observed for nanoglasses characterized by high density of nanointerfaces and free volume between the different clusters forming the film [71, 80]. Moreover, it can be observed also that the transition from compact to nanogranular morphology doesn't reduce the density in a uniform way with the nanogranular $Zr_{50}Cu_{50}$ being 4.5% less dense than its compact counterpart while nanogranular $Zr_{46}Cu_{46}Al_8$ is 11% less dense than compact $Zr_{46}Cu_{46}Al_8$.

This could indicate that the presence of Al influences the clusters growth during deposition increasing of the free volume content with respect to $Zr_{50}Cu_{50}$ possibly leading to improved strength and plasticity.

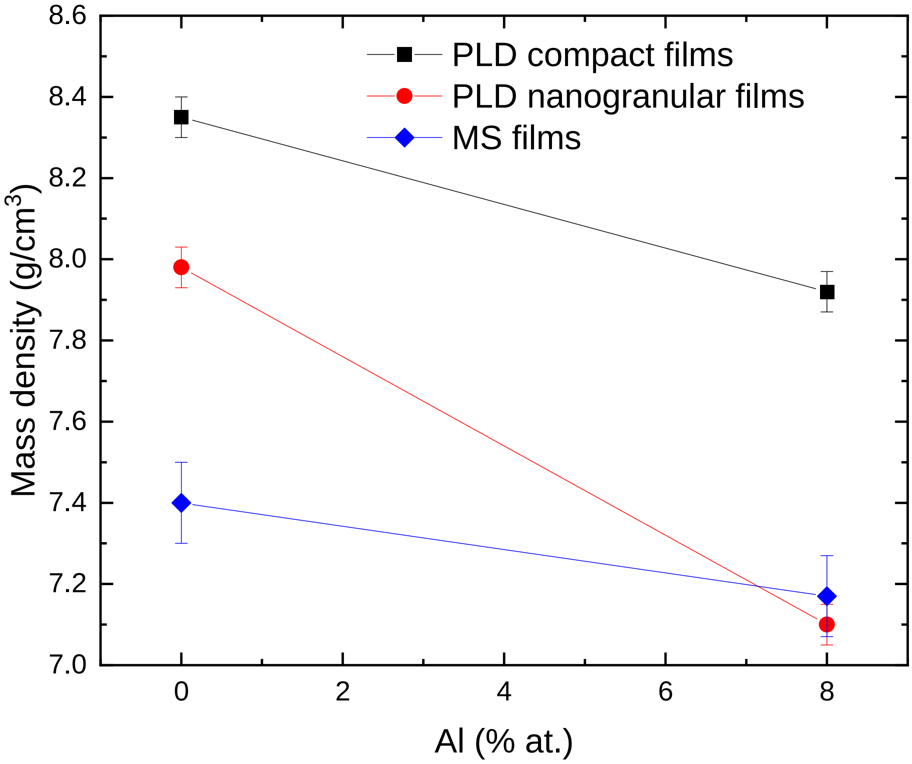

Figure 4.2: *Evolution of the mass density of the TFMGs deposited by PLD and magnetron sputtering as a function of the Al content and different morphologies.*

4.3 Mechanical properties:

4.3.1 Evolution of the elastic moduli and hardness

The evolution of the Young's modulus (*E)* and hardness (*H*) are presented in Figure 4.3a,b.

Firstly, it can be observed that the difference between the *E* and *H* of compact and nanogranular films are very low suggesting that the change in morphology does not have a major effect on the elastic properties of the films which instead are mainly governed by the chemical bonds between the elements forming the TFMGs. The elastic and plastic behavior of the films deposited by PLD is different when compared to their MS counterparts. The first major difference is that for the PLD TFMGs the addition of Al decreases *E* and *H* from 120 and 8.6 GPa respectively for $Zr_{50}Cu_{50}$ down to 109 and 7.8 GPa for $Zr_{46}Cu_{46}Al_8$. Meanwhile, in the case of MS TFMGs *E* and *H* increase with the addition of Al raising from 85 and 6.7 GPa respectively for $Zr_{50}Cu_{50}$ to 88 and 7.3 GPa for $Zr_{46}Cu_{46}Al_8$.

In literature, the increase of the mechanical properties of MS $ZrCuAl_x$ TFMGs when increasing the concentration of Al for x < 10 %at. is explained with the formation of short and strong Zr-Al and Cu-Al bonds decreasing the atomic mobility and delocalizing the formation of shear bands while increasing the free volume of the structure [171, 175, 176]. Voronoi tessellations generated with molecular dynamics (MD) simulations based on synchrotron diffraction patterns show that the addition of Al generates Al-centered icosahedra in the ZrCu atomic structure reaching their maximum concentration around 8 - 9 %at. Al. The Al-centered icosahedra act as pins hindering atomic rearrangement and improving the shear resistance and thus increasing the mechanical properties of the $ZrCuAl_x$ film [167, 177, 178]. The decrease of *E* and *H* with the addition of Al in PLD deposited films could be connected to their larger mass density which is responsible for their large *E* and *H* which are at least 20% - 30% above the values of the magnetron sputtered films.

Similar trends have been already observed for W films by PLD in which the increase of the elastic properties of the films is directly proportional to their density [137, 179]. A denser atomic structure could be related to different short and medium range order structures with respect to the ones calculated with MD simulations based on MS films which would have a different mechanical behavior. The possible presence of nanoscale segregations caused by the out-of-equilibrium deposition conditions of PLD could also be the cause of the softening of $Zr_{46}Cu_{46}Al_8$ PLD TFMGs. However, the true reasons behind the decrease of the mechanical properties of the PLD deposited $Zr_{46}Cu_{46}Al_8$ films are still an open question in this study and more advanced characterizations of the local structure are needed.

For this reason, synchrotron XRD and TEM characterization will be carried out to better understand the local structure of these films and connect them to their mechanical properties.

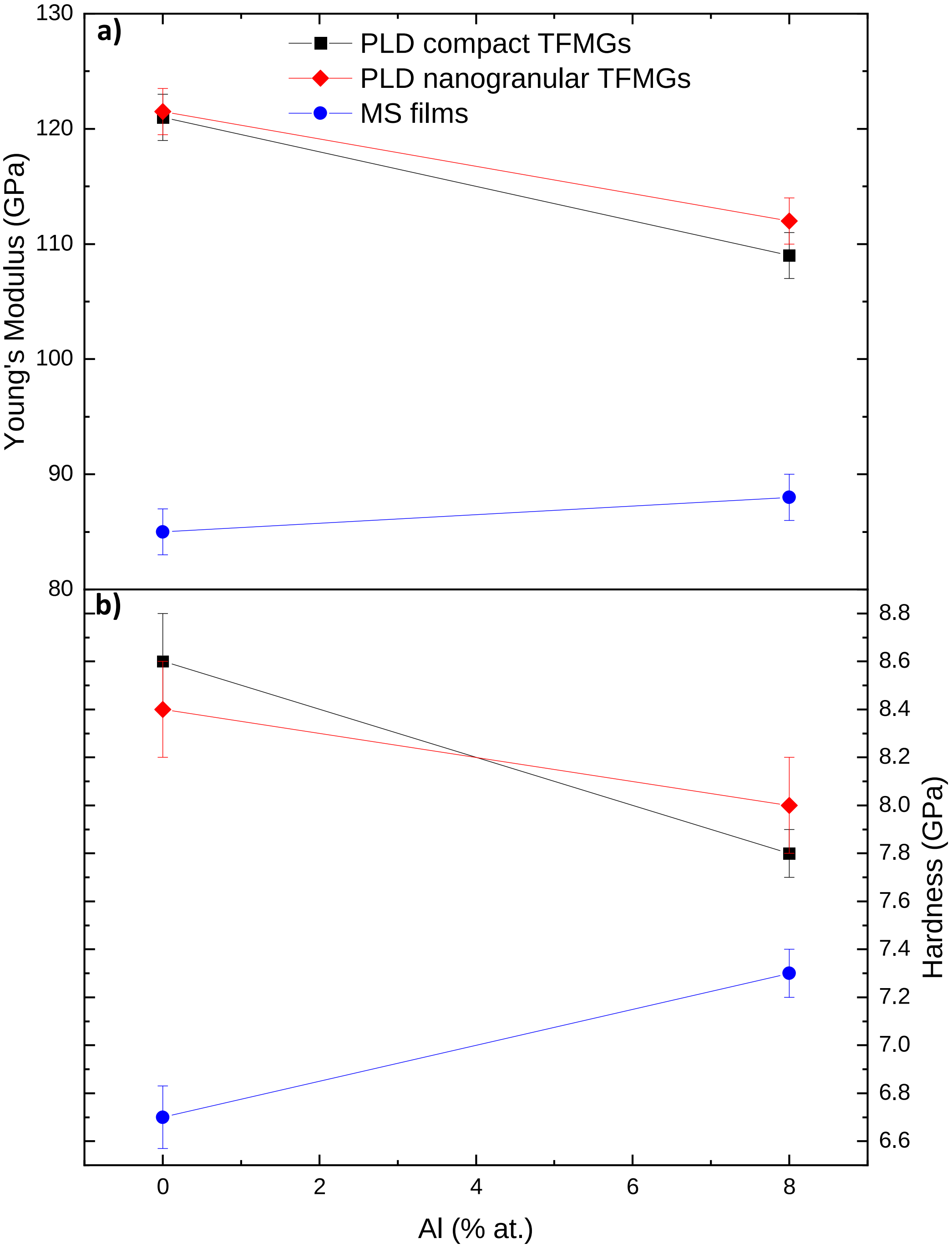

Figure 4.3: *Evolution of the (a) Young's modulus and (b) hardness of the TFMGs deposited by PLD and magnetron sputtering as a function of the Al content and different morphologies.*

4.3.2 Microscale stress-strain curve by micropillar compression

The strength and plasticity of $Zr_{50}Cu_{50}$ and $Zr_{46}Cu_{46}Al_8$ with compact and nanogranular morphology are further examined through micropillar compression to better understand the effects of composition and morphology on the mechanical response of the films.

The engineering stress-strain curves of compact $Zr_{50}Cu_{50}$ and $Zr_{46}Cu_{46}Al_8$ pillars when compressed with a strain rate $\dot{\varepsilon}$ of 10^{-2} s^{-1} are examined in Figure 4.4a. Compact $Zr_{50}Cu_{50}$ deform elastically up 3% engineering strain upon which the yield strength (σ_y) is reached (3.2 ± 0.06 GPa) followed by homogeneous plastic deformation up to 3.2 ± 0.2 % when few big shear bands (SBs) develop from the top of the pillar as shown in

Figure 4.4b. The value of *E* obtained from the fit of the loading curve is 108 ± 10 GPa, a value lower than the *E* shown in Figure 4.3 but coherent with the differences between real and measured moduli related to compression tests in literature [180]. The σ_y of the $Zr_{50}Cu_{50}$ films deposited by PLD is above the literature values (2.5 GPa) due to the high density of the PLD films responsible for the improved mechanical properties already discussed in section 4.2.3 [62]. Compact $Zr_{46}Cu_{46}Al_8$ deform elastically up 3.7% engineering strain, then yields reaching a σ_y equal to 2.8 ± 0.06 GPa and then deforming homogeneously up to 4.1 ± 0.2 % strain upon which multiple small SBs appear on top of the pillar as shown in Figure 4.4c.

The improved strain at SB propagation and the appearance of a larger number of SBs in $Zr_{46}Cu_{46}Al_8$ with respect to the $Zr_{50}Cu_{50}$ pillars (Figure 4.4b) can be related to the increased amount of free volume and formation of strong Zr-Al bonds related to the addition of Al [171, 178]. This delays the formation of mature SBs by favoring the nucleation of multiple embryonic SBs which then hinder each other's propagation [171].

Like in the case of compact $Zr_{50}Cu_{50}$, the value of *E* of compact $Zr_{46}Cu_{46}Al_8$ obtained from the fit of the loading curve is 90 ± 15 GPa, a value lower than the *E* shown in Figure 4.3 but coherent with the differences between real and measured moduli related to compression tests in literature [180]. Lastly, it can be observed that the plastic strain necessary for the formation of SBs in films by PLD is larger than what it is usually expected for MS TFMGs which usually fail at 2% strain [181, 182] possibly due to the denser atomics structure and larger mechanical properties of the PLD films.

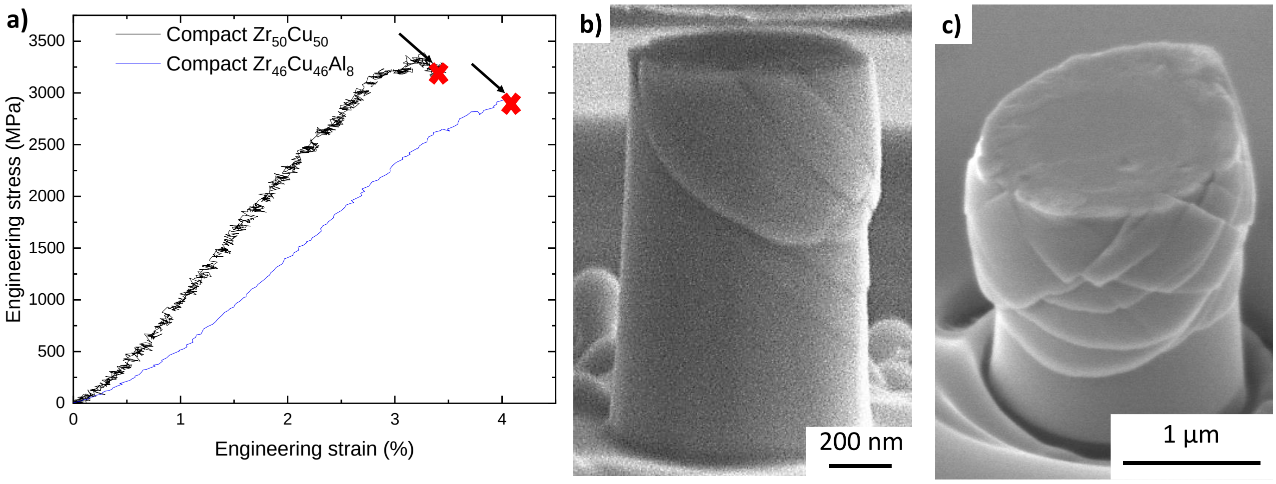

Figure 4.4: *(a) Engineering stress vs engineering strain curves of compact $Zr_{50}Cu_{50}$ and $Zr_{46}Cu_{46}Al_8$ TFMGs deposited by PLD with black arrows indicating the formation of the first shear bands and (b,c) postmortem SEM images of the compressed micropillars after the experiment.*

The engineering stress-strain curves of the nanogranular $Zr_{50}Cu_{50}$ and $Zr_{46}Cu_{46}Al_8$ pillars when compressed with a strain rate $\dot{\varepsilon}$ of 10^{-2} s^{-1} are reported in Figure 4.5a.

Nanogranular $Zr_{50}Cu_{50}$ pillars also deform elastically up to 3% and have σ_y equal to 2.9 ± 0.07 GPa, a value slightly lower than its compact counterpart and in line with the *H* values of Figure 4.3b and connected to the higher amount of free volume present in the nanogranular morphology activating plastic deformation at lower stresses [85, 183]. After yielding, the pillar continues to deform homogeneously up to 6 ± 0.2 % when the first SB develops on the top of the pillar as shown in Figure 4.5b. The value of *E* obtained from the fit of the loading curve is 106 ± 12 GPa, a value like the *E* of compact $Zr_{50}Cu_{50}$ and coherent with the differences in *E* reported in Figure 4.3.

The compressed nanogranular pillar shown in Figure 4.5b has a lower number and more superficial SBs with respect to its compact counterpart of Figure 4.4b as in what it is observed for nanoglasses which partially suppress the propagation of mature SBs through the sample and promote a more homogeneous deformation of the material [74]. Nanogranular $Zr_{46}Cu_{46}Al_8$ pillars deform elastically up to 4% and have σ_y equal to 3.2 ± 0.06 GPa and after yielding, the pillar continues to deform homogeneously up to 6.7 ± 0.2 % when small SBs start to form on the surface of the pillar as shown in Figure 4.5c. A possible reason behind the increase in σ_y

of nanogranular $Zr_{46}Cu_{46}Al_8$ TFMGs with respect to compact $Zr_{46}Cu_{46}Al_8$, which is opposite respect to what is observed in PLD $Zr_{50}Cu_{50}$, could be related to the presence of large chemical heterogeneities in the structure, similar to some $Zr_{50}Cu_{50}$ [73] and $Fe_{25}Sc_{75}$ [81] nanoglasses in which the chemical gradient between cores and shells of the nanoglass hinders SB propagation. The nanogranular $Zr_{46}Cu_{46}Al_8$ could have similar chemical fluctuations in their structure thanks to the presence of Al which already favors the formation of inhomogeneities in the amorphous matrix and future TEM characterizations will improve our understanding of the local structure of the TFMGs.

The value of *E* obtained from the fit of the loading curve is 91 ± 12 GPa, a value like the *E* of nanogranular $Zr_{46}Cu_{46}Al_8$ and coherent with the differences in *E* reported in Figure 4.3.

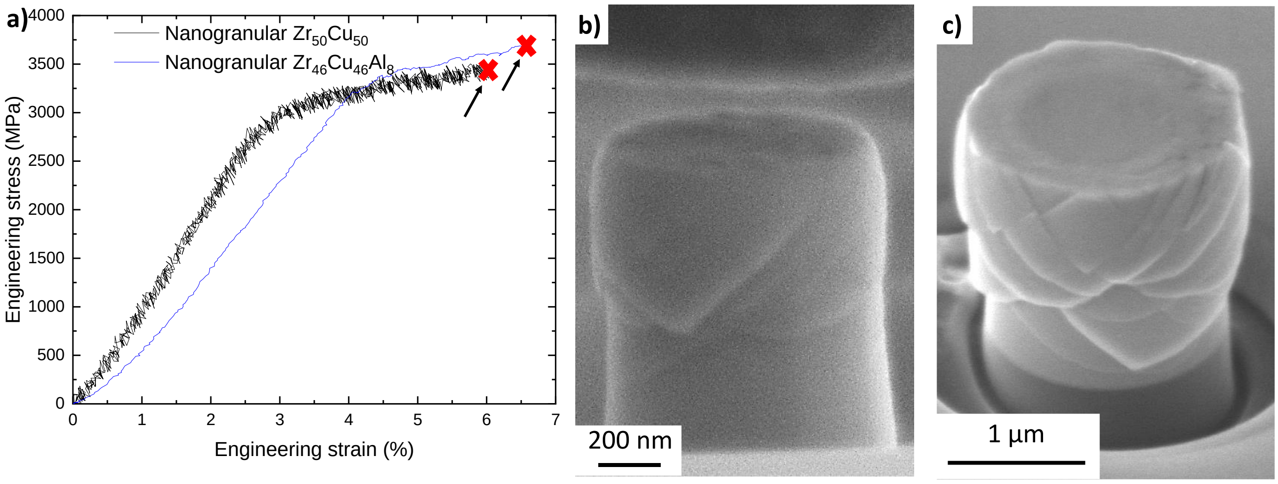

Figure 4.5: *(a) Engineering stress vs engineering strain curves of nanogranular $Zr_{50}Cu_{50}$ and $Zr_{46}Cu_{46}Al_8$ TFMGs deposited by PLD with black arrows indicating the formation of the first shear bands and (b,c) postmortem SEM images of the compressed micropillars after the experiment.*

4.3.3 Effect of deformation rate on mechanical response

The mechanical behavior of the compact and nanogranular $Zr_{46}Cu_{46}Al_8$ TFMGs is further examined by performing micropillar compression at different $\dot{\varepsilon}$ ranging from 10^{-3} (quasi-static loading) to 10 s^{-1} to study the possible differences in strain rate sensitivity *m* caused by the morphology which could be interesting for ballistic coatings or for high-speed impact resistance protective coatings. The engineering stress-strain curves of compact and nanogranular $Zr_{46}Cu_{46}Al_8$ for different $\dot{\varepsilon}$ are presented in Figure 4.6a,b. For compact $Zr_{46}Cu_{46}Al_8$, shown in Figure 4.6a, the σ_y decreases with the increase of $\dot{\varepsilon}$ from 2.9 GPa for $\dot{\varepsilon}$ equal to 10^{-3} s^{-1} to 2.55 GPa for $\dot{\varepsilon}$ equal to 10 s^{-1} resulting in a negative strain rate sensitivity *m*, as reported in Figure 4.6c and calculated as $dln\sigma_y/dln\dot{\varepsilon}$, equal to -0.0142. Negative strain rate sensitivities have already been observed in many metallic glasses and are connected to the inhomogeneous plastic flow typical of mature SBs propagation called “serrated” flow [18, 184-186]. The serrated flow of compact films is confirmed by the presence of SBs in the postmortem SEM images of Figure 4.6a confirming the SBs propagation independently from $\dot{\varepsilon}$.

Another indicator of the serrated flow is the value of the stress drop related to SB propagation, presented in Figure 4.6d and calculated as the difference in engineering stress caused by the propagation of a SB, which is decreasing with the increase of $\dot{\varepsilon}$ since less time is given for the rearrangement of STZs causing the propagation of cracks after SB initiation at the lower stress with respect to the ones that are reached in quasi-static loading [187, 188]. It must be underlined that the absence of stress drop values for $\dot{\varepsilon} > 0.1$ s^{-1} is caused by the increase of the floor noise of the machine for high strain rates and it doesn’t have a physical meaning.

As shown Figure 4.6b nanogranular $Zr_{46}Cu_{46}Al_8$ has an opposite behavior with respect to its compact counterpart with σ_y increasing with the $\dot{\varepsilon}$ passing from 3.08 GPa ($\dot{\varepsilon} = 10^{-3}$ s^{-1}) up to 3.5 GPa ($\dot{\varepsilon} = 10$ s^{-1}) resulting in a positive *m* equal to 0.0137 (Figure 4.6c). The transition from a negative to a positive value of *m* can be associated to a more homogeneous deformation of the material in which the propagation of mature SBs is suppressed, as suggested also by the fact that the stress drop values of nanogranular $Zr_{46}Cu_{46}Al_8$ are much lower than their compact counterparts and are weakly influenced by the change of $\dot{\varepsilon}$ as shown in Figure 4.6d [166, 186, 189]. However, the postmortem SEM images in Figure 4.6b show that all the pillars have cracks that can connected to SBs propagation in contrast to the hypothesis of homogeneous deformation and further investigation of the literature shows that TFMGs can have a positive m and still deform through SB propagation [170, 190, 191].

Nevertheless, the possibility to have either a strain rate hardening or softening film by changing the morphology remains interesting and further characterizations of the local structure will be able to identify possible changes in the nanostructure responsible for the change in m.

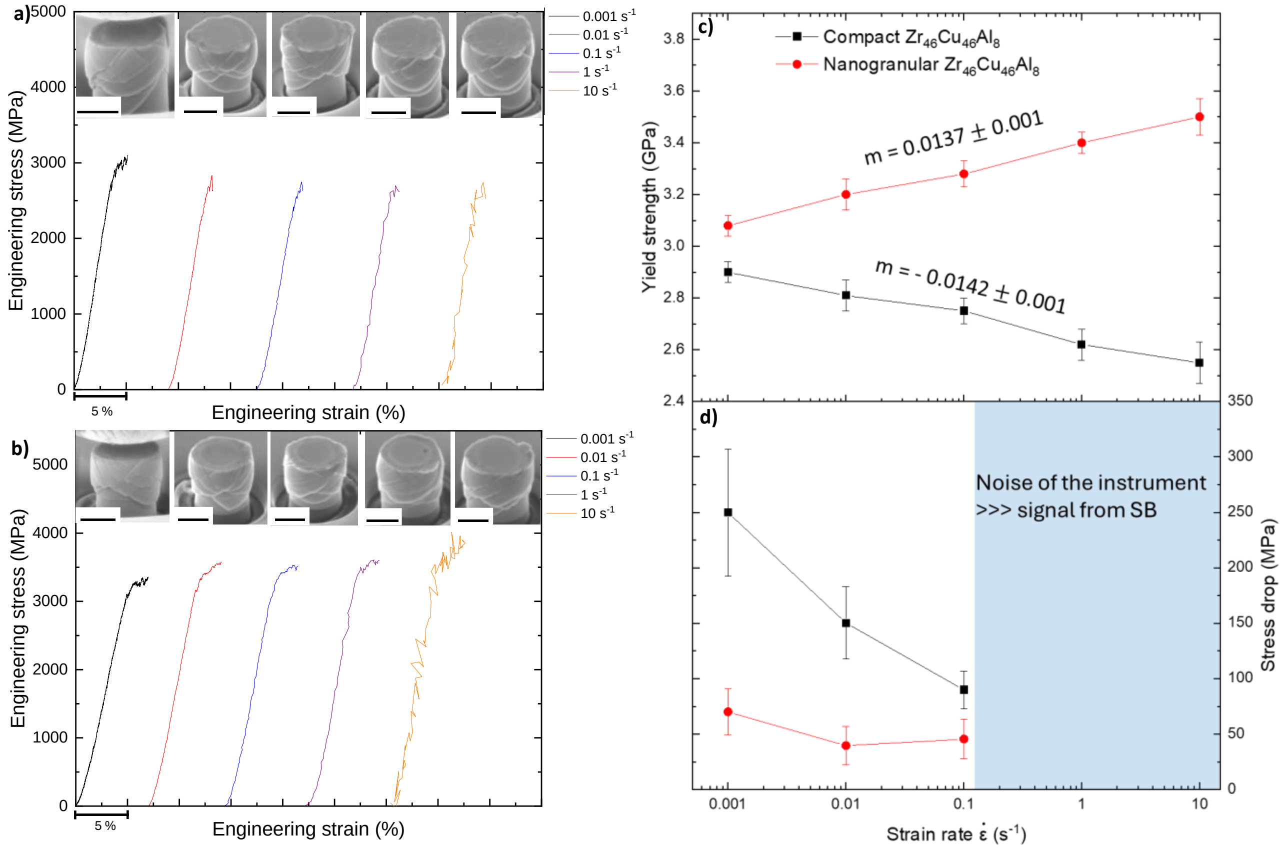

Figure 4.6: *Engineering stress-strain curves of (a) compact and (b) nanogranular $Zr_{46}Cu_{46}Al_8$ TFMGs by PLD tested with different $\dot{\varepsilon}$ with associated post-mortem SEM images of the pillars after compression, the scale bar for all the images is 1 µm. Evolution of the (c) σ_y and (d) stress drop during shear banding as a function of the strain rate for the compact and nanogranular $Zr_{46}Cu_{46}Al_8$ TFMGs deposited by PLD. The stress drops values for $\dot{\varepsilon} > 0.1\ s^{-1}$ are absent due to the increased measurement noise related to the high-speed experiments.*

4.3.4 Tensile tests on polymer substrate

Uniaxial tensile tests of films deposited on Kapton® substrates were performed to observe their mechanical response in tension when coupled with a flexible substrate and compare it to their MS counterparts.

The evolution of the crack density vs the engineering strain of the TFMGs depending on the composition, morphology and deposition method are shown in Figure 4.7a.

Compact films show that the crack onset strain (*COS*) increases with the addition of Al going from 1.3% for $Zr_{50}Cu_{50}$ to 2.03% for compact $Zr_{46}Cu_{46}Al_8$ (Figure 4.7a,b). The compact $Zr_{46}Cu_{46}Al_8$ film also shows some crack deviations and blocking (red arrows in the inset of Figure 4.7d) with respect to the purely straight cracks of compact $Zr_{50}Cu_{50}$ (Figure 4.7c).

These values are higher than the ones of their MS counterparts (1% for $Zr_{50}Cu_{50}$ and 1.7% for $Zr_{46}Cu_{46}Al_8$) possibly due to the combination of high elastic moduli of the PLD films and compressive residual stresses (-270 ± 50 MPa for compact PLD films vs -60 ± 20 MPa for MS films obtained from sample curvature measurements [161]) which help to improve the crack resistance in tensile loading [92, 192].

Nanogranular PLD films instead have an opposite trend of crack resistance with a crack initiation strain of 1.04% nanogranular $Zr_{50}Cu_{50}$ which goes down to 0.57% for nanogranular $Zr_{46}Cu_{46}Al_8$ and the surface of the films after loading present only straight cracks without crack deviations and blocking phenomena present in compact and MS $Zr_{46}Cu_{46}Al_8$ (Figures 4.7c,d).

The reduced crack resistance of the nanogranular films with respect to their compact counterparts can't be connected to different residual stresses since both compact and nanogranular films have similar compressive stresses (-270 ± 50 MPa for compact films and -290 ± 55 MPa for nanogranular films) and it can be instead related to the more disordered local structure of nanogranular films.

In literature it is observed that the presence of local interfaces in a film can act as preferential crack initiation sites like in the case of nanocolumnar $Zr_{52}Cu_{48}$ of Brognara *et al*. [92] and nanocolumnar $Zr_{25}Cu_{75}$ of K. Wu *et al*. [193] which result much more fragile with respect to fully homogeneous MS films (0.5% vs 1% for $Zr_{52}Cu_{48}$, 0.51% vs 2% for $Zr_{25}Cu_{75}$).

The local density and chemistry fluctuations of nanogranular films could have a similar effect and favor the fragmentation of the film during tensile loading and compromise their toughness when deposited on a polymer substrate.

The increased brittleness of nanogranular films is also underlined by their high crack saturation density (*CSD*) with respect to compact films which have similar stiffness (Figure 4.3a) as shown in Figure 4.7c while MS TFMGs have a lower crack saturation density due to their lower stiffness with respect to PLD films [160].

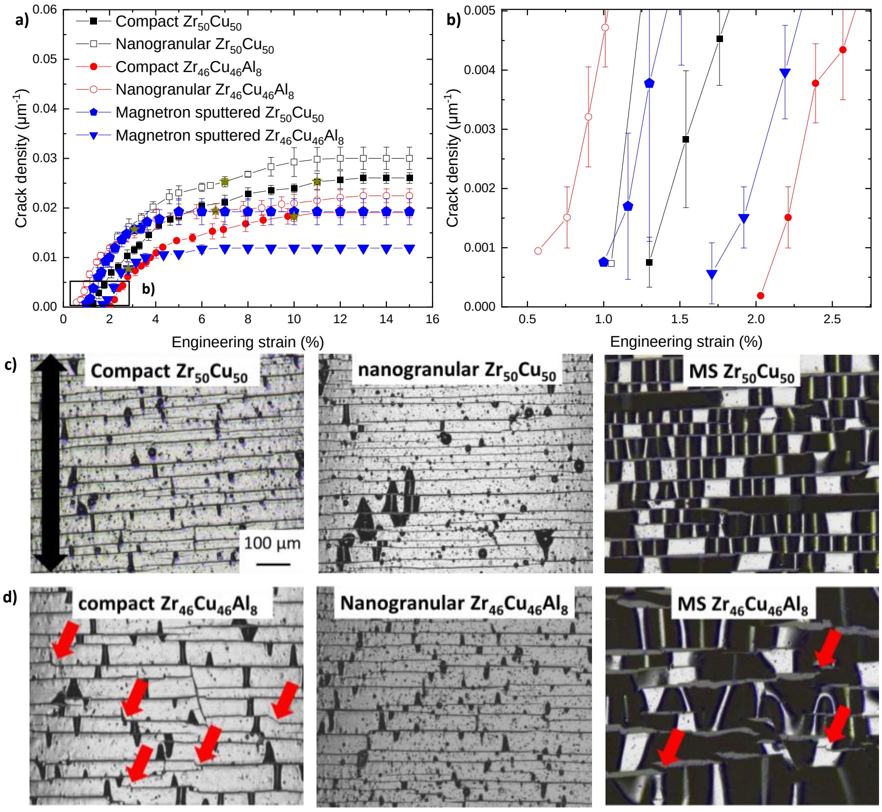

Figure 4.7: *(a) Crack density vs engineering strain curves of the compact and nanogranular* $Zr_{50}Cu_{50}$ *and* $Zr_{46}Cu_{46}Al_8$ *films by PLD with relative images of the surface after the experiments. The golden stars indicate the strain at which the films start to delaminate from the substate. (b) Magnification of the initial region of the crack density-engineering strain curve highlighting the crack initiation strain of each film. Post-mortem optical images of the compact, nanogranular and MS (c)* $Zr_{50}Cu_{50}$ *and (d)* $Zr_{46}Cu_{46}Al_8$ *films after 15% strain. The vertical black arrow indicates the loading direction during the experiment.*

The fracture toughness of the compact and nanogranular $Zr_{50}Cu_{50}$ and $Zr_{46}Cu_{46}Al_8$ are shown in Figure 4.8a and compared with their MS counterparts. The Beuth model [162] combines *COS*, *CSD*, the reduced modulus of the film E_r, and the stress at fracture of the film ($COS{*}E{+}\sigma_{res}$) to obtain the fracture energy G_{Beuth} = $\frac{(COS{*}E{*}\sigma_{res})^2}{1.34CSDE_r}$ which can be used to calculate the fracture toughness expressed as $\sqrt{E_r G_{Beuth}}$.

It is observed that for compact films the toughness increases with the Al content rising from 6.8 MPa*m$^{1/2}$ for $Zr_{50}Cu_{50}$ to 12.2 MPa*m$^{1/2}$ for $Zr_{46}Cu_{46}Al_8$. MS films follow the same trend with the toughness increasing from 5.3 MPa*m$^{1/2}$ for $Zr_{50}Cu_{50}$, a value comparable with other Zr-based TFMGs found in literature [194, 195], to 10.8 MPa*m$^{1/2}$ for $Zr_{46}Cu_{46}Al_8$. As expected from the low values of crack initiation strain and high crack saturation density the toughness of nanogranular films is lower than its compact counterparts and decreases with the addition of Al passing from 5 MPa*m$^{1/2}$ for $Zr_{50}Cu_{50}$ down to 2.1 MPa*m$^{1/2}$ for $Zr_{46}Cu_{46}Al_8$ reaching values comparable to the ones of nanocolumnar TFMGs [92].

Lastly, the adhesion energy J_0 of the films to the substrate is presented in Figure 4.8b. J_0 can be estimated from the buckling initiation strain (*BIS*), *CSD*, film's thickness *h*, the reduced modulus of the film E_r, and σ_{res} by using strain energy delamination model [163] with J_0 = $\frac{E_r h\beta^2}{2}\left(BIS + \frac{\sigma_{res}}{E_r\beta}\right)^2$ with β being a dimensionless factor depending on *CSD* equal to -0.47 – 0.475 for the films examined here. The adhesion energy seems mainly independent on the composition of the films and mainly determined by the morphology and deposition method. Compact films by PLD have an adhesion energy in the order of 100 J/m^2 which decreases to 50 J/m^2 for nanogranular films and goes down to 6 J/m^2 for MS films. The adhesion energy of the MS films is in line with the values found in literature for MS TFMGs [193], HEAs [160] and crystalline single [196] and multilayer [197] metallic films.

This would suggest that main parameter determining the adhesion between substrate and film could be the energy with which the atoms impinge on the polymer substrate during deposition and since the plasma of PLD has much more energy than conventional magnetron sputtering it would be reasonable to observe higher adhesion energy in PLD which results in delayed delamination with respect to MS films [88, 198].

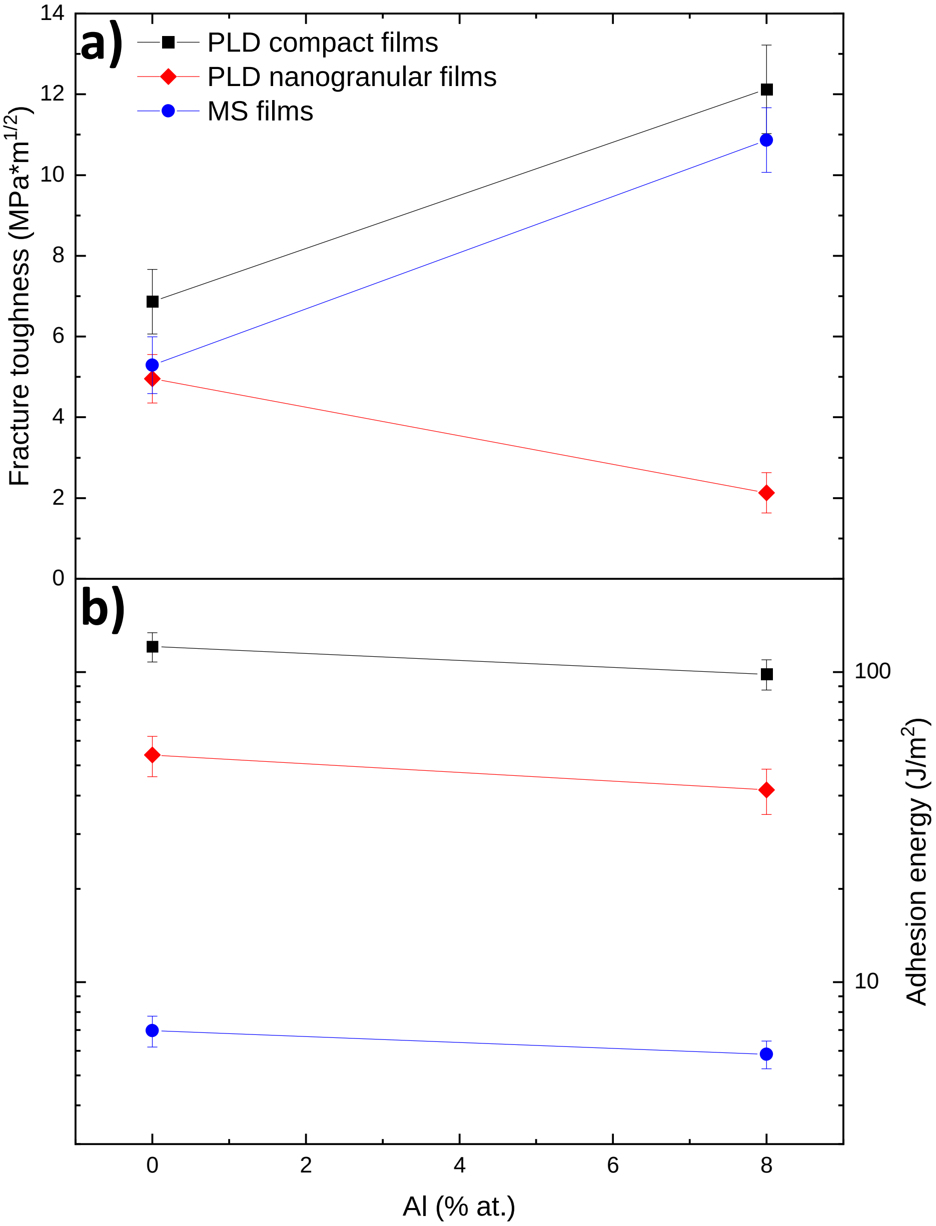

Figure 4.8: *Evolution of (a) fracture toughness and (b) adhesion energy of the compact and nanogranular $Zr_{50}Cu_{50}$ and $Zr_{46}Cu_{46}Al_8$ films by PLD compared with their MS counterparts.*

4.4 Conclusions

In this chapter $Zr_{50}Cu_{50}$ and $Zr_{46}Cu_{46}Al_8$ TFMGs are deposited by PLD in vacuum and 5 Pa He to tune the morphology by changing the film's growth mechanism from atom-by-atom (compact) or cluster-assembled growth (nanogranular) regime and these nanostructured TFMGs are compared with MS counterparts. From their structural and mechanical characterization, it is shown that:

- PLD films have a higher mass density than their MS counterparts (8.35 vs 7.4 g/cm^3) due to the high kinetic energy of the plasma involved in PLD deposition.
- Compact and nanogranular films by PLD have very similar E and H and are much higher with respect to MS films (E = 120 GPa and H = 8.6 GPa for compact $Zr_{50}Cu_{50}$ vs E = 85 GPa and H = 6.7 GPa for MS $Zr_{50}Cu_{50}$) thanks to the higher mass density leading to a more compact structure. However, the E and H of PLD films decrease with the addition of Al instead of increasing like in the case of MS films (E = 109 and H = 7.8 GPa for compact $Zr_{46}Cu_{46}Al_8$ vs E = 88 and H = 7.3 GPa for MS $Zr_{46}Cu_{46}Al_8$) suggesting that the local structure of PLD films integrates Al atoms in a different way with respect MS films.

- Micropillar compression tests show that the PLD films possess high yield strength >2.8 GPa following the same trend observed for *H*. Compact films fail shortly after yielding, after reaching values of homogeneous deformation of 3.3% for $Zr_{50}Cu_{50}$ and 4.1% for $Zr_{46}Cu_{46}Al_8$, while nanogranular $Zr_{50}Cu_{50}$ and $Zr_{46}Cu_{46}Al_8$ can deform homogeneously after yielding and fail after 6%-6.7% homogeneous deformation by delaying and suppressing SBs propagation.
- The study of the strain rate sensitivity *m* of compact and nanogranular $Zr_{46}Cu_{46}Al_8$ shows that compact $Zr_{46}Cu_{46}Al_8$ has a negative *m* indicating a strain rate softening behavior while nanogranular $Zr_{46}Cu_{46}Al_8$ has a positive *m* indicating a strain rate hardening behavior and a lower degree of localization of plastic deformation.
- Tensile tests of TFMGs deposited on a polymer substrate indicate that PLD compact films have a good combination of fracture properties reaching the peak for compact $Zr_{46}Cu_{46}Al_8$ combining a crack initiation strain of 2.03% and a toughness of 12.2 MPa*$m^{1/2}$ while nanogranular films have reduced crack resistance due to their cluster-assembled morphology favoring crack initiation.

Overall, PLD can produce nanoengineered TFMGs with improved mechanical properties with respect to traditional magnetron sputtering by simply changing the deposition pressure inside the chamber.

While compact films behave mostly like strong MGs, having higher strength than conventional MGs due to their higher density but still failing due to SB propagation, nanogranular films can deform more homogeneously and prevent the sudden propagation of SBs through the sample making them more interesting for industrial applications.

These results prove the versatility of PLD as a deposition technique for the deposition of strong and plastic MG coatings with a controlled nanostructure which can be very interesting for a variety of applications ranging from structural coatings in high loading environments to flexible electronics.

V. Synthesis of $Zr_{50}Cu_{50}$/Al amorphous/crystalline ultrafine-nanolaminates with large and tunable mechanical properties

5.1 Overview on the investigated samples

In this chapter the structure and mechanical properties of the $Zr_{50}Cu_{50}$/Al films deposited by PLD in vacuum ($1x10^{-3}$ Pa) and in 5 Pa He are presented. A $Zr_{50}Cu_{50}$ target (purity >99.95%) modified with the addition of Al strips with different widths was used to obtain ultrafine nanolaminates alternating 6 – 9 nm of $Zr_{50}Cu_{50}$ and 4 nm Al as explained in Section 3.1.2 of Chapter III. The films were deposited with an IR (1064 nm) laser with an average energy around 1650 ± 10 mJ with the optics set up to have a fluence of 14 J/cm^2.

In this study, we focus on U-NLs with a $t_a/ t_c > 1$, expecting a high strength due to the larger fraction of amorphous phase, while keeping a high plasticity due to the presence of FCC Al sublayers. The characteristics of the films examined in this Chapter can be found in Table 3.3.

5.2 Structural properties:

5.2.1 Morphology

The SEM cross-section (Figures 1a,b) displays the absence of macroscopic defects such as porosities and phase segregations, which could affect the mechanical behavior while showing the presence of corrugations, induced by the propagation of SBs typical of MGs [168]. This is expected since $t_a/ t_c > 1$ leading to deformation process dominated by SBs propagation especially when performing cleavage cuts which force sharp crack propagation from Si substrate to the U-NLs [63, 168].

The XRD patterns for the compact and nanogranular $Zr_{50}Cu_{50}$/Al U-NLs presented in Figures 5.1c,d respectively, show that the pure $Zr_{50}Cu_{50}$ is completely amorphous with a main peak centered at 2θ = 37° - 38° as expected from literature [92]. However, the full width at half maximum (FWHM) of the nanogranular film in Figure 5.1d is wider (9°) than that of the compact film counterpart in Figure 1c (7.5°), indicating a more disordered and heterogeneous structure due to their cluster-assembled growth such as for nanoglasses [73, 199].

The U-NLs also show a peak at 2θ = 38.5° which corresponds to the (111) plane of FCC Al, indicating a textured growth of the crystalline layer. The peak is more pronounced with increased Al relative fraction. The size of the Al crystallites, obtained by Scherrer's equation on the Al (111) reflection, is ~4.0 ± 0.5 nm.

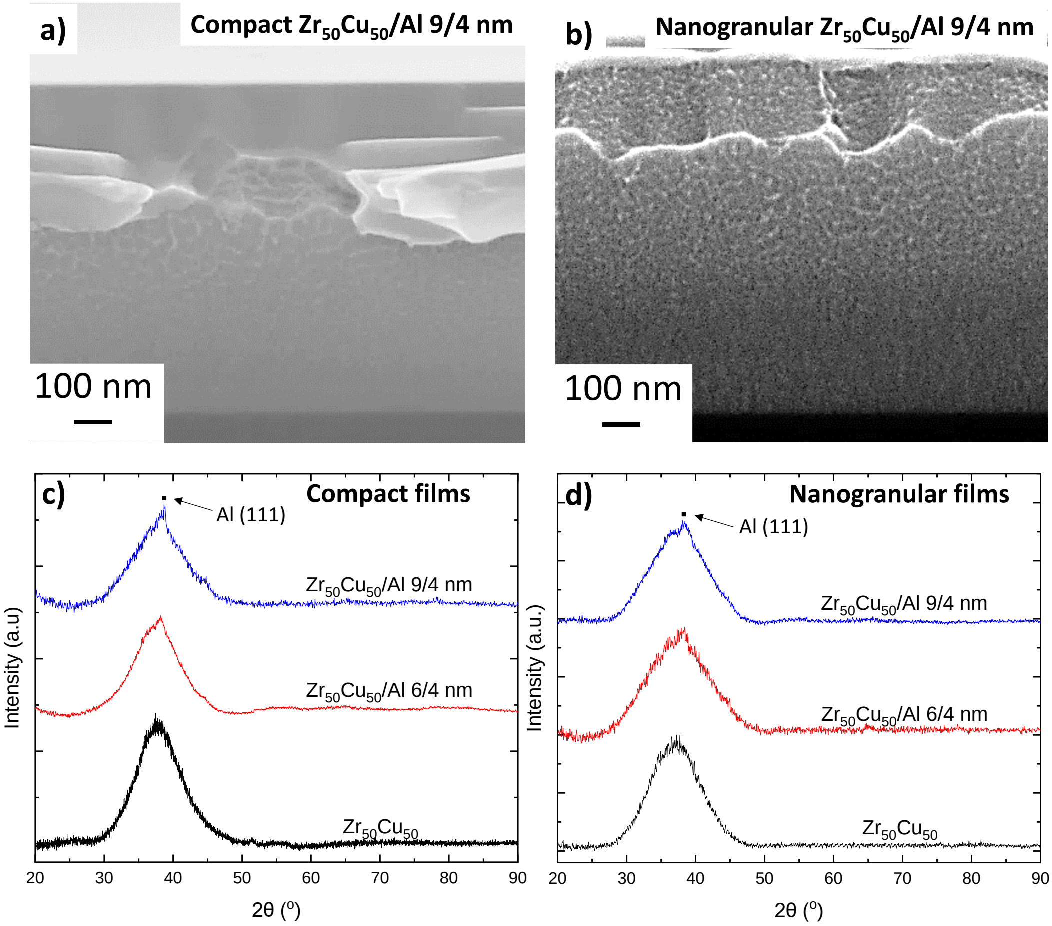

Figure 5.1. *Cross sectional SEM and XRD patterns as a function of bilayer period of compact (a,c) and nanogranular (b,d)* $Zr_{50}Cu_{50}$*/Al U-NLs, respectively.*

5.2.2 Evolution of density

Figure 5.2 shows the evolution of the mass density for U-NLs compared to magnetron sputtered (MS) deposited ZrCu films [167, 176]. Firstly, the nanogranular U-NLs are slightly less dense than their compact counterparts due to the higher amount of free volume originated by the cluster-assembled growth [199].

Moreover, the density of compact $Zr_{50}Cu_{50}$ PLD films (8.35 g/cm^3) is at least 10% higher than their traditional MS counterparts (7.4 g/cm^3) [167, 176]. This phenomenon, already observed in literature for oxides [143] and carbon films [174], is related to the high fluence used in PLD which confers higher amounts of kinetic energy to the atoms in the plasma plume allowing the growth of films with a more closely packed atomic structure [144]. Lastly, for both compact and nanogranular nanolaminates, the density decreases with increasing the Al volume fraction (an element with lower mass density) varying from 8.35 and 7.98 g/cm^3 for compact and nanogranular $Zr_{50}Cu_{50}$ down to 7.9 and 7.6 g/cm^3 for the corresponding U-NLs alternating 4 nm of Al and 6 nm of $Zr_{50}Cu_{50}$. However, such values are still higher than the density of MS $Zr_{50}Cu_{50}$ with 7.4 g/cm^3 even considering a 40% Al volume fraction within the PLD deposited U-NLs.

This can be explained by the high energies of PLD and high chemical intermixing between the Al and $Zr_{50}Cu_{50}$ layers forming a denser ZrCuAl amorphous phase (~7.1 g/cm^3) [167, 176] than pure Al (2.7 g/cm^3) [200]. This result reduces the drop in density that could be expected for high volume fractions of pure Al.

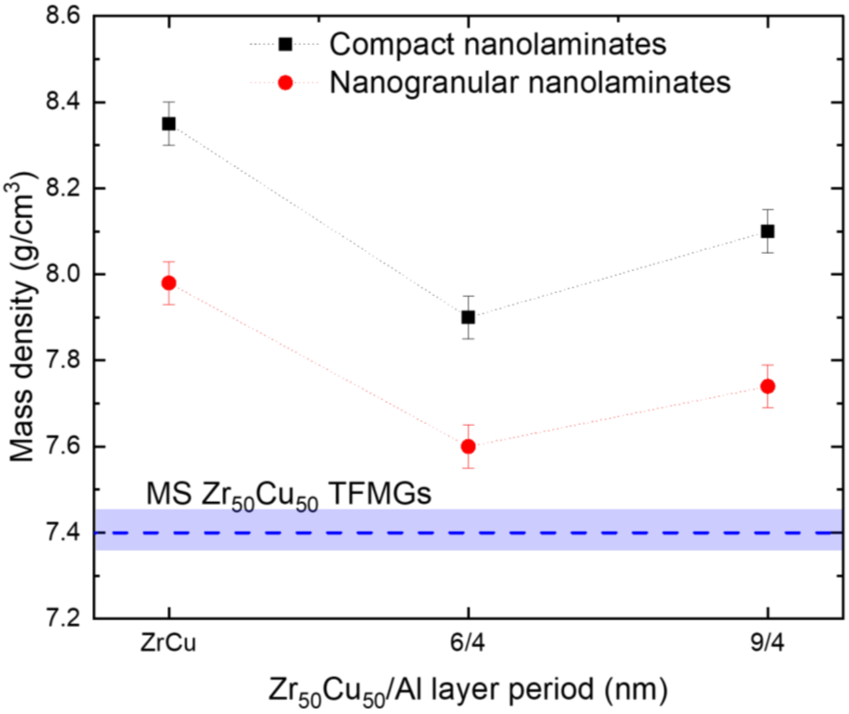

Figure 5.2. *Evolution of the mass density of compact and nanogranular $Zr_{50}Cu_{50}$/Al U-NLs with different layered structure.*

5.2.3 TEM highlighting the nanolayered structure

A more detailed investigation of the nanostructure of the U-NLs alternating 4.0 ± 0.5 nm of Al and 9.0 ± 0.5 nm of $Zr_{50}Cu_{50}$ (referred as $Zr_{50}Cu_{50}$/Al 9/4 nm) was conducted by STEM.

Figures 5.3a,b display HAADF STEM images of compact (a) and nanogranular U-NLs (b) revealing a nanolayered structure with straight interfaces. Such structure differs from previously reported nanolaminates with similar bilayer periods (6 – 20 nm) deposited by magnetron sputtering which usually have undulating interfaces due to the incomplete coalescence of the islands during the sputtering of the single interlayers [58, 201, 202]. As a matter of facts, PLD enable larger energy of the deposited species (> 15 eV) vs magnetron sputtering (~1 eV) allowing a faster percolation of the islands, forming the defined interlayers with large chemical intermixing [144]. Figure 5.3b also shows that the single layers composing the nanogranular U-NLs are not homogeneous, but formed by nano-size clusters due to the in-plume cluster formation induced by the background deposition pressure [199].

These clusters have brighter cores and darker surroundings indicating a change in the relative density from the center (denser) to the interfaces (less dense) due to chemical segregation during the cluster formation and the formation of topological defects during the bonding of adjacent clusters such as in nanoglasses [71, 74]. SAED patterns in the insets of Figures 5.3a,b reveal a single band in agreement with the XRD, but without spot patterns expected from the crystalline Al layers. This could be related with the elemental chemical intermixing phenomena (formation of the ZrCuAl) for both compact and nanogranular U-NLs (Figure 2c,d) as well as with the difficulty to obtain SAED patterns of the nanocrystalline Al, which possesses very small intrinsic sizes (≤ 4nm). The thickness of the layers estimated by HAADF STEM and STEM-EDX line profile are quite similar and can be considered equal. In both cases we show chemical intermixing between the Al and the $Zr_{50}Cu_{50}$ layers with high concentrations of Zr and Cu in the Al layers and with the peaks of Al concentrations (dash vertical lines) being in counterphase with the Cu concentration (dash – dot vertical lines) due to the low miscibility between Al and Cu ($\Delta H_{mix\ Al\text{-}Cu}$ = -1 kJ/mol) [13]. The intermixing between the layers is favored by the thin thickness of the sublayers of the U-NLs [65, 202], the high mixing enthalpy between Zr and Al (*$\Delta H_{mix\ Zr\text{-}Al}$ = -44 kJ/mol)* [13], the high reactivity of the Al nanocrystalline grain boundaries [129] and the high surface mobility of the atoms during the film growth due to the high energies of PLD [144].

This chemical diffusion of Al and ZrCu between the different sublayers generate a ZrCuAl phase with interatomic distance close to $Zr_{50}Cu_{50}$ (2.5 Å) [167]. However, a more accurate analysis by using atom probe tomography (APT) will be necessary to achieve higher spatial resolution, especially for the case of U-NLs with nm-sized bilayer periods explored in this study. The SAED signal of this new phase would then reduce the intensity of the SAED of the base components such as in TiAl intermetallic grown during the annealing of Al/Ti multilayers [141].

The formation of the ZrCuAl phase slightly reduce the effective thickness of the crystalline layer (t_c), consequentially increasing the t_a/t_c ratio which, however, remains >1. This results in comparable mechanical properties and deformation behavior as shown in Ref. [63].

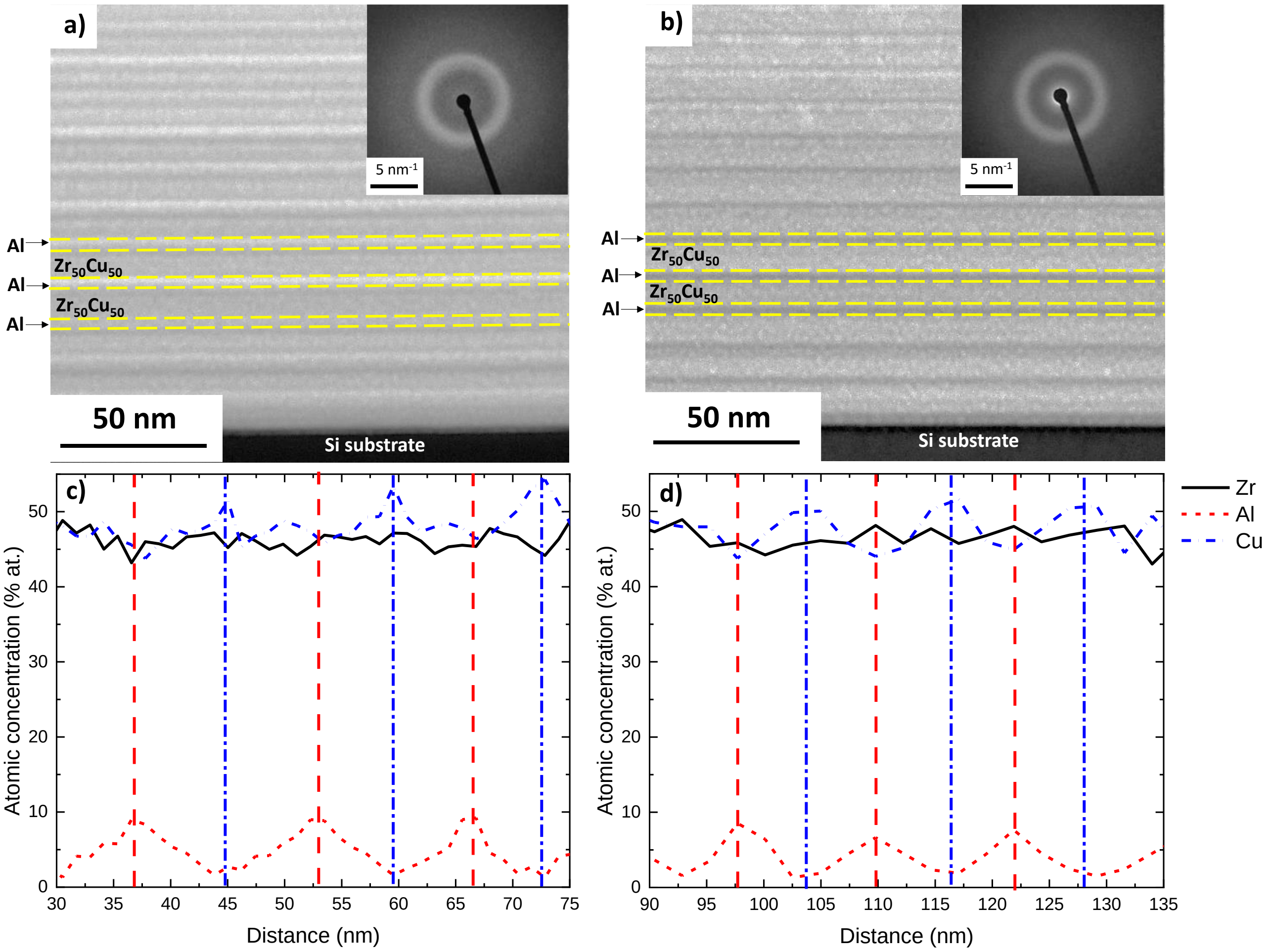

Figure 5.3. *HAADF-STEM images of compact (a) and nanogranular (b) $Zr_{50}Cu_{50}$/Al U-NLs showing the nanolayered microstructure with $Zr_{50}Cu_{50}$ layer thickness of 9.0 ± 0.5 separated by 4.0 ± 0.5 nm Al layers. The corresponding SAED pattern in the inset of a) and b) highlight the main amorphous structure of both samples. The averaged STEM-EDX line profiles across several layers for both compact (c) and nanogranular (d) U-NLs shows a large intermixing between the nanolayers.*

5.3 Mechanical properties:

5.3.1 Evolution of the elastic moduli and hardness

Figure 5.4 presents the evolution of the Young's modulus (*E*) obtained by optoacoustic techniques and hardness (*H)* obtained by nanoindentation. Both compact and nanogranular U-NLs follow the same trend and have similar values of *E* and *H* as a function of the layer period indicating that the transition from compact to nanogranular morphology has only a minor effect on the elastic properties of the U-NLs.

This is probably because elastic constants are essentially linked to structure (at the bond scale), rather than microstructure.

Furthermore, we observe that *E* and *H* of our PLD deposited films are much higher (30%) than those of sputter-deposited ZrCu TFMGs [92, 203] and similar multilayers [54, 55].

This results from the higher density of the PLD films as observed in the W and W-O films deposited with different densities by Besozzi *et al*. [137, 179] in which the increase of the elastic moduli is directly proportional to the densification of the films.

The introduction of the Al nanolayering increases *E* and *H* from 120 and 8.6 GPa of $Zr_{50}Cu_{50}$ up to 139 and 9.3 GPa for the corresponding U-NLs with $Zr_{50}Cu_{50}$/Al 9/4 nm. This value is higher than the theoretical average of *E* and *H* of the single $Zr_{50}Cu_{50}$ and Al layers based on the relative volume fraction of Al, namely 105 and 6.4 GPa, because of the formation of a U-NL structure.

However, such trend is opposite to what observed in the literature of amorphous/crystals multilayers reporting decrement of *H* for larger fraction of the FCC crystalline phase such as in the case of ZrCu/Cu multilayers [55, 204] which show a reduction of *H* down 5.9 GPa for 50% Cu volume fraction. The behavior observed of U-NLs can be related to a combination of many factors among which the high density of crystalline/amorphous interfaces, which have been demonstrated to increase the mechanical strength of the structure [65] since the interfaces can confine and deviate the propagation of SBs increasing the stress necessary for plastic deformation [57].

A second factor to be considered is the large chemical intermixing with the formation of a ZrCuAl phase involving the formation of strong Zr-Al and Cu-Al bonds and by creating short range order Al-centered polyhedral clustered structures, providing high strength as well as a delay to the propagation of SBs [167, 171]. To sum up, the formation of the ZrCuAl phase and the ultrafine nanolayered structure reinforces the mechanical properties of the Al layers, that normally would have *E* and *H* equal to 69 GPa and 1.5 Gpa respectively [205], preventing the drop in mechanical properties usually associated with crystalline/amorphous multilayers.

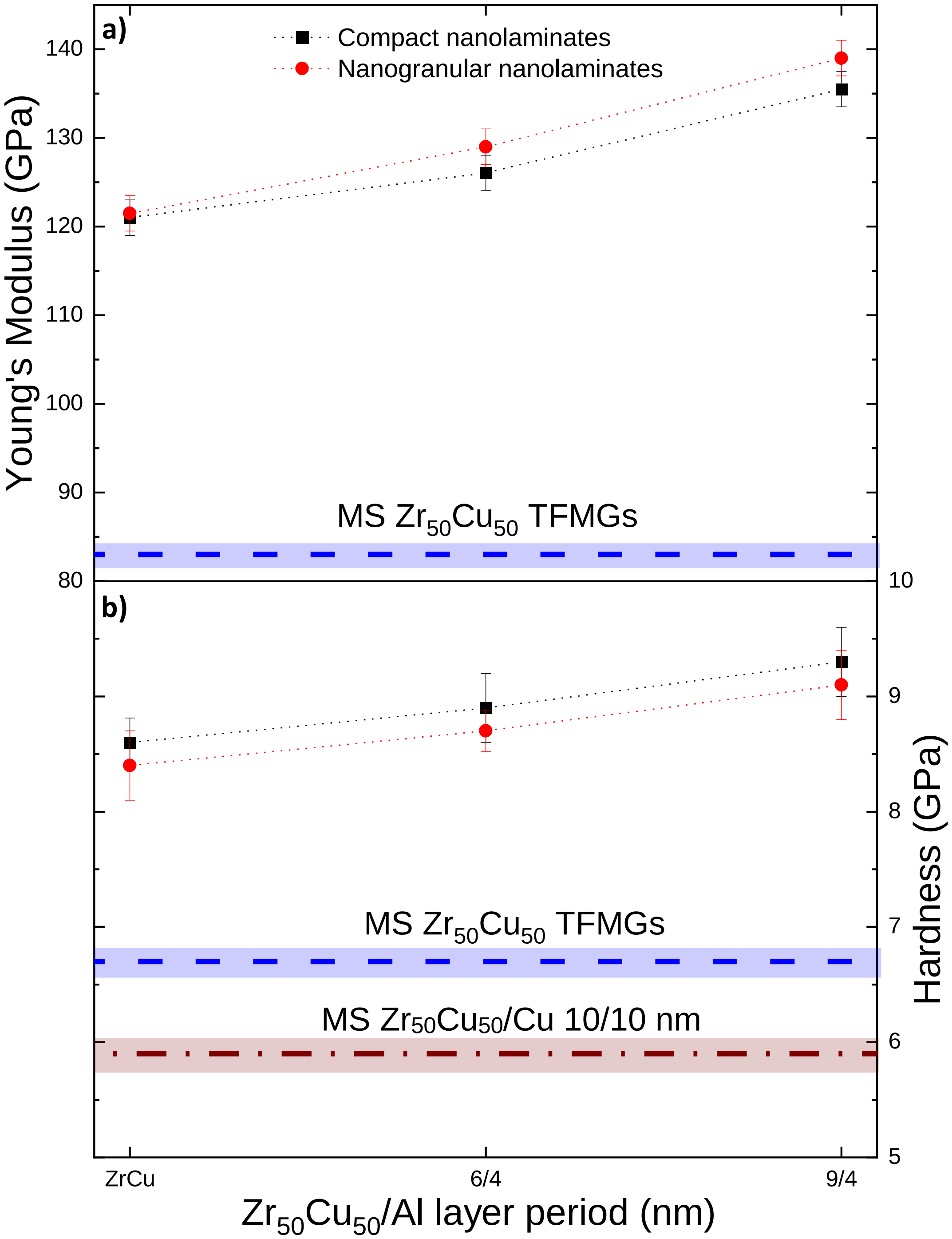

Figure 5.4. *Evolution of elastic modulus (a) and hardness (b) of compact and nanogranular $Zr_{50}Cu_{50}$/Al U-NLs for different U-NLs configurations. Data are compared with traditional MS ZrCu and ZrCu/Cu multilayers.*

5.3.2 Evolution of yield strength and plasticity through micropillar compression

Micropillar compression tests were carried out on both compact and nanogranular $Zr_{50}Cu_{50}$/Al 9/4 nm U-NLs which had the highest density and *H* (Figures 5.3 - 5.4), thus expecting higher plasticity.

Moreover, the higher fraction of ZrCu (vs the $Zr_{50}Cu_{50}$/Al 9/4 U-NLs) is expected to provide enhanced mechanical size effects [165], while the crystalline Al is expected to have beneficial SB booking effects.

For the compact U-NLs, Figure 5.5a shows that after the elastic behavior up to 3.3 %, the stress-strain curve is interrupted by the propagation of the first SB. The yield stress (σ_y) is equal to 3.60 ± 0.08 GPa which is 1.1 GPa higher than of MS-deposited ZrCu homogeneous TFMGs and of ZrCu amorphous/crystalline multilayers [54, 62], due to the high mass density of the PLD U-NLs, significant chemical intermixing and the high density of crystalline/amorphous interfaces [65]. The first SB starts to appear at 3.60 ± 0.22 % strain, a value significantly larger than the monolithic TFMG threshold which is usually around 2% [181, 206].

This improvement of plasticity is connected to the presence of Al layers which confine and block the SBs in the amorphous ones promoting a more homogeneous deformation. This is confirmed in Figures 5.5b,c reporting the post-mortem SEM and TEM images of the pillar, highlighting the SB blocking effect of Al-rich layers, while showing the nanoscale periodicity of the Al and $Zr_{50}Cu_{50}$ layers (Figure 5.5d). The formation of through-the-specimen percolative SBs occurring in U-NL is also expected since the t_a/t_c (thickness of amorphous layer/thickness of crystalline layer) ratio >1, showing a dominant fraction of amorphous sublayers. As a matter of facts, molecular dynamic simulations show that if $t_a/t_c > 1$ the deformation by nucleation and propagation of SB is predominant with respect to the grain boundary and dislocation plasticity of crystalline sublayer [63].

For this reason, the compact U-NLs fail mainly by shear banding, while the chemical heterogeneities and high density of interfaces can only block and delay the SBs propagation thanks to the difference in mechanical properties between the sublayers thus increasing the yield strength and providing only a limited increase of the plasticity with respect monolithic TFMGs (a value which is however ~40% higher) [207].

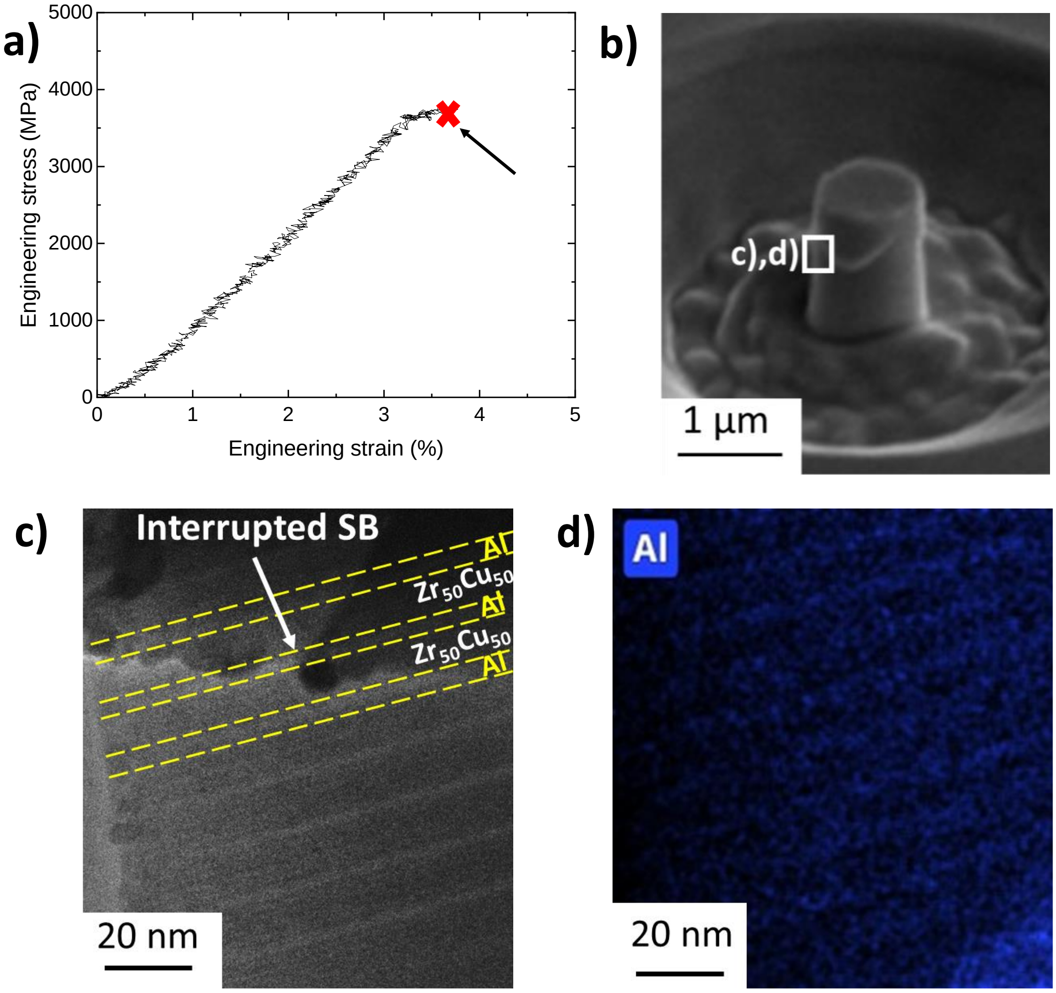

Figure 5.5. *(a) Engineering stress vs engineering strain curve of compact $Zr_{50}Cu_{50}$/Al 9/4 nm U-NLs with a black arrow highlighting the formation of the first SB causing brittle failure. (b, c, d) Postmortem SEM, TEM and EDX-STEM cross-section of the micropillar showing preliminary SB blocking at Al layers.*

In Figure 5.6 we show a representative stress-strain curve from a compression of the nanogranular $Zr_{50}Cu_{50}$/Al 9/4 nm U-NLs and corresponding post-mortem SEM and TEM images. The stress increases linearly up to 2.5 % deformation upon which the pillar yields with a σ_y~3.40 ± 0.06 GPa, a value slightly below the compact counterpart (Figure 5.5) and in agreement with the trend of hardness (Figure 5.4b) and related to the higher amount of free volume of cluster-assembled U-NLs which activates plastic deformation at lower stresses and strains with respect to the more ordered compact U-NLs [85, 183].

However, the nanogranular U-NLs show homogeneous deformation up to 6.00 ± 0.36 % and then SB start to appear on the surface of the pillar as revealed by TEM observation (Fig. 5.6c). However, this event is not followed by a percolation even at larger deformations (>15%), as shown in Figure 5.6b,c in which only some superficial shear band events are found. This phenomenon is similar to the one observed in nanoglasses in the literature [48, 74] in which the large amount of free volume between amorphous clusters prevents the percolation of embryonic SB in a single major event such as in traditional MGs [85, 183], while favoring a pseudo-homogeneous deformation of the specimen through the propagation of fine SBs which are confined in the external surface [74].

Another class of nanolaminates which show a similar deformation mechanism are the CoCrNi/TiZrNbHf 18/12 nm crystalline/amorphous multilayers which could achieve σ_y ~3.6 GPa and large deformations with non-percolative cracking events similar to nanogranular U-NLs (Figure 5.6) due to the high density of interfaces and chemical partitioning between the two sublayers, managing to block crack percolation [135].

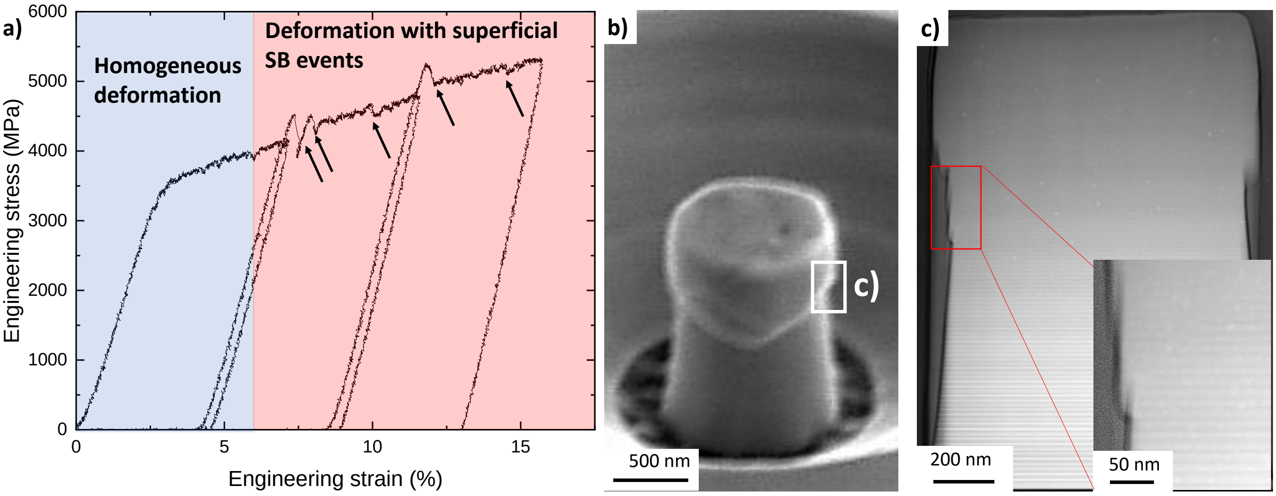

__Figure 5.6.__ (a) Engineering stress-strain curve of nanogranular $Zr_{50}Cu_{50}$/Al 9/4 nm U-NLs highlighting the different deformation regimes (homogeneous and plastic with superficial SB events underlined by black arrows). (b,c) Post-mortem SEM image of the micropillar and HAADF-STEM cross-section highlighting superficial non-percolative shear bands.

5.4 Conclusions

In this work, we push the limits of pulsed laser deposition (PLD) to develop crystal/glass (Al/$Zr_{50}Cu_{50}$) ultrafine nanolaminates (U-NLs), with controllable nm-scale bilayer period and with tunable (compact and nanogranular) morphology. We show that:

- Both compact and nanogranular U-NLs are characterized by a fine nanolayering alternating ~4 nm Al with 6-9 nm $Zr_{50}Cu_{50}$ sublayers. This results in a high density of crystalline/amorphous interfaces, coupled with significant interlayer chemical intermixing with the formation of a ZrCuAl phase.
- The mass density of the U-NLs is larger than monolithic ZrCu metallic glasses, despite the addition of Al (~30-40% vol.). This is attributed to the high kinetic energy of the ablated species during PLD process, leading to densification and chemical intermixing promoted by the high out-of-equilibrium conditions.
- The unique microstructure of U-NLs results in significantly enhanced *E* and *H,* reaching up to 139 and 9.3 GPa, respectively. These values surpass by 30% those reported in the literature counterparts due to the high density of nanointerfaces, the increased mass density and the formation of a ZrCuAl phase, enhancing the stress necessary for SB propagation and the mechanical properties.

- Micropillar compression tests reveal that compact U-NLs exhibit the highest yield strength (σ_y) ~3.6 GPa. However, the deformation involves the propagation of SBs which are partially mitigated by the Al-rich layers, resulting in failure ∼3.6% deformation. In contrast, nanogranular U-NLs have slightly lower σ_y ~3.4 GPa, but their higher free volume content enables to accommodate more extensive homogeneous elasto-plastic deformation without catastrophic failure even for >15% deformations.

Overall, we demonstrate the effective manipulation of atomic and microstructural heterogeneities within ultrafine crystalline/amorphous (Al/$Zr_{50}Cu_{50}$) nanolaminates as a successful approach to finely tune and enhance the mechanical properties beyond the single-phase constituents and surpassing traditional tread-off between strength and ductility. Our findings offer crucial insights for the design of new metallic thin films with exceptional mechanical performances capable to resist to intense and complex loading configurations, which are relevant across various application domains such as of microelectronics and structural coatings.

VI. Controlling the mechanical behavior of monolithic thin film metallic glasses through the addition of oxygen

6.1 Overview on the investigated samples

In this Chapter, the structure and mechanical properties of compact and nanogranular $Zr_{50}Cu_{50}$ and $Zr_{46}Cu_{46}Al_8$ amorphous films which have incorporated O in their structure are presented.

These films were deposited from the monolithic $Zr_{50}Cu_{50}$ and $Zr_{46}Cu_{46}Al_8$ targets using an IR laser with a fluence equal to 14 J/cm^2 and the characteristics of the samples examined in this chapter are reported in the Table 3.4 of Chapter III. The baseline pressure of the depositions was increased from 1x10^{-3} Pa to 3x10^3 Pa before starting deposition, to increase the amount of residual O in the chamber during the deposition process and promote the interaction between the plasma and the atmosphere of the chamber leading to the deposition of films with a non-negligible amount of O.

It must be noted that from EDX analysis of the $Zr_{50}Cu_{50}$/O and $Zr_{46}Cu_{46}Al_8$/O films it seems that nanogranular films deposited in He have an O concentration around 40 %at. while compact films deposited in vacuum have an O concentration around 20 %at while The O concentration of the TFMGs of Chapter IV is around 6 – 7 % at. can be related to surface oxidation after exposition to atmosphere. The reason why nanogranular films have a larger concentration of O despite being deposited in the same base vacuum of compact films (before the introduction of He in the chamber) is related to the reduction of the plasma energy during the deposition in inert gas which allows the nucleation of the clusters whose surface is more sensible to the gases present in the deposition chamber [179].

In addition to the nanoclustering, the lower kinetic energy of the plasma would reduce the preferential sputtering of light O atoms adsorbed on the surface of the growing film caused by the plasma plume in a way similar to the preferential sputtering of N in TaN films by increasing the energy of the ions bombarding the film's surface described in C. Palacio *et al.* [208].

6.2 Structural properties:

6.2.1 Morphology

The morphology of the SEM cross-sections of the $Zr_{50}Cu_{50}$/O and $Zr_{46}Cu_{46}Al_8$/O films after mechanical cleavage are shown in Figure 6.1. The cross-sections of compact $Zr_{50}Cu_{50}$/O (Fig 6.1a) and $Zr_{46}Cu_{46}Al_8$/O (Fig 6.1b) have the typical corrugation pattern related to the propagation of shear bands (SBs) during cleavage [168].

The size of the corrugations decreases with the addition of Al passing from 56 $\pm$ 7 nm for compact $Zr_{50}Cu_{50}$/O to 47 $\pm$ 9 nm for compact $Zr_{46}Cu_{46}Al_8$/O following the same trend of their counterparts without O described in Chapter IV (Figure 4.1).

Furthermore, the size of the corrugations of the compact films with O is ~20% lower than the one of the compact films without O indicating that the addition of O causes the activation of a higher number of plastic zones during the propagation of the fracture.

A similar result is observed in literature for Zr-based BMGs with small amounts of O like the $(Zr_{60}Cu_{25}Al_{15})_{99.75}O_{0.25}$ of T. Wang *et al.* [209] and the $(Zr_{20}Cu_{20}Hf_{20}Ti_{20}Ni_{20})_{99.8}O_{0.2}$ of Y. Wu *et al.* [93] and result in an improved plasticity in compression with respect to their undoped counterparts.

SEM cross-sections of Nanogranular $Zr_{50}Cu_{50}$/O (Figure 6.1c) and $Zr_{46}Cu_{46}Al_8$/O (Figure 6.1d) do not report any corrugations as observed for their counterparts without O of Chapter IV showing a more homogeneous surface similarly to other oxides [210] and metallic [91, 137] films deposited by PLD in inert gas.

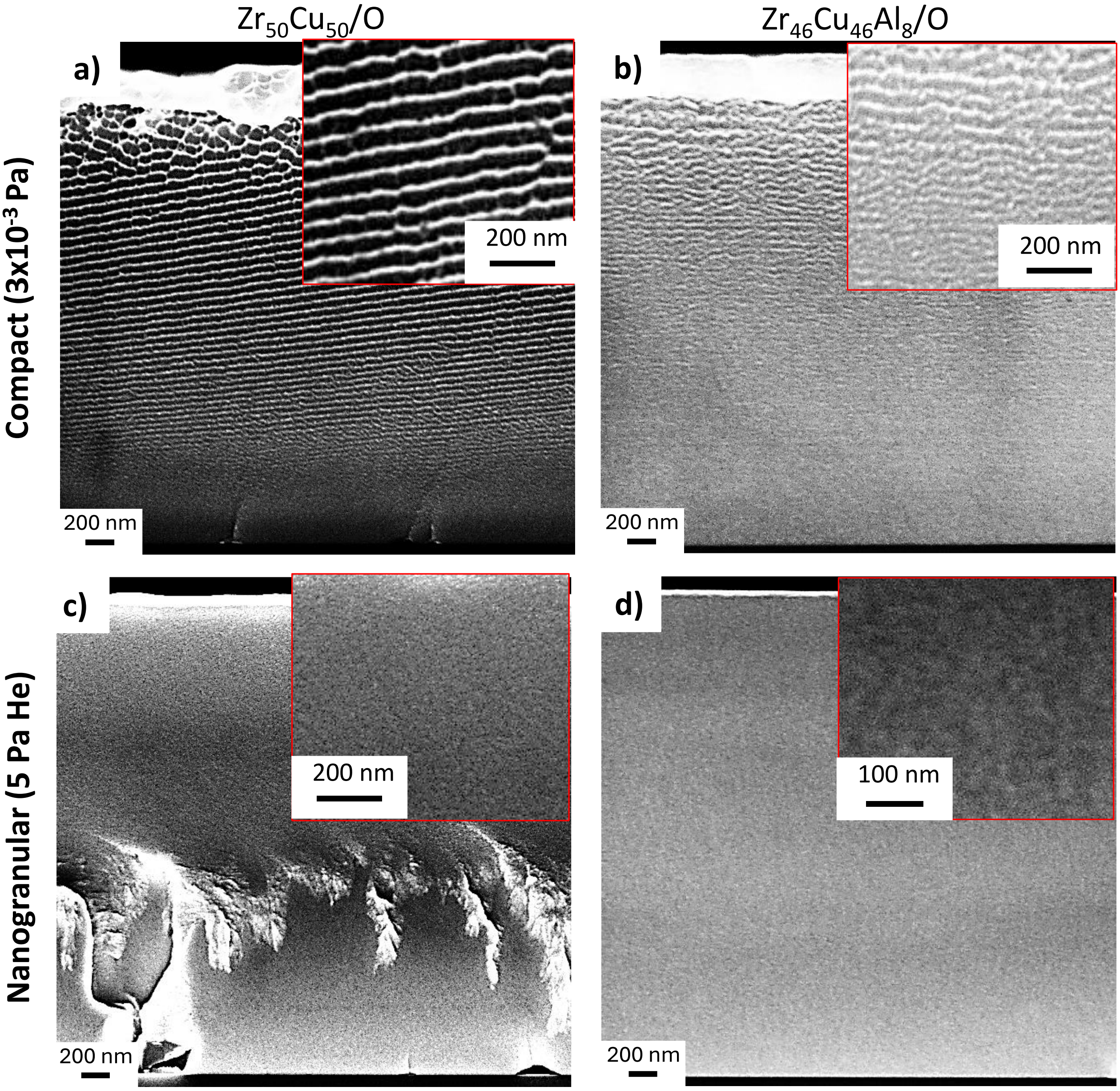

Figure 6.1: *SEM cross-section of compact (a,b) and nanogranular (c,d) $Zr_{50}Cu_{50}$/O and $Zr_{46}Cu_{46}Al_8$/O TFMGs deposited by PLD.*

The XRD diffractograms of compact and nanogranular $Zr_{50}Cu_{50}$/O are presented in Figure 6.2a. Compact $Zr_{50}Cu_{50}$/O shows a single hump centered ~2θ = 37°-38° in agreement with its counterpart without O (Figure 4.1e, Chapter IV) and in line with peak position of MS $Zr_{50}Cu_{50}$ from literature [211]. However, ZrCu/O has a FWHM larger than the $Zr_{50}Cu_{50}$ of chapter IV (10° vs 7.5°), similarly to BMGs with O [209], indicating that the presence of O increases the disorder of the atomic structure while not forming visible oxides. Nanogranular $Zr_{50}Cu_{50}$/O diffraction pattern instead shows two partially merged diffraction peaks centered around ∼32.5° (FWHM = 6.58°) and ∼40.1° (FWHM =7.45°) which, in literature, are connected to two possible phases.

The first corresponding to a Zr-O rich phase (∼32.5°) similar to an amorphous ZrO_2 phase precursor to a monoclinic crystal phase [212, 213] with larger interatomic distance with respect to compact $Zr_{50}Cu_{50}$/O. The second one corresponding to a Cu-rich ZrCu amorphous phase which in literature is identified as $Zr_{33}Cu_{67}$ with lower interatomic distance with respect to $Zr_{50}Cu_{50}$ due to higher Cu content favoring a denser atomic packing [92, 211], generated by the imbalance in the Cu-Zr ratio due to the preferential bonding between Zr and O related to their high chemical affinity [214].

The formation of the two phases in the nanogranular films is favored by the high O content connected to the cluster-assembled growth favoring the chemical interaction between the ablated clusters in the plasma plume and the residual O in the chamber, combined with the lower kinetic energy associated with the deposition in atmosphere. The XRD patterns of compact and nanogranular $Zr_{46}Cu_{46}Al_8/O$ are shown in Figure 6.2b. The diffraction pattern of compact $Zr_{46}Cu_{46}Al_8/O$ has two partially merged peaks with the first one centered around ~32.5° similar to the amorphous ZrO-rich phase of nanogranular $Zr_{50}Cu_{50}/O$ of Figure 6.2a and a second peak centered around ~39.8° corresponding to amorphous $Zr_{36}Cu_{64}$ [92, 211].

The formation of two phases in compact $Zr_{46}Cu_{46}Al_8/O$ can be connected to the presence of Al which has an even higher chemical affinity for O with respect to Zr [214] and the high enthalpy of mixing between Zr and Al ($\Delta H_{mix\ Zr\text{-}Al}$ = -44 kJ/mol) [13] which indicate a preferred bonding between Zr and Al with respect to Cu ($\Delta H_{mix\ Al\text{-}Cu}$ = -1 kJ/mol) [13]. Furthermore, the absence of a peak around ~21.5° related to amorphous Al_2O_3 [215] indicates that Al has not segregated in its oxide form and still remains together with Zr forming a Zr-Al-O structure. Nanogranular $Zr_{46}Cu_{46}Al_8/O$ XRD patterns show two clearly distinguished peaks centered around ~31° and 42.7°. The first peak corresponds to an oxide phase that is similar to the ZrAlO phase observed in Z. Hu *et al.* [216] and the second peak can be related to an extremely Cu-rich $Zr_{15}Cu_{85}$ phase [92].

The cluster-assembled growth of the film combined with the presence of Al would increase the amount of O which bonds directly with Zr and Al thus greatly reducing the Zr available for bonding with Cu, leading to the formation of a phase which is near the border between amorphous and crystalline ZrCu with high Cu concentration [92].

Nevertheless, the exact reason why $Zr_{50}Cu_{50}/O$ and $Zr_{46}Cu_{46}Al_8/O$ show very different structures despite incorporating the same nominal amount of O is still not clear and future TEM characterization of the films will help to understand in detail the nature and distribution of the phases observed by XRD.

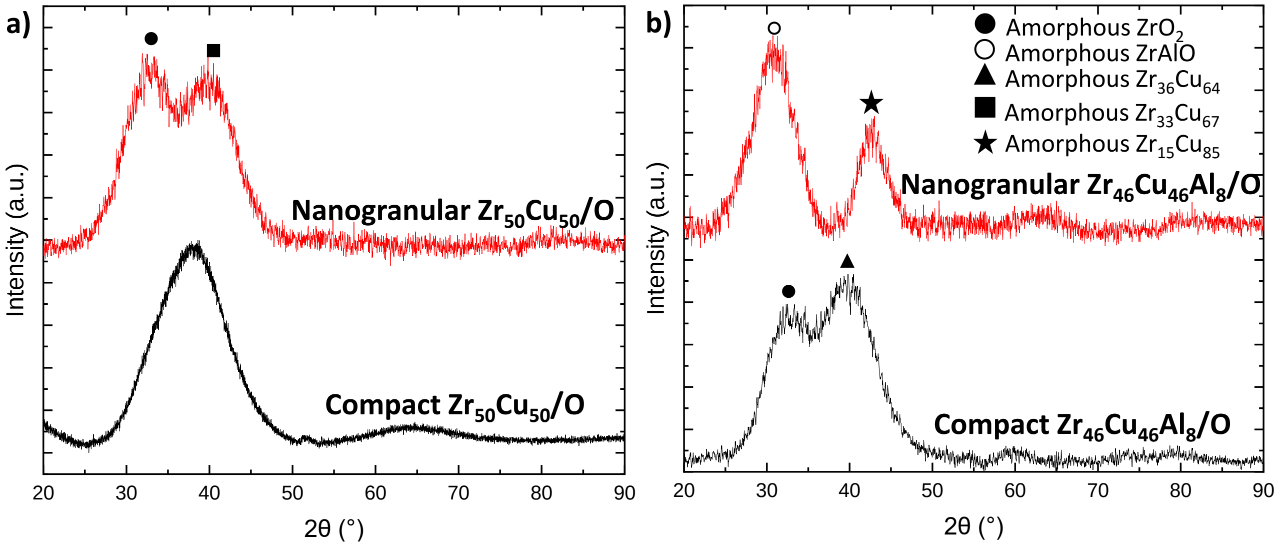

Figure 6.2: *XRD diffraction of (a) $Zr_{50}Cu_{50}/O$ and (b) $Zr_{46}Cu_{46}Al_8/O$ TFMGs deposited by PLD in vacuum (compact) and in 5 Pa He (nanogranular).*

6.2.2 Evolution of the local structure and density by X-ray Reflectivity (XRR)

The evolution of the density and local structure depending on the morphology and Al concentration for $Zr_{50}Cu_{50}/O$ and $Zr_{46}Cu_{46}Al_8/O$ films are presented in Figure 6.3.

All diffractograms possess satellite peaks indicating that the two phases observed with XRD in Figure 6.2 could be arranged in a self-assembled nanolayered structure in which the Zr-O rich and Cu-rich phases are arranged as alternating sublayers.

By knowing the critical angle θ_C and the satellite angle θ_i it is possible to estimate the bilayer period of the films *a* through the equation ($\boldsymbol{\lambda} = 2a(\sin^2\theta_i - \sin^2\theta_C)^{1/2}$, with λ being the Cu Kα, which results equal to

~8-10 nm for the compact and nanogranular $Zr_{50}Cu_{50}/O$, in agreement with the previous study on ZrCu films deposited by PLD of M. Ghidelli *et al.* [91]. On the other hand, the compact and nanogranular $Zr_{46}Cu_{46}Al_8/O$ have a bilayer period of ~20-22 nm due to the presence of Al favoring the growth of the single O-rich sublayer during the deposition. However, further TEM characterizations will be performed to fully investigate the structure of the $Zr_{50}Cu_{50}/O$ and $Zr_{46}Cu_{46}Al_8/O$ films and confirm the presence and the exact thickness of the sublayers.

The evolution of mass density of the films depending on the composition and morphology is presented in the Table of Figure 6.3b. Compact $Zr_{50}Cu_{50}/O$ has a mass density equal to 7.4 g/cm^3, a value which is ~10% lower than its counterpart without O of chapter IV (8.35 g/cm^3) due to the presence of O (an element with much lower atomic mass vs Zr and Cu) distorting the local structure and increasing the free volume of the film, as already hinted by the larger FWHM with respect to the one of pure $Zr_{50}Cu_{50}$.

The transition from the compact to the nanogranular morphology drastically reduces the density of $Zr_{50}Cu_{50}/O$ down to 5.93 g/cm^3 due to higher amount of O (40 %at. vs 20 %at. of compact films) incorporated in the more heterogeneous cluster assembled structure with the local chemical and structural fluctuations between the cores and interfaces of the clusters. The addition of Al decreases the density of compact films down to 6.84 g/cm^3 similarly to the trend of the compact films without O but with a larger density drop (0.56 g/cm^3 for O films vs 0.43 g/cm^3 for films without O) due to the formation of the O rich phase with larger interatomic distance (diffraction peak at 32.5°) with respect to the one the TFMG (diffraction peak at 37.7°).

Unlike its compact counterparts, the addition of Al to nanogranular films increases the density up to 6.27 g/cm^3 for nanogranular $Zr_{46}Cu_{46}Al_8/O$. This can be related to the formation of a more ordered Cu-rich phase with larger Cu content ($Zr_{15}Cu_{85}$) with respect to the Cu-rich phase of $Zr_{50}Cu_{50}/O$ ($Zr_{33}Cu_{67}$), leading to denser Cu-rich sublayers in $Zr_{46}Cu_{46}Al_8/O$ since for binary ZrCu TFMGs the mass density increases with the Cu content [92].

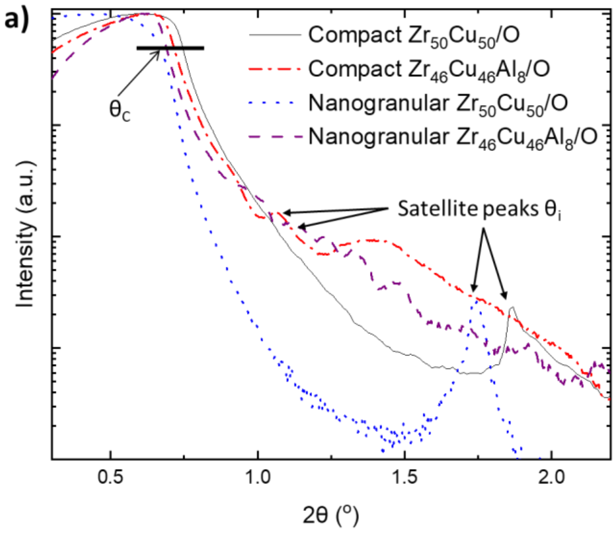

b)

Sample	**Composition**	**Density [g/cm^3]**
Compact $Zr_{50}Cu_{50}/O$	$(Zr_{50}Cu_{50})_{80}O_{20}$	7.4±0.05
Nanogranular $Zr_{50}Cu_{50}/O$	$(Zr_{50}Cu_{50})_{60}O_{40}$	5.93±0.05
Compact $Zr_{46}Cu_{46}Al_8/O$	$(Zr_{46}Cu_{46}Al_8)_{80}O_{20}$	6.84±0.05
Nanogranular $Zr_{46}Cu_{46}Al_8/O$	$(Zr_{46}Cu_{46}Al_8)_{60}O_{40}$	6.27±0.05

Figure 6.3: *(a) XRR spectra of compact $Zr_{50}Cu_{50}/O$ and $Zr_{46}Cu_{46}Al_8/O$ highlighting the presence of satellite peaks that can be related to a self-assembled nanolayered structure and (b) Table of the mass density of the different films with O.*

6.3 Mechanical properties:

6.3.1 Evolution of the elastic moduli and hardness

The evolution of the Young's modulus (*E*) and hardness (*H*) obtained by optoacoustic techniques and nanoindentation depending on the relative morphology and O content for $Zr_{50}Cu_{50}$/O and $Zr_{46}Cu_{46}Al_8$/O films is presented in the Table 6.1.

The *E* of $Zr_{50}Cu_{50}$/O and $Zr_{46}Cu_{46}Al_8$/O films increases when the O content raises due to the transition from compact to nanogranular morphology going from 125 and 138 GPa for compact $Zr_{50}Cu_{50}$/O and $Zr_{46}Cu_{46}Al_8$/O to 130 and 145 GPa for nanogranular $Zr_{50}Cu_{50}$/O and $Zr_{46}Cu_{46}Al_8$/O.

The increase of *E* with Al content, opposite to what it is observed for the TFMGs without O of chapter IV (120 and 109 GPa for $Zr_{50}Cu_{50}$ and $Zr_{46}Cu_{46}Al_8$), could be related to the presence of strong covalent bonds between O, Zr and Al in the O-rich layer which would increase the overall stiffness of the film [217]. Compact $Zr_{50}Cu_{50}$/O has *H* equal to 10.2 GPa thanks to the fine nanolayered structure blocking SBs propagation and increasing the stress necessary for the activation of plastic deformation [54, 218] combined with the presence of O increasing the atomic bond strength. *H* slightly decreases down to 9.9 GPa for compact $Zr_{46}Cu_{46}Al_8$/O due to the larger bilayer period (~20-22 nm) with respect compact $Zr_{50}Cu_{50}$/O (~8-10 nm) which means having a lower density of interfaces preventing the propagation of SBs [69, 218].

The *H* of nanogranular films is slightly lower with respect to their compact counterparts passing from 9.8 GPa for $Zr_{50}Cu_{50}$/O to 9.5 GPa for $Zr_{46}Cu_{46}Al_8$/O due to the cluster-assembled structure with less ordered interatomic bonds at the interfaces between the clusters, resulting in a larger amount of free volume reducing the stresses necessary for the yielding of the material [85, 183].

Lastly, when compared to the $Zr_{50}Cu_{50}$ and $Zr_{46}Cu_{46}Al_8$ TFMGs without O studied in Chapter IV the $Zr_{50}Cu_{50}$/O and $Zr_{46}Cu_{46}Al_8$/O presented here have a *H* which are ~20% higher than the *E* and *H* of the TFMGs (8.6 and 7.8 GPa for $Zr_{50}Cu_{50}$ and $Zr_{46}Cu_{46}Al_8$) thanks to the self-assembled nanolayered structure and the covalent bonds with O, strengthening the local structure.

Sample	**Composition**	**Young's Modulus [GPa]**	**Hardness [GPa]**
Compact $Zr_{50}Cu_{50}$/O	$(Zr_{50}Cu_{50})_{80}O_{20}$	125±2	10.2±0.3
Nanogranular $Zr_{50}Cu_{50}$/O	$(Zr_{50}Cu_{50})_{60}O_{40}$	131±2	9.8±0.25
Compact $Zr_{46}Cu_{46}Al_8$/O	$(Zr_{46}Cu_{46}Al_8)_{80}O_{20}$	138±2	9.9±0.3
Nanogranular $Zr_{46}Cu_{46}Al_8$/O	$(Zr_{46}Cu_{46}Al_8)_{60}O_{40}$	145±2	9.5±0.2

Table 6.1: *Table with the values of Young's modulus and hardness of the $Zr_{50}Cu_{50}$/O and $Zr_{46}Cu_{46}Al_8$/O with different O content and relative morphologies.*

6.3.2 *Evolution of yield strength and plasticity through micropillar compression*

After having studied the mechanical properties of the 800 nm films, micropillars were milled from 3 µm thick films to study more in detail the effects of local chemistry and morphology on the mechanical response to uniaxial compression.

The engineering stress-strain curves of compact $Zr_{50}Cu_{50}/O$ and $Zr_{46}Cu_{46}Al_8/O$ when compressed with a strain rate $\dot{\varepsilon}$ of 10^{-2} s^{-1} are presented in Figure 6.5a.

Compact $Zr_{50}Cu_{50}/O$ deforms elastically up to 3.8% strain after which it yields reaching a yield strength σ_y of 4.4 ± 0.1 GPa after which the pillar deforms homogeneously up to 4.6% ± 0.3% when the first shear band (SB) propagates from the top of the pillar as shown in Figure 6.5b. The improvement of the strength and plasticity of compact $Zr_{50}Cu_{50}/O$ respect to $Zr_{50}Cu_{50}$ of Chapter IV (σ_y = 3.2 GPa, homogeneous deformation 3.3%) can be attributed to presence of the self-assembled nanolayered structure hinted by the XRR spectra of Figure 6.3a whose interfaces would delay the propagation of SBs in favor of a more homogeneous deformation [55, 58]. Compact $Zr_{46}Cu_{46}Al_8/O$ deforms elastically up to 4% upon which it yields reaching a σ_y equal to 4.7 ± 0.1 GPa and then it deforms homogeneously up to 6% ± 0.3% when SBs start to propagate.

Compact $Zr_{46}Cu_{46}Al_8/O$ can deform homogeneously for larger strains than compact $Zr_{50}Cu_{50}/O$ since the O in its ZrAl-O rich sublayers has formed clear covalent bonds (see XRD Figure 6.2b) introducing more free volume in the structure allowing larger homogeneous deformations before SB propagation.

This phenomenon is like what it is observed for SiO_2 micropillars studied in literature which can compress homogeneously for strains > 15% despite the inherent brittleness of bulk silica [187, 219, 220]. The explanation for this behavior can be found in a combination of densification of the structure during the compression (reduction of free volume) and shear flow mediated by uniformly distributed shear transformation zones (STZ) which do not coalesce into SBs until the free volume is annihilated [187, 219, 220].

The densification of the amorphous oxide sublayers would also increase their strength and stiffness improving the overall σ_y explaining why σ_y of $Zr_{46}Cu_{46}Al_8/O$ is bigger than the σ_y of $Zr_{50}Cu_{50}/O$ despite having similar *H* values (Table 6.1) [221].

The Young's moduli obtained from the fit of the loading curves of compact $Zr_{50}Cu_{50}/O$ and $Zr_{46}Cu_{46}Al_8/O$ are 121.5 ± 10 and 140 ± 11 GPa respectively, which are very similar to the values of Table 6.1 for *E* obtained from optoacoustic techniques indicating a good quality of the compression measurements.

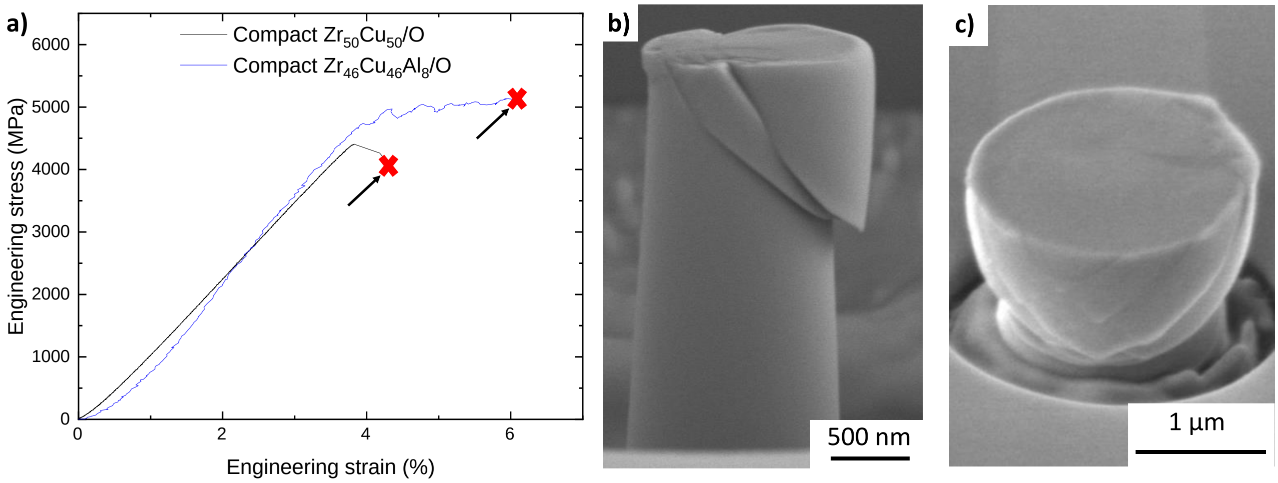

Figure 6.5: *(a) Engineering stress vs engineering strain curves of compact $Zr_{50}Cu_{50}/O$ and $Zr_{46}Cu_{46}Al_8/O$ films deposited by PLD with a black arrow indicating the formation of the first SB and (b,c) postmortem SEM images of the compressed micropillars.*

The engineering stress-strain curves of nanogranular $Zr_{50}Cu_{50}/O$ and $Zr_{46}Cu_{46}Al_8/O$ when compressed with a strain rate $\dot{\varepsilon}$ of 10^{-2} s^{-1} are presented in Figure 6.6a

Nanogranular $Zr_{50}Cu_{50}/O$ instead deforms elastically up to 3.5% - 3.6% upon which it yields with a σ_y equal to 4.1 $\pm$ 0.09 GPa, a value slightly lower than the σ_y of compact $Zr_{50}Cu_{50}/O$, and then it deforms homogeneously without SB propagation up to 15% $\pm$ 0.5% strain when the experiment stops as shown in Figure 6.6b. Nanogranular $Zr_{46}Cu_{46}Al_8/O$ deforms elastically up to 3.8% after which it yields reaching a σ_y equal to 4.55 $\pm$ 0.09 GPa and then it deforms homogeneously up to 14.9% $\pm$ 0.3% when the experiment ends without forming SBs as shown in Figure 6.6c. This drastic increase of the plasticity and suppression of SB nucleation and propagation process can be connected to a combination of the nanogranular structure with the fluctuations of local structures between the cores and the interfaces of the clusters and the self-assembled nanolayered structure of Zr-O rich sublayers like the ZrO_2 and Cu-rich sublayers (XRD of Figure 6.2a).

Like in the case of compact $Zr_{46}Cu_{46}Al_8/O$ the presence of covalent O bonds, enhanced by the high O concentration in the nanogranular films, could grant a surplus of free volume in the confined Zr-O rich layers combined with the one due to the cluster-assembled growth, thus resulting in a large interval of homogeneous deformation.

The Young's moduli obtained from the fit of the loading curves of nanogranular $Zr_{50}Cu_{50}/O$ and $Zr_{46}Cu_{46}Al_8/O$ are 127 $\pm$ 9 and 149 $\pm$ 12 GPa respectively, which are very similar to the values of Table 6.1 for *E* obtained from optoacoustic techniques indicating a good quality of the compression measurements.

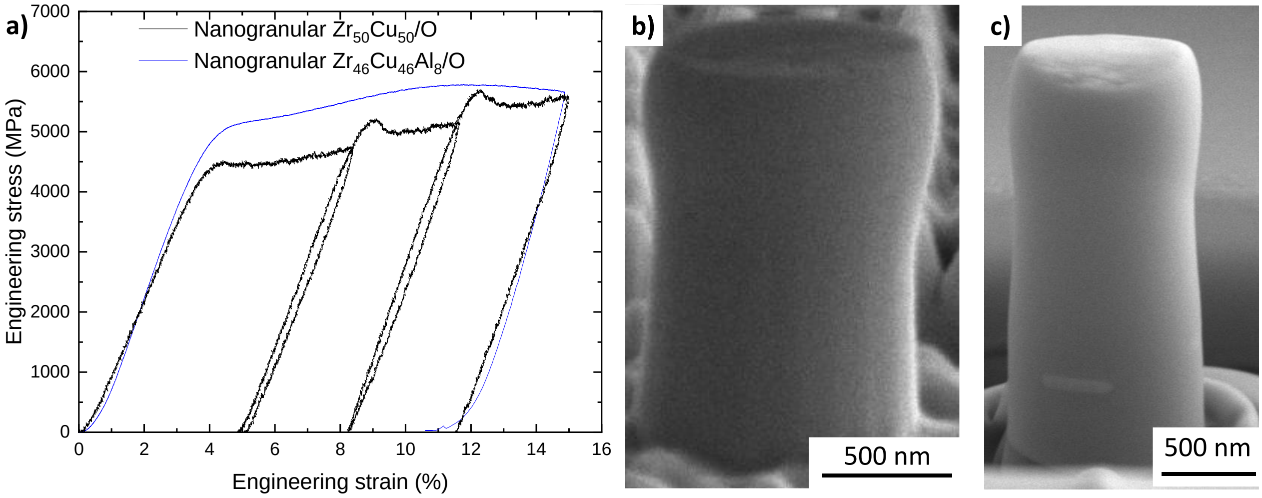

Figure 6.6: *(a) Engineering stress vs engineering strain curves of the nanogranular $Zr_{50}Cu_{50}/O$ and $Zr_{46}Cu_{46}Al_8/O$ films deposited by PLD and (b,c) postmortem SEM images of the compressed micropillars.*

An objection that could be done to these results is that the large homogeneous deformation observed in these experiments is an extrinsic effect related to the interaction between the pillar and the electron beam of the SEM in a way similar to the tests on SiO_2 performed in a TEM described in Ref. [222].

While it can be observed that the energy of the electron beam of a TEM is much larger than the one of a SEM, future compression experiments with the SEM beam off will be performed to exclude that the degree of homogeneous deformation reported here is caused by extrinsic effects related to the measure.

6.3.3 Tensile tests on polymer substrate

After having examined the mechanical behavior of the films in compression, the tensile response of compact and nanogranular $Zr_{50}Cu_{50}/O$ and $Zr_{46}Cu_{46}Al_8/O$ with thickness equal to 800 nm deposited on a Kapton® substrate are presented in Figure 6.7.

The crack onset strain (*COS*) of the compact films decreases with the addition of Al passing from 1.9% for compact $Zr_{50}Cu_{50}/O$ to 1.15% for compact $Zr_{46}Cu_{46}Al_8/O$ to which is connected an increase of the crack saturation density (*CSD*) from 0.026 μm^{-1} to 0.031 μm^{-1} as shown in Figures 6.7a,b.

The images of the surface after the experiment in Figure 6.7c show a series of straight cracks orthogonal to the loading direction which are the signature of brittle films [223]. The reduction in *COS* of compact $Zr_{46}Cu_{46}Al_8/O$ could be connected to a combination of factors among which the more prominent presence of bonded O in the Zr-O rich sublayers which leads to a more rigid structure [224] and the larger bilayer period with respect to $Zr_{50}Cu_{50}/O$ being less efficient in blocking the SB propagation, thus leading to brittle fracture. Residual stresses σ_{res} (-281 ± 50 MPa for $Zr_{50}Cu_{50}/O$ and -305 ± 60 MPa $Zr_{46}Cu_{46}Al_8/O$ from film's curvature evaluation [161]) are not sufficiently different to magnitude between the different compositions and morphologies to justify the changes in cracking behavior.

Lastly, compact films start to delaminate for strains $\geqslant$ 9% (golden stars in Figure 6.7a) indicating a good adherence of the films to the polymer substrate.

The change of morphology has an embrittling effect on $Zr_{50}Cu_{50}/O$ and $Zr_{46}Cu_{46}Al_8/O$ reducing the *COS* and increasing the *CSD* with respect to their compact counterparts. Nanogranular $Zr_{50}Cu_{50}/O$ has a *COS* equal to 1.5% and then decreases down to 0.88% for nanogranular $Zr_{46}Cu_{46}Al_8/O$ while the *CSD* increases from 0.03 μm^{-1} to 0.045 μm^{-1} as shown in Figure 6.8a,b following the same trend observed for compact films with the addition of Al and keeping similar σ_{res} (-276 ± 55 MPa for $Zr_{50}Cu_{50}/O$ and -309 ± 63 Mpa $Zr_{46}Cu_{46}Al_8/O$). The surfaces of the films after deformation shown in Figure 6.7c present brittle straight cracks like their compact counterparts.

The decrease in crack resistance could be related to the large number of heterogeneities present in the nanogranular structure which act as preferential sites for the nucleation of cracks like in the case of nanocolumnar films [92, 193]. Furthermore, nanogranular films start to delaminate at lower strains with respect to compact films (6%-7% vs 9.5%-10%) indicating a lower adhesion of the nanogranular films to the polymer substrate possibly related to the lower kinetic energy of the species in the plasma plume confined by He, with respect to the plasma expanding in vacuum used for the growth of compact films [90].

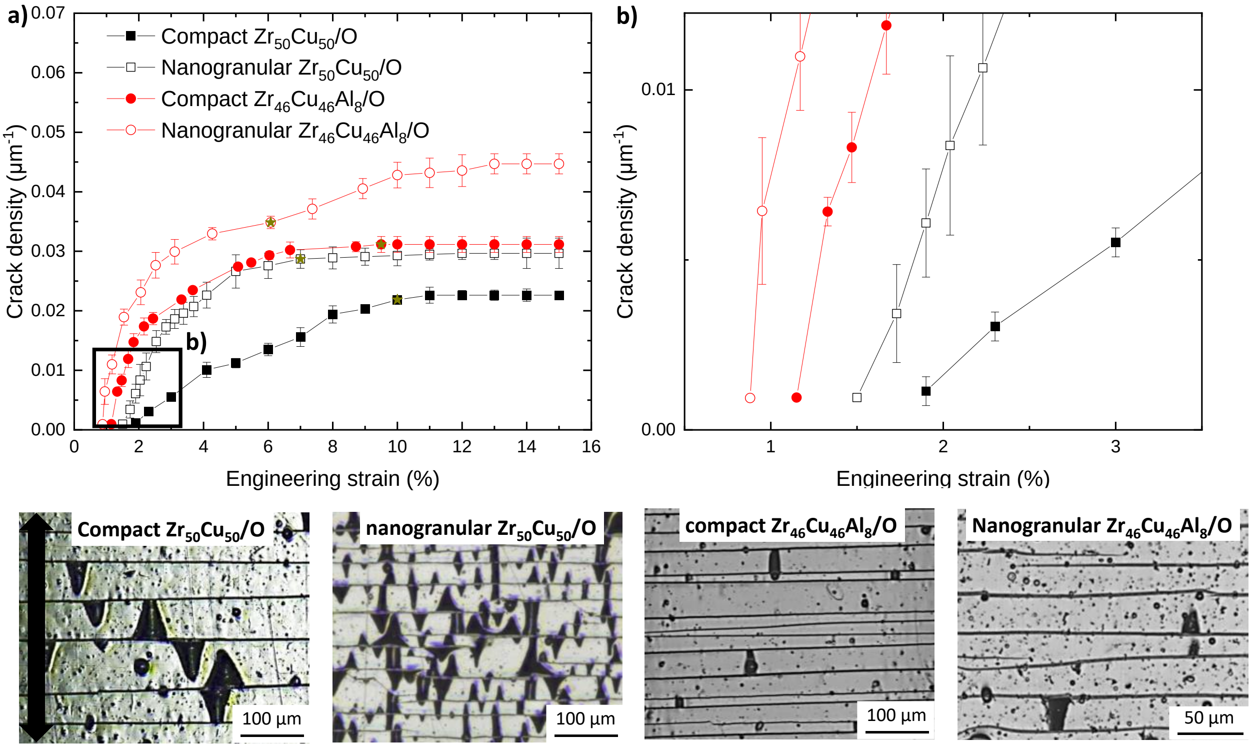

Figure 6.7: *(a) Crack density vs engineering strain curves of the compact and nanogranular $Zr_{50}Cu_{50}/O$ and $Zr_{46}Cu_{46}Al_8/O$ films by PLD. The golden stars indicate the strain at which the films start to buckle from the*

substrate. (b) Magnification of the initial region of the crack density-engineering strain curve highlighting the crack initiation strain of each film. (c) Pos-mortem optical images of the compact and nanogranular films after 15% strain. The vertical black arrow indicates the loading direction during the experiment.

The fracture toughness and adhesion energy J_0 of the compact and nanogranular $Zr_{50}Cu_{50}/O$ and $Zr_{46}Cu_{46}Al_8/O$ are reported in Table 6.2. The Beuth model [162] combines *COS*, *CSD*, the reduced modulus of the film E_r, and the stress at fracture of the film ($COS*E+\sigma_{res}$) to obtain the fracture energy $G_{Beuth} = \frac{(COS*E*\sigma_{res})^2}{1.34CSD*E_r}$ which can be used to calculate the fracture toughness expressed as $\sqrt{E_r G_{Beuth}}$. As expected from the trend of *COS* compact $Zr_{50}Cu_{50}/O$ has the highest toughness among the examined samples being equal to 12 MPa*m$^{1/2}$ and decreasing down to 6.4 MPa*m$^{1/2}$ for compact $Zr_{46}Cu_{46}Al_8/O$ due to the changes in the local structure related to the interaction between O and Al.

Nanogranular films follow the same trend of their compact counterparts but with lower toughness due to the heterogenous cluster-assembled structure favoring crack nucleation with nanogranular $Zr_{50}Cu_{50}/O$ having a toughness equal to 8.3 MPa*m$^{1/2}$ and decreasing down to 4.1 MPa*m$^{1/2}$ for nanogranular $Zr_{46}Cu_{46}Al_8/O$.

J_0 can be estimated from the buckling initiation strain (*BIS*), *CSD*, film's thickness *h*, the reduced modulus of the film E_r, and σ_{res} by using strain energy delamination model [163] with $J_0 = \frac{E_r h \beta^2}{2}\left(BIS + \frac{\sigma_{res}}{E_r \beta}\right)^2$ with β being a dimensionless factor depending on *CSD* and equal to -0.47 for the samples examined here.

Compact films have a J_0 in the order of 120 J/m^2 and nanogranular films have a J_0 in the order of 60 J/m^2 seemingly independent on the Al and O content with only the change in morphology being relevant. This trend is similar to the one observed in chapter IV for the PLD TFMGs in which the lower plasma energy of the films deposited in He reduces the adhesion of the nanogranular film on the polymer surface [90, 198].

Sample	**Composition**	**Fracture toughness [Mpa*m$^{1/2}$]**	**Adhesion energy [J/m^2]**
Compact $Zr_{50}Cu_{50}/O$	$(Zr_{50}Cu_{50})_{80}O_{20}$	12.2±1.5	125±20
Nanogranular $Zr_{50}Cu_{50}/O$	$(Zr_{50}Cu_{50})_{60}O_{40}$	8.35±1.2	64±10
Compact $Zr_{46}Cu_{46}Al_8/O$	$(Zr_{46}Cu_{46}Al_8)_{80}O_{20}$	6.44±1	115±20
Nanogranular $Zr_{46}Cu_{46}Al_8/O$	$(Zr_{46}Cu_{46}Al_8)_{60}O_{40}$	4.07±0.9	58±10

Table 6.2: *Fracture toughness and adhesion energy of the compact and nanogranular* $Zr_{50}Cu_{50}/O$ *and* $Zr_{46}Cu_{46}Al_8/O$ *films by PLD.*

6.4 Conclusions

In this Chapter, the $Zr_{50}Cu_{50}$ and $Zr_{46}Cu_{46}Al_8$ films with compact and nanogranular morphology deposited in controlled conditions to favor O incorporation are examined to study the effects of the presence of O on the local structure and mechanical properties depending on the morphology of the films.
From their structural and mechanical characterization, it is shown that:

- Nanogranular films contain higher amounts of O with respect to compact ones (40 % at. vs 20 % at.) due to the higher reactivity of the clusters with the O in the chamber.
- The presence of O generates two amorphous phases: an O-rich phase mainly bonded with Zr and Al atoms and a Cu-rich phase as shown from the XRD spectra. The XRR spectra present some satellite peaks which can be connected to a nanolayered structure of 5 – 10 nm sublayers alternating the Zr-O rich and the Cu-rich phases.
- Nanogranular films have larger elastic moduli due to larger amount of O present in nanogranular films while the trend of the hardness is more connected to the morphology with the compact films being harder than the nanogranular films (10.2 vs 9.8 GPa for $Zr_{50}Cu_{50}/O$) despite having less O.
- Micropillar compression shows that the $Zr_{50}Cu_{50}/O$ and $Zr_{46}Cu_{46}Al_8/O$ films have large yield strength > 4 GPa and while compact films fail by shear banding nanogranular films can deform homogeneously for large strains (15%) without the propagation of SBs thanks to the combination of high O concentration and cluster-assembled structure.

To sum up, the controlled addition of O in thin film metallic glasses operated by changing the baseline deposition pressure has an overall positive effect on their mechanical performances.

The formation of a self-assembled nanolayered structure of O-rich sublayers similar to oxides and Cu-rich metallic glass sublayers drastically increases the modulus and strength of the films and the nanogranular morphology is able to suppress localized plastic deformation through SBs in favor of homogeneous deformation even at high strains.

The combination of different finely tuned nanostructuring strategies (cluster-assembled structure and nanolayering through O absorption) possible through PLD offers the possibility to produce new classes of high performance nanoengineered metallic/oxide glasses for structural applications.

Nevertheless, more in-depth structural characterizations like TEM will be performed in the future to further understand the nature of the local structure of these films.

VII. Towards the development of new amorphous multilayered nanoarchitectures by alternating compact and nanogranular layers

7.1 *Overview on the investigated samples*

In this chapter the structure and mechanical properties of an exploratory series of fully amorphous multilayer samples alternating compact sublayers deposited in vacuum and nanogranular sublayers deposited in He is presented.

This first batch of multilayers were deposited to understand if it possible to combine the points of strength of the single morphologies presented in Chapter IV and see if this line of research is interesting enough for future experiments. These multilayers are expected to have a yield strength comparable to the one of compact films and the capability to deform homogeneously for large strains like the nanogranular films. These films were deposited from the monolithic $Zr_{50}Cu_{50}$ target using an IR laser with a fluence equal to 14 J/cm^2 and the base deposition pressure was kept to $1x10^{-3}$ Pa to keep the O content to negligible levels with the compact sublayers deposited in vacuum and the nanogranular sublayers deposited in 5 Pa He.

All the characteristics of the multilayers studied in this Chapter can be found in the Table 3.2 of Chapter III.

7.2 Structural properties:

7.2.1 Morphology

The SEM cross-sections after mechanical cleavage of compact/nanogranular $Zr_{50}Cu_{50}$ multilayers are shown in Figure 7.2a-c. All cross-sections show a clear multilayered structure with straight interfaces which delimit the single sublayers.

The shape and width of the corrugations inside the different sublayers depend on their morphology and relative thickness, with the compact sublayers having more defined veins with width that increases with the thickness of the sublayer depending on the bilayer period Λ. The width of the corrugations goes from 40 ± 10 nm corrugation width for the 200 nm Λ multilayer (Figure 8.2a) to 55 ± 14 nm width for the 400 nm bilayer period multilayers (Figure 7.2c) following a trend similar to the fracture morphology of ZrNi TFMGs with different thicknesses studied by M. Ghidelli *et al.* [168] in which it is shown that the increasing geometrical confinement (by reducing the thickness of the films) reduces the dimensions of the corrugations. The nanogranular sublayers have much smaller corrugations with respect to compact sublayers due to the increased heterogeneity related to the cluster-assembled structure, like in the case of the cross-sections of nanogranular $Zr_{50}Cu_{50}$ of chapter IV.

The XRD patterns of the different multilayers are shown in Figure 7.2d. All films present a main broad peak centered around $2\theta=37°-38°$ independent of the bilayer period and corresponding to the position of amorphous $Zr_{50}Cu_{50}$ observed for monolithic $Zr_{50}Cu_{50}$ PLD films in Chapter IV and for magnetron sputtered films in literature [172, 173]. The full width half maximum (FWHM) of the multilayers is larger than the one of the single components (7.5° for compact $Zr_{50}Cu_{50}$ and 8.8° for nanogranular $Zr_{50}Cu_{50}$) and seems to be weakly dependent on the bilayer period, going from 10.2° for the 400 nm bilayer period multilayers to 11.5° for the 200 nm bilayer period multilayers indicating that the increasing number of interfaces contributes to a larger amount of disorder of the local structure.

The structural characterizations shown in this section can only explore the basic structure of the multilayers and in the future HRTEM characterization of the best performing samples will be done to investigate more in detail the interfaces and the differences in local order between the single sublayers.

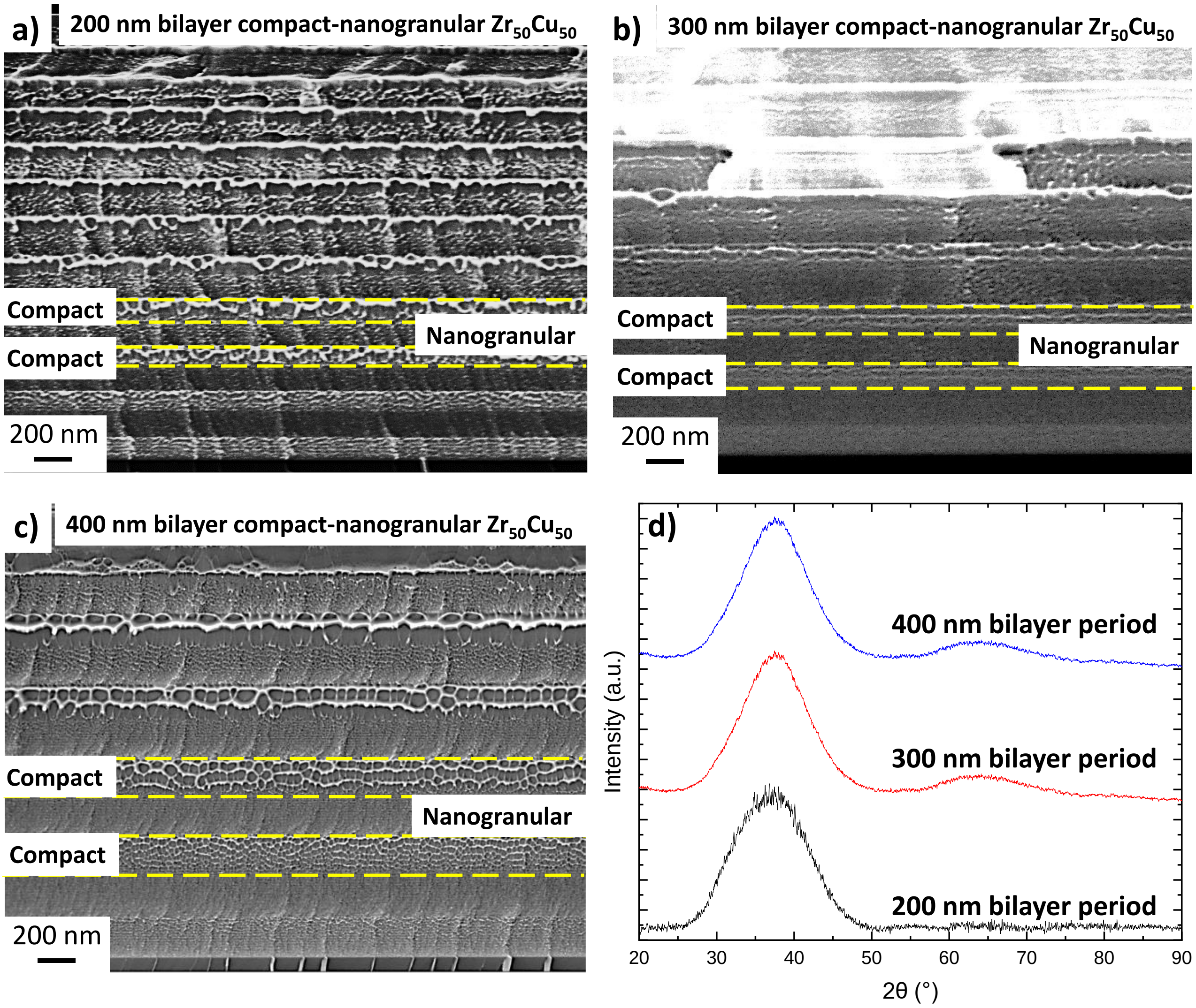

Figure 7.2: *SEM cross-sections of the (a) 200 nm, (b) 300 nm and (c) 400 nm bilayer periods compact/nanogranular* $Zr_{50}Cu_{50}$ *multilayers deposited by PLD and (d) XRD spectra of compact/nanogranular* $Zr_{50}Cu_{50}$ *multilayers as a function of the bilayer period.*

7.3 Mechanical properties:

7.3.1 Evolution of the elastic moduli and hardness

The evolution of the Young's modulus E from optoacoustic techniques and hardness H from nanoindentation as a function of the bilayer period Λ of the compact/nanogranular $Zr_{50}Cu_{50}$ multilayers are shown in Figure 7.3 and compared with the E and H of the single layers presented in Chapter IV.

The E of the multilayers doesn't seem to be strongly dependent on Λ and remains around values equal to 121.5 GPa (Λ = 200 nm) and 122 GPa (Λ = 400 nm) which are in the same range of the E of the single components as shown in Figure 7.3a. This is in line with other fully amorphous multilayers with large thickness (>500 nm) present in literature in which the E of the multilayers is not strongly affected by Λ and tends to be equal to the average of the single components.

This is related to the fact that E is mostly dependent on the strength of the chemical bonds of the elements of the single sublayers and is weakly affected by changes in the nanostructure due to the interfaces [58, 68, 194]. The trend of H as a function of Λ shown in Figure 7.3b is also weakly dependent on the bilayer period with H staying between 8.63 GPa (L = 200 nm) and 8.65 GPa (Λ = 400 nm) which are very close to the H of the compact $Zr_{50}Cu_{50}$ sublayer (8.6 GPa).

While the *H* of the multilayers does not present superhardness phenomena, in which the *H* of the multilayer is much bigger than the *H* of the single components, related to the interfaces acting as SBs blockers [54, 194], its value is also not lowered due to the interfaces acting as defects activating prematurely plastic deformation [58].

The study of the mechanical behavior of compact/nanogranular $Zr_{50}Cu_{50}$ multilayers deposited by PLD is still at its beginnings and future micropillar compression experiments will be performed to observe in detail how the number of interfaces influences the strength and the deformation mechanism of the multilayers.

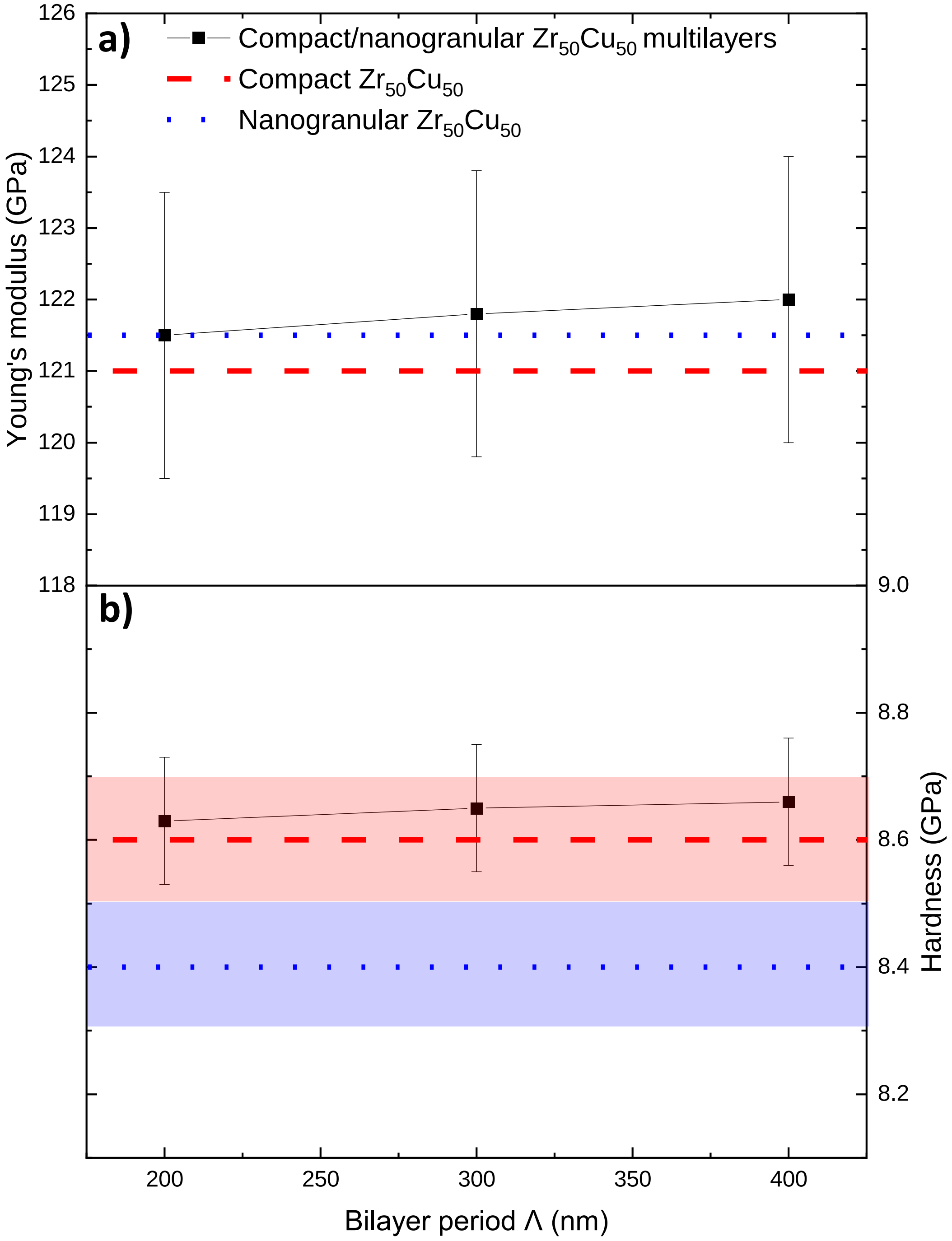

Figure 7.3: *Evolution of (a) Young's modulus and (b) hardness of the compact/nanogranular* $Zr_{50}Cu_{50}$ *multilayers deposited by PLD compared with the modulus and hardness of their components.*

7.3.2 Tensile tests on polymer substrate

After having studied the evolution of the elastic properties and hardness of the PLD multilayers, uniaxial tensile tests on the films deposited on Kapton® substrate are performed to qualitatively evaluate the ductility of the multilayers when coupled with a polymer substrate.

The evolution of the crack density as a function of the engineering strain for the PLD multilayers is shown in Figure 7.4a,b. The crack onset strain (*COS*) of the multilayers decreases with Λ, as shown in Figure 7.4b, going from 1.03% for Λ equal to 400 nm to 0.71% for Λ equal to 200 nm and at the same time the crack saturation density (*CSD*) increases when lowering Λ going from 0.012 mm^{-1} for Λ equal to 400 nm up to 0.024 mm^{-1} for Λ equal to 200 nm, as shown in Figure 7.4a, suggesting that the increasing number of interfaces causes an embrittlement of the multilayers. Furthermore, the residual stresses σ_{res} evaluated from film's curvature [161] are not sufficiently different as a function of Λ to justify the differences in *COS,* with σ_{res} being compressive and around ~-200 ± 60 MPa for all the samples.

The brittle failure of the PLD multilayers is also confirmed by the post-mortem images of sample surface presented in Figure 7.4c, which are all characterized by straight cracks perpendicular to the loading direction typical of brittle materials [92, 193]. The inversely proportional connection between the brittleness of the multilayers and the bilayer period Λ observed for these multilayers could be connected to the smaller thickness of the sublayers being less effective at blocking the SBs responsible for the failure of the film during tensile loading [67, 223, 225].

Lastly, it is observed that the PLD multilayers do not buckle even at strains >15%, indicating a strong adhesion of the films to the substrate which can be related to the initial $Zr_{50}Cu_{50}$ sublayer (Figure 7.1) deposited in vacuum which have been observed in precedent Chapters to be very adherent due to the high kinetic energy of deposition, related to vacuum plasma plumes [198].

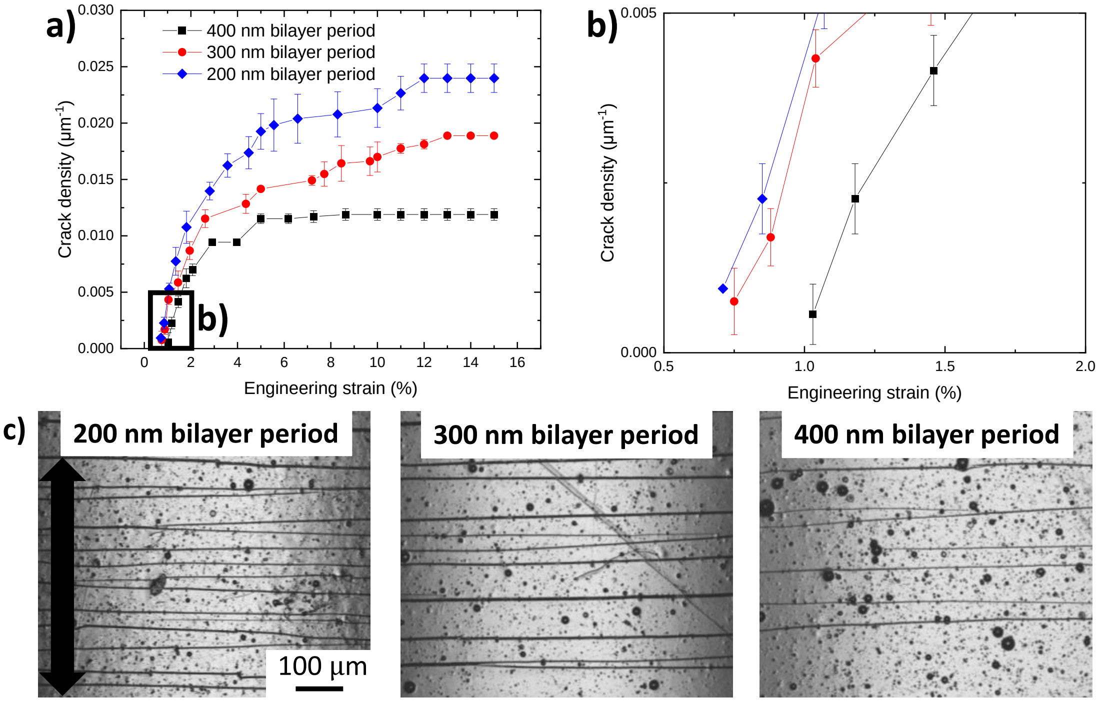

Figure 7.4: *(a) Crack density vs engineering strain curves of the compact/nanogranular* $Zr_{50}Cu_{50}$ *multilayers deposited by PLD. (b) Magnification of the initial region of the crack density-engineering strain curve highlighting the crack initiation strain of each film. (c) Pos-mortem optical images of the compact and nanogranular films after 15% strain. The vertical black arrow indicates the loading direction during the experiment.*

The fracture toughness of the PLD multilayers as a function of L is shown in Figure 7.5. The Beuth model [162] combines COS, CSD, the reduced modulus of the film E_r, and the stress at fracture of the film ($COS*E+ s_{res}$) to obtain the fracture energy $G_{Beuth} = \frac{(COSE\sigma_{res})^2}{1.34CSDE_r}$ which can be used to calculate the fracture toughness expressed as $\sqrt{E_r G_{Beuth}}$.

The fracture toughness decreases with L going from 13.6 MPa*m$^{1/2}$ for L equal to 400 nm to 3.7 MPa*m$^{1/2}$ for L equal to 200 nm further confirming the embrittlement of the multilayered structure with the increasing number of interfaces.

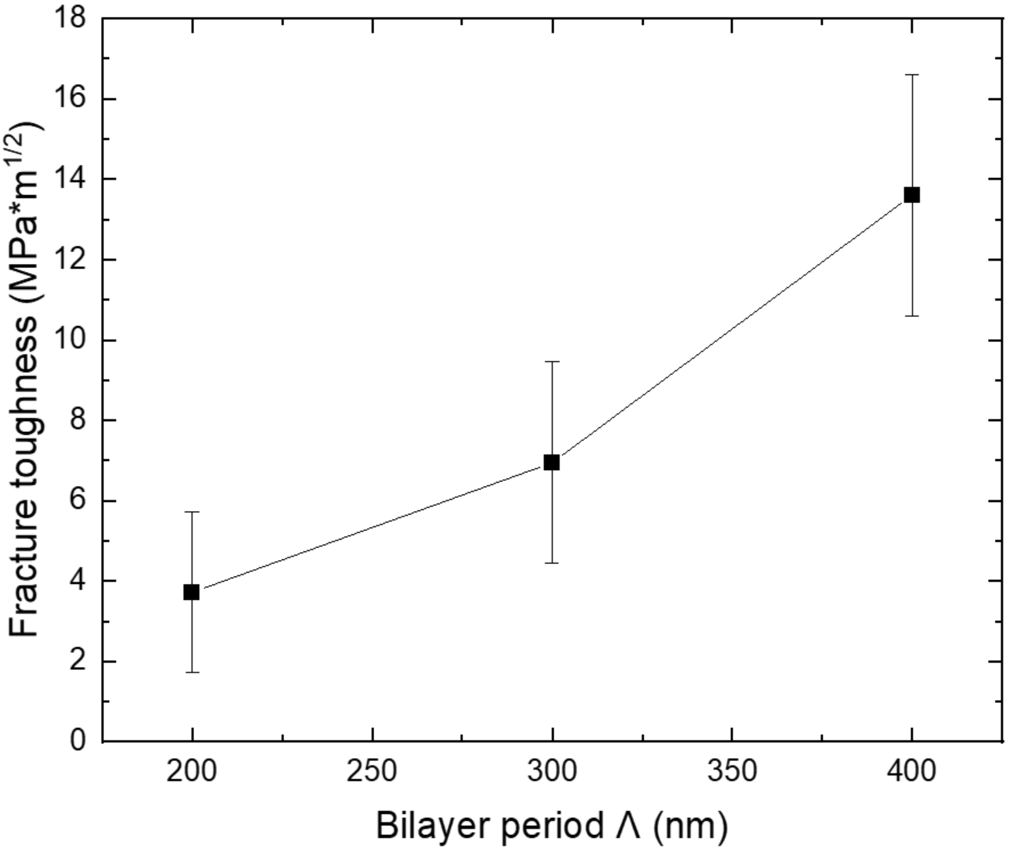

Figure 7.5: *Evolution of fracture toughness of the compact/nanogranular $Zr_{50}Cu_{50}$ multilayers as a function of the bilayer period.*

7.4 Conclusions and future perspectives

In this chapter the local structure and the basic mechanical properties of a first series of multilayers alternating compact and nanogranular $Zr_{50}Cu_{50}$ sublayers are studied to observe if it is possible to combine the advantages related to the different morphologies shown in the previous chapters.

From the characterizations performed in this chapter it is observed that:

- In the SEM cross-sections after cleavage the interfaces between the compact and nanogranular sublayers are straight and clear and the compact sublayers have larger SB corrugations with respect to their nanogranular counterparts.
- The Young's modulus E of the multilayers is mostly independent from the bilayer period Λ and around 121.5-122 GPa, which is in the same range of the E of nanogranular $Zr_{50}Cu_{50}$, while the hardness H of the multilayers remains between 8.63 GPa (Λ = 200 nm) and 8.65 GPa (Λ = 400 nm) close to the H of the compact $Zr_{50}Cu_{50}$ sublayer (8.6 GPa) and indicating a strengthening effect of the interfaces which increases H from the theoretical H average of the sublayers (8.5 GPa).

- Preliminary uniaxial tensile tests on polymer substrates indicate that the crack resistance of the PLD multilayers increases with Λ suggesting that smaller periods are less effective in containing the SBs responsible for the failure of the films.

Overall, these first results are positively interesting showing that the high mechanical properties of the PLD films observed in Chapter IV are still maintained in these multilayers and promising for future practical applications.

However, the study of compact/nanogranular multilayers is still at its beginnings and in the future characterizations like TEM cross-sections and micropillar compression will be performed to study more in detail the local structure of the interfaces between compact and nanogranular sublayers and how the bilayer period L influences the strength and deformation behavior of the films. The range of Λ could be expanded going down to values like 100 and 50 nm periods to further observe possible changes in the mechanical behavior as a function of Λ.

VIII. Synthesis and mechanical properties of nanostructured high entropy alloy thin films

8.1 Overview on the samples

In this Chapter, the structure and mechanical properties of nanostructured CoCrCuFeNi high entropy alloys thin films (HEA-TF) deposited by PLD is presented. Different deposition pressures have been used to investigate the effect of the transition from an atom-by-atom to a cluster assembled growth on the atomic and microstructure and consequently on the mechanical properties.

A CoCrCuFeNi equiatomic target (purity >99.95%) was used for all the depositions. The films were deposited with a green (532 nm) laser with an average energy around 600 ± 10 mJ with the optics set up to have a fluence of 3.1 J/cm^2 and in different pressures ranging from vacuum (2x10^{-3} Pa) to 0.1, 1, 5 Pa of He. The characteristics of the PLD samples studied here are presented in the Table 3.1 of Chapter III. Magnetron sputtered (MS) CoCrCuFeNi films were produced for comparison purposes using a CoCrCuFeNi equiatomic target (purity >99.95%) mounted on a radiofrequency cathode. The deposition was carried out in 0.5 Pa Ar pressure and 200 W power were applied to the cathode.

The characteristics of the MS samples can be found in in table 3.5 of Chapter III.

8.2 Structural properties:

8.2.1 *Morphology*

The SEM cross-sections after mechanical cleavage of the HEA films deposited by PLD and magnetron sputtering are shown in Figures 8.1a-e. The cross-sections of the films deposited in vacuum (Figure 8.1a) and in 0.1 Pa He (Figure 8.1b) do not present particular features, suggesting a homogeneous morphology.

The films deposited in 1 and 5 Pa (Figures 8.1c,d) instead have a more nanogranular morphology due to cluster- assembled growth of the films which leads to a less compact structure [199]. On the other hand, MS films in Figure 8.1e present a nanocolumnar morphology with column diameter of 36 ± 4 nm and height equal to the film thickness (800 nm) due to the low energy and mobility of the sputtered atoms which leads to self-shadowing effects which limits the grain growth along the surface plane [87, 226].

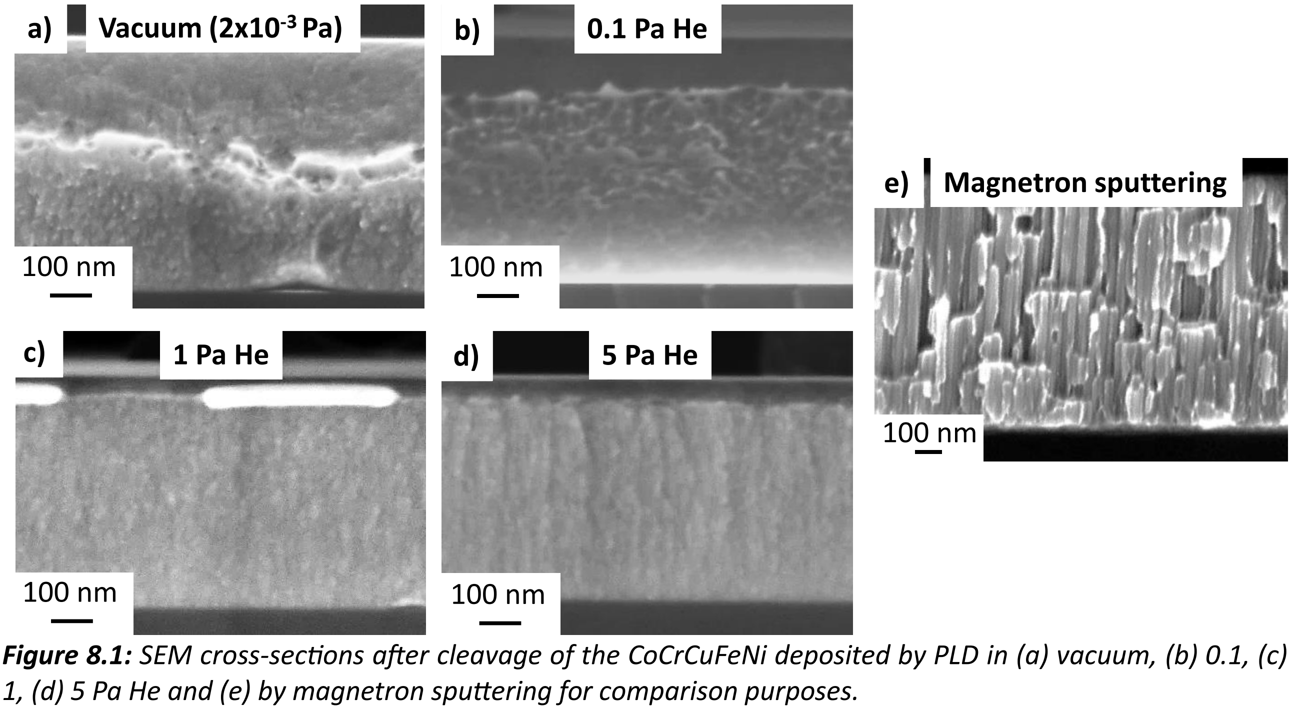

Figure 8.1: *SEM cross-sections after cleavage of the CoCrCuFeNi deposited by PLD in (a) vacuum, (b) 0.1, (c) 1, (d) 5 Pa He and (e) by magnetron sputtering for comparison purposes.*

The XRD diffractograms of the CoCrCuFeNi HEA-TF by PLD and magnetron sputtering are shown in Figures 8.2a,b. In Figure 8.2a the grazing incidence XRDs of the films deposited by PLD and magnetron is presented.

TFHEAs have a peak around 42.5° - 43° corresponding to the (111) peak of the FCC CoCrCuFeNi crystalline structure, which is the growth direction which minimizes the configurational energy in FCC crystals [227], with a lattice parameter around 3.6-3.7 Å in line with previous reports from literature [126, 140]. The films deposited by PLD also show a weak peak around 49° corresponding to the (200) peak of the FCC CoCrCuFeNi structure, which is instead absent in the magnetron sputtered films, indicating a lower degree of texturing of the PLD films.

However, the grazing incidence XRD fails to see the small differences between films deposited in vacuum (compact) and the ones deposited in 5 Pa He (nanogranular), corresponding to a grain size equal to 15-16 nm for both morphologies, and for this reason XRD in Bragg-Brentano configuration was performed to better evaluate the different FWHMs and correctly measure the grain size of the crystallites of the different morphologies.

The XRD spectra in Bragg-Brentano configuration for compact, nanogranular and magnetron sputtered CoCrCuFeNi films are presented in Figure 8.2b and the differences between the FWHMs of the different morphologies is much more evident. The films deposited by magnetron sputtering present only the (111) diffraction peak confirming the strong texturization of the film related to the nanocolumnar structure and that the crystallite size is equal to the thickness of the film as previously hypothesized [228].

In the case of the PLD films the FWHMs are larger than the one of magnetron sputtered films and increase with the deposition pressure indicating a smaller grain size which is equal to 35 ± 1 nm for the compact films and 12.5 ± 1 nm for the nanogranular films. The smaller grain size of the films deposited by PLD in vacuum with respect to the MS films can be related to the higher energy of the atomic species of the PLD plasma that increases the mobility of the adatoms on the substrate surface preventing shadowing effects which favor nanocolumnar growth and instead promote a layer-by-layer growth of the film [229].

The decrease of grain size with the transition from compact films deposited in vacuum to nanogranular films deposited in inert gas atmosphere, a trend already observed in literature for other metals deposited by PLD like W [137, 230], Pt [231] and Au [232], is related to the confinement of the plasma plume in He atmosphere. The plume confinement reduces the kinetic energy of the atomic species arriving on the substrate and, combined with the formation of small nanoclusters inside the plume, result in a reduced growth of the crystalline grains with respect to the films deposited in vacuum while avoiding the strong texturing of magnetron sputtered films.

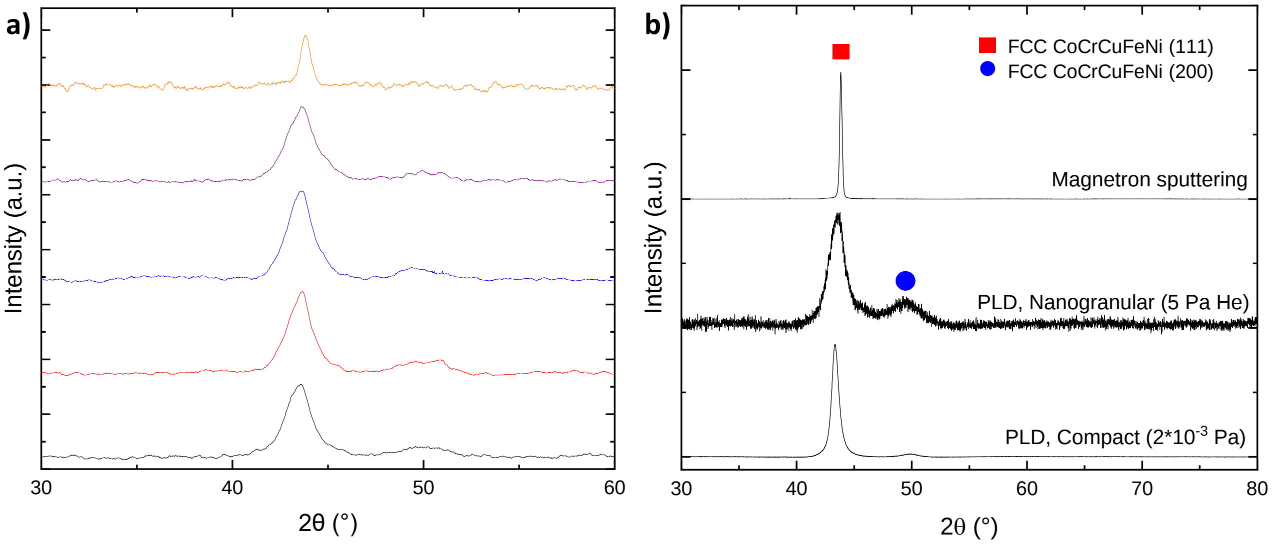

Figure 8.2: *XRD diffractograms in (a) grazing incidence and in (b) Bragg-Brentano configuration of the CoCrCuFeNi films deposited by PLD and magnetron sputtering.*

8.2.2 TEM characterization

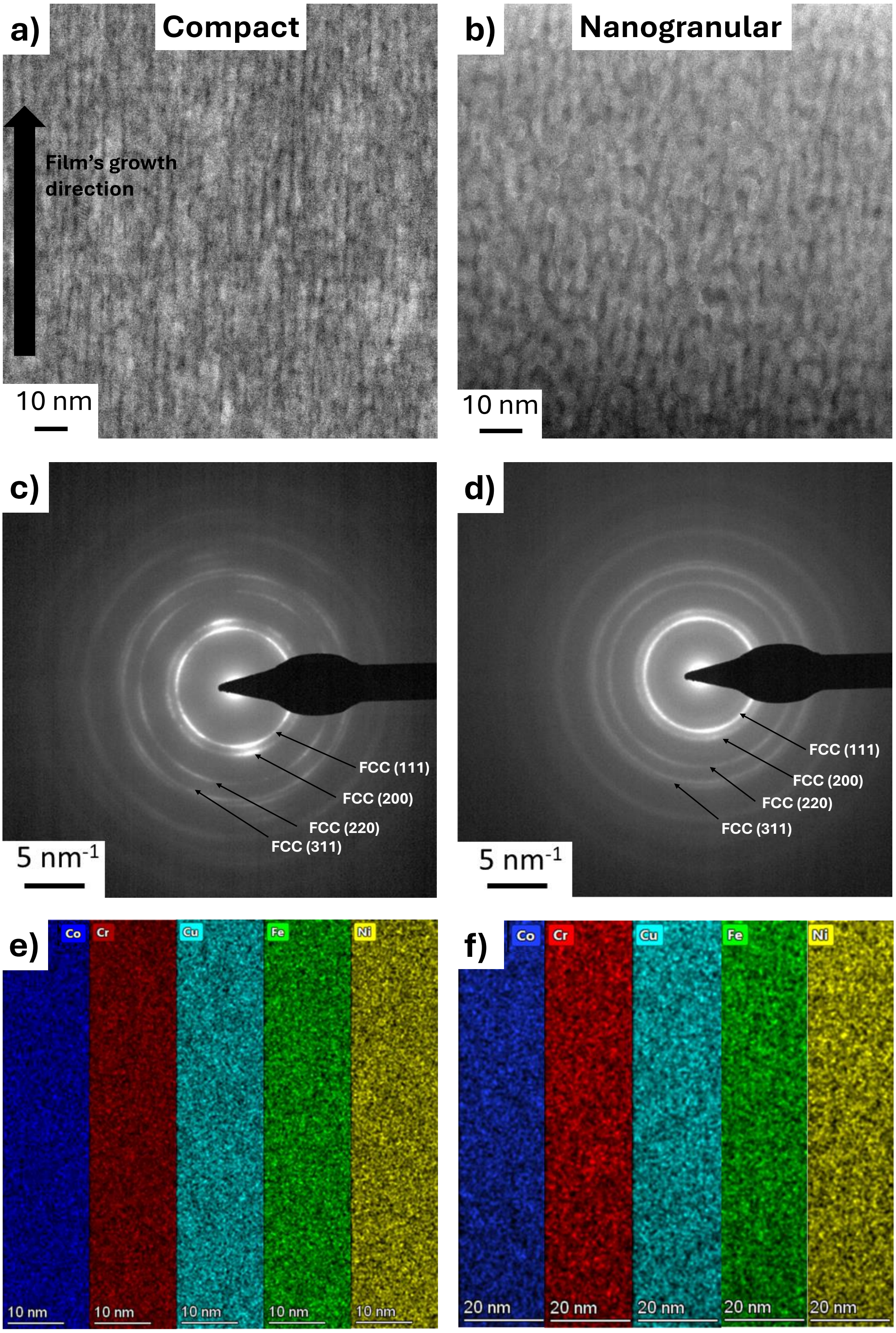

Figure 8.3: *HAADF-TEM, SAED and STEM-EDX images of compact (a,c,e) and nanogranular (b,d,f) CoCrCuFeNi films by PLD.*

The CoCrCuFeNi films deposited in vacuum (compact) and in 5 Pa He (nanogranular) were chosen for more advanced TEM characterization to observe more in detail the local structure and the results are shown in Figure 8.3.

Figure 8.3a shows the HAADF-TEM cross-section of vacuum deposited CoCrCuFeNi which appears to be formed by small nanocolumns parallel to the growth direction with the diameter of the order of few nanometers (4-6 nm) and with the height of the order of tens of nanometers (40 – 100 nm). The HAADF-TEM cross-section of the films deposited in He, shown in Figure 8.3b, seems instead to be formed by interconnected globular and cylindrical nanoclusters (10-20 nm diameter) branching in different directions resulting in a more disordered structure with respect to the ordered nanocolumns of Figure 3a confirming the cluster-assembled growth of the films deposited in He.

The SAED of the films is shown in Figures 8.3c,d. Both morphologies show the diffraction rings of (111), (200), (220) and (311) FCC CoCrCuFeNi crystalline structure demonstrating that the films have a randomly oriented grain structure. The SAED of compact films (Figure 8.3c) shows that there are intensity fluctuations along the rings' pattern which can be connected to the presence of a preferred texturization or crystallite orientation. This can supported by the structure observed in Figure 8.3a, while the SAED of nanogranular films of Figure 8.3d has a uniform intensity indicating a non-textured polycrystalline structure which can be related to the cluster-assembled growth [233].

Lastly, Figures 8.3e,f report the STEM-EDX of the compact and nanogranular CoCrCuFeNi films and in both cases it seems the elements composing the alloy are all homogeneously mixed without the Cu segregations that can be present in bulk samples [124].

This phenomenon can be related to the fast cooling rates of physical vapor deposition techniques which limit the movement of atoms after the film's growth thus reducing the possibility to develop significant segregations favoring instead a solid solution [126].

8.2.3 Evolution of density

The evolution of the mass density of CoCrCuFeNi HEA-TF deposited by PLD as a function of deposition pressure is shown in Figure 8.4.

The density of the compact PLD films is equal to 8 g/cm^3, a value lower than the theoretical value from the rule of mixture of the densities of the single components which is equal to 8.37 g/cm^3. This reduction of mass density could be connected to the low grain size observed by XRD combined with the partial reported by TEM characterization resulting in a more disordered local structure than the ideal structure connected to the theoretical density [234].

However, MS films, which have bigger columnar grains vs PLD compact films, have a density equal to 7.66 g/cm^3 which is lower than the density of PLD compact films. While the lower density of MS films vs compact films could be related to the lower energies of the sputtered particles (1-10 eV) with respect to the plasma particles in a PLD plume (>15 eV) [88, 143], this could also indicate that the theoretical density ignore local lattice distortions and/or effects of the different growth's mechanisms.

By increasing the deposition pressure goes up to 0.1 Pa He the density decreases to 7.85 g/cm^3 due to the reduced kinetic energy of the particles in the plasma plume interacting with the He atmosphere. When the pressure is above 1 Pa He the mass density decreases to values around 6.8 g/cm^3, a sharp transition connected to the change in the growth mechanisms of the film from the atom-by-atom to cluster-assembled growth increasing the fraction of grain boundaries, a trend similar to other metals deposited by PLD [137, 230-232].

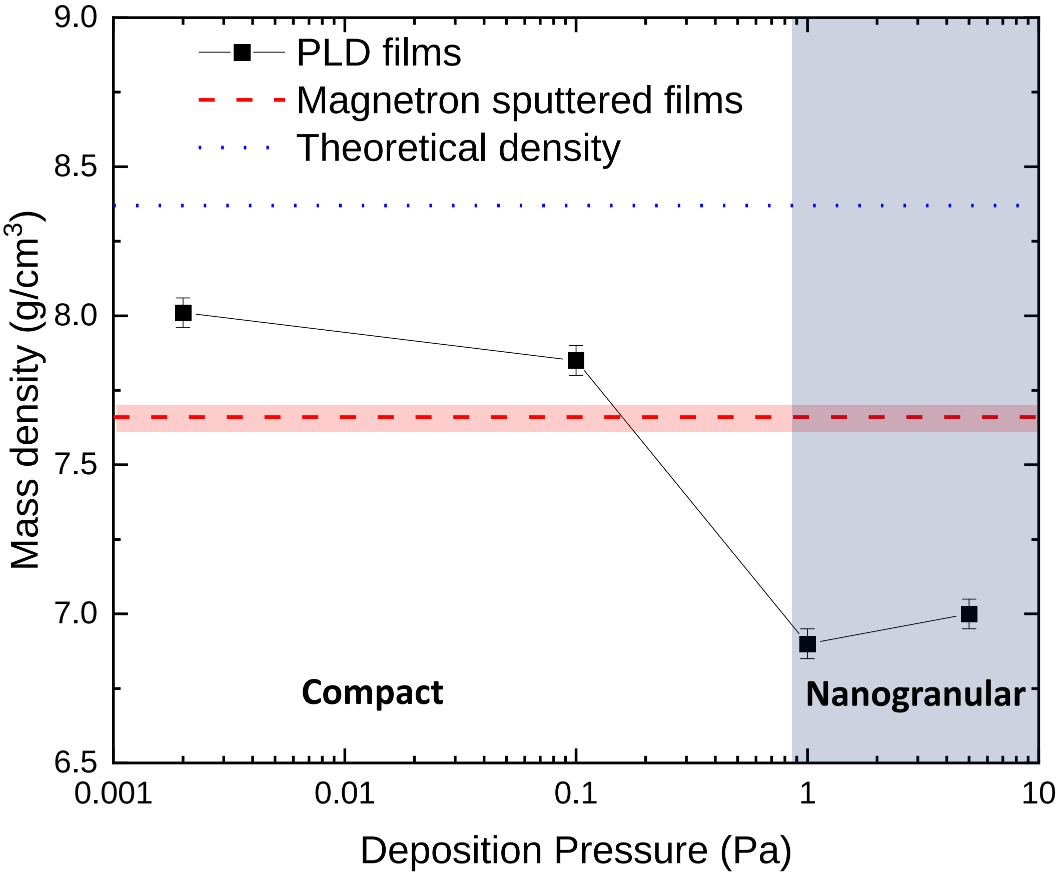

Figure 8.4: *Evolution of mass density of CoCrCuFeNi as a function of deposition pressure.*

8.3 Mechanical properties:

8.3.1 Evolution of the elastic moduli and hardness

The evolution of the Young's modulus (*E*), investigated with optoacoustic techniques, and of the hardness (*H*), investigated with nanoindentation, as a function of the deposition pressure is presented in Figure 8.5.

As shown in Figure 8.5a, compact CoCrCuFeNi films have an *E* of 149 GPa, which slightly decreases by increasing the deposition pressure reaching a plateau of 127 GPa after the transition to a nanogranular morphology for deposition pressures ⩾ 1 Pa He. The decrease of *E* with the increase of deposition pressure is related to the reduction of grain size increasing the volume of disordered grain boundaries in the films which have weaker atomic bonds with respect to the main crystalline structure [235-237].

MS films have an *E* of 175 GPa, a value significantly higher than the PLD films and similar to the value of *E* of other MS CoCrCuFeNi films found in literature [238, 239]. The large value of *E* of the MS films seems to be connected to their relatively big grains with respect to PLD films and due to their strong texturization along the (111) crystallographic direction related to the nanocolumnar films which in literature is associated with high theoretical *E* values [240]. Consequently, a strongly textured film with a low fraction of grain boundaries, like the MS CoCrCuFeNi, would have a larger *E* with respect to a weakly textured (PLD compact) or non-textured (PLD nanogranular) film with random grain orientation.

The hardness (*H*) of CoCrCuFeNi films deposited by magnetron sputtering and different PLD morphologies plotted against the grain size of the different films is reported in Figure 8.5b. The *H* of the PLD films seems to be weakly dependent on the deposition pressure passing from the 10.8 GPa of compact films to 11.2 GPa for the nanogranular films. More importantly, the *H* of PLD films is much larger than the one MS films which is instead equal to 8.3 GPa.

The drastic change of *H* between PLD and MS films can be related to their different grain sizes and seems to follow the Hall-Petch relationship in which the reduction of the grain sizes *d* progressively improves the *H* of the films following the equation $H = H_0 + kd^{-1/2}$, where H_0 and *k* are parameters dependent on the chemistry of the material [241].

A physical explanation of the Hall-Petch relationship is the work hardening model in which the stress necessary to activate plastic flow is proportional to the density of dislocations of the material, which is inversely proportional to *d*, which results in a large density of dislocations hindering each other movement for nanocrystalline structures [242, 243]. However, the increase of *H* caused by the transition from compact to nanogranular films is much smaller than the one expected from pure Hall-Petch behavior.

This a phenomenon which in literature is explained as the transition from Hall-Petch to inverse Hall-Petch behavior in which the hardness decreases with the grain size since other deformation mechanisms like grain boundary sliding, diffusion and rotation substitute the dislocation pile-up easing the plastic flow [244]. The transition from Hall-Petch to inverse Hall-Petch behavior would occur after an interval in which *H* would be weakly dependent on grain size, which MD simulations of CoCrCuFeNi put between 10 and 20 nm as reported in the article of L. Zhang *et al*. [245].

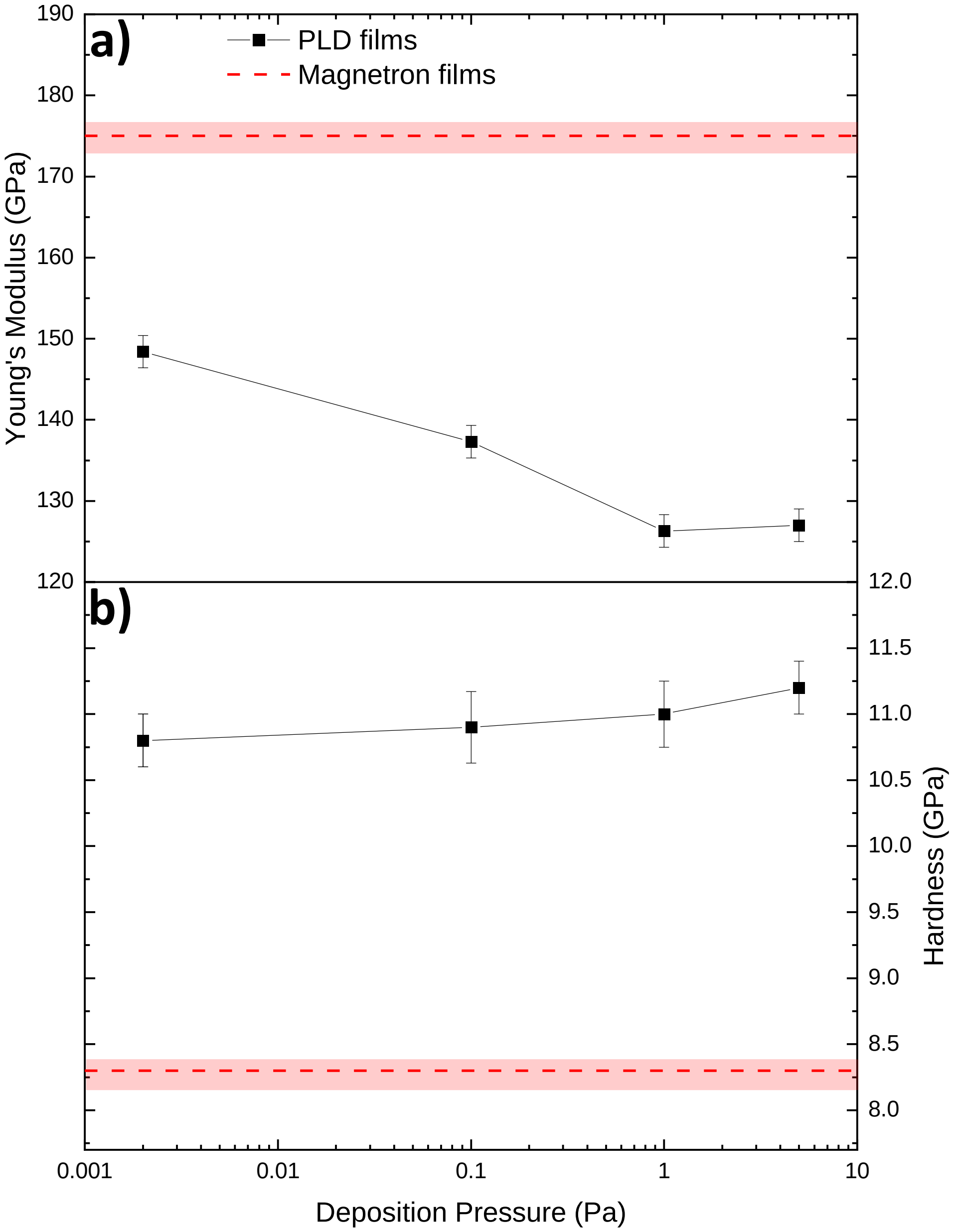

Figure 8.5: *Evolution of the (a) Young's modulus and the (b) hardness of the CoCrCuFeNi PLD films as a function of the deposition pressure and compared with magnetron sputtered films.*

8.3.2 Tensile tests on polymer substrate

After having studied the effect of the deposition pressure on the elastic properties and hardness of the CoCrCuFeNi by PLD, tensile tests of films deposited on polymer substrate (Kapton®) were performed to further investigate the mechanical behavior of these films when coupled with a flexible substrate.

Compact CoCrCuFeNi films have a onset of crack formation strain (*COS*) of 3.44% which decreases after the transition to the nanogranular structure (>1 Pa He) to 2.73% strain for films deposited in 5 Pa He, as shown by Figures 8.6a,b. The transition from compact to nanogranular morphology also marks an increase of the crack saturation density (*CSD*) indicating an embrittlement of the film [167]. The type of cracks observed in the plain views of Figures 8.6c confirm this trend with the films deposited in vacuum showing cracks with 45° inclination (direction of maximum shear stress) with respect to the loading direction (black arrow) which are typical of ductile films [246, 247] and can be associated with local necking phenomena [248].

The cracks become progressively straighter with the increase of the deposition pressure becoming fully straight for the films deposited in 5 Pa He like the ones of brittle materials like metallic glasses [92, 223]. It is shown that the PLD films, independently of the deposition conditions, are more ductile with respect to magnetron sputtered CoCrCuFeNi films found in literature which have a crack initiation strain around 2% and break by forming straight cracks like brittle materials [160].

The large difference in crack onset strain between PLD and MS films can be related to the nanocolumnar structure of MS CoCrCuFeNi favoring intergranular crack formation combined with lower values of *H* and higher values of *E* with respect to PLD films suggesting lower yielding and fracture strains. PLD and MS films also have drastically different residual stresses, which can greatly change the crack resistance of a film, with the PLD CoCrCuFeNi having compressive stresses around 380 MPa, measured through the estimation of the curvature of the substrate [161], increasing the necessary fracture strain in tension [192].

MS CoCrCuFeNi, instead, has tensile residual stresses > 500 MPa [160] further reducing the strain necessary for the nucleation of cracks during tensile loading [192]. While the reduced crack resistance of MS films when compared to PLD films can be explained with the difference in residual stresses, the difference in residual stresses between compact and nanogranular PLD films is not sufficient to explain the embrittlement of nanogranular films.

The reduction of crack resistance with the change of grain size is similar to what it is observed in literature for bulk nanocrystalline metals in which the ductility decreases with the grain size due to the high density of dislocations quickly reaching saturation level during tensile loading and consequently promoting phenomena of localized deformation [249].

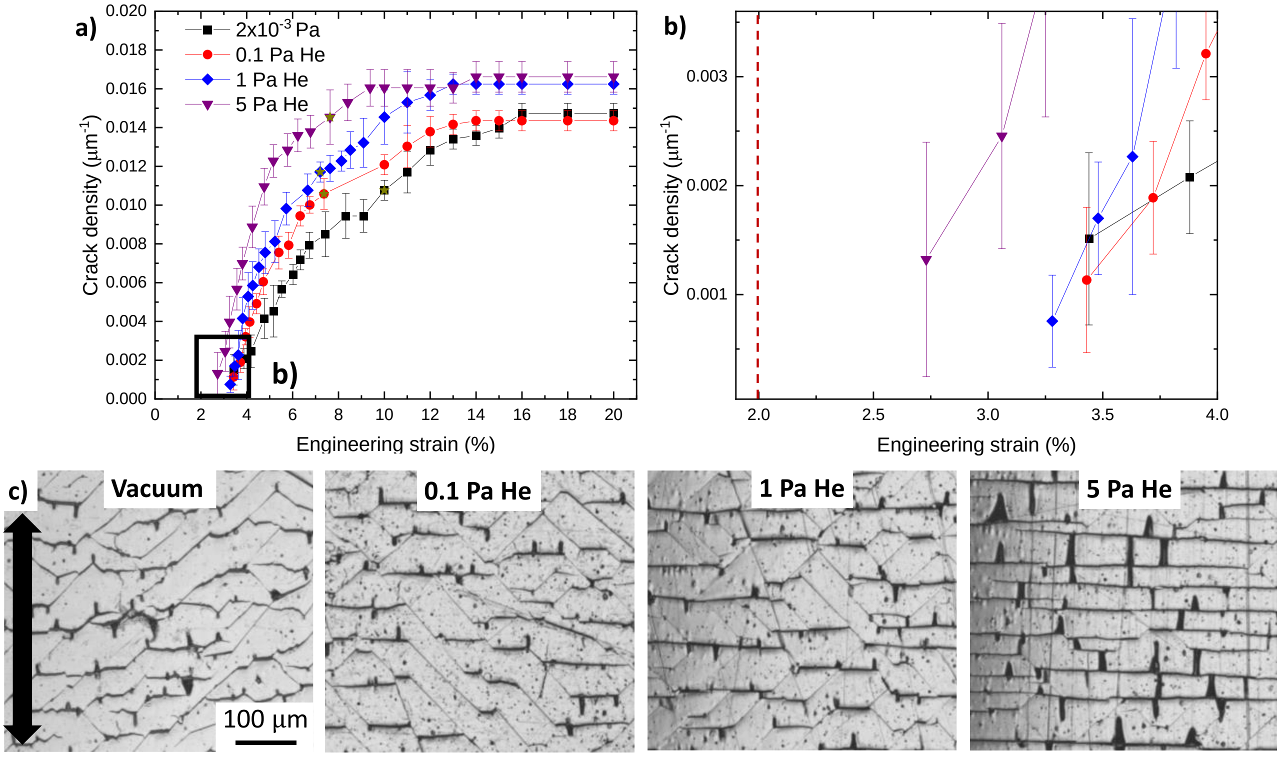

Figure 8.6: *(a) Crack density – engineering strain curves of the CoCrCuFeNi films by PLD as a function of the deposition pressure. The golden stars indicate the strain at which the films start to buckle from the substrate. (b) Magnification of the initial region of the crack density-engineering strain curve highlighting the crack initiation strain of each film, the dashed line indicates the onset of crack formation of magnetron sputtered CoCrCuFeNi. (c) Plain views of CoCrCuFeNi films by PLD in vacuum, 0.1, 1 and 5 Pa He after tensile test. The black arrow indicates the direction of the tensile loading during the experiment.*

The fracture toughness of the CoCrCuFeNi PLD films as a function of the deposition pressure are shown in Figure 8.7a. The Beuth model [162] combines *COS*, *CSD*, the reduced modulus of the film E_r, and the stress at fracture of the film ($COS*E+\sigma_{res}$) to obtain the fracture energy $G_{Beuth} = \frac{(COSE\sigma_{res})^2}{1.34CSDE_r}$ which can be used to calculate the fracture toughness expressed as $\sqrt{E_r G_{Beuth}}$.

As expected from the trend of *COS* compact CoCrCuFeNi has the highest toughness among the examined samples being equal to 33.6 MPa*m$^{1/2}$ and decreasing down to 21 MPa*m$^{1/2}$ for the nanogranular films deposited in 5 Pa He confirming the embrittlement caused by the grain refinement while MS CoCrCuFeNi has a fracture toughness equal to 25.4 MPa*m$^{1/2}$ intermediate between compact and nanogranular films [160].

Lastly, the adhesion energy J_0 of the films to the substrate is presented in Figure 8.7b. J_0 can be estimated from the buckling initiation strain (*BIS*), *CSD*, film's thickness *h*, the reduced modulus of the film E_r, and σ_{res} by using strain energy delamination model [163] with $J_0 = \frac{E_r h \beta^2}{2}\left(BIS + \frac{\sigma_{res}}{E_r \beta}\right)^2$ with β being a dimensionless factor depending on *CSD* roughly equal to -0.47 for all PLD films.

Compact films have a J_0 in the order of 147 J/m^2 and decreases with the increase of the deposition pressure going down to 75 J/m^2.

The adhesion energy of the MS films is 4.5 J/m^2 [160] and is in line with the values found in literature for MS TFMGs [193], crystalline single [196] and multilayer [197] metallic films.

This would indicate, as already presented in Chapter IV, that the main parameter determining the adhesion between substrate and film is the energy with which the atoms impinge on the polymer substrate during deposition and since the plasma of PLD has much more energy than magnetron sputtering it is reasonable to observe higher adhesion energy in PLD with respect to MS films [88, 198].

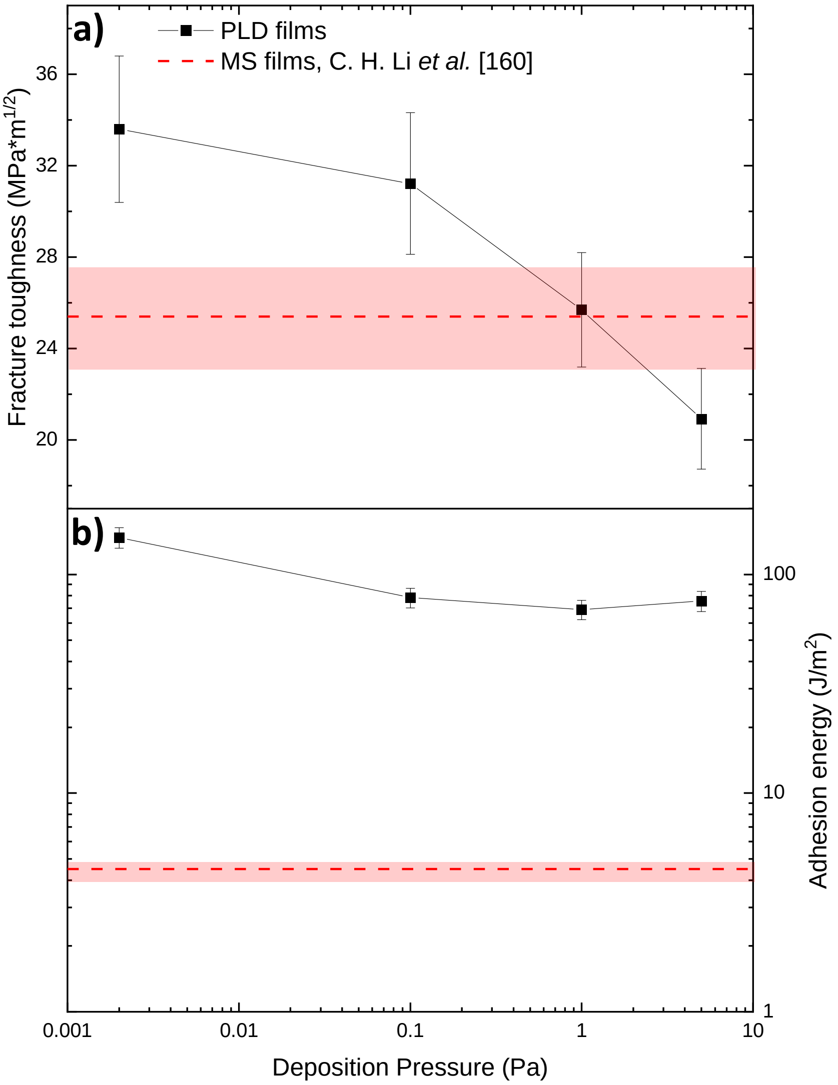

Figure 8.7: *(a) Fracture toughness and (b) adhesion energy of the the CoCrCuFeNi films by PLD as a function of the deposition pressure.*

8.4 Conclusions

In this chapter I studied the structure and the mechanical properties of CoCrCuFeNi thin films deposited by PLD with different deposition pressures and compared them with their MS counterparts.

The main results presented in this chapter are:

- CoCrCuFeNi films deposited by PLD in vacuum have a compact morphology due to the atom-by-atom growth and a transition towards a cluster-assembled growth mechanism when the deposition pressure is above 1 Pa He obtains nanogranular films. MS CoCrCuFeNi, instead, has a nanocolumnar structure.
- Films deposited by PLD present a polycrystalline FCC structure with the (111), (200), (220), (311) peaks observed in literature for bulk samples with the compact films showing a partial texturing of the crystalline structure and grain size equal to 35 nm while nanogranular do not have a preferred crystalline orientation or texturization and grain size equal to 12.5 nm due to the cluster-assembled growth of the film. MS films show a strongly textured FCC (111) crystalline structure due to the nanocolumnar structure with grains having a diameter of 36 nm and height equal to the thickness of the film (800 nm).
- The Young's modulus *E* and hardness *H* of the films are directly correlated to their relative grain size and morphology with magnetron sputtered film having the highest *E* equal to 175 GPa due to the strong texturing and lowest *H* equal to 8.3 GPa due to their large grain size. Compact CoCrCuFeNi

films have smaller *E* equal to 149 GPa which is further lowered to 127 GPa for nanogranular films due to the loss of texturing while the *H* is much bigger around 10.8-11.2 GPa due to the reduced grain size following the Hall-Petch relationship.

- Tensile tests of the films deposited on a polymer substrate show that compact films have a high crack onset strain equal to 3.44%, a value much larger than the 2% observed in literature for CoCrCuFeNi MS films, coupled with improved toughness and adhesion fracturing like ductile metals. The transition to nanogranular films causes an embrittlement of the film with a reduction of the crack initiation strain to 2.73% which can be related to the grain refinement of the films that can cause localization of the deformation which results in premature failure like in the case of bulk nanocrystalline metals.

To sum up, PLD can easily control the texturing and grain size of nanocrystalline HEAs films by changing the deposition pressure which allows the production of nanoengineered thin films with controllable mechanical properties. The nanoengineered films by PLD can achieve better hardness and plastic behavior when coupled with a polymer substrate with respect to MS thin films opening new paths for the design of high performance TFHEAs for structural coatings and flexible electronics applications.

8.5 Future perspectives

After having studied the effect of the deposition pressure on the structure and mechanical properties of the master alloy CoCrCuFeNi, exploratory depositions of Al/CoCrCuFeNi nanolaminates by PLD following the same approach used for the deposition of the $Zr_{50}Cu_{50}$/Al nanolaminates described in Chapter V were performed.

The objective is to try to improve the mechanical properties of the base alloy by introducing interfaces able to hinder the movement of dislocations and/or possibly cause a phase transformation of one of the two components due to the confinement of the sublayer growth [51]. Al was chosen as the second component since it is a very ductile metal and because in literature the addition of Al to CoCrCuFeNi can cause a phase transition from FCC to BCC crystalline structure increasing the hardness of the material [124, 250].

The first Al/CoCrCuFeNi samples were deposited in vacuum and in 5 Pa He with their XRD showing two peaks at 38.5° and 42°-43° corresponding to the (111) peaks of FCC Al and CoCrCuFeNi.

The local structure of these nanolaminates is investigated with HAADF-TEM and STEM-EDX in Figure 8.8. In both samples a clear ultrafine nanolayered structure alternating 2 nm Al and 5 nm base CoCrCuFeNi and in the case of the nanolaminates deposited in vacuum of Figure 8.8a it is possible to observe that Cu is not well confined with the other elements of the base alloy and diffuses in the Al layers since Cu has more chemical affinity with Al with respect to the other elements as shown by the fact that Cu has a positive enthalpy of mixing with Co, Cr, Fe, Ni (4, 6, 13, 12 kJ/mol) and negative enthalpy with Al (-1 kJ/mol) [13].

This diffusion of Cu in the Al layers is reduced in the nanogranular nanolaminates of Figure 8.7b due to the reduction of the kinetic energy of the plasma species in He atmosphere which reduce the mobility of the atoms on the growing surface of the film thus limiting diffusion phenomena.

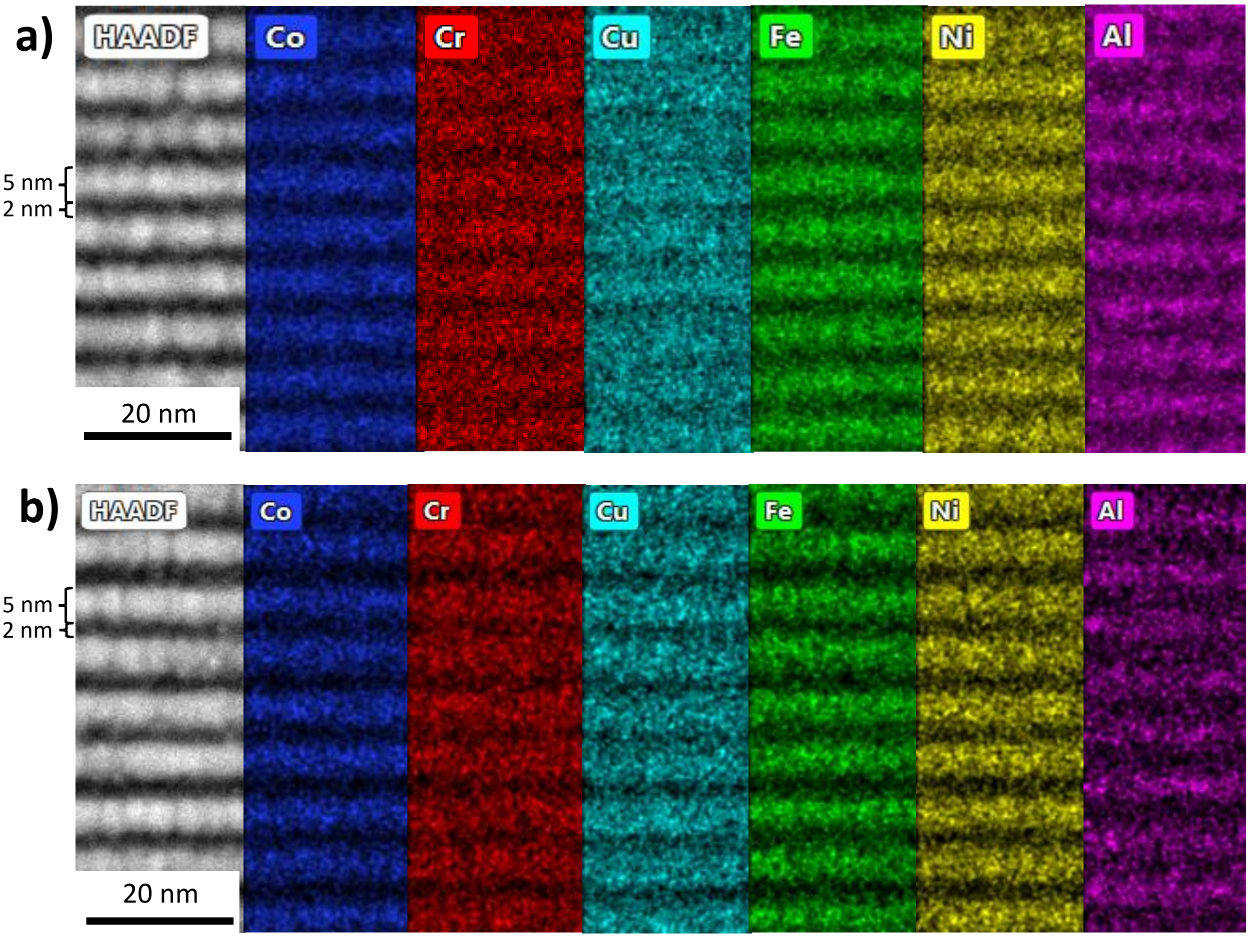

Figure 8.8: *HAADF-STEM and STEM-EDX images of (a) compact and (b) nanogranular 2/5 nm Al/CoCrCuFeNi films by PLD.*

Preliminary investigation of the mechanical properties of the Al/CoCrCuFeNi nanolaminates was conducted by nanoindentation and the results are shown in Figure 8.9. The *E* and *H* of the nanolaminates do not seem to be affected by the change in deposition pressure, unlike the base alloy, being equal to 161 and 9.2 GPa, respectively.

The absence of effects of the deposition pressure on the mechanical properties of the nanolaminates is correlated with the relative thickness of the sublayers, smaller than the grain sizes obtained for both compact and nanogranular base alloys. This becomes the main limiting factor for the grain growth, as observed in many multilayers studied in literature [55, 202, 251], thus eliminating the differences introduced by the deposition pressure. The very small grain size of the nanolaminates would explain why their mechanical properties are lower than the base CoCrCuFeNi films since small grain sizes would result in a very disordered structure with weaker atomic bonds (lower *E*) and the activation of the so called "inverse Hall-Petch" behavior in which the hardness decreases with the grain size due to the activation of deformation mechanisms requiring less stress to activate [244].

However, it must be noted that the *E* and *H* of these nanolaminates are still higher than the theoretical values of *E* and *H* which could be obtained by using the rule of mixture on pure CoCrCuFeNi and Al, which 143 and 8.1 GPa respectively, indicating that there are still some reinforcing mechanisms related to the nanolayered structure which are currently under investigation.

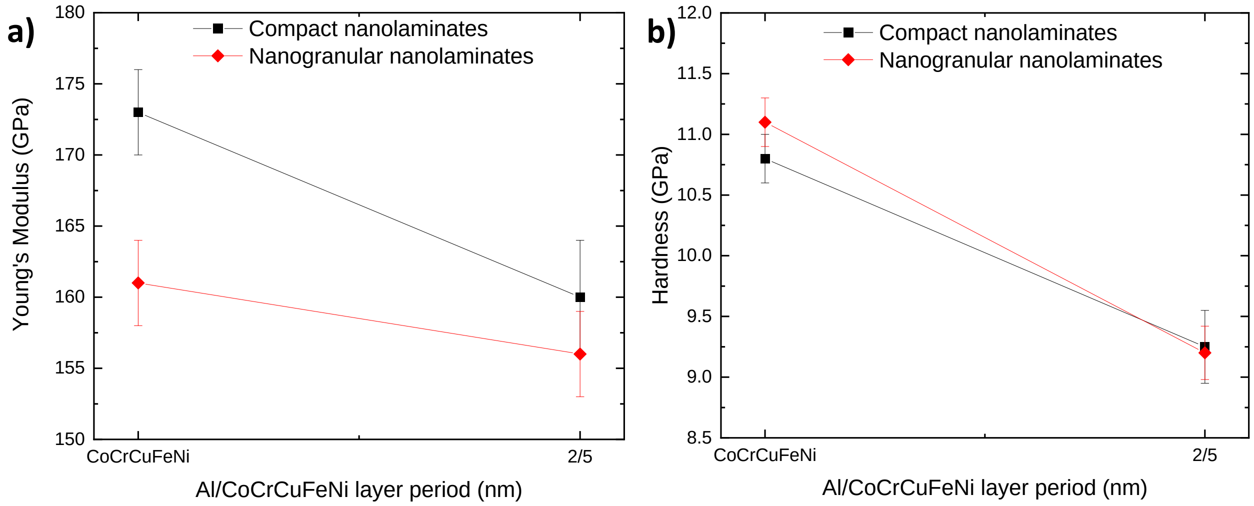

Figure 8.9: *(a) Young's modulus and (b) hardness of the Al/CoCrCuFeNi nanolaminates with base CoCrCuFeNi films.*

In parallel to the study of the PLD nanolaminates, MS $Al_x(CoCrCuFeNi)_{100-x}$ with Al content between 10 and 32 %at. are being studied to observe the effects of Al on the local structure and mechanical properties of the films in order to choose new compositions for the targets for PLD. The preliminary results on the effects of Al on the structure and mechanical properties of $Al_x(CoCrCuFeNi)_{100-x}$ are presented in Figure 8.10.

The XRD patterns of Figure 8.10a show that $Al_x(CoCrCuFeNi)_{100-x}$ keeps a FCC crystalline structure up to 15 %at. Al and then forms a BCC/FCC mixed phase for 15 < Al %at. < 22 which becomes full BCC for x > 22 %at. Al since Al has bigger atomic radius when compared to Co, Cr, Cu, Fe and Ni and distorts the crystalline lattice of CoCrCuFeNi forcing it to transform in a BCC structure with lower packing factor [124].

This affects the *H* of the films, as shown in Figure 8.10b, which is initially reduced since Al has lower mechanical properties than the base quinary alloy but then *H* increases up to 8.8 - 8.9 GPa when the crystalline structure fully transforms in a BCC phase which is harder but less ductile than the FCC phase due to the lower number of dislocation movement planes available [250, 252].

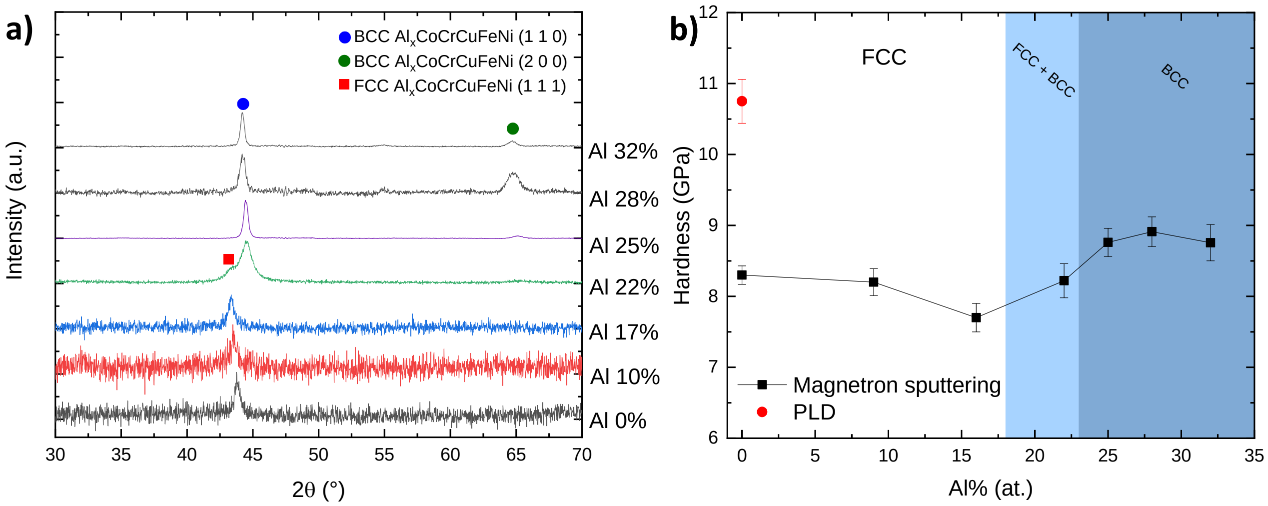

Figure 8.10: *(a) XRD diffraction patterns of MS $Al_x(CoCrCuFeNi)_{100-x}$, and (b) hardness of of MS $Al_x(CoCrCuFeNi)_{100-x}$ as a function of the Al content associating the Al content with the different phases.*

The new hard BCC phase is then combined with ductile FCC Al in multilayers to improve the total properties of the system by introducing incoherent FCC/BCC interfaces which can interfere with the movement of dislocations in the material increasing the strength of the multilayer while the soft Al layers deform homogeneously preventing localized brittle deformation[253]. As an example, in Figure 8.11 the results of the compression of a MS50/50 nm $Al/Al_{25}(CoCrCuFeNi)_{75}$ FCC/BCC pillars are reported.

The pillar yields at 2.4 GPa and it can deform homogeneously up to 30% strain, as shown from Figures 8.11a-c, a combination of strength and plasticity that would be impossible for the single components of the multilayer. The study of the MS films will help to select the most interesting combinations which will be then deposited by PLD in the future.

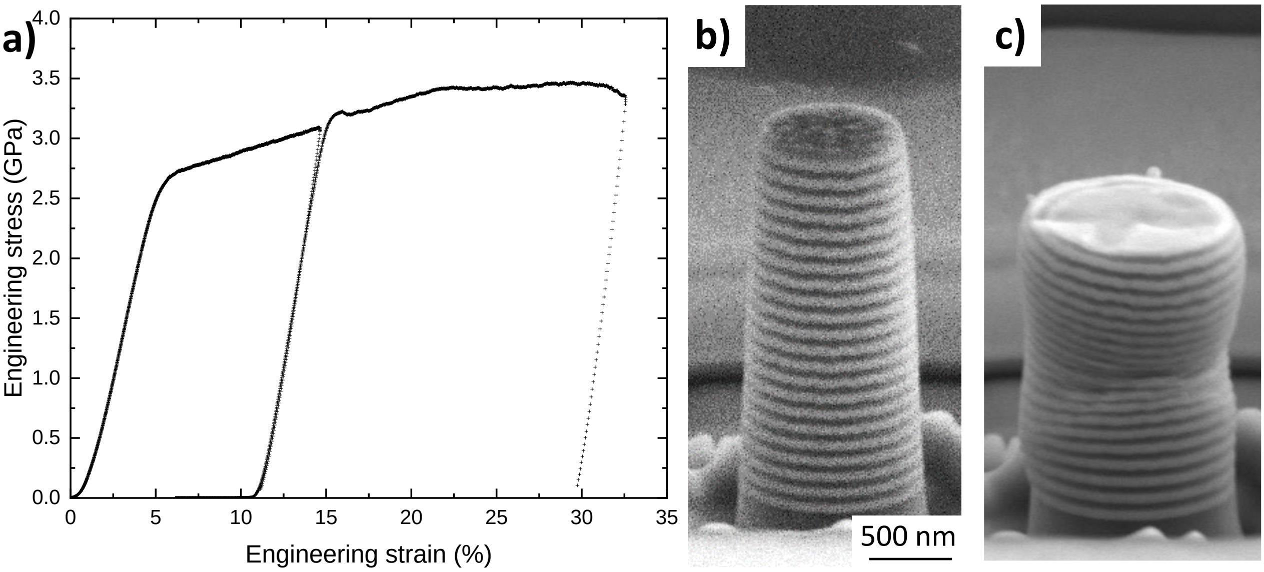

Figure 8.11: *(a) Engineering stress vs engineering strain curves of the MS M S50/50 nm Al/*$Al_{25}(CoCrCuFeNi)_{75}$ *FCC/BCC pillar and (b,c) SEM images of the micropillar before and after compression.*

Lastly, the relationship between *H* and grain size of the PLD CoCrCuFeNi will continue to be studied through the annealing of the films to favor the growth of the grains to see if the *H* of the annealed films will diminish the following the Hall-Petch relationship or new phases unique to the PLD process will emerge during annealing.

Chapter IX – Conclusions & future perspectives

The versatility of Pulsed Laser Deposition (PLD) has been exploited to produce nanostructured TFMGs and TFHEAs by changing the deposition parameters in order to obtain films with improved and controllable mechanical properties with respect to traditional deposition methods like magnetron sputtering.

Different nanostructures including compact and cluster-assembled films obtained by changing the deposition pressure, crystalline amorphous nanolaminates and fine control of the chemical composition were used to produce thin films with improved mechanical properties.

Chapter IV has been dedicated to the study $Zr_{50}Cu_{50}$ and $Zr_{46}Cu_{46}Al_8$ TFMGs deposited by PLD in vacuum and 5 Pa He to obtain compact and nanogranular morphologies. This Chapter highlights how the high density of PLD films with respect to traditionally sputtered TFMGs grant larger strength to the PLD TFMGs how the change in morphology from compact to nanogranular can double the plastic deformation necessary for SB propagation (from 3% to 6%) by preventing the maturation of SBs.

Chapter V has been used to expose the results on the $Zr_{50}Cu_{50}$/Al amorphous/crystalline nanolaminates deposited in vacuum and 5 Pa He to deposit compact and nanogranular morphologies studying in detail the nanolayered structure and the interaction between different nanostructuring strategies (nanolayering and nanoclustering). The presence of interfaces blocks the propagation of SBs increasing the strength of material and when the nanolayering is associated with the nanogranular structure large deformation values (up to 15%) can be achieved since the two nanostructures can work together to suppress the SB propagation.

Chapter VI has been dedicated to the structure and properties of $Zr_{50}Cu_{50}$ and $Zr_{46}Cu_{46}Al_8$ films deposited in higher vacuum baseline ($2x10^{-3}$ Pa) with respect to the films of **Chapter IV** to incorporate the O inside compact and nanogranular films to further control the amount of local heterogeneities in the structure. These films possess a dual phase amorphous structure of Zr-O rich and Cu-rich phases which seem to be organized as a self-assembled nanolayered structure which has quite high Young's modulus and hardness (10 GPa) with respect to the TFMGs without O of **Chapter IV**. The combination of O incorporation and cluster-assembled structure also show extremely high values of plastic deformation in compression (15%) possibly due to high amount of free volume present in these films similarly to other oxides like SiO_2 in literature.

Chapter VII has presented the preliminary results regarding the compact/nanogranular fully amorphous $Zr_{50}Cu_{50}$ multilayers deposited by PLD with bilayer period between 200 and 400 nm. Structural characterization from SEM and XRD confirms the amorphous structure of the multilayers showing cross-sections with straight interfaces between the different layers each having a specific corrugation imprint. The elastic moduli and hardness of the multilayers seem to be independent from the bilayer period and remain around 121 and 8.6 GPa. The study of this class of multilayers is still at its beginnings and the possible future characterizations of this materials will be expanded in Future Perspectives section.

Chapter VIII has been used to present the local structure and mechanical properties of CoCrCuFeNi HEAs deposited by PLD in different morphologies (i.e. compact and nanogranular) and compared them with MS CoCrCuFeNi. The change of deposition pressure allows to control the grain size and texturing of the PLD films which have smaller grains with respect to the sputtered films deposited for comparison purposes. PLD films have higher hardness (11 GPa) than the sputtered films (8.3 GPa) due to their lower grain size and possess higher plasticity and toughness as shown in the tensile tests on polymer substrate.

9.1 Main conclusions

This project has successfully demonstrated the versatility of PLD in producing thin film metallic glasses (TFMGs) with vastly different nanostructures, ranging from the local fluctuations in chemistry and density related to cluster-assembled growth to fine multilayered structures with sublayer thicknesses < 10 nm and dual-phase amorphous oxide – metallic glass systems.

A common characteristic of these TFMGs deposited by PLD is their high mass density with respect to traditional MS counterparts which is related to the high kinetic energy of the particles in the PLD plasma plume. This high density improves the mechanical performances of the films obtaining high values of elastic moduli and hardness while the different nanostructures allow to finely tune the strength and the deformation behavior delaying or suppressing the propagation of shear bands.

To show in a quantitative way the level of mechanical performance of the PLD films and nanolaminates their normalized shear strength τ_y/G (τ_y is calculated as $\sigma_y/2$ [254], G = shear modulus) vs homogeneous deformation are shown in Figure 9.1. and compared to MS TFMGs found in literature [67, 206, 255].

PLD compact $Zr_{50}Cu_{50}$ and $Zr_{46}Cu_{46}Al_8$ have similar normalized shear strengths values equal to $35*10^{-3}$ and $34*10^{-3}$ respectively and homogeneous deformations equal to 3% and 4% respectively. These values are much higher than the normalized strengths and homogeneous deformations found in literature for TFMGs thanks to the larger density related to the high kinetic energy of the particles in the PLD plasma plume which leads to improved elastic and plastic properties. The transition from compact to nanogranular PLD TFMGs increases the homogeneous deformation achievable before SB propagation reaching values equal to 6% for nanogranular $Zr_{50}Cu_{50}$ and 6.7% for nanogranular $Zr_{46}Cu_{46}Al_8$ while keeping similar values of normalized strengths. This is possible thanks to the larger amount of free volume present in the nanogranular structure with respect to the compact one and the presence of local fluctuations of density in the nanogranular structure which prevent the maturation of STZs in a single big SB and instead create multiple small SBs promoting a less localized deformation.

The incorporation of O in the PLD films further increases both the normalized strength and homogeneous deformation with compact $Zr_{50}Cu_{50}/O$ and $Zr_{46}Cu_{46}Al_8/O$ reaching normalized strength values around $47*10^{-3}$-$48*10^{-3}$, a value near the half of the theoretical strength reported in literature for ceramics and glasses [256], and deformation values ranging from 4.4% for $Zr_{50}Cu_{50}/O$ to 6% for $Zr_{46}Cu_{46}Al_8/O$.

The transition from compact to nanogranular $Zr_{50}Cu_{50}/O$ and $Zr_{46}Cu_{46}Al_8/O$ drastically increases the plasticity of the PLD films reaching homogeneous deformation values > 15% without formation of SBs while keeping normalized strengths around $45*10^{-3}$ due to the combination of the nanogranular morphology and the structure of O-rich and Cu-rich phases resulting in large amounts of free volume able to suppress SB formation.

This improved plasticity can be related to densification of the structure during the compression combined with shear flow mediated by uniformly distributed STZs which do not coalesce into SBs until the free volume is annihilated.

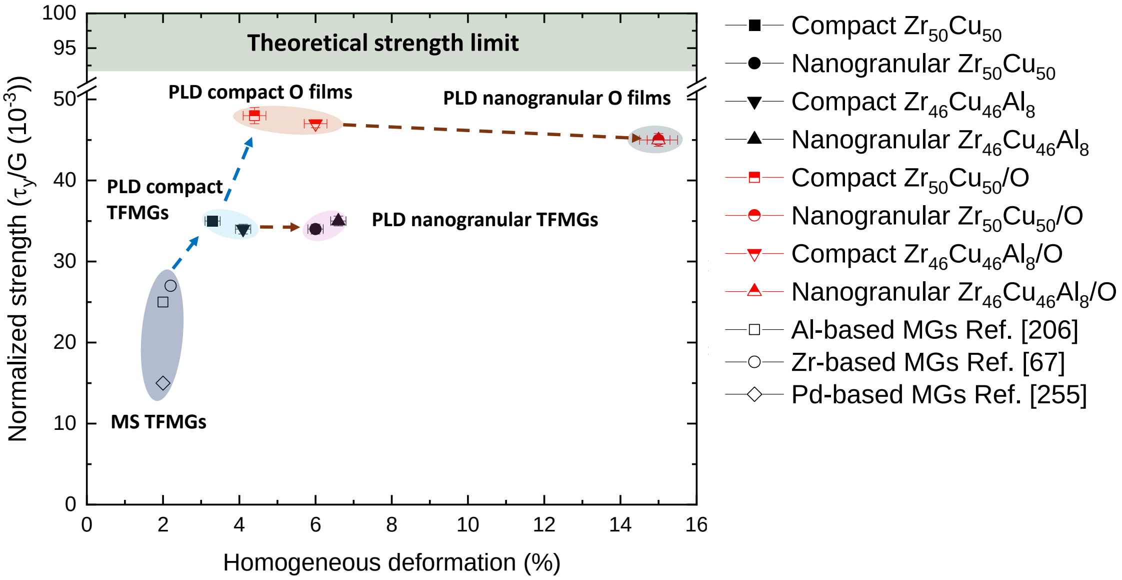

Figure 9.1: *Map of the normalized strength vs homogeneous deformation comparing PLD TFMGs with and without O with traditional MGs fabricated by MS.*

The normalized strength of PLD nanolaminates is shown in Figure 9.2 compared to MS TFMGs found in literature [67, 206, 255], MS multilayers with a similar bilayer period to the PLD nanolaminates alternating amorphous/crystalline sublayers [54, 182], fully crystalline metallic nanolaminates [141] and crystalline metal/ceramic nanolaminates [50, 201]. PLD U-NLs have very high τ_y/G values equal to $37*10^{-3}$ for compact U-NLs and $34*10^{-3}$ for the nanogranular U-NLs, which are roughly half the theoretical strength limit for metallic materials [16] and comparable to the PLD TFMGs of Figure 9.1 and above traditional MS nanolaminates and multilayers. The presence of interfaces confining and deviating the SBs developing in the amorphous layers improves the plasticity of compact nanolaminates with respect to compact $Zr_{50}Cu_{50}$ (3.6% vs 3%). Most importantly the nanogranular nanolaminates prevent the propagation of mature SB events thanks to the combination of the inter-layer chemical heterogeneities and the intra-layer density fluctuations related to the cluster assembled growth developing only superficial non percolative shear bands even for deformations >15%.

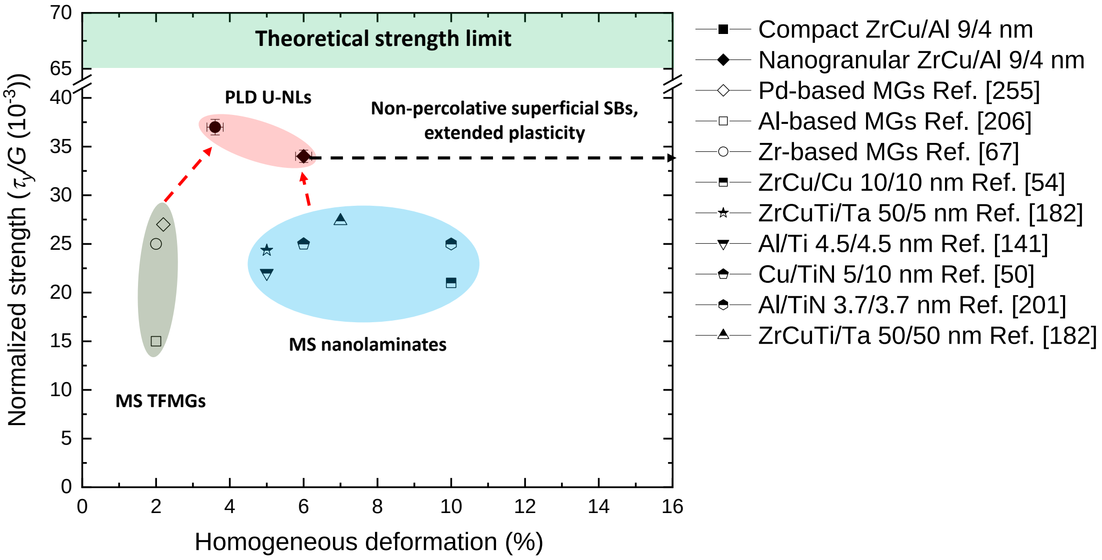

Figure 9.2: *Map of the normalized strength vs homogeneous deformation comparing PLD nanolaminates with MGs and crystalline/amorphous multilayers fabricated by MS reported in the literature. A black dashed arrow indicates the interval of extended plasticity of the nanogranular U-NLs in which only superficial non-percolative SBs appears.*

Figures 9.1 and 9.2 overall demonstrate the strength of the amorphous films deposited by PLD with respect to traditional MS and how the plasticity can be controlled by changing the local structure of the films by simply controlling the deposition parameters like deposition pressure and the vacuum level of the chamber.

The study of CoCrCuFeNi TFHEAs deposited by PLD has yielded great results showing that it is possible to control the crystalline structure by changing the deposition pressure tuning the grain size and degree of oriented growth. This allows to control the stiffness of the PLD films and the smaller grain size of PLD CoCrCuFeNi with respect to its MS counterparts confers to PLD CoCrCuFeNi larger values of hardness. PLD CoCrCuFeNi has also demonstrated remarkable ductility in tension when coupled with a polymer substrate reaching crack onset strains as big as 3.44% combined with large toughness and film – substrate adhesion with respect to MS counterparts making them good candidates for industrial applications.

Overall, this project shows that PLD can synthesize metallic glasses and high entropy alloys possessing superior and controllable mechanical properties when compared to traditional deposition methods like magnetron sputtering.

In the case of metallic glasses, the different nanostructures offered by PLD were able to delay or completely suppress localized plastic failure mediated by shear banding, their main weakness in practical applications, and instead promote a more homogeneous deformation which reached quite large strain values when multiple nanostructures worked together making them interesting for high performance structural coatings.

In the case of high entropy alloys the initial results presented in this project show a great potential for PLD to deposit films with different grain size and preferential orientation to which correspond improved mechanical properties making them interesting for applications as protection coatings and in flexible electronics.

9.2 Future perspectives

While this project has strived to study in detail the correlation between structure and mechanical properties of nanostructured metallic glasses and high entropy alloys deposited by PLD there are still some unanswered questions that could be examined in the future.

On a short-term timespan, the local structure of PLD TFMGs with and without O still needs a deeper study and for this reason advanced TEM characterization would be able to observe fine differences in the atomic structure of the PLD films. In parallel a synchrotron X-ray diffraction (s-XRD) campaign is in progress to study the short and medium range order of the PLD $Zr_{50}Cu_{50}$ and $Zr_{46}Cu_{46}Al_8$ films and compare it to their MS counterparts which will be associated to *ab initio* molecular dynamics to fully map the different local orders related to the PLD nanostructures.

The mechanical characterization of PLD $Zr_{50}Cu_{50}$/O and $Zr_{46}Cu_{46}Al_8$/O films in both morphologies will also be continued with micropillar compression tests performed with the SEM beam off to confirm definitively that the high degree of plasticity observed is not an extrinsic effect related to the electron beam, something that can happen in other oxides like SiO_2 [222]. The experiments will be done at LSPM which recently acquired a new advanced *in situ* SEM nanoindenter from FemtoTools to further advance the quality of the mechanical characterizations performed in the laboratory.

The study of TFHEAs deposited by PLD is being continued at USPN in the project MICRO-scale mechanical characterization of advanced thin film High Entropy Alloys (MICRO-HEAs) which focuses on the production and characterization of nanostructured HEA films by PLD and MS focusing on multilayers combining FCC CoCrCuFeNi, FCC Al and BCC AlCoCrCuFeNi with different bilayer periods.

The project aims to continue the collaboration between Nanolab and LSPM is studying Al/CoCrCuFenNi PLD multilayers with different bilayer periods to optimize their mechanical properties and continuing the characterization of base PLD CoCrCuFeNi by examining its fatigue behavior and the thermal stability of the crystalline structure following the grain growth and phase separation.

There is also a focus on magnetron sputtered Al/AlCoCrCuFeNi and Al/CoCrCuFenNi to observe the effect of coherent (FCC/FCC) and incoherent (FCC/BCC) interfaces on the mechanical behavior of the films.

On a long-term timespan, the study of the mechanical properties of the compact/nanogranular PLD multilayers could be continued with micropillar compression characterization to study the plastic behavior of the films and observe how the different sublayers contribute to the strength and total plastic deformation.

New bilayer periods <200 nm could be deposited to try to observe if the increasing number of interfaces can change the mechanical properties of the multilayer.

The thermal stability and the evolution of the mechanical properties of PLD TFMGs as a function of the annealing temperature could be examined to use annealing as a nanostructuring strategy to improve the mechanical properties of the films by causing the recrystallization of specific phases in multilayers and controlling the free volume content.

Lastly, in order to get closer to a possible application of the amorphous nanostructures studied in this project it would be interesting to try to replicate them with large scale MS systems able to cover uniformly large areas, something extremely difficult if not impossible with PLD.

In this field high power impulse magnetron sputtering (HiPIMS) can use high voltage short duration pulses of energy to ionize the material sputtered from the target increasing its kinetic energy to levels similar to the one of PLD plasma plume [257] allowing to replicate the deposition conditions of compact films and, with the correct calibrations, deposit nanogranular films continuing the collaboration between LSPM and Nanolab.

The future applications of these new films would range from structural protective coating in harsh and difficult environments to applications in electronics, flexible and non-flexible.

Bibliography

[1] C. Suryanarayana, A. Inoue, Bulk metallic glasses, CRC press2017.

[2] P. Chaudhari, D. Turnbull, Structure and properties of metallic glasses, Science 199(4324) (1978) 11-21.

[3] A.L. Greer, Metallic glasses… on the threshold, Mater. Today 12(1-2) (2009) 14-22.

[4] Y.H. Liu, G. Wang, R.J. Wang, D.Q. Zhao, M.X. Pan, W.H. Wang, Super plastic bulk metallic glasses at room temperature, Science 315(5817) (2007) 1385-1388.

[5] E. Ma, Z. Zhang, Reflections from the glass maze, Nat. Mater. 10(1) (2011) 10-11.

[6] L. Chen, Z. Fu, G. Zhang, X. Hao, Q. Jiang, X. Wang, Q. Cao, H. Franz, Y. Liu, H. Xie, New class of plastic bulk metallic glass, Phys. Rev. Lett. 100(7) (2008) 075501.

[7] P. Ossi, Disordered materials: an introduction, Springer Science & Business Media2010.

[8] Y. Cheng, E. Ma, Atomic-level structure and structure–property relationship in metallic glasses, Prog. Mater. Sci. 56(4) (2011) 379-473.

[9] H. Sheng, W. Luo, F. Alamgir, J. Bai, E. Ma, Atomic packing and short-to-medium-range order in metallic glasses, Nature 439(7075) (2006) 419-425.

[10] G. Guo, Quasi-icosahedral clusters in Zr-based metallic glasses, Metals - Basel 10(9) (2020) 1135.

[11] M. Celtek, S. Sengul, U. Domekeli, Glass formation and structural properties of Zr50Cu50-xAlx bulk metallic glasses investigated by molecular dynamics simulations, Intermetallics 84 (2017) 62-73.

[12] Y.Q. Cheng, H.W. Sheng, E. Ma, Relationship between structure, dynamics, and mechanical properties in metallic glass-forming alloys, Phys. Rev. B 78(1) (2008) 014207.

[13] A. Takeuchi, A. Inoue, Classification of bulk metallic glasses by atomic size difference, heat of mixing and period of constituent elements and its application to characterization of the main alloying element, Mater. Trans. 46(12) (2005) 2817-2829.

[14] O. Senkov, J. Scott, Specific criteria for selection of alloy compositions for bulk metallic glasses, Scripta Mater. 50(4) (2004) 449-452.

[15] M. Telford, The case for bulk metallic glass, Mater. Today 7(3) (2004) 36-43.

[16] M. Ashby, A.L. Greer, Metallic glasses as structural materials, Scripta Mater. 54(3) (2006) 321-326.

[17] S. Tao, T. Ma, H. Jian, Z. Ahmad, H. Tong, M. Yan, Glass forming ability, magnetic and mechanical properties of (Fe72Mo4B24) 100− xDyx (x= 4–7) bulk metallic glasses, Mater. Sci. Eng. A 528(1) (2010) 161-164.

[18] C.A. Schuh, T.C. Hufnagel, U. Ramamurty, Mechanical behavior of amorphous alloys, Acta Mater. 55(12) (2007) 4067-4109.

[19] M.M. Khan, A. Nemati, Z.U. Rahman, U.H. Shah, H. Asgar, W. Haider, Recent advancements in bulk metallic glasses and their applications: a review, Crit. Rev. Solid State 43(3) (2018) 233-268.

[20] A. Greer, K. Rutherford, I. Hutchings, Wear resistance of amorphous alloys and related materials, Int. Mater. Rev. 47(2) (2002) 87-112.

[21] S. Madge, A. Caron, R. Gralla, G. Wilde, S.K. Mishra, Novel W-based metallic glass with high hardness and wear resistance, Intermetallics 47 (2014) 6-10.

[22] J. Xu, U. Ramamurty, E. Ma, The fracture toughness of bulk metallic glasses, Jom-US 62 (2010) 10-18.

[23] J. Lewandowski*, W. Wang, A. Greer, Intrinsic plasticity or brittleness of metallic glasses, Phil. Mag. Lett. 85(2) (2005) 77-87.

[24] S. Madge, D. Louzguine-Luzgin, J. Lewandowski, A. Greer, Toughness, extrinsic effects and Poisson's ratio of bulk metallic glasses, Acta Mater. 60(12) (2012) 4800-4809.

[25] Y. Cheng, E. Ma, Intrinsic shear strength of metallic glass, Acta Mater. 59(4) (2011) 1800-1807.

[26] A.L. Greer, Y.Q. Cheng, E. Ma, Shear bands in metallic glasses, Mater. Sci. Eng. R 74(4) (2013) 71-132.

[27] A. Argon, Plastic deformation in metallic glasses, Acta Metall. 27(1) (1979) 47-58.

[28] D. Richard, G. Kapteijns, J.A. Giannini, M.L. Manning, E. Lerner, Simple and broadly applicable definition of shear transformation zones, Phys. Rev. Lett. 126(1) (2021) 015501.

[29] Y. Zhang, A.L. Greer, Thickness of shear bands in metallic glasses, Appl. Phys. Lett. 89(7) (2006) 071907.

[30] F. Shimizu, S. Ogata, J. Li, Yield point of metallic glass, Acta Mater. 54(16) (2006) 4293-4298.

[31] J. Lewandowski, A. Greer, Temperature rise at shear bands in metallic glasses, Nat. Mater. 5(1) (2006) 15-18.

[32] N. Nagendra, U. Ramamurty, T. Goh, Y. Li, Effect of crystallinity on the impact toughness of a La-based bulk metallic glass, Acta Mater. 48(10) (2000) 2603-2615.

[33] B. Sun, W. Wang, The fracture of bulk metallic glasses, Prog. Mater. Sci. 74 (2015) 211-307.

[34] J.R. Greer, J.T.M. De Hosson, Plasticity in small-sized metallic systems: Intrinsic versus extrinsic size effect, Prog. Mater. Sci. 56(6) (2011) 654-724.

[35] P. Yiu, W. Diyatmika, N. Bönninghoff, Y.-C. Lu, B.-Z. Lai, J.P. Chu, Thin film metallic glasses: Properties, applications and future, J. Appl. Phys. 127(3) (2020) 030901.

[36] P. Tandaiya, R. Narasimhan, U. Ramamurty, On the mechanism and the length scales involved in the ductile fracture of a bulk metallic glass, Acta Mater. 61(5) (2013) 1558-1570.

[37] C.A. Volkert, A. Donohue, F. Spaepen, Effect of sample size on deformation in amorphous metals, J. Appl. Phys. 103(8) (2008).

[38] Y. Shi, Size-dependent mechanical responses of metallic glasses, Int. Mater. Rev. 64(3) (2019) 163-180.

[39] D. Jang, J.R. Greer, Transition from a strong-yet-brittle to a stronger-and-ductile state by size reduction of metallic glasses, Nat. Mater. 9(3) (2010) 215-219.

[40] D. Tönnies, R. Maaß, C.A. Volkert, Room temperature homogeneous ductility of micrometer-sized metallic glass, Adv. Mater. 26(32) (2014) 5715-5721.

[41] Z. Han, W. Wu, Y. Li, Y. Wei, H. Gao, An instability index of shear band for plasticity in metallic glasses, Acta Mater. 57(5) (2009) 1367-1372.

[42] Y. Yang, C.T. Liu, Size effect on stability of shear-band propagation in bulk metallic glasses: an overview, J. Mater. Sci. 47 (2012) 55-67.

[43] B. Schuster, Q. Wei, T. Hufnagel, K. Ramesh, Size-independent strength and deformation mode in compression of a Pd-based metallic glass, Acta Mater. 56(18) (2008) 5091-5100.

[44] X. Wu, Y. Guo, Q. Wei, W. Wang, Prevalence of shear banding in compression of Zr41Ti14Cu12. 5Ni10Be22. 5 pillars as small as 150 nm in diameter, Acta Mater. 57(12) (2009) 3562-3571.

[45] A. Dubach, R. Raghavan, J.F. Löffler, J. Michler, U. Ramamurty, Micropillar compression studies on a bulk metallic glass in different structural states, Scripta Mater. 60(7) (2009) 567-570.

[46] C. Lee, J. Huang, T. Nieh, Sample size effect and microcompression of Mg65Cu25Gd10 metallic glass, Appl. Phys. Lett. 91(16) (2007).

[47] Y. Shi, Size-independent shear band formation in amorphous nanowires made from simulated casting, Appl. Phys. Lett. 96(12) (2010).

[48] X. Wang, F. Jiang, H. Hahn, J. Li, H. Gleiter, J. Sun, J. Fang, Sample size effects on strength and deformation mechanism of Sc75Fe25 nanoglass and metallic glass, Scripta Mater. 116 (2016) 95-99.

[49] A.F. Jankowski, Superhardness effect in Au/Ni multilayers, Journal of magnetism and magnetic materials 126(1-3) (1993) 185-191.

[50] R. Raghavan, J. Wheeler, D. Esqué-De los Ojos, K. Thomas, E. Almandoz, G. Fuentes, J. Michler, Mechanical behavior of Cu/TiN multilayers at ambient and elevated temperatures: Stress-assisted diffusion of Cu, Mater. Sci. Eng. A 620 (2015) 375-382.

[51] B. Clemens, H. Kung, S. Barnett, Structure and strength of multilayers, Mrs Bull. 24(2) (1999) 20-26.

[52] Y. Chen, R. Cui, J. Shen, G. Wang, Progress on the glassy-crystal laminates: from design, microstructure to deformation and future solutions, J. Mater. Sci. Technol. (2023).

[53] J.P. Chu, J. Jang, J. Huang, H. Chou, Y. Yang, J. Ye, Y. Wang, J. Lee, F. Liu, P. Liaw, Thin film metallic glasses: Unique properties and potential applications, Thin solid films 520(16) (2012) 5097-5122.

[54] J. Zhang, G. Liu, S. Lei, J. Niu, J. Sun, Transition from homogeneous-like to shear-band deformation in nanolayered crystalline Cu/amorphous Cu–Zr micropillars: Intrinsic vs. extrinsic size effect, Acta Mater. 60(20) (2012) 7183-7196.

[55] W. Guo, E. Jägle, J. Yao, V. Maier, S. Korte-Kerzel, J.M. Schneider, D. Raabe, Intrinsic and extrinsic size effects in the deformation of amorphous CuZr/nanocrystalline Cu nanolaminates, Acta Mater. 80 (2014) 94-106.

[56] I. Knorr, N. Cordero, E.T. Lilleodden, C.A. Volkert, Mechanical behavior of nanoscale Cu/PdSi multilayers, Acta Mater. 61(13) (2013) 4984-4995.

[57] S. Kuan, X. Du, H. Chou, J. Huang, Mechanical response of amorphous ZrCuTi/PdCuSi nanolaminates under nanoindentation, Surf. Coat. Tech. 206(6) (2011) 1116-1119.

[58] Z.Q. Chen, M.C. Li, J.S. Cao, F.C. Li, S.W. Guo, B.A. Sun, H.B. Ke, W.H. Wang, Interface dominated deformation transition from inhomogeneous to apparent homogeneous mode in amorphous/amorphous nanolaminates, J. Mater. Sci. Technol. 99 (2022) 178-183.

[59] P. Sharma, K. Yubuta, H. Kimura, A. Inoue, Brittle metallic glass deforms plastically at room temperature in glassy multilayers, Phys. Rev. B 80(2) (2009) 024106.

[60] J. Zhang, G. Liu, J. Sun, Crystallization-aided extraordinary plastic deformation in nanolayered crystalline Cu/amorphous Cu-Zr micropillars, Sci. Rep-UK 3(1) (2013) 2324.

[61] J.-Y. Kim, D. Jang, J.R. Greer, Nanolaminates Utilizing Size-Dependent Homogeneous Plasticity of Metallic Glasses, Adv. Funct. Mater. 21(23) (2011) 4550-4554.

[62] M. Liu, X. Du, I. Lin, H. Pei, J. Huang, Superplastic-like deformation in metallic amorphous/crystalline nanolayered micropillars, Intermetallics 30 (2012) 30-34.

[63] B. Cheng, J.R. Trelewicz, Design of crystalline-amorphous nanolaminates using deformation mechanism maps, Acta Mater. 153 (2018) 314-326.

[64] M. Liu, C. Lee, Y. Lai, J. Huang, Microscale deformation behavior of amorphous/nanocrystalline multilayered pillars, Thin solid films 518(24) (2010) 7295-7299.

[65] Y. Cui, P. Huang, F. Wang, T. Lu, K. Xu, The hardness and related deformation mechanisms in nanoscale crystalline–amorphous multilayers, Thin solid films 584 (2015) 270-276.

[66] C. Lee, H. Lin, J. Huang, S. Kuan, Tension behavior of free-standing amorphous film and amorphous–crystalline nanolaminates in submicron scale, Scripta Mater. 65(8) (2011) 695-698.

[67] S.Y. Kuan, H.S. Chou, M.C. Liu, X.H. Du, J.C. Huang, Micromechanical response for the amorphous/amorphous nanolaminates, Intermetallics 18(12) (2010) 2453-2457.

[68] Q. Zhou, Y. Du, Y. Ren, W. Kuang, W. Han, H. Wang, P. Huang, F. Wang, J. Wang, Investigation into nanoscratching mechanical performance of metallic glass multilayers with improved nano-tribological properties, J. Alloy Compd. 776 (2019) 447-459.

[69] X. Zhou, C. Chen, Strengthening and toughening mechanisms of amorphous/amorphous nanolaminates, Int. J. Plasticity 80 (2016) 75-85.

[70] C. Packard, C. Schuh, Initiation of shear bands near a stress concentration in metallic glass, Acta Mater. 55(16) (2007) 5348-5358.

[71] Y. Ivanisenko, C. Kübel, S.H. Nandam, C. Wang, X. Mu, O. Adjaoud, K. Albe, H. Hahn, Structure and properties of nanoglasses, Adv. Eng. Mater. 20(12) (2018) 1800404.

[72] H. Gleiter, Nanoglasses: a new kind of noncrystalline materials, Beilstein J. Nanotech. 4(1) (2013) 517-533.

[73] S.H. Nandam, Y. Ivanisenko, R. Schwaiger, Z. Śniadecki, X. Mu, D. Wang, R. Chellali, T. Boll, A. Kilmametov, T. Bergfeldt, Cu-Zr nanoglasses: Atomic structure, thermal stability and indentation properties, Acta Mater. 136 (2017) 181-189.

[74] S.H. Nandam, R. Schwaiger, A. Kobler, C. Kübel, C. Wang, Y. Ivanisenko, H. Hahn, Controlling shear band instability by nanoscale heterogeneities in metallic nanoglasses, J. Mater. Res. 36(14) (2021) 2903-2914.

[75] N. Chen, R. Frank, N. Asao, D. Louzguine-Luzgin, P. Sharma, J. Wang, G. Xie, Y. Ishikawa, N. Hatakeyama, Y. Lin, Formation and properties of Au-based nanograined metallic glasses, Acta Mater. 59(16) (2011) 6433-6440.

[76] N. Chen, D. Louzguine-Luzgin, G. Xie, P. Sharma, J. Perepezko, M. Esashi, A. Yavari, A. Inoue, Structural investigation and mechanical properties of a representative of a new class of materials: nanograined metallic glasses, Nanotechnology 24(4) (2013) 045610.

[77] J. Jing, A. Krämer, R. Birringer, H. Gleiter, U. Gonser, Modified atomic structure in a Pd・ Fe・ Si nanoglass: A Mössbauer study, J. Non-cryst. Solids 113(2-3) (1989) 167-170.

[78] M. Ghafari, S. Kohara, H. Hahn, H. Gleiter, T. Feng, R. Witte, S. Kamali, Structural investigations of interfaces in Fe90Sc10 nanoglasses using high-energy x-ray diffraction, Appl. Phys. Lett. 100(13) (2012).

[79] J.X. Fang, U. Vainio, W. Puff, R. Würschum, X.L. Wang, D. Wang, M. Ghafari, F. Jiang, J. Sun, H. Hahn, H. Gleiter, Atomic Structure and Structural Stability of Sc75Fe25 Nanoglasses, Nano Lett. 12(1) (2012) 458-463.

[80] C. Wang, D. Wang, X. Mu, S. Goel, T. Feng, Y. Ivanisenko, H. Hahn, H. Gleiter, Surface segregation of primary glassy nanoparticles of Fe90Sc10 nanoglass, Mater. Lett. 181 (2016) 248-252.

[81] O. Franke, D. Leisen, H. Gleiter, H. Hahn, Thermal and plastic behavior of nanoglasses, J. Mater. Res. 29(10) (2014) 1210-1216.
[82] Z. Wang, J. Pan, Y. Li, C.A. Schuh, Densification and strain hardening of a metallic glass under tension at room temperature, Phys. Rev. Lett. 111(13) (2013) 135504.
[83] A. Sharma, S. Hirmukhe, S.H. Nandam, H. Hahn, I. Singh, R.L. Narayan, K.E. Prasad, Strain rate sensitivity of a Cu60Zr40 metallic and nanoglass, J. Alloy Compd. 921 (2022) 165991.
[84] X.L. Wang, F. Jiang, H. Hahn, J. Li, H. Gleiter, J. Sun, J.X. Fang, Plasticity of a scandium-based nanoglass, Scripta Mater. 98 (2015) 40-43.
[85] D. Şopu, Y. Ritter, H. Gleiter, K. Albe, Deformation behavior of bulk and nanostructured metallic glasses studied via molecular dynamics simulations, Phys. Rev. B 83(10) (2011) 100202.
[86] S. Adibi, P.S. Branicio, Y.-W. Zhang, S.P. Joshi, Composition and grain size effects on the structural and mechanical properties of CuZr nanoglasses, J. Appl. Phys. 116(4) (2014).
[87] J.A. Thornton, The microstructure of sputter-deposited coatings, J. Vac. Sci. Technol. A 4(6) (1986) 3059-3065.
[88] J.T. Gudmundsson, A. Anders, A. von Keudell, Foundations of physical vapor deposition with plasma assistance, Plasma sources Sci. T. 31(8) (2022) 083001.
[89] H.U. Krebs, O. Bremert, Pulsed laser deposition of thin metallic alloys, Appl. Phys. Lett. 62(19) (1993) 2341-2343.
[90] C.S. Casari, A. LI BASSI, Pulsed laser deposition of nanostructured oxides: from clusters to functional films, J. Opt. 12(3/4) (2011) 1-37.
[91] M. Ghidelli, A. Orekhov, A. Li Bassi, G. Terraneo, P. Djemia, G. Abadias, M. Nord, A. Béché, N. Gauquelin, J. Verbeeck, J.P. Raskin, D. Schryvers, T. Pardoen, H. Idrissi, Novel class of nanostructured metallic glass films with superior and tunable mechanical properties, Acta Mater. 213 (2021) 116955.
[92] A. Brognara, J.P. Best, P. Djemia, D. Faurie, G. Dehm, M. Ghidelli, Effect of composition and nanostructure on the mechanical properties and thermal stability of Zr100-xCux thin film metallic glasses, Mater. Design 219 (2022) 110752.
[93] Y. Wu, D. Cao, Y. Yao, G. Zhang, J. Wang, L. Liu, F. Li, H. Fan, X. Liu, H. Wang, Substantially enhanced plasticity of bulk metallic glasses by densifying local atomic packing, Nat. Commun. 12(1) (2021) 6582.
[94] Y. Jien-Wei, Recent progress in high entropy alloys, Ann. Chim. Sci. Mat 31(6) (2006) 633-648.
[95] J.W. Yeh, S.K. Chen, S.J. Lin, J.Y. Gan, T.S. Chin, T.T. Shun, C.H. Tsau, S.Y. Chang, Nanostructured high-entropy alloys with multiple principal elements: novel alloy design concepts and outcomes, Adv. Eng. Mater. 6(5) (2004) 299-303.
[96] X. Wang, W. Guo, Y. Fu, High-entropy alloys: emerging materials for advanced functional applications, J. Mater. Chem. A 9(2) (2021) 663-701.
[97] B. Cantor, I. Chang, P. Knight, A. Vincent, Microstructural development in equiatomic multicomponent alloys, Mater. Sci. Eng. A 375 (2004) 213-218.
[98] J.-W. Yeh, S.-J. Lin, T.-S. Chin, J.-Y. Gan, S.-K. Chen, T.-T. Shun, C.-H. Tsau, S.-Y. Chou, Formation of simple crystal structures in Cu-Co-Ni-Cr-Al-Fe-Ti-V alloys with multiprincipal metallic elements, Metall. Mater. Trans. A 35 (2004) 2533-2536.
[99] C.-Y. Hsu, T.-S. Sheu, J.-W. Yeh, S.-K. Chen, Effect of iron content on wear behavior of AlCoCrFexMo0. 5Ni high-entropy alloys, Wear 268(5-6) (2010) 653-659.
[100] M.-H. Chuang, M.-H. Tsai, W.-R. Wang, S.-J. Lin, J.-W. Yeh, Microstructure and wear behavior of AlxCo1. 5CrFeNi1. 5Tiy high-entropy alloys, Acta Mater. 59(16) (2011) 6308-6317.
[101] X. Yan, Y. Zhang, Functional properties and promising applications of high entropy alloys, Scripta Mater. 187 (2020) 188-193.
[102] D.B. Miracle, J.D. Miller, O.N. Senkov, C. Woodward, M.D. Uchic, J. Tiley, Exploration and development of high entropy alloys for structural applications, Entropy 16(1) (2014) 494-525.
[103] J.-W. Yeh, Alloy design strategies and future trends in high-entropy alloys, Jom-US 65 (2013) 1759-1771.
[104] D.B. Miracle, O.N. Senkov, A critical review of high entropy alloys and related concepts, Acta Mater. 122 (2017) 448-511.
[105] A. Takeuchi, A. Inoue, Calculations of mixing enthalpy and mismatch entropy for ternary amorphous alloys, Mater. T. JIM 41(11) (2000) 1372-1378.

[106] Y. Zhang, Y.J. Zhou, J.P. Lin, G.L. Chen, P.K. Liaw, Solid-solution phase formation rules for multi-component alloys, Adv. Eng. Mater. 10(6) (2008) 534-538.
[107] S. Guo, Q. Hu, C. Ng, C. Liu, More than entropy in high-entropy alloys: Forming solid solutions or amorphous phase, Intermetallics 41 (2013) 96-103.
[108] Y. Ye, Q. Wang, J. Lu, C. Liu, Y. Yang, Design of high entropy alloys: A single-parameter thermodynamic rule, Scripta Mater. 104 (2015) 53-55.
[109] Y. Ye, Q. Wang, J. Lu, C. Liu, Y. Yang, High-entropy alloy: challenges and prospects, Mater. Today 19(6) (2016) 349-362.
[110] L.M. Martyushev, V.D. Seleznev, Maximum entropy production principle in physics, chemistry and biology, Phys. Rep. 426(1) (2006) 1-45.
[111] J.-W. Yeh, S.-Y. Chang, Y.-D. Hong, S.-K. Chen, S.-J. Lin, Anomalous decrease in X-ray diffraction intensities of Cu–Ni–Al–Co–Cr–Fe–Si alloy systems with multi-principal elements, Mater. Chem. Phys. 103(1) (2007) 41-46.
[112] B. Murty, JW Yeh i S. Ranganathan, High-Entropy Alloys, Elsevier, Amsterdam, 2014.
[113] K.-Y. Tsai, M.-H. Tsai, J.-W. Yeh, Sluggish diffusion in co–cr–fe–mn–ni high-entropy alloys, Acta Mater. 61(13) (2013) 4887-4897.
[114] E.P. George, W. Curtin, C.C. Tasan, High entropy alloys: A focused review of mechanical properties and deformation mechanisms, Acta Mater. 188 (2020) 435-474.
[115] W. Li, D. Xie, D. Li, Y. Zhang, Y. Gao, P.K. Liaw, Mechanical behavior of high-entropy alloys, Prog. Mater. Sci. 118 (2021) 100777.
[116] K.M. Youssef, A.J. Zaddach, C. Niu, D.L. Irving, C.C. Koch, A novel low-density, high-hardness, high-entropy alloy with close-packed single-phase nanocrystalline structures, Mater. Res. Lett. 3(2) (2015) 95-99.
[117] M.-R. Chen, S.-J. Lin, J.-W. Yeh, M.-H. Chuang, S.-K. Chen, Y.-S. Huang, Effect of vanadium addition on the microstructure, hardness, and wear resistance of Al 0.5 CoCrCuFeNi high-entropy alloy, Metall. Mater. Trans. A 37 (2006) 1363-1369.
[118] J.-M. Wu, S.-J. Lin, J.-W. Yeh, S.-K. Chen, Y.-S. Huang, H.-C. Chen, Adhesive wear behavior of AlxCoCrCuFeNi high-entropy alloys as a function of aluminum content, Wear 261(5-6) (2006) 513-519.
[119] O. Senkov, C. Woodward, D. Miracle, Microstructure and properties of aluminum-containing refractory high-entropy alloys, Jom-US 66 (2014) 2030-2042.
[120] Y. Shi, B. Yang, X. Xie, J. Brechtl, K.A. Dahmen, P.K. Liaw, Corrosion of Al xCoCrFeNi high-entropy alloys: Al-content and potential scan-rate dependent pitting behavior, Corros. Sci. 119 (2017) 33-45.
[121] Y. Shi, B. Yang, P.K. Liaw, Corrosion-resistant high-entropy alloys: A review, Metals - Basel 7(2) (2017) 43.
[122] W. Li, P. Liu, P.K. Liaw, Microstructures and properties of high-entropy alloy films and coatings: a review, Mater. Res. Lett. 6(4) (2018) 199-229.
[123] N.I. Muhammad Nadzri, D.S.C. Halin, M.M. Al Bakri Abdullah, S. Joseph, M.A.A. Mohd Salleh, P. Vizureanu, D.-P. Burduhos-Nergis, A.V. Sandu, High-Entropy Alloy for Thin Film Application: A Review, Coatings 12(12) (2022) 1842.
[124] C.-J. Tong, Y.-L. Chen, J.-W. Yeh, S.-J. Lin, S.-K. Chen, T.-T. Shun, C.-H. Tsau, S.-Y. Chang, Microstructure characterization of Al x CoCrCuFeNi high-entropy alloy system with multiprincipal elements, Metall. Mater. Trans. A 36 (2005) 881-893.
[125] B. Braeckman, F. Boydens, H. Hidalgo, P. Dutheil, M. Jullien, A.-L. Thomann, D. Depla, High entropy alloy thin films deposited by magnetron sputtering of powder targets, Thin solid films 580 (2015) 71-76.
[126] Z. An, H. Jia, Y. Wu, P.D. Rack, A.D. Patchen, Y. Liu, Y. Ren, N. Li, P.K. Liaw, Solid-solution CrCoCuFeNi high-entropy alloy thin films synthesized by sputter deposition, Mater. Res. Lett. 3(4) (2015) 203-209.
[127] D. Hardwick, The mechanical properties of thin films: a review, Thin solid films 154(1-2) (1987) 109-124.
[128] M. El Garah, P. Briois, F. Sanchette, Recent progress on high-entropy films deposited by magnetron sputtering, Crystals 12(3) (2022) 335.
[129] C.A. Schuh, K. Lu, Stability of nanocrystalline metals: The role of grain-boundary chemistry and structure, Mrs Bull. 46 (2021) 225-235.

[130] Y. Zou, H. Ma, R. Spolenak, Ultrastrong ductile and stable high-entropy alloys at small scales, Nat. Commun. 6(1) (2015) 1-8.

[131] Z. Wang, C. Wang, Y.-L. Zhao, T.-H. Huang, C.-L. Li, J.-J. Kai, C.-T. Liu, C.-H. Hsueh, Growth, microstructure and mechanical properties of CoCrFeMnNi high entropy alloy films, Vacuum 179 (2020) 109553.

[132] X. Li, Z. Zheng, D. Dou, J. Li, Microstructure and properties of coating of FeAlCuCrCoMn high entropy alloy deposited by direct current magnetron sputtering, Materials Research 19 (2016) 802-806.

[133] M. Hu, Q. Cao, X. Wang, D. Zhang, J.-Z. Jiang, Tuning nanostructure and mechanical property of Fe–Co–Ni–Cr–Mn high-entropy alloy thin films by substrate temperature, Materials Today Nano 15 (2021) 100130.

[134] J. Wang, A. Misra, An overview of interface-dominated deformation mechanisms in metallic multilayers, Current Opinion in Solid State and Materials Science 15(1) (2011) 20-28.

[135] G. Wu, C. Liu, A. Brognara, M. Ghidelli, Y. Bao, S. Liu, X. Wu, W. Xia, H. Zhao, J. Rao, Symbiotic crystal-glass alloys via dynamic chemical partitioning, Mater. Today 51 (2021) 6-14.

[136] S.G. Rao, R. Shu, S. Wang, R. Boyd, F. Giuliani, A. le Febvrier, P. Eklund, Thin film growth and mechanical properties of CrFeCoNi/TiNbZrTa multilayers, Mater. Design 224 (2022) 111388.

[137] E. Besozzi, D. Dellasega, A. Pezzoli, C. Conti, M. Passoni, M. Beghi, Amorphous, ultra-nano-and nano-crystalline tungsten-based coatings grown by Pulsed Laser Deposition: mechanical characterization by Surface Brillouin Spectroscopy, Mater. Design 106 (2016) 14-21.

[138] T.-W. Lu, C.-S. Feng, Z. Wang, K.-W. Liao, Z.-Y. Liu, Y.-Z. Xie, J.-G. Hu, W.-B. Liao, Microstructures and mechanical properties of CoCrFeNiAl0. 3 high-entropy alloy thin films by pulsed laser deposition, Appl. Surf. Sci. 494 (2019) 72-79.

[139] E.A. Laszlo, D. Crăciun, G. Dorcioman, G. Crăciun, V. Geantă, I. Voiculescu, D. Cristea, V. Crăciun, Characteristics of Thin High Entropy Alloy Films Grown by Pulsed Laser Deposition, Coatings 12(8) (2022) 1211.

[140] B. Braeckman, P. Djemia, F. Tetard, L. Belliard, D. Depla, Impurity-controlled film growth and elastic properties of CoCrCuFeNi thin films, Surf. Coat. Tech. 315 (2017) 475-483.

[141] Y. Zhang, R. Su, T. Niu, N. Richter, S. Xue, Q. Li, J. Ding, B. Yang, H. Wang, X. Zhang, Thermal stability and deformability of annealed nanotwinned Al/Ti multilayers, Scripta Mater. 186 (2020) 219-224.

[142] D.B. Chrisey, G.K. Hubler, Pulsed laser deposition of thin films, (1994).

[143] C.N. Afonso, J. Gonzalo, Pulsed laser deposition of thin films for optical applications, Nucl. Instrum. Meth. B 116(1-4) (1996) 404-409.

[144] M.J. Aziz, Film growth mechanisms in pulsed laser deposition, Appl. Phys. A 93 (2008) 579-587.

[145] B. Ngom, T. Mpahane, N. Manyala, O. Nemraoui, U. Buttner, J. Kana, A. Fasasi, M. Maaza, A. Beye, Structural and optical properties of nano-structured tungsten-doped ZnO thin films grown by pulsed laser deposition, Appl. Surf. Sci. 255(7) (2009) 4153-4158.

[146] A. Hussein, P. Diwakar, S. Harilal, A. Hassanein, The role of laser wavelength on plasma generation and expansion of ablation plumes in air, J. Appl. Phys. 113(14) (2013).

[147] P. Willmott, J. Huber, Pulsed laser vaporization and deposition, Rev. Mod. Phys. 72(1) (2000) 315.

[148] A. Maffini, A. Pazzaglia, D. Dellasega, V. Russo, M. Passoni, Growth dynamics of pulsed laser deposited nanofoams, Phys. Rev. Mater. 3(8) (2019) 083404.

[149] A. Macrelli, M. Olivieri, A. Lamperti, V. Russo, B. Bozzini, M. Menegazzo, G. Bussetti, C.S. Casari, A.L. Bassi, Nanostructured ZnxMn3–xO4 thin films by pulsed laser deposition: A spectroscopic and electrochemical study towards the application in aqueous Zn-ion batteries, Electrochim. Acta 442 (2023) 141909.

[150] J.T. Gudmundsson, D. Lundin, Introduction to magnetron sputtering, High power impulse magnetron sputtering, Elsevier2020, pp. 1-48.

[151] O. Rachek, X-ray diffraction study of amorphous alloys Al–Ni–Ce–Sc with using Ehrenfest's formula, J. Non-cryst. Solids 352(36-37) (2006) 3781-3786.

[152] C.G. Pope, X-ray diffraction and the Bragg equation, J. Chem. Educ. 74(1) (1997) 129.

[153] A. Monshi, M.R. Foroughi, M.R. Monshi, Modified Scherrer equation to estimate more accurately nano-crystallite size using XRD, World j. Nano sci. Eng. 2(3) (2012) 154-160.

[154] L.G. Parratt, Surface studies of solids by total reflection of X-rays, Phys. Rev. 95(2) (1954) 359.

[155] P. Djemia, F. Ganot, P. Moch, V. Branger, P. Goudeau, Brillouin scattering investigation of elastic properties of Cu–Mo solid solution thin films, J. Appl. Phys. 90(2) (2001) 756-762.

[156] A. Kueny, M. Grimsditch, Surface waves in a layered material, Phys. Rev. B 26(8) (1982) 4699.

[157] C. Thomsen, J. Strait, Z. Vardeny, H.J. Maris, J. Tauc, J.J. Hauser, Coherent Phonon Generation and Detection by Picosecond Light Pulses, Phys. Rev. Lett. 53(10) (1984) 989-992.

[158] W.C. Oliver, G.M. Pharr, An improved technique for determining hardness and elastic modulus using load and displacement sensing indentation experiments, J. Mater. Res. 7(6) (2011) 1564-1583.

[159] W.C. Oliver, G.M. Pharr, Measurement of hardness and elastic modulus by instrumented indentation: Advances in understanding and refinements to methodology, J. Mater. Res. 19(1) (2004) 3-20.

[160] C.H. Li, R. Dedoncker, L.W. Li, F. Sedghgooya, F. Zighem, V. Ji, D. Depla, P. Djemia, D. Faurie, Mechanical properties of CoCrCuFeNi multi-principal element alloy thin films on Kapton substrates, Surf. Coat. Tech. 402 (2020) 126474.

[161] M. Gueye, P. Lupo, F. Zighem, D. Faurie, M. Belmeguenai, A.O. Adeyeye, Unambiguous magnetoelastic effect on residual anisotropy in thin films deposited on flexible substrates, Europhys. Lett. 114(1) (2016) 17003.

[162] J. Beuth Jr, Cracking of thin bonded films in residual tension, International Journal of Solids and Structures 29(13) (1992) 1657-1675.

[163] F.F. Schlich, R. Spolenak, Size-and phase-dependent mechanical properties of ultrathin Si films on polyimide substrates, Acta Mater. 110 (2016) 122-130.

[164] H. Guo, P.F. Yan, Y.B. Wang, J. Tan, Z.F. Zhang, M.L. Sui, E. Ma, Tensile ductility and necking of metallic glass, Nat. Mater. 6(10) (2007) 735-739.

[165] M. Ghidelli, H. Idrissi, S. Gravier, J.-J. Blandin, J.-P. Raskin, D. Schryvers, T. Pardoen, Homogeneous flow and size dependent mechanical behavior in highly ductile Zr65Ni35 metallic glass films, Acta Mater. 131 (2017) 246-259.

[166] R. Ramachandramoorthy, F. Yang, D. Casari, M. Stolpe, M. Jain, J. Schwiedrzik, J. Michler, J.J. Kruzic, J.P. Best, High strain rate in situ micropillar compression of a Zr-based metallic glass, J. Mater. Res. 36 (2021) 2325-2336.

[167] C. Poltronieri, A. Brognara, F. Bignoli, S. Evertz, P. Djemia, D. Faurie, F. Challali, C. Li, L. Belliard, G. Dehm, J.P. Best, M. Ghidelli, Mechanical properties and thermal stability of ZrCuAlx thin film metallic glasses: Experiments and first-principle calculations, Acta Mater. 258 (2023) 119226.

[168] M. Ghidelli, S. Gravier, J.-J. Blandin, J.-P. Raskin, F. Lani, T. Pardoen, Size-dependent failure mechanisms in ZrNi thin metallic glass films, Scripta Mater. (89) (2014) 4.

[169] M. Apreutesei, C. Esnouf, A. Billard, P. Steyer, Impact of local nanocrystallization on mechanical properties in the Zr-59 at.% Cu metallic glass thin film, Mater. Design 108 (2016) 8-12.

[170] M. Ghidelli, S. Gravier, J.J. Blandin, P. Djemia, F. Mompiou, G. Abadias, J.P. Raskin, T. Pardoen, Extrinsic mechanical size effects in thin ZrNi metallic glass films, Acta Mater. 90 (2015) 232-241.

[171] J. Das, M.B. Tang, K.B. Kim, R. Theissmann, F. Baier, W.H. Wang, J. Eckert, “Work-hardenable” ductile bulk metallic glass, Phys. Rev. Lett. 94(20) (2005) 205501.

[172] T. Cheung, C. Shek, Thermal and mechanical properties of Cu–Zr–Al bulk metallic glasses, J. Alloy Compd. 434 (2007) 71-74.

[173] N. Barekar, S. Pauly, R. Kumar, U. Kühn, B. Dhindaw, J. Eckert, Structure–property relations in bulk metallic Cu–Zr–Al alloys, Mater. Sci. Eng. A 527(21-22) (2010) 5867-5872.

[174] V. Apakina, A. Karuzskii, M. Kogan, A. Kvit, N. Melnik, Y.A. Mityagin, V. Murzin, A. Orlikovsky, A. Perestoronin, S. Tkachenko, Studies of nanoscale structure and its transformation in pulsed-laser deposited dense diamond-like carbon films, Diam. Relat. Mater. 6(5-7) (1997) 564-568.

[175] R. Limbach, K. Kosiba, S. Pauly, U. Kühn, L. Wondraczek, Serrated flow of CuZr-based bulk metallic glasses probed by nanoindentation: Role of the activation barrier, size and distribution of shear transformation zones, J. Non-cryst. Solids 459 (2017) 130-141.

[176] P. Yu, H.Y. Bai, Poisson's ratio and plasticity in CuZrAl bulk metallic glasses, Mater. Sci. Eng. A 485(1-2) (2008) 1-4.

[177] Y.Q. Cheng, A.J. Cao, H.W. Sheng, E. Ma, Local order influences initiation of plastic flow in metallic glass: Effects of alloy composition and sample cooling history, Acta Mater. 56(18) (2008) 5263-5275.

[178] M.H. Abbasi, S.G. Shabestari, R. Tavakoli, On the glass-forming ability of (Zr0.5Cu0.5)100−xAlx ternary alloys: A molecular dynamics study, Mater. Today Commun. 31 (2022) 103474.

[179] E. Besozzi, D. Dellasega, V. Russo, C. Conti, M. Passoni, M.G. Beghi, Thermomechanical properties of amorphous metallic tungsten-oxygen and tungsten-oxide coatings, Mater. Design 165 (2019) 107565.

[180] Y. Yang, J. Ye, J. Lu, F. Liu, P. Liaw, Effects of specimen geometry and base material on the mechanical behavior of focused-ion-beam-fabricated metallic-glass micropillars, Acta Mater. 57(5) (2009) 1613-1623.

[181] J. Ye, J. Chu, Y. Chen, Q. Wang, Y. Yang, Hardness, yield strength, and plastic flow in thin film metallic-glass, J. Appl. Phys. 112(5) (2012).

[182] H. Chou, X. Du, C. Lee, J. Huang, Enhanced mechanical properties of multilayered micropillars of amorphous ZrCuTi and nanocrystalline Ta layers, Intermetallics 19(7) (2011) 1047-1051.

[183] Y. Ritter, D. Şopu, H. Gleiter, K. Albe, Structure, stability and mechanical properties of internal interfaces in Cu64Zr36 nanoglasses studied by MD simulations, Acta Mater. 59(17) (2011) 6588-6593.

[184] A. Bhattacharyya, G. Singh, K.E. Prasad, R. Narasimhan, U. Ramamurty, On the strain rate sensitivity of plastic flow in metallic glasses, Mater. Sci. Eng. A 625 (2015) 245-251.

[185] B.P. Sahu, A. Dutta, R. Mitra, Mechanism of negative strain rate sensitivity in metallic glass film, J. Alloy Compd. 784 (2019) 488-499.

[186] A. Dubach, F.H. Dalla Torre, J.F. Löffler, Constitutive model for inhomogeneous flow in bulk metallic glasses, Acta Mater. 57(3) (2009) 881-892.

[187] R. Ramachandramoorthy, J. Schwiedrzik, L. Petho, C. Guerra-Nunez, D. Frey, J.-M. Breguet, J. Michler, Dynamic plasticity and failure of microscale glass: Rate-dependent ductile–brittle–ductile transition, Nano Lett. 19(4) (2019) 2350-2359.

[188] H. Li, G. Subhash, X.-L. Gao, L.J. Kecskes, R.J. Dowding, Negative strain rate sensitivity and compositional dependence of fracture strength in Zr/Hf based bulk metallic glasses, Scripta Mater. 49(11) (2003) 1087-1092.

[189] A. Dubach, F.H. Dalla Torre, J.F. Löffler, Deformation kinetics in Zr-based bulk metallic glasses and its dependence on temperature and strain-rate sensitivity, Phil. Mag. Lett. 87(9) (2007) 695-704.

[190] Y. Gu, X. Han, F. Yan, L. Li, The Strain Rate Sensitivity of Heterogeneous Thin Film Metallic Glasses: Interplay Between Nanoscale Heterogeneity and Dynamic Plasticity, Frontiers in Materials 9 (2022) 925096.

[191] D. Pan, A. Inoue, T. Sakurai, M.W. Chen, Experimental characterization of shear transformation zones for plastic flow of bulk metallic glasses, P. Natl. Acad. Sci. 105(39) (2008) 14769-14772.

[192] S.A. Husain, P. Kreiml, C. Trost, D. Faurie, M. Cordill, P.-O. Renault, Residual stress and thickness effects on fracture behavior of trilayer films during uniaxial loading, Thin solid films 788 (2024) 140173.

[193] K. Wu, Y.Q. Wang, H.Z. Yuan, J.Y. Zhang, G. Liu, J. Sun, Fragmentation and adhesion properties of Cu-Zr amorphous thin films on polyimide substrates, Phil. Mag. Lett. 98(10) (2018) 464-472.

[194] A.B. Behboud, A. Motallebzadeh, S. Özerinç, Nanoheterogeneous ZrTa metallic glass thin films with high strength and toughness, J. Alloy Compd. 901 (2022) 163578.

[195] C.-L. Li, J.P. Chu, J.-W. Lee, Measuring notch toughness of thin film metallic glasses using focused ion beam-based microcantilever method: Comparison with Ti and TiN crystalline films, Mater. Sci. Eng. A 698 (2017) 104-109.

[196] K. Wu, Y. Xia, H. Yuan, J. Zhang, G. Liu, J. Sun, Cohesive and adhesive properties of nanocrystalline Ti thin films on polyimide substrates, Mater. Sci. Eng. A 744 (2019) 746-753.

[197] K. Wu, J.-Y. Zhang, G. Liu, J. Li, G.-J. Zhang, J. Sun, An easy way to quantify the adhesion energy of nanostructured cu/X (X= Cr, Ta, Mo, Nb, Zr) multilayer films adherent to polyimide substrates, Acta Metallurgica Sinica (English Letters) 29 (2016) 181-187.

[198] J.M. Lackner, W. Waldhauser, T. Schöberl, Film growth phenomena in high-energetic room temperature pulsed laser deposition on polymer surfaces, Surf. Coat. Tech. 201(7) (2006) 4037-4039.

[199] M. Ghidelli, A. Orekhov, A. Li Bassi, G. Terraneo, P. Djemia, G. Abadias, M. Nord, A. Béché, N. Gauquelin, J. Verbeeck, J.-P. Raskin, D. Schryvers, T. Pardoen, H. Idrissi, Novel class of nanostructured metallic glass films with superior and tunable mechanical properties, Acta Mater. 213 (2021) 9.

[200] K. Anderson, J. Weritz, J.G. Kaufman, 1xxx Aluminum Alloy Datasheets, Properties and Selection of Aluminum Alloys. ASM Handbooks, ASM International 2B (2019) 1.

[201] D. Bhattacharyya, N. Mara, P. Dickerson, R. Hoagland, A. Misra, Compressive flow behavior of Al–TiN multilayers at nanometer scale layer thickness, Acta Mater. 59(10) (2011) 3804-3816.

[202] M. Nasim, Y. Li, C. Wen, Length-scale dependent deformation, strengthening, and ductility of fcc/fcc Ni/Al nanolaminates using micropillar compression testing, Acta Mater. 193 (2020) 318-328.

[203] M. Apreutesei, P. Steyer, L. Joly-Pottuz, A. Billard, J. Qiao, S. Cardinal, F. Sanchette, J.M. Pelletier, C. Esnouf, Microstructural, thermal and mechanical behavior of co-sputtered binary Zr–Cu thin film metallic glasses, Thin solid films (561) (2014) 7.

[204] F. Xue, P. Huang, M. Liu, K. Xu, F. Wang, T. Lu, Unusual strain rate sensitivity of nanoscale amorphous CuZr/crystalline Cu multilayers, Mater. Sci. Eng. A 684 (2017) 84-89.

[205] Z. Farhat, Y. Ding, D. Northwood, A. Alpas, Effect of grain size on friction and wear of nanocrystalline aluminum, Mater. Sci. Eng. A 206(2) (1996) 302-313.

[206] G. Wu, C. Liu, L. Sun, Q. Wang, B. Sun, B. Han, J.-J. Kai, J. Luan, C.T. Liu, K. Cao, Hierarchical nanostructured aluminum alloy with ultrahigh strength and large plasticity, Nat. Commun. 10(1) (2019) 5099.

[207] G. Wu, K.-C. Chan, L. Zhu, L. Sun, J. Lu, Dual-phase nanostructuring as a route to high-strength magnesium alloys, Nature 545(7652) (2017) 80-83.

[208] C. Palacio, J. Sanz, J. Martinez-Duart, Preferential sputtering effects in tantalum nitride thin films, Thin solid films 124(3-4) (1985) 243-247.

[209] T. Wang, Q. Hou, L. Zhang, Enhanced heterogeneity and plasticity in a Zr-Cu–Al bulk metallic glass with micro-addition of oxygen, Mater. Sci. Eng. A 831 (2022) 142222.

[210] P. Gondoni, M. Ghidelli, F. Di Fonzo, V. Russo, P. Bruno, J. Martí-Rujas, C.E. Bottani, A. Li Bassi, C.S. Casari, Structural and functional properties of Al:ZnO thin films grown by Pulsed Laser Deposition at room temperature, Thin solid films 520(14) (2012) 4707-4711.

[211] M. Apreutesei, P. Steyer, L. Joly-Pottuz, A. Billard, J. Qiao, S. Cardinal, F. Sanchette, J.M. Pelletier, C. Esnouf, Microstructural, thermal and mechanical behavior of co-sputtered binary Zr–Cu thin film metallic glasses, Thin solid films 561 (2014) 7.

[212] V.G. Keramidas, W.B. White, Raman scattering study of the crystallization and phase transformations of ZrO2, Journal of the American Ceramic Society 57(1) (1974) 22-24.

[213] H. Dan, L. Chen, Z. Li, X. He, Y. Ding, Preparation of amorphous ZrO2 powders by hydrothermal-assisted sol-gel method, Inorganic Chemistry Communications 138 (2022) 109272.

[214] O. Kubaschewski, C.B. Alcock, P. Spencer, Materials thermochemistry, (No Title) (1993).

[215] P. Nayar, A. Khanna, D. Kabiraj, S. Abhilash, B.D. Beake, Y. Losset, B. Chen, Structural, optical and mechanical properties of amorphous and crystalline alumina thin films, Thin solid films 568 (2014) 19-24.

[216] Z. Hu, Y. Xu, Y. Chen, P. Schützendübe, J. Wang, Y. Huang, Y. Liu, Z. Wang, Anomalous formation of micrometer-thick amorphous oxide surficial layers during high-temperature oxidation of ZrAl2, J. Mater. Sci. Technol. 35(7) (2019) 1479-1484.

[217] W. Zhao, J. Cheng, S. Feng, G. Li, R. Liu, Intrinsic correlation between elastic modulus and atomic bond stiffness in metallic glasses, Mater. Lett. 175 (2016) 227-230.

[218] P. Kontis, M. Köhler, S. Evertz, Y.-T. Chen, V. Schnabel, R. Soler, J. Bednarick, C. Kirchlechner, G. Dehm, D. Raabe, Nano-laminated thin film metallic glass design for outstanding mechanical properties, Scripta Mater. 155 (2018) 73-77.

[219] G. Kermouche, G. Guillonneau, J. Michler, J. Teisseire, E. Barthel, Perfectly plastic flow in silica glass, Acta Mater. 114 (2016) 146-153.

[220] R. Lacroix, G. Kermouche, J. Teisseire, E. Barthel, Plastic deformation and residual stresses in amorphous silica pillars under uniaxial loading, Acta Mater. 60(15) (2012) 5555-5566.

[221] T. Rouxel, H. Ji, J. Guin, F. Augereau, B. Rufflé, Indentation deformation mechanism in glass: densification versus shear flow, J. Appl. Phys. 107(9) (2010).

[222] M. Mačković, F. Niekiel, L. Wondraczek, E. Spiecker, Direct observation of electron-beam-induced densification and hardening of silica nanoballs by in situ transmission electron microscopy and finite element method simulations, Acta Mater. 79 (2014) 363-373.

[223] O. Glushko, M. Mühlbacher, C. Gammer, M.J. Cordill, C. Mitterer, J. Eckert, Exceptional fracture resistance of ultrathin metallic glass films due to an intrinsic size effect, Sci. Rep-UK 9(1) (2019) 8281.

[224] A.K. Varshneya, Fundamentals of inorganic glasses, Elsevier2013.
[225] K. Madani, M. Belhouari, B. Bachir Bouiadjra, B. Serier, M. Benguediab, Crack deflection at an interface of alumina/metal joint: A numerical analysis, Comp. Mater. Sci. 38(4) (2007) 625-630.
[226] S. Mahieu, P. Ghekiere, D. Depla, R. De Gryse, Biaxial alignment in sputter deposited thin films, Thin solid films 515(4) (2006) 1229-1249.
[227] B. Koslowski, H.-G. Boyen, C. Wilderotter, G. Kästle, P. Ziemann, R. Wahrenberg, P. Oelhafen, Oxidation of preferentially (1 1 1)-oriented Au films in an oxygen plasma investigated by scanning tunneling microscopy and photoelectron spectroscopy, Surf. Sci. 475(1-3) (2001) 1-10.
[228] D. Mukherjee, M. Hordagoda, R. Hyde, N. Bingham, H. Srikanth, S. Witanachchi, P. Mukherjee, Nanocolumnar interfaces and enhanced magnetic coercivity in preferentially oriented cobalt ferrite thin films grown using oblique-angle pulsed laser deposition, ACS Appl. Mater. Inter. 5(15) (2013) 7450-7457.
[229] M. Ohring, Materials Science of Thin Films: Depositon and Structure, Elsevier2001.
[230] D. Dellasega, G. Merlo, C. Conti, C.E. Bottani, M. Passoni, Nanostructured and amorphous-like tungsten films grown by pulsed laser deposition, J. Appl. Phys. 112(8) (2012).
[231] D. Riabinina, E. Irissou, B. Le Drogoff, M. Chaker, D. Guay, Influence of pressure on the Pt nanoparticle growth modes during pulsed laser ablation, J. Appl. Phys. 108(3) (2010).
[232] E. Irissou, B. Le Drogoff, M. Chaker, D. Guay, Influence of the expansion dynamics of laser-produced gold plasmas on thin film structure grown in various atmospheres, J. Appl. Phys. 94(8) (2003) 4796-4802.
[233] M. Sivakumar, A. Dasgupta, Selected Area Electron Diffraction, a technique for determination of crystallographic texture in nanocrystalline powder particle of Alloy 617 ODS and comparison with Precession Electron Diffraction, Mater. Charact. 157 (2019) 109883.
[234] M. Alymov, A. Ankudinov, K. Agafonov, V. Zelenskii, S. Averin, Effect of the grain size on the density of bulk nanocrystalline materials, Russ. Metall-Metall-U 3 (2005) 273.
[235] H.S. Kim, M.B. Bush, The effects of grain size and porosity on the elastic modulus of nanocrystalline materials, Nanostruct. Mater. 11(3) (1999) 361-367.
[236] A. Latapie, D. Farkas, Effect of grain size on the elastic properties of nanocrystalline α-iron, Scripta Mater. 48(5) (2003) 611-615.
[237] R. Chaim, M. Hefetz, Effect of grain size on elastic modulus and hardness of nanocrystalline ZrO 2-3 wt% Y 2 O 3 ceramic, J. Mater. Sci. 39 (2004) 3057-3061.
[238] R. Dedoncker, G. Radnóczi, G. Abadias, D. Depla, Reactive sputter deposition of CoCrCuFeNi in oxygen/argon mixtures, Surf. Coat. Tech. 378 (2019) 124362.
[239] B. Braeckman, F. Misják, G. Radnóczi, M. Caplovicová, P. Djemia, F. Tétard, L. Belliard, D. Depla, The nanostructure and mechanical properties of nanocomposite Nbx-CoCrCuFeNi thin films, Scripta Mater. 139 (2017) 155-158.
[240] F. Tian, L.K. Varga, N. Chen, L. Delczeg, L. Vitos, Ab initio investigation of high-entropy alloys of 3 d elements, Phys. Rev. B 87(7) (2013) 075144.
[241] Z.C. Cordero, B.E. Knight, C.A. Schuh, Six decades of the Hall–Petch effect–a survey of grain-size strengthening studies on pure metals, Int. Mater. Rev. 61(8) (2016) 495-512.
[242] Y. Li, A.J. Bushby, D.J. Dunstan, The Hall–Petch effect as a manifestation of the general size effect, P. Roy. Soc. A-Math. Phy. 472(2190) (2016) 20150890.
[243] B. Yang, H. Vehoff, Grain size effects on the mechanical properties of nanonickel examined by nanoindentation, Mater. Sci. Eng. A 400 (2005) 467-470.
[244] S.N. Naik, S.M. Walley, The Hall–Petch and inverse Hall–Petch relations and the hardness of nanocrystalline metals, J. Mater. Sci. 55(7) (2020) 2661-2681.
[245] L. Zhang, Y. Shibuta, Inverse Hall-Petch relationship of high-entropy alloy by atomistic simulation, Mater. Lett. 274 (2020) 128024.
[246] J. Lohmiller, N. Woo, R. Spolenak, Microstructure–property relationship in highly ductile Au–Cu thin films for flexible electronics, Mater. Sci. Eng. A 527(29-30) (2010) 7731-7740.
[247] F. Macionczyk, W. Brückner, Tensile testing of AlCu thin films on polyimide foils, J. Appl. Phys. 86(9) (1999) 4922-4929.

[248] V.M. Marx, F. Toth, A. Wiesinger, J. Berger, C. Kirchlechner, M.J. Cordill, F.D. Fischer, F.G. Rammerstorfer, G. Dehm, The influence of a brittle Cr interlayer on the deformation behavior of thin Cu films on flexible substrates: Experiment and model, Acta Mater. 89 (2015) 278-289.
[249] M.A. Meyers, A. Mishra, D.J. Benson, Mechanical properties of nanocrystalline materials, Prog. Mater. Sci. 51(4) (2006) 427-556.
[250] C.-J. Tong, M.-R. Chen, J.-W. Yeh, S.-J. Lin, S.-K. Chen, T.-T. Shun, S.-Y. Chang, Mechanical performance of the Al x CoCrCuFeNi high-entropy alloy system with multiprincipal elements, Metall. Mater. Trans. A 36 (2005) 1263-1271.
[251] Y. Zhao, B. Chen, Y. Wang, J. Zhang, S. Li, K. Wu, G. Liu, J. Sun, Size-dependent microstructural evolution and mechanical properties of crystalline/amorphous high-entropy alloy nanostructured multilayers: Cu/FeCoCrNiBSi vs Ni/FeCoCrNiBSi, Acta Mater. 246 (2023) 118706.
[252] Z. Tang, M.C. Gao, H. Diao, T. Yang, J. Liu, T. Zuo, Y. Zhang, Z. Lu, Y. Cheng, Y. Zhang, Aluminum alloying effects on lattice types, microstructures, and mechanical behavior of high-entropy alloys systems, Jom-US 65 (2013) 1848-1858.
[253] I.N. Mastorakos, H.M. Zbib, D.F. Bahr, Deformation mechanisms and strength in nanoscale multilayer metallic composites with coherent and incoherent interfaces, Appl. Phys. Lett. 94(17) (2009).
[254] W. Johnson, K. Samwer, A universal criterion for plastic yielding of metallic glasses with a (T/T g) 2/3 temperature dependence, Phys. Rev. Lett. 95(19) (2005) 195501.
[255] J. Ye, J. Chu, Y. Chen, Q. Wang, Y. Yang, Hardness, yield strength, and plastic flow in thin film metallic-glass, J. Appl. Phys. 112(5) (2012) 1-9.
[256] A. Kelly, N. Macmillan, Oxford University Press, Walton Street, Oxford OX 2 6 DP, UK, 1986.
[257] J.T. Gudmundsson, Physics and technology of magnetron sputtering discharges, Plasma sources Sci. T. 29(11) (2020) 113001.